DOKUZ EYLÜL UNIVERSITY

GRADUATE SCHOOL OF NATURAL AND APPLIED SCIENCES

APPLICATION OF COLD SPRAY TECHNIQUE IN DEFENCE INDUSTRY

by

Buğra KARAHAN

February, 2024

İZMİR

APPLICATION OF COLD SPRAY TECHNIQUE IN DEFENCE INDUSTRY

A Thesis Submitted to the
Graduate School of Natural and Applied Sciences of Dokuz Eylül University
In Partial Fulfillment of the Requirements for the Degree of Doctor of Philosophy in Department of Metallurgical and Materials Engineering, Metallurgical and Materials Engineering Program

by

Buğra KARAHAN

February, 2024

İZMİR

Ph.D. THESIS EXAMINATION RESULT FORM

We have read the thesis entitled **"APPLICATION OF COLD SPRAY TECHNIQUE IN DEFENCE INDUSTRY"** completed by Buğra KARAHAN under supervision of **PROF.DR. UĞUR MALAYOĞLU** and we certify that in our opinion it is fully adequate, in scope and in quality, as a thesis for the degree of Doctor of Philosophy.

Prof.Dr. Uğur MALAYOĞLU

Supervisor

Prof.Dr. Yusuf ARMAN	Doç.Dr. Mustafa EROL
Thesis Committee Member	Thesis Committee Member
Prof.Dr. Uğur ÇAVDAR	Prof.Dr. Mücahit SÜTÇÜ
Examining Committee Member	Examining Committee Member

Prof. Dr. Okan FISTIKOĞLU

Director

Graduate School of Natural and Applied Sciences

ACKNOWLEDGMENT

During the culmination of this thesis, which has served as a pivotal and integral component of my life for a total of eight years, I find myself experiencing a simultaneous joining of joy and pride. Throughout this study, individuals mentioned below and many others have played a significant role in shaping my development. First and foremost, I express profound gratitude and thanks to my esteemed advisor, Professor Dr. Uğur MALAYOĞLU, for his valuable insights, guidance, support and trust, most notably for providing the opportunity to conduct research freely. I extend my boundless gratitude to Dr. Kadir Cihan TEKİN, who holds a special place for me as both a friend and mentor, for his unwavering support and invaluable advice. Expressing in a few lines the debt and dedication I owe him is an impossible. Additionally, I express my appreciation to the committee members, Professor Dr. Yusuf ARMAN and Associate Professor Dr. Mustafa EROL, for their valuable insights and contributions to the content of my thesis through their meticulous examination.

In moments of hopelessness, tiredness and contemplation of giving up, I express my boundless gratitude and thanks to Nilüfer GENÇ, the compassionate individual from the student affairs office, who consistently provided support and motivation without withholding assistance. I express my gratitude to Dr. Saadet GÜLER, whose friendship and assistance I closely felt during the most challenging times of experimental studies. I extend my thanks to Dr. Aslı ŞAHİNER, particularly for her valuable contributions, insights and support in the execution of microbiologically influenced corrosion tests. I extend my infinite gratitude and thanks to Norm Cıvata A.Ş. and BMC Otomotiv A.Ş., whose contributions played a pivotal role in the initiation and completion of my doctoral studies. Additionally, my appreciation goes to my colleagues for their assistance in this period. I owe the utmost gratitude to my parents, who provided unwavering support throughout my studies. Without their constant love, trust and motivation, the successful completion of this work would not have been possible.

Buğra KARAHAN

APPLICATION OF COLD SPRAY TECHNIQUE IN DEFENCE INDUSTRY

ABSTRACT

Aluminum and its alloys find widespread applications in various industries including aerospace, defense and automotive due to their distinctive mechanical properties, low density and favorable processing characteristics. Considering the operational conditions of these materials, the primary factors limiting their service life are poor corrosion and wear resistance. In this study, Cu-based metal matrix composite coatings were produced on 7075 aluminum alloy using a low-pressure cold gas dynamic spray process with four different coating powders. The investigation focused on the effects of coating composition and thickness on corrosion and wear resistances. The coating powders employed in the study are denoted as CA (100% Cu-Al_2O_3), CNZA15 (85% Cu-Al_2O_3 + 15% Ni-Zn-Al_2O_3), CNZA30 (70% Cu-Al_2O_3 + 30% Ni-Zn-Al_2O_3), and CZA (100% Cu-Zn-Al_2O_3). Within the scope of coating powder characterization, particle size distribution, SEM and XRD analyses were conducted. In the characterization of the coatings, Vickers hardness, surface roughness, XRD, optical microscope and SEM analyses and scratch tests were performed. Electrochemical corrosion tests were carried out using cyclic polarization and electrochemical impedance spectroscopy techniques. Microbiologically influenced corrosion (MIC) tests were conducted in the presence of bacteria (*Pseudomonas aeruginosa*) and fungus (*Aspergillus niger*) and the specimens were incubated for a duration of four weeks. Tribological behavior of the coatings was investigated through sliding wear tests against steel balls in dry and lubricated conditions. In conclusion, it has been determined that coatings of CA exhibit successful outcomes in aggressive corrosion conditions, CZA is effective in MIC environments and CNZA demonstrate favorable results in applications involving wear.

Keywords: Aluminum alloy, cold gas dynamic spray, metal matrix composite coating, corrosion, wear

SOĞUK PÜSKÜRTME TEKNİĞİNİN SAVUNMA SANAYİ UYGULAMALARI

ÖZ

Alüminyum ve alaşımları; ayırt edici mekanik özellikleri, düşük yoğunlukları ve uygun işlenme özellikleri nedeniyle havacılık-uzay, savunma sanayi, otomotiv dahil olmak üzere çeşitli endüstrilerde yaygın kullanım alanı bulmaktadır. Bu malzemelerin operasyonel koşulları göz önünde bulundurulduğunda servis ömürlerini kısıtlayan en önemli faktörler zayıf korozyon ve aşınma direncidir. Bu çalışmada dört farklı kompoziyondaki kaplama tozları kullanılarak 7075 AA üzerinde düşük basınçlı cold gas dynamic spray prosesi ile Cu esaslı metal metrisli kompozit kaplamalar üretilmiş, kaplama bileşiminin ve kalınlığının korozyon ve aşınma direnci üzerindeki etkileri araştırılmıştır. Çalışmada kullanılan kaplama tozları CA (100% Cu-Al_2O_3), CNZA15 (85% Cu-Al_2O_3+15% Ni-Zn-Al_2O_3), CNZA30 (70% Cu-Al_2O_3+30% Ni-Zn-Al_2O_3) ve CZA (100% Cu-Zn-Al_2O_3) olarak belirlenmiştir. Kaplama tozlarının partikül boyut dağılım analizleri gerçekleştirilmiş, toz morfolojileri taramalı elektron mikroskobu kullanılarak belirlenmiş, faz yapıları ve faz oranları X-ışını kırınımı ile tespit edilmiştir. Kaplamaların mikroyapısı optik mikroskop ve taramalı elektron mikroskobu kullanılarak incelenmiştir. Kaplamaların faz yapıları ve faz oranları X-ışını kırınımı ile belirlenmiş, yapışma mukavemetini belirlemek için kazıma testi kullanılmıştır. Elektrokimyasal korozyon testleri, sodyum klorür çözeltisi içerisinde çevrimsel polarizasyon ve elektrokimyasal empedans spektroskopi teknikleri kullanılarak gerçekleştirilmiştir. Mikrobiyolojik korozyon testleri bakteri (Pseudomonas aeruginosa) ve fungus (Aspergillus niger) ortamında gerçekleştirilmiş ve numuneler 4 hafta boyunca inkübasyona bırakılmıştır. Kaplamaların tribolojik davranışını araştırmak amacıyla çelik bilyalara karşı kuru ve yağlayıcı ortamlarda aşınma testleri yürütülmüştür. Sonuç olarak agresif korozyon şartlarında CA, mikrobiyolojik korozyon ortamında CZA ve aşınmanın söz konusu olduğu uygulamalarda CNZA kaplamalarının başarılı sonuçlar ortaya çıkaracağı bulunmuştur.

Anahtar kelimeler: Alüminyum alaşımı, soğuk dinamik gaz püskürtme, metal matrisli kompozit kaplama, korozyon, aşınma

CONTENTS

Page

Ph.D. THESIS EXAMINATION RESULT FORM ii
ACKNOWLEDGMENT iii
ABSTRACT iv
ÖZ v
LIST OF FIGURES xiii
LIST OF TABLES xix

CHAPTER ONE - INTRODUCTION 1

1.1 Background……...1
1.2 Thesis Outline……...3

CHAPTER TWO - ALUMINUM AND ITS ALLOYS IN DEFENSE INDUSTRY 6

2.1 Background……...…..……..….6
2.2 Aluminum and its alloys in defense industry……9
2.3Development of 7XXX Alloys for Civil and Military Structures……13

CHAPTER THREE - SURFACE MODIFICATION BY COLD GAS DYNAMIC SPRAY PROCESS 18

3.1 Background……18
3.2. Thermal Spray Basics and Processes……20
3.2.1 Limitations of Traditional Thermal Spray Process……...21
3.2.2 Comparison of CGDS with Traditional Thermal Spray Process.....21
3.3 Historical Background of The CGDS Process……...24
3.4 An Overview of The CGDS Process…….....26
3.4.1 The Physics of CGDS Process……28

3.4.2 Fundamental Concept of CGDS…….29
3.4.2.1 LPCS Process ……....…….30
3.4.2.2 HPCS Process…….....30
3.4.2.3 Adhesion Mechanism in LPCS and HPCS....…….....31
3.4.3 Deposit with a Single Powder Nature: Cold Sprayability of Materials.33
3.5 Parameters of The CGDS Process…….35
3.5.1 Deposition Efficiency……36
3.5.2 Critical Velocity…….36
3.5.3 Effect of Particle Impact Velocity…….....38
3.5.4 Effect of Particle Morphology……...39
3.5.5 Effect of Powder Feed Rate 40
3.5.6 Effect of Spray Angle.....41
3.5.7 Effect of Standoff Distance 43
3.5.8 Effect of Particle and Substrate Temperature.....43
3.5.9 Gas Temperature and Pressure.....44
3.5.10 Role of Surface Preparations.....45
3.6. Advantages of The CGDS Process.....47
3.6.1 High Deposition Efficiency.....48
3.6.2 High Deposition Rate.....48
3.6.3 No or Little Masking.....49
3.6.4 No Grit Blast.....49
3.6.5 High Density.....50
3.6.6 Flexibility in Substrate-Coating Selection.....50
3.6.7 Minimum Thermal Input to The Substrate.....51
3.6.8 No Powder Melting.....51
3.6.9 High Bond Strength.....52
3.6.10 Compressive Residual Stresses.....52
3.6.11 Ultra-thick Coatings.....53
3.6.12 No Phase Changes.....53

3.6.13 No Oxidation.....54
3.6.14 No Grain Growth 55
3.6.15 High Conductivity.....55
3.6.16 High Corrosion Resistance.....56
3.6.17 High Strength and Hardness.....57
3.7. Limitations of the CGDS process.....57
3.7.1 Near-Zero Ductility.....57
3.7.2 Restricted Selection of Sprayable Materials.....57
3.7.3 Need for a Substrate Material with Adequate Hardness.....58
3.7.4 Gas Consumption.....58
3.8. Mechanism of Coating Formation of The CGDS Process.....59
3.8.1 Impact Phenomena and Bonding Mechanisms in CDGS Process.....59
3.8.1.1 Mathematical Modelling Using Numerical Methods.....64
3.8.1.1.1 Numerical Modelling of Copper Single Particle Impact.....64
3.8.1.1.2 Critical Impact Velocity and Critical Particle Diameter.....65
3.8.1.1.3 Deposition Window in Cold Spray Process.....68
3.8.1.1.4 Particle-substrate Impact Behavior.....69
3.8.1.1.5 Adhesion and Rebounding Energy.....72
3.8.1.2 Experimental Investigations.....74
3.8.1.2.1 Shear Lips and Craters Formation.....74
3.8.1.2.2 Bonding in Low Pressure CGDS Process.....75
3.8.1.2.3 Removal of Surface Oxides.....76
3.8.1.2.4 Contributions of Mechanical and Metallurgical Components on Adhesion 77

CHAPTER FOUR - APPLICATIONS OF COLD GAS DYNAMIC SPRAY PROCESS 79

4.1. Background.....79
4.2. Potential industrial applications of CGDS.....80
4.2.1. Coatings.....82
4.2.1.1 Corrosion protection.....84
4.2.1.2 Wear protection.....84
4.2.2. Restoration/Repair.....84
4.2.3. Additive manufacturing.....85
4.2.4. Biological applications.....87
4.2.4.1 Antimicrobial.....87
4.2.4.2 Antifouling.....88
4.3. Cold Spray Applications in the Defense Industry.....88
4.3.1. Cold Spray Application Examples in the Defense Industry.....90
4.3.1.1 Cast Magnesium Transmission and Gearbox Housings.....90
4.3.1.2 Fretting Damage on an A357 Transmission Housing.....91
4.3.1.3. B-1 Forward Equipment Bay Panel.....92
4.3.1.4. TD-63 Hydraulic Actuator Body. (Navy Valve Actuator Repair).92
4.3.1.5. 2024AA and 7075AA Aircraft Components.....93
4.3.1.6. B-1 Nose Landing Gear False Axle.....93
4.3.1.7. LAU-128 Missile Rail.....93
4.3.1.8. Aging Aircraft Hinge Fitting.....94
4.3.1.9. B-1B Chafing.....94

CHAPTER FIVE - CORROSION AND TRIBOLOGICAL PROPERTIES OF ALUMINIUM ALLOYS 95

5.1 Corrosion of Aluminum and Its Alloys.....95
5.2 Types of Corrosion.....97
5.2.1 General Corrosion.....97
5.2.2 Bimetallic or Galvanic Corrosion.....98

5.2.3 Crevice Corrosion.....99
5.2.4 Pitting Corrosion.....99
5.2.5 Localized Corrosion: Intergranular and Exfoliation.....100
5.2.6 Environmentally Assisted Cracking.....102
5.2.6.1 Stress Corrosion Cracking.....102
5.2.6.2 Corrosion Fatigue.....103
5.2.6.3 Hydrogen Embrittlement.....104
5.2.7 Microbiologically influenced corrosion.....104
5.3 Corrosion Protection in Aluminum Alloys.....106
5.4 Sliding Wear of Aluminum and Its Alloys.....110
5.4.1 Chemical composition.....110
5.4.2 Microstructure.....111
5.4.3 Hardness.....112
5.4.4 Counterface.....112
5.4.5 Temperature1.....112
5.5 Corrosion and Wear Behavior of Cold Gas Dynamic Sprayed Coatings...113

CHAPTER SIX - EXPERIMENTAL DETAILS.....127

6.1 Specimen Preparation.....127
6.2 Coating Powders and Characterization.....128
6.3 Low Pressure CGDS Equipments and Design of Spray Process Experiments.....130
6.4 Coating Characterization.....133
6.4.1 Preparation of Cross-Section of Coating.....133
6.4.2 Microstructural Investigation and Coating Thickness Measurement..134
6.4.3 Measurement of Hardness.....135
6.4.4 Scratch Test.....135
6.4.5 X-Ray Diffraction Measurement.....136

6.4.5.1 Through-Thickness Phase Profile.....137
6.4.5.2 Quantitative Phase Analysis.....137
6.4.6 Surface Profilometry.....138
6.5 Electrochemical Corrosion Tests.....139
6.5.1 Experimental Setup.....139
6.5.2 Cyclic Polarization.....140
6.5.3 Electrochemical Impedance Spectroscopy (EIS).....141
6.6 Microbiologically Influenced Corrosion Tests.....142
6.6.1 Preparation of Test Specimens.....142
6.6.2 Preparation and Revitalization of Microorganisms.....142
6.6.3 Assessment of Microbiologically Influenced Corrosion Tests.....143
6.7 Wear Tests.....144

CHAPTER SEVEN - RESULTS 147

7.1 Characterization of Coating Powders.....147
7.1.1 Particle Size Distribution Analysis.....147
7.1.2 SEM Analysis.....148
7.1.3 Phase Analysis.....156
7.2 Characterization of Cu Based MMC Coatings.....157
7.2.1 Microstructural Investigation and Coating Thickness Measurement...157
7.2.2 Measurement of Hardness.....163
7.2.3 Scratch Test.....164
7.2.4 Phase Analysis.....166
7.2.5 Surface Roughness Analysis.....168
7.3 Electrochemical Corrosion Properties.....168
7.3.1 Cyclic Polarization.....168
7.3.2 Electrochemical Impedance Spectroscopy.....175
7.3.3 Optical microscopy examinations after corrosion tests.....179

7.4 Microbiologically Influenced Corrosion Properties.....184
7.5 Tribological Properties.....192
7.5.1 Wear Behavior.....192
7.5.2 Optical microscopy examinations after wear tests.....197

CHAPTER EIGHT - CONCLUSIONS AND RECOMMENDATIONS..... 203

8.1 Cold Gas Dynamic Spray Process.....203
8.2 Characterization of Coating Powders.....204
8.3 Electrochemical Corrosion Behavior of Cu Based Coatings.....206
8.4 MIC Behavior of Cu Based Coatings.....207
8.5 Wear Behavior of Cu Based Coatings.....208
8.6 Future Works.....210

REFERENCES..... 212

LIST OF FIGURES

Page

Figure 1.1 Comparison of gas temperature and particle velocity in thermal spraying technologies (M. F. Smith, 2007)..... 2

Figure 2.1 Top-down approach used in material selection (Pavel et al., 2020).....7

Figure 2.2 Materials used in military and civil aviation and their usage rates: (a) military and (b) civil (Zhou et al,2021).....10

Figure 2.3 Flow chart for the development of 7XXX alloys (Zhou et al., 2021)…....14

Figure 2.4 Relationships between alloys in the 7XXX series (J. R. Davis, 1996a)….17

Figure 3.1 Various commercial coating processes in practical application (Goyal, 2010)……..…18

Figure 3.2 Comparison of traditional thermal spray processes and CGDS technology in terms of energy source (Pathak & Saha, 2017)……..22

Figure 3.3 Particle behavior depending on velocity in the CGDS process(Karthikeyan, 2004).....27

Figure 3.4 Comparison of the CGDS process with other coating technologies in terms of coating thickness ability (Botef & Villafuerte, 2015).....28

Figure 3.5 Working principle and schematic representation of the LPCS system (H. Singh et al., 2013).....30

Figure 3.6 Working principle and schematic representation of the HPCS system (H. Singh et al., 2013).....31

Figure 3.7 Cross-sectional optical micrographs of copper coatings: (a) HPCS system on steel substrate and (b) LPCS system on aluminum substrate (Cavaliere, 2017).....32

Figure 3.8 Schematic illustration of splat formation in coatings deposited via (a) HPCS and (b) LPCS processes (Cavaliere, 2017).....33

Figure 3.9 The influence of particle velocity on DE in CGDS (Gärtner, Stoltenhoff, Schmidt, et al., 2006a).....37

Figure 3.10 Incubation time versus mean particle velocity of aluminum particles on a polished Cu substrate (V. K. Champagne et al., 2005).....39

Figure 3.11 Disintegration of particle impact velocity at spray angle θ (Ajdelsztajn et al., 2006).....41

Figure 3.12 Impact of spray angle on DE: **(a)** copper and **(b)** titanium (Ajdelsztajn et al., 2006).....42

Figure 3.13 Impact of spray angles on particle bonding and associated deformation (X. Wang et al., 2015).....43

Figure 3.14 Advantages of process properties in CGDS (Botef & Villafuerte, 2015).48

Figure 3.15 Comparing porosity, oxygen content, and thermal properties: Thermal spray vs. cold spray. (*OFHC* oxygen-free high conductivity) (Botef & Villafuerte, 2015).....54

Figure 3.16 Conductivity characteristics of cold-sprayed Cu coatings. (*IACS* International Annealed Copper Standard) (Botef & Villafuerte, 2015). 56

Figure 3.17 Sequential impact of a Cu particle on an aluminum substrate at different time intervals: (a) 5 ns, (b) 20 ns, (c) 35 ns, (d) 50 ns (V. K. Champagne et al., 2005).....60

Figure 3.18 Illustration of coating formation in the CGDS process (V. K. Champagne, 2007).....61

Figure 3.19 Stages of coating development in the CGDS process (Tokarev, 1996)....62

Figure 3.20 Bonding mechanism in a sample case: (a) without and (b) with native surface oxides (Adaan-Nyiak & Tiamiyu, 2023).....62

Figure 3.21 Illustration of interfacial plastic deformation in the CGDS process (Assadi et al., 2016).....63

Figure 3.22 SEM of a Cu particle on a Cu substrate (Assadi et al., 2003) 64

Figure 3.23 Threshold particle diameter for localized ASI in various materials (Schmidt, Gärtner, et al., 2006).....67

Figure 3.24 Correlating particle velocity, DE and impact effects in a schematic at constant temperature (Schmidt et al., 2009).....69

Figure 3.25 Four scenarios of particle impact on substrate: **(a)** soft/soft (Al onto Al), **(b)** hard/hard (Ti onto Ti), **(c)** soft/hard (Al onto Mild Steel), **(d)** hard/soft (Ti onto Al) (Bae et al., 2008).....70

Figure 3.26 A diagram illustrating the impact behavior of various particle-substrate hardness combinations (Rokni et al., 2017).....71

Figure 3.27 Potential particle dynamics upon impact in the context of CGDS using a two-component powder blend with hard and soft components (Lapushkina & Sova, 2019).....72

Figure 3.28 Computed adhesion energy and rebounding energy for Al-Si feedstock of different sizes impacting mild steel (J. Wu, Fang, et al., 2006).....74

Figure 3.29 Views of **(a)** Al particle on Cu substrate and **(b)** Cu particles on Al substrate (Hussain et al., 2009).....75

Figure 3.30 Illustration of jet formation on an aluminum substrate induced by an approaching Cu particle (Hussain et al., 2009).....78

Figure 5.1 Pourbaix diagram for pure aluminum (Pourbaix, 1966).....97

Figure 6.1 Technical drawing of the specimen.....127

Figure 6.2 **(a)** Reitel Sanduret-2K sandblasting device and **(b)** images of specimens following sandblasting process.....128

Figure 6.3 Images of semi-automated coating bench.....131

Figure 6.4 Schematic of DYMET-423 low pressure CGDS equipment and its components.....131

Figure 6.5 Images of Cu-based coatings produced with the CGDS process.....133

Figure 6.6 Three-electrode electrochemical cell configuration utilized in corrosion tests (Tekin, 2016).....139

Figure 6.7 Petri dish specimens: **(a)** *P. aeruginosa* growth medium and **(b)** *A. niger* growth medium.....144

Figure 6.8 CSM instruments standard tribometer configuration utilized in wear tests (Tekin,2016).....145

Figure 7.1 Particle size distribution graphs of coating powders.....148

Figure 7.2 SEM images and EDS mapping outputs of coating powders: **(a)** CA, **(b)** NZA, **(c)** CNZA15, **(d)** CNZA30 and **(e)** CZA.....149

Figure 7.3 Results of point EDS analysis for CNZA30 powder.....155

Figure 7.4 XRD patterns of coating powders.....156

Figure 7.5 Cross-sectional OM images of Cu-based coatings **(a)** 100x and **(b)** 500x magnification.....159

Figure7.6 Cross-sectional SEM images of the Cu-based coatings at 1000x magnification.....160

Figure 7.7 Results of point EDS analysis for CNZA30 coating.....161

Figure 7.8 Graphical presentation of data obtained from scratch tests on Cu-based coatings.....164

Figure 7.9 OM images of scratch tracks on Cu-based coatings.....165

Figure 7.10 XRD patterns of Cu-based coatings: **(a)** 10 passes **(b)** 20 passes.....167

Figure 7.11 Cyclic polarization curves of specimens: **(a)** 10 passes and **(b)** 20 passes.....170

Figure 7.12 Transition regions from forward to reverse scans for cyclic polarization curves of the specimens: **(a)** 10 passes and **(b)** 20 passes.....173

Figure 7.13 Nyquist plots of specimens: DC Voltage **(a)** 0 V (vs OCP) and **(b)** 0.1 V (vs OCP).....176

Figure 7.14 Equivalent circuit models that were used in fitting the impedance spectra of **(a)** 7075 AA, **(b)** CA and CNZA coatings, **(c)** CZA coatings.....177

Figure 7.15 Surface images of specimens after corrosion tests: (a) 7075 AA (b) CA and (c) CZA.....180

Figure 7.16 Cross-sectional images of specimens after corrosion tests: (a) 7075 AA, (b) CA and (c) CZA.....181

Figure 7.17 SEM analysis outputs for the dezincification region: **(a)** point EDS **(b)** EDS mapping.....183

Figure 7.18 Petri dish images containing specimens at the end of the incubation period: **(a)** 7075 AA, **(b)** Bulk Cu, **(c)** CA, **(d)** CNZA15, **(e)** CNZA30 and **(f)** CZA.....185

Figure 7.19 Inhibition zone identified in the *A. niger* medium for the CZA coating.187

Figure 7.20 Images of specimens removed and cleaned from the growth medium: **(a)** 7075 AA, **(b)** Bulk Cu, **(c)** CA, **(d)** CNZA15, **(e)** CNZA30 and **(f)** CZA.....188

Figure 7.21 Wear rates of specimens against AISI 52100 steel ball at an applied load of 1 N.....193

Figure 7.22 Wear profiles of specimens against AISI 52100 steel ball at an applied load of 1 N: **(a)** 10 passes and **(b)** 20 passes.....194

Figure 7.23 Friction coefficients of specimens with dry sliding condition and lubricated condition.....196

Figure 7.24 The wear traces observed on specimens: **(a)** 7075 AA, **(b)** CA 10p, **(c)** CA 20p, **(d)** CNZA15 10p, **(e)** CNZA15 20p, **(f)** CNZA30 10 p, **(g)** CNZA30 20 p, **(h)** CZA 10p and **(i)** CZA 20p.....199

Figure 7.25 The OM image of flattened surface of steel ball rubbed against CNZA30 coating.....202

LIST OF TABLES

Page

Table 2.1 The areas of usage and quantities of various structural materials in military platforms(KPMGin India, 2020)……8

Table 2.2 AAs used specifically for component/subsystem and defense applications (Pavel & Tzimas, 2016)……..12

Table 2.3 Current and recommended uses of conventional aluminum alloys in aircraft body structures (Prasad Rambabu, N. Eswara Prasad & Wanhill, 2017)….13

Table 2.4 Main properties and applications of 7XXX alloys (Zhou et al., 2021)……15

Table 3.1 Characteristic parameters of various thermal spray processes (Bala et al., 2007).....23

Table 3.2 Comparison of CGDS process with competitive technologies (Goyal, 2010).....23

Table 3.3 Operational parameters of HPCS and LPCS systems (Ning et al., 2007)....33

Table 3.4 Typical successful deposits with a single powder nature (Raoelison et al., 2017).....34

Table 3.5 Common combinations of MMCs developed through CGDS process (Raoelison et al., 2017).....35

Table 3.6 Overview of bond strength in various substrate/coating combinations (Jeandin et al., 2015).....46

Table 3.7 Summary of the influence of processing parameters on CGDS deposits (Pathak & Saha, 2020).....47

Table 3.8 Measured critical velocities for Cu particle (King et al., 2015).....67

Tablo 4.1 Current perspectives on the capabilities of the CGDS process (Raoelison et al., 2017).....81

Table 4.2 Applications of CGDS coating materials in manufacturing and engineering industries (Kumar et al., 2020).....83

Table 4.3 Comparison of advantages and disadvantages between CSAM and other fusion-based additive manufacturing (Yin et al., 2018).....86

Table 5.1 Comparison of measured corrosion potentials in 1M NaCl containing H_2O_2 (Birbilis & Hinton, 2010).....98

Table 5.2 Qualitative SCC resistance of aluminum alloys (J. R. (Joseph R. . Davis, 1999).....103

Table 6.1 Experimental sets considered in the production of coatings on 7075 AA.132

Table 6.2 Microorganisms commonly observed in the jet fuel environment (Graef, 2003).....142

Table 7.1 Quantitative analysis results for coating powders.....157

Table 7.2 Thickness measurement results for Cu-based coatings.....162

Table 7.3 Vickers hardness values for the substrate and Cu-based coatings.....163

Table 7.4 Critical load values of Cu-based coatings.....166

Table 7.5 Surface roughness values for the substrate and Cu-based coatings.....168

Table 7.6 Corrosion parameter values of specimens that were obtained by Tafel extrapolation.....169

Table 7.7 Passivation parameter values of specimens that were obtained by cyclic polarization.....172

Table 7.8 The equivalent circuit element values obtained by fitting the EIS curves of specimens.....178

Table 7.9 Volume loss values of specimens that were obtained by TrueSurf program.....192

Table 7.10 Wear track width values of specimens that were obtained by OM investigation.....197

CHAPTER ONE
INTRODUCTION

1.1 Background

Aluminum alloys represent a class of materials widely employed in various industrial applications owing to their favorable combination of lightweight properties and mechanical strength. As these alloys continue to find extensive use in sectors ranging from automotive to aerospace, understanding and mitigating the detrimental effects of corrosion and wear on their structural integrity is of paramount importance. The corrosion and wear behaviors of aluminum alloys are multifaceted phenomena influenced by a myriad of intrinsic and extrinsic factors. Corrosion, an electrochemical process, poses a significant threat to the long-term durability of aluminum alloys, particularly in aggressive environments. Microbiologically influenced corrosion (MIC), mediated by microbial activities, introduces an additional layer of complexity to the degradation of aluminum alloys. The interaction between microorganisms and metal surfaces can accelerate corrosion rates and alter the corrosion morphology. Consequently, a dedicated examination of MIC becomes imperative to provide a holistic understanding of the challenges posed by biocorrosion in aluminum alloy applications. Concurrently, wear, resulting from the interaction between surfaces, further challenges the performance and longevity of these materials. The intricate interplay between corrosion and wear mechanisms necessitates a comprehensive investigation to elucidate the underlying processes and develop effective strategies for enhancing the resistance of aluminum alloys.

A variety of surface modification techniques, including thermal spraying, chemical vapor deposition (CVD), physical vapor deposition (PVD), laser coating, anodization, and plasma electrolytic oxidation (PEO), are available to address the issues mentioned above. Nevertheless, the technologies embedded within the protective scheme exhibit certain drawbacks, including potential environmental and human health risks, the risk of altering the microstructure of the substrate material through thermal effects, the necessity for periodic reapplication at specific maintenance intervals, the requirement for comprehensive equipment and the need for an additional protective layer etc. Cold

gas dynamic spray (CGDS) technology, commonly known as the cold spray process, stands as a transformative advancement in the realm of materials engineering, offering an innovative solution for coating and repair applications. Rooted in the principles of solid-state particle deposition, this technique involves the high-velocity impact of solid powder particles onto a substrate, yielding a dense and cohesive coating. What sets cold spray apart from conventional thermal spray methods is the absence of a melting phase during deposition, presenting distinctive advantages, particularly in addressing challenges related to corrosion and wear. Fundamentally, cold spray operates by accelerating fine powder particles to supersonic velocities through a high-pressure carrier gas. Upon impact with the substrate, these particles undergo plastic deformation, enabling their bonding to the surface without the need for elevated temperatures. This characteristic not only facilitates the deposition of a wide range of materials, including heat-sensitive alloys and composites but also minimizes thermal stress and distortion in the substrate material. The comparison of gas temperatures and particle velocities for cold spray and traditional thermal spraying technologies is presented in Figure 1.1. This comparison demonstrates the relatively unique position of cold spray compared to other spraying technologies, showcasing its capability to provide very high particle velocities along with extremely low process temperatures.

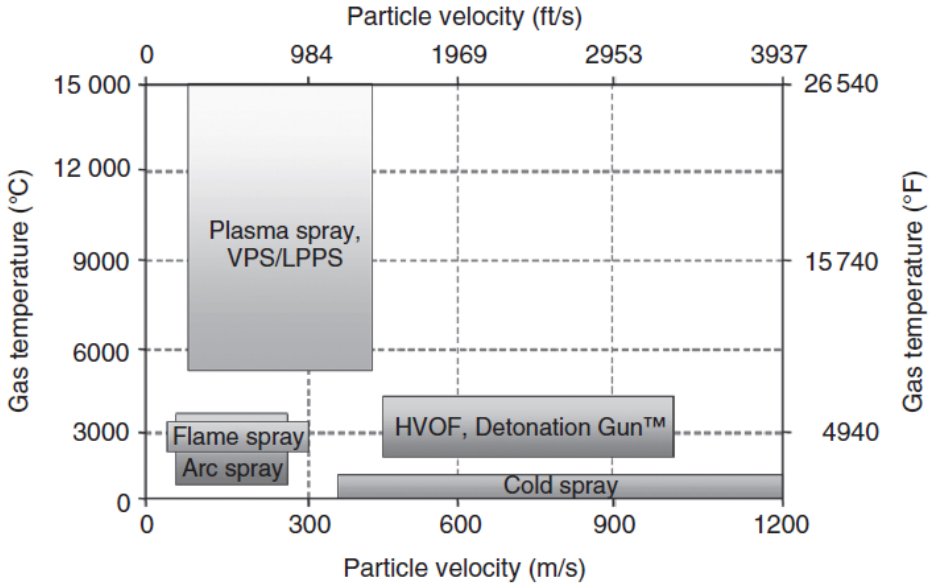


Figure 1.1 Comparison of gas temperature and particle velocity in thermal spraying technologies (M. F. Smith, 2007).

One of the paramount advantages of cold spray technology lies in its inherent ability to enhance corrosion resistance. By avoiding the thermal degradation associated with traditional thermal spray methods, cold spray preserves the integrity of the substrate material, thereby mitigating vulnerabilities to corrosion. The deposition of corrosion-resistant materials through cold spray offers a robust protective layer, presenting a promising avenue for extending the service life of components exposed to corrosive environments. Similarly, cold spray technology demonstrates significant advantages in the realm of wear resistance. The solid-state deposition process ensures minimal alteration to the microstructure of the substrate, resulting in coatings with enhanced mechanical properties. This property, combined with the ability to deposit wear-resistant materials, positions cold spray as a valuable tool in mitigating wear-induced degradation of components subjected to abrasive forces and mechanical wear.

In this study, Cu-based coatings were produced on 7075 aluminum alloy (AA) using a low-pressure CGDS process with four different coating powder compositions. The corrosion and wear resistances of the produced coatings were comprehensively investigated and the influence of coating composition and thickness on these properties was examined. While there is a certain level of research in the literature regarding the corrosion and wear behaviors of coatings produced by the CGDS process, studies specifically addressing the MIC phenomenon are limited. Furthermore, different operational conditions in defense industry applications introduce varied damage mechanisms for AAs. Therefore, this study aims to obtain optimal composition and thickness information for coatings to applications where aggressive corrosion conditions, MIC and wear are predominant.

1.2 Thesis Outline

Chapter two provides a methodology for material selection in defense industry applications, outlining the types and quantities of materials used in military platforms. It summarizes the historical development and applications of aluminum and its alloys in the defense industry, with a particular focus on the 7XXX series aluminum alloys, detailing their historical evolution, fundamental properties and applications.

Chapter three encompasses the fundamentals and limitations of the thermal spray coating family, a comparison between traditional thermal spray coatings and the CGDS technology, the historical development and fundamentals of the CGDS technology, parameters of the CGDS process, as well as the advantages and limitations inherent to the CGDS process. It delves into the details of the coating formation mechanism in the CGDS process.

Chapter four encompasses the potential industrial applications of the CGDS process, the functional characteristics of cold-sprayed coatings, typical application areas, examples and a literature review specifically focusing on defense industry applications.

Chapter five includes a literature review on the corrosion and wear behaviors of aluminum and its alloys, general protective methods and the effects of cold-sprayed coatings on corrosion and wear resistances.

Chapter six provides a summary of the coating production stages and the experimental methodologies employed in the CGDS process. Experimental investigations are categorized into two primary groups: powder characterization and coating characterization. Powder characterization studies encompass particle size distribution analysis, determination of powder morphologies using scanning electron microscopy (SEM) and phase analysis through X-ray diffraction (XRD). Coating characterization studies include specimen preparation, phase analysis using XRD, microstructural examinations using optical microscopy (OM) and SEM, Vickers hardness analysis and scratch testing. Additionally, details regarding electrochemical corrosion, MIC and wear tests for Cu-based coatings are presented in this section.

Chapter seven incorporates the results obtained from the characterization studies of coating powders and Cu-based coatings. The experimental outcomes of electrochemical corrosion, MIC and wear tests for Cu-based coatings are also presented. Furthermore, details obtained from microstructural examinations after corrosion and wear tests are shared in this section. Ultimately, composition and thickness information for Cu-based coatings to applications involving aggressive corrosion conditions, MIC and wear is provided.

Chapter eight encapsulates the principal findings derived from this study and proffers recommendations for prospective research endeavors.

CHAPTER TWO
ALUMINUM AND ITS ALLOYS IN DEFENSE INDUSTRY

2.1 Background

Materials serve as a foundational element in engineering, contributing to the development of diverse applications across various fields. Consequently, the research and development of new materials play a crucial role in advancing science and technology. Material research can be tailored to meet the specific requirements of particular application areas. For instance, in the defense industry, materials must endure the challenging conditions of air, land, and sea platforms. These materials are crafted by combining pure metals, alloys, or non-metallic substances to enhance military capabilities. The resilience and longevity of devices and systems utilized in demanding environments hinge on the quality of materials and their correct utilization. The durability and advancement of materials play a pivotal role in ensuring the effective life cycle of weapon systems, military vehicles, and electronic devices (Özkan et al., 2020).

As technology continues to advance, the demand for enhanced performance steadily rises, placing increased pressure on designers and manufacturers. Alleviating this pressure is achievable through the utilization of diverse raw and advanced materials that confer unique properties to products. A top-down methodology was employed for conducting this evaluation. In the initial phase, relevant defense applications across various sectors (land, air, naval, space, electronics and missiles) were identified. Subsequently, these applications were decomposed into subsystems and components. The next step involved a comprehensive analysis, wherein both processed and raw materials employed in the production of these subsystems and components were identified. The systematic approach applied in this study is illustrated in Figure 2.1.

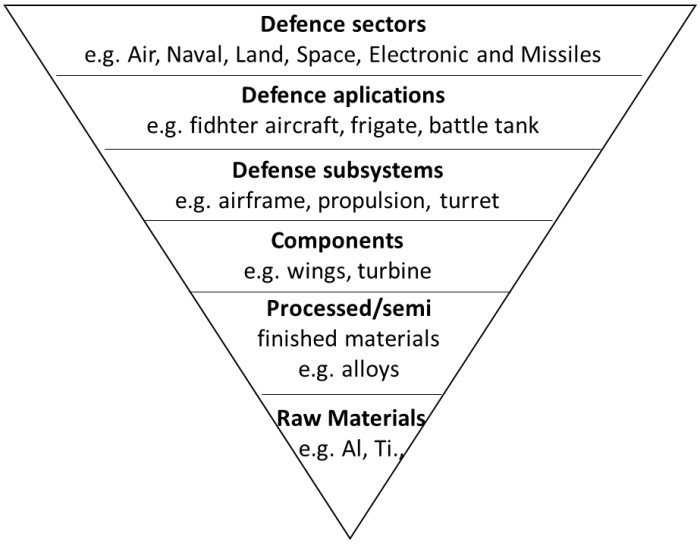


Figure 2.1 Top-down approach used in material selection (Pavel et al., 2020)

The material selection for defense products is guided by three fundamental criteria: (1) the choice of applications demanding substantial material quantities and produced at high volumes, such as navy vessels and main battle tanks, (2) the prioritization of strategic assets, with a special emphasis on critical defense systems like warplanes, and (3) a concentration on high-tech systems necessitating specific or highly pure materials, as seen in satellites. These criteria offer strategic direction for material selection across a diverse range of applications within the defense industry (Pavel et al., 2020).

The analysis indicates that the predominant materials employed in the manufacturing of defense equipment are processed and semi-finished materials, including metallic alloys, composites, and similar materials. It is observed that a variety of alloys are utilized in the production of different defense applications. For instance, aluminum-based alloys (from the 2000 and 7000 series) and the titanium-based alloy TA6V (consisting of 90% titanium, 6% aluminum, and 4% vanadium) are incorporated into the airframes of fighter jets. Jet fighter turbines incorporate nickel and single crystal superalloys. Equipment designed for high-temperature and corrosive environments typically comprises aluminum, titanium, and steel alloys. In marine applications, ultra-high strength steel alloys, incorporating nickel, molybdenum, manganese, and vanadium, are favored in the construction of submarine hulls. Gun

barrels and missile bodies are crafted from special steels and nickel alloys. Torpedoes are generally manufactured using aluminum alloys (Pavel et al., 2020).

Materials utilized in the aerospace and defense industry are typically categorized into primary groups such as steel, aluminum, titanium, copper, copper-nickel, tungsten, composites, and ceramics. These materials are frequently alloyed with other metals like nickel, vanadium, zinc, cobalt, antimony, molybdenum, borates, chromium, germanium, and lithium, enabling the formation of alloys with distinct properties and characteristics tailored for specific applications. Details regarding platforms and usage quantities in kilograms of materials employed in defense industry applications can be found in Table 2.1. The table highlights that aluminum, steel, and composite materials are prominent in the utilization within defense industry applications.

Table 2.1 The areas of usage and quantities of various structural materials in military platforms (KPMG in India, 2020).

	Direct structural materials (kg)				
Platform	**Aluminum**	**Steel**	**Titanium**	**Composites**	**Others**
Twin engine aircraft	2350	800	1200	2300	1170
Single engine aircraft	2240	280	280	2240	560
Helicopters	945	315	470	945	473
Unmanned aerial vehicle	80	25	0	640	60
Missiles	260	200	160	200	200
Frigate/Destroyer/ Corvettes	122500	1400000	0	87500	140000
Submarines	77000	639100	0	23100	30800
Auxiliary ships	35000	400000	0	25	40000
Patrol boats	40500	162000	0	40500	27000
Main Battle Tanks	5000	12500	3750	2500	1250
Infantry Combat Vehicles	4900	8800	2900	1900	1000
Artillery	0	3600	0	0	400
Smal arms	0	3,5	0	0	0.5
Special vehicles	2250	4050	1350	900	450
Small arms and ammunitions	0	0	0.05	0	0

2.2 Aluminum and its alloys in defense industry

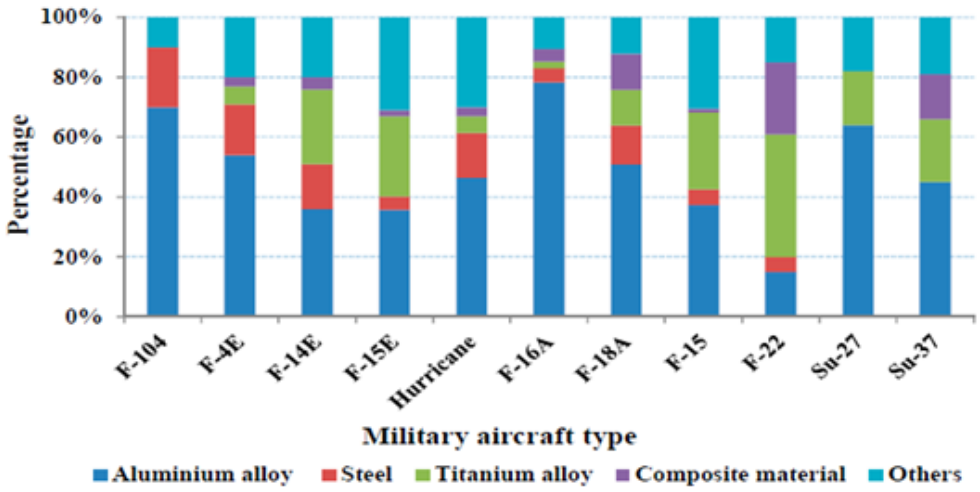
Aluminum alloys (AA) play a pivotal role in various industries such as aerospace, automotive, weapons, and defense due to their distinctive mechanical properties and low density. These characteristics render AAs well-suited for applications requiring a notably high strength-to-weight ratio (Cagan et al., 2020). Despite the increasing prevalence of composite materials in the aircraft industry, high-strength AAs continue to be deemed crucial for airframe materials, playing a vital role. The cost-effectiveness of aluminum and its other appealing properties, including lightweight construction, position it as an ideal metal for various applications. It can undergo heat treatment to attain high strength levels and is easily manufacturable, generally resulting in lower costs. However, aluminum also exhibits some drawbacks, such as a low elastic modulus and limited high-temperature capability. Additionally, high-strength AAs may be vulnerable to corrosion (Prasad Rambabu, N. Eswara Prasad & Wanhill, 2017).

Since approximately the 1930s, AAs have maintained their status as the preferred material for structural components in aircraft. While polymer matrix composites are currently utilized in specific applications for high-performance military and modern civil aircraft, AAs persist as the material of choice for the fuselage, wing, and support structure of civilian aircraft, as well as military cargo and transport aircraft. This preference is attributed to various factors, including well-established performance characteristics, known production costs, extensive design experience, and established production methods and facilities. Additionally, significant advancements in aluminum aircraft alloys have been achieved, allowing them to remain competitive in the market (Starke & Staley, 2010).

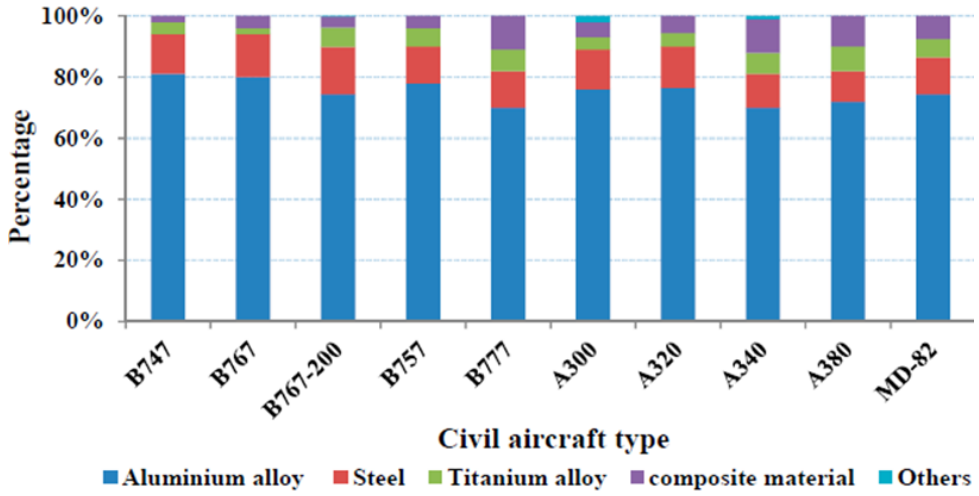
In the 1920s, pioneers in aircraft design, such as Dr. Hugo Junkers, Claudius Dornier, and Adolph Rohrbach, conducted experiments with aluminum in aviation. Their findings revealed that aluminum's high specific properties, stemming from its low specific gravity, made it an exceptional choice for applications where weight was a critical factor. Specifically, Hugo Junkers favored an AA known as 'duralumin', which includes copper, magnesium, and manganese and has the capability to harden over time. The discovery of duralumin dates back to 1906 when German chemist Alfred Wilm sought a lightweight alternative to brass for cartridge cases. Although

duralumin was initially used in zeppelins, it did not find application in load-bearing aircraft components before Junkers' design due to susceptibility to exfoliation corrosion when exposed to air. However, in 1927, metallurgists at Alcoa developed a method to coat AAs with pure aluminum, providing protection in harsh environments and mitigating exfoliation corrosion risks. Concurrently, in England, the technique of anodizing aluminum was developed. Anodizing, a process that enhances corrosion resistance by generating a thick, protective oxide film on the surface of aluminum, marked a significant shift in aviation structures. As a result, AAs began to be extensively used in aircraft fuselages after 1927 (Starke & Staley, 2010).

The utilization of materials in both military and civilian aircraft, along with their respective usage percentages, is illustrated in Figure 2.2. Despite notable shifts in the primary structural materials employed in military aircraft, AAs continue to be a prevalent selection. The utilization rate of AAs in military aircraft surpasses 35%, with the exception of the F-22. In contrast, AAs constitute over 70% of the materials used in civil aircraft.



(a)



(b)

Figure 2.2 Materials used in military and civil aviation and their usage rates: (a) military and (b) civil (Zhou et al., 2021)

The advancement of AAs has been a pivotal driving force not only in aviation but also in various defense industry equipment and the space sector, and this influence persists to the present day. Following World War II, AAs found applications in space technologies as well. The initial rockets developed by the United States, such as the Avantgarde and Titan, incorporated AAs. Presently, key components such as NASA's space shuttle and the international space station utilize aluminum-lithium alloys, including those from the 2000 series of AAs (Runge, 2018). By the late 1950s, AAs had emerged as the preferred material for armored fleets. In this context, weldable AAs were favored and extensively employed, even with certain compromises in terms of strength and ballistic performance. Criteria like weight variability, ease of production, ballistic performance, and ease of maintenance play a pivotal role in selecting alloys for vehicle defense applications. Specifically, AAs such as 2024 AA, 2519 AA, 5059 AA, 5083 AA, 6061 AA, 7039 AA, and 7075 AA are widely used as armor materials for military vehicles (Wino et al., 2022). The commonly used AAs in the defense industry and detailed examples of their applications are presented in Table 2.2.

Table 2.2 AAs used specifically for component/subsystem and defense applications (Pavel & Tzimas, 2016).

Processed materials	Typical component/ subsystem	Example of defense applications
2000 and 7000 series AAs (2024, 7010, 7040, 7050, etc.)	Interior paneling and fuselage structural components	Fighter aircraft, transport aircraft and maritime patrol aircraft
Light AAs (e.g. 5059, 6061) and others (e.g. aluminum-copper-lithium alloys)	Lightweight defense vehicle engineering structures and components, such as armor structures, rocket and missile casings, fuel pipe systems, frames, and structural elements	Fighter aircraft, transport aircraft, main battle tank and infantry fighter vehicle

Within AAs, the high-strength 2XXX alloys (such as 2024, 2224, 2324, 2424, 2524, etc.) and the ultra-high-strength 7XXX alloys (including 7050, 7055, 7075, 7085, 7150, 7475, etc.) stand out as the most prevalent. Despite the rapid development of new materials since the 1980s, such as aluminum-lithium alloys, fast-solidifying AAs, and aluminum matrix composite materials, traditional 2XXX and 7XXX alloys continue to be favored for their superior performance. The classification of aviation aluminum can be based on various production techniques, such as cast AA, extruded AA, rolled AA, and forged AA. Table 2.3 provides a comprehensive overview of the current and planned applications of conventional 2XXX and 7XXX AAs in airframe structures. Manufacturers offer similar variations tailored for different product forms and applications. The creation of a variety of alloy tempers plays a crucial role in enhancing versatility, allowing for property optimization and the selection of the most suitable alloy for a specific application.

Table 2.3 Current and recommended uses of conventional aluminum alloys in aircraft body structures (Prasad Rambabu, N. Eswara Prasad & Wanhill, 2017).

Product	Strength levels	Alloy/temper	Applications
Sheet	Damage tolerant	2024-T3, 2524-T3/351	Fuselage/pressure cabin skins
	Damage tolerant	2024-T351, 2324-T39, 2624-T351, 2624-T39	Lower wing covers
	Medium strength	2024-T62	Tactical aircraft fuselage panels
	Medium strength	2124-T851	Tactical aircraft bulkheads
Plate	Medium strength	7050-T7451, 7X75-T7XXX	Internal fuselage structures
	High strength	7150-T7751, 7055-T7751, 7055-T7951, 7255-T7951	Upper wing covers
	Medium strength	7050-T7451	Spars, ribs, other internal structures
Forgings	High strength	7175-T7351, 7050-T7452	Wing/fuselage attachments
	Damage tolerant	2024-T3511, 2026-T3511, 2024-T4312, 6110-T6511	Lower wing stringers and fuselage/pressure cabin stringers
Extrusions	Medium/high strength	7075-T73511, 7075-T79511, 7150-T6511, 7175-T79511, 7055-T77511, 7055-T79511	Fuselage stringers and frames, upper wing stringers, floor beams, seat rails

2.3 Development of 7XXX Alloys for Civil and Military Structures

Between 1923 and 1924, a significant breakthrough in the study of aluminum alloys took place when a team of German scientists led by Sander and Meissner made a noteworthy discovery concerning the Al-Mg-Zn alloy. Through the process of solid solution, quenching, and aging, they found that a strengthening phase known as $MgZn_2$ was formed, resulting in a substantial enhancement in its strength. This pivotal discovery laid the groundwork for subsequent research on 7XXX alloys. Building on this, in 1932, Webber and colleagues further advanced the understanding of Al-Mg-Zn alloys. They determined that incorporating small amounts of copper and manganese into these alloys could enhance their resistance to stress corrosion cracking (SCC).

This revelation marked the development of the initial versions of 7XXX alloys, forming the basis for the evolution of later iterations (Sander & Meissner, 1926).

Between 1935 and 1939, the Japanese scientist Igarashi made remarkable strides in advancing high-strength AAs. His breakthroughs involved the addition of chromium, manganese, and molybdenum to Al-Mg-Zn-Cu alloys. These investigations led to the formulation of a novel extra super duralumin alloy characterized by exceptional strength and resistance to SCC. This alloy found its initial application in carrier-based aircraft due to its superior performance. In 1943, the United States introduced the 7075 alloy, a development that was incorporated into the B-29 bomber and played a pivotal role in propelling the progress of high-strength AAs in the aviation industry. Subsequently, in 1948, the former Soviet Union developed the B95 AA, featuring a composition akin to the 7075 alloy. This achievement marked another crucial milestone in the advancement of high-strength AAs (Zhou et al., 2021).

The enhancement of 7XXX alloys encompasses improvements targeted at various aspects while building upon existing properties. These improvements entail reducing the content of impurities, increasing the degree of alloying, and optimizing the utilization of trace transition group elements, as illustrated in Figure 2.3.

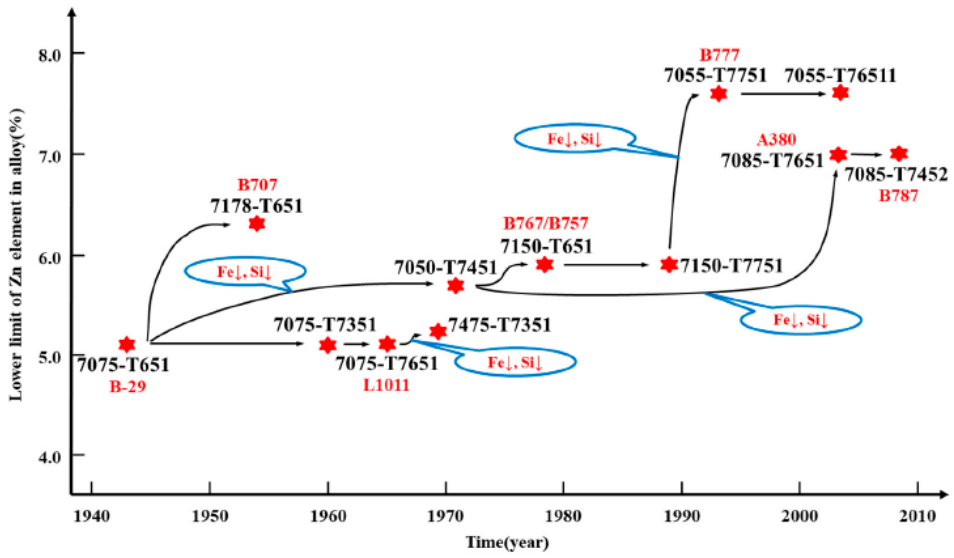


Figure 2.3 Flow chart for the development of 7XXX alloys (Zhou et al., 2021).

Table 2.4 furnishes a thorough summary of the fundamental properties and applications of 7XXX alloys. The data reveals that 7075 alloys are predominantly employed in fuselage bulkheads, wing upper fairings, wing upper panels, and vertical tails. In contrast, the 7475 alloy is generally favored for wing skins, while 7050 alloys typically find primary application in fuselage bulkheads. For long fuselage stringers, fuselage beams, and upper fuselage stringers, 7055 alloys are commonly utilized. Wing spars and ribs are mostly made from 7085 alloys.

Table 2.4 Main properties and applications of 7XXX alloys (Zhou et al., 2021).

Alloy	Main Features	Main Applications
7075	Low temperature strength, poor weldability and low SCC resistance	Skins of the upper and lower wings, stringers, and frames
7049	High strength, good SCC resistance, as opposed to 7079	Primary landing gear
7149	Superior to 7049 in terms of strength, SCC resistance, and fracture toughness	Primary landing gear
7249	Superior all-encompassing qualities compared to 7149	Primary landing gear
7175	Strong and resistant to corrosion	Main landing gear and spares
7475	Excellent resistance to fatigue, good corrosion resistance, high strength and high fracture toughness	Skins of the fuselage, wings, bulkheads, spars, and central wing structures
7050	Excellent resistance to SCC, high strength, and good fracture toughness inadequate sensitivity to hardening	Stringers, bulkheads, wing skins, fuselage frame and stiffener
7150	Excellent strength, resistance to corrosion, and ability to withstand fatigue	Fuselage reinforcement, skeletons, seat tracks, upper wing structures, fixed leading edge, and upper wing stringers
7055	Comparable to 7150 in terms of corrosion resistance and fracture toughness, but with greater compressive and tensile strengths	Skeletons, seat tracks, cargo tracks, horizontal stabilizer, upper wing skins and stringers
7085	Strong hardening, high strength, high fracture toughness, good SCC, and good comprehensive properties	Stringers and spars on wings

The 7XXX series alloys are comprised of a combination of zinc, magnesium, and copper, often with the inclusion of manganese. Alloys containing copper exhibit the

highest strength and are extensively utilized, particularly in aircraft applications. Nevertheless, copper-free alloys within this series possess several desirable properties, including medium to high strength, excellent toughness, good machinability, formability, and weldability. In recent years, the use of these copper-free alloys has witnessed an increase, extending to various applications such as the automotive industry, military vehicles, and other transportation equipment. Both 7XXX wrought and 7XXX cast alloys are more anodic than 1XXX wrought aluminums and other AAs due to their zinc content, rendering them more susceptible to SCC. However, appropriate alloy and temper selection, along with careful design, assembly, and application measures, can mitigate the risk of SCC. Copper-free wrought 7XXX alloys exhibit good resistance to general corrosion and possess properties closely resembling those of wrought 3XXX, 5XXX, and 6XXX alloys. In contrast, copper-containing alloys in the 7XXX series demonstrate lower resistance to general corrosion compared to their copper-free counterparts within the same series (J. R. Davis, 1996a; Xiong et al., 2015).

High-strength AAs, notably examples like 7075-T6, find extensive use in aircraft structures due to their remarkable strength-to-weight ratio, processability, and cost-effectiveness. However, these alloys are susceptible to corrosion owing to their composition. Corrosion is a critical factor that can significantly diminish the lifespan of aircraft structures. During routine operations, aircraft are exposed to natural corrosive elements such as humidity, rainfall, temperature fluctuations, oil, hydraulic fluids, and saltwater. Given the vulnerability of high-strength AAs to corrosion, protective measures are crucial. Methods for corrosion protection include coating with pure aluminum and anodizing for sheet alloys, as well as anodizing or ion vapor deposition, primer, and paint systems for other types of products. Nevertheless, some AAs may remain susceptible to SCC, a phenomenon that arises when a specific corrosive environment and consistent tensile stress coincide. Important aerospace aluminum alloys prone to SCC encompass those in the 2XXX-T8XX, 7XXX-T6XX, and 7XXX-T7XX tempers (Prasad Rambabu, N. Eswara Prasad & Wanhill, 2017).

AAs in the 7XXX series, while offering greater strength, are generally more prone to SCC. To mitigate this susceptibility, a slightly overaged tempering process is often

employed. This approach aims to enhance strength, corrosion resistance, and fracture toughness. Figure 2.4 illustrates the relationships between some of the most frequently utilized alloys in the 7XXX series.

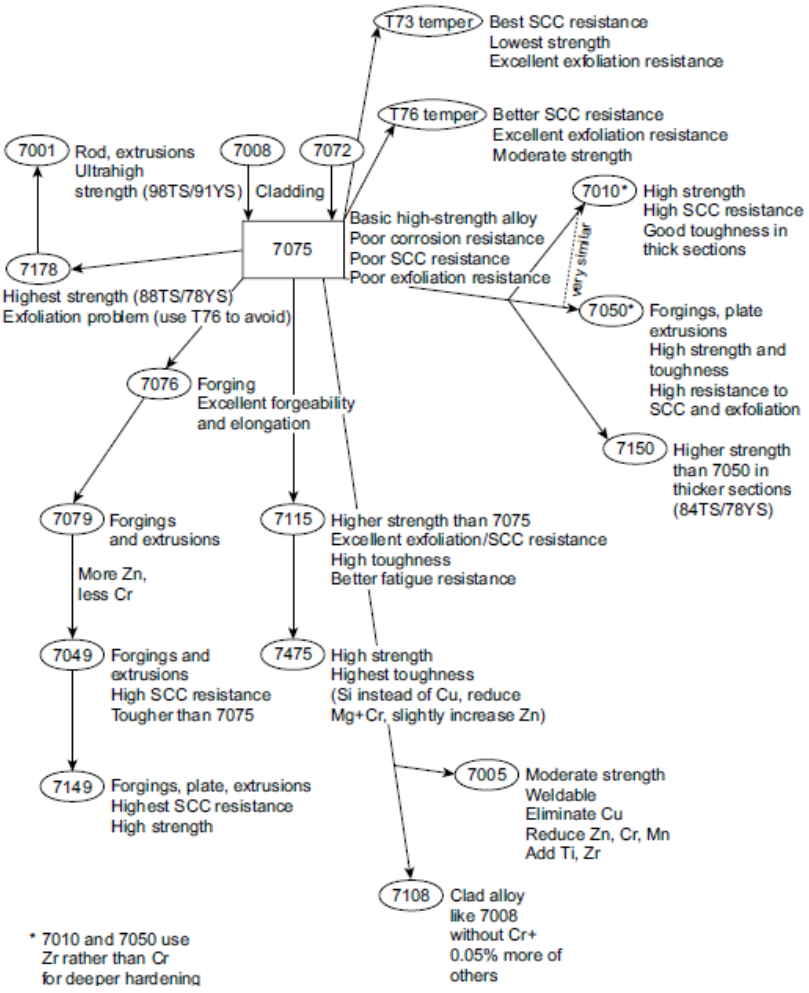


Figure 2.4 Relationships between alloys in the 7XXX series (J. R. Davis, 1996a).

CHAPTER THREE
SURFACE MODIFICATION BY COLD GAS DYNAMIC SPRAY PROCESS

3.1 Background

Surface engineering is a field dedicated to enhancing the surface properties of materials with the goal of extending the functionality and lifespan of components. Coatings play a crucial role in this endeavor, imparting various functional attributes by forming a thin film layer on the material's surface. These coatings are strategically applied to augment thermal and corrosion resistance, elevate wear resistance, diminish the coefficient of friction, or enhance the aesthetic and decorative qualities of the material. A variety of coating techniques and surface engineering methods are employed in this pursuit, each tailored to specific requirements. Notable methods include physical vapor deposition (PVD), chemical vapor deposition (CVD), electroplating, anodization, thermal spraying, laser processing and sol-gel processes. These techniques contribute to the development of surfaces with optimized properties, aligning with the desired functionalities and applications. Figure 3.1 illustrates some of the commercially utilized coating processes, providing a visual representation of the diverse methods employed in surface engineering (Goyal, 2010).

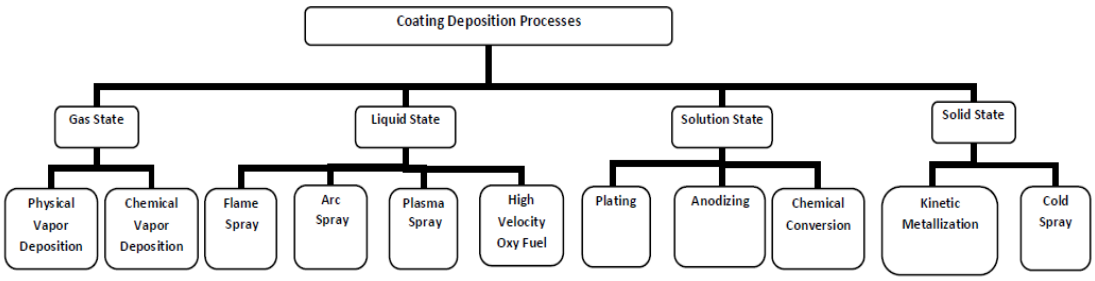


Figure 3.1 Various commercial coating processes in practical application (Goyal, 2010).

Enhancing the performance and durability of components is achieved through surface engineering and the proper application of coatings, leading to reduced energy consumption, extended lifespan and minimized maintenance costs. To ensure the effective utilization of these technologies, it is essential to consider various factors for the accurate selection and optimization of coating materials and application

techniques. Choosing the right coating for a specific application involves careful consideration of factors such as operating conditions, material compatibility, surface preparation, substrate material, application time or speed, cost, safety, environmental impact, coating properties and structural design (Dobler, 2006).

Thermal Spray technology is extensively employed in the defense, aerospace and gas turbine industries, serving various purposes such as component manufacturing, protective surface preparation and the restoration of parts affected by mis-machined or service-related damage (J. R. Davis, 2004). In response to the growing demand for metallic coatings across industrial sectors, thermal spray technologies have undergone significant advancements, evolving into more specialized and precise tools. This versatile technology now generates coatings for a wide array of applications, ranging from thermal barriers to corrosion protection, wear resistance, biomedical implants, and complex industrial uses. Traditional thermal spraying methods involve melting or partially melting feed materials in powder or wire form, followed by cooling and solidification to form the desired coating. However, the elevated temperatures in this process can lead to substantial oxidation, limiting the applicability of these coatings in commercial settings, especially for temperature-sensitive materials. To address these challenges, Cold Gas Dynamic Spray (CGDS) technology, commonly known as the cold spray process, has emerged as a solution, allowing for effective coating deposition at lower temperatures (Lupoi & O'Neill, 2011; Villafuerte, 2010).

CGDS technology harnesses a supersonic gas jet to achieve elevated particle velocities, enabling the formation of coatings on substrates through the impact and coalescence of metal and alloy particles at low temperatures. This innovative approach effectively prevents or minimizes reactions such as oxidation, evaporation and melting in materials sensitive to high temperatures. The CGDS process distinguishes itself by relying on high-velocity rather than high-temperature conditions, offering several advantages over conventional thermal spraying techniques (Lupoi & O'Neill, 2011; *US5302414A - Gas-Dynamic Spraying Method for Applying a Coating - Google Patents*, n.d.). Coatings produced through CGDS exhibit notable benefits, including the presence of compressive stresses instead of tensile stresses, a microstructure akin to wrought materials, density closely approaching theoretical density, oxide-free

coatings and the generation of a high-density particle beam (Bhagat et al., 1997; *US5302414A - Gas-Dynamic Spraying Method for Applying a Coating - Google Patents*, n.d.).

3.2. Thermal Spray Basics and Processes

Thermal spraying is a broad term encompassing the application of both metallic and non-metallic coatings onto a substrate, achieved through the deposition of molten or semi-molten particles. In this method, particles are heated and propelled towards the substrate. The elevated temperature and/or velocity of the particles result in the formation of a deformed spatter on the substrate. As successive splashes accumulate, they create a coating on the substrate, with the thickness of the coating ranging from a few microns to several millimeters(J. R. Davis, 2004).

Thermal spraying processes can be broadly categorized into three main types: flame spraying, electric arc spraying and plasma arc spraying (J. R. Davis, 2004). In these methods, diverse energy sources, including flame, electric arc, and plasma, are employed to melt coating materials such as powder, wire or rod and propel them towards the substrate. Fundamentally, all traditional thermal spray processes share the same basic principles and these principles trace back to a significant patent filed by M. A. Schoop and co-workers in 1911 (M. F. Smith, 2007).

Thermal spraying offers a notable advantage in its capability to apply coatings made of partially meltable materials or composites without experiencing fragmentation. Figure 1.1 in Chapter 1 presents a comparison of the temperature of the gas and the particle velocity in different thermal spray processes. Flame spraying includes high-velocity oxygen-fuel (HVOF) techniques, wire flame and low-velocity powder flame techniques. HVOF techniques are distinguished by comparatively low gas temperatures. When using flame spraying, the coating material is heated and carried towards the substrate by the flame after being absorbed into the oxygen-fuel flow. Two consumable wire electrodes are inserted into the gun for arc (wire) spraying. An arc forms between the wire ends when they melt. The molten metal is then driven toward the substrate by a gas flow that has atomized it. Particle velocity is low, but the

temperature is higher than in flame spraying operations. With a powder heating zone that ranges from 2500 °C to 14000 °C—well above the melting point of many materials—the plasma spraying process stands out. Typically, plasma is generated by heating argon or an argon-hydrogen mixture with a DC arc. This method enables the spraying of various materials, including ceramics (J. R. Davis, 2004).

3.2.1 Limitations of Traditional Thermal Spray Process

Conventional thermal spraying processes exhibit two primary limitations: porosity and the formation of oxides within the sprayed material. These flaws in the microstructure of the sprayed coating can significantly impact the mechanical, electrical and thermal properties compared to materials obtained through conventional processing methods. Excessive porosity poses a risk of corrosion or other issues when the coating is intended to protect the underlying substrate from the influence of liquid or gaseous substances. During the spraying of metals, the reaction between hot molten metal and oxygen in the surrounding atmosphere leads to the formation of metal oxide impurities within the coating. Residual stresses are another drawback of traditional thermal spraying processes. As each molten droplet solidifies and cools to room temperature, it undergoes thermal contraction in direct proportion to the temperature change (ΔT) and the thermal expansion coefficient (α) of the material. Given that the underlying material is generally cooler, each successive layer of material retains a state of residual stress, causing the total residual stress in the coating to continuously accumulate with the addition of successive layers. An additional limitation of thermal spraying processes is that coating is restricted to surfaces directly accessible to the spray stream. In other words, only surfaces with a direct line of sight to the spray gun can undergo coating (M. F. Smith, 2007).

3.2.2 Comparison of CGDS with Traditional Thermal Spray Process

In the development of thermal spray coatings, the energy source plays a crucial role in transforming the material into a molten or semi-molten state. The resultant heated particles are then propelled and directed towards a prepared substrate through process gases or atomization jets. This process creates a bond with the surface and forms a

lamellar structure through the accumulation of successive particles. The properties of the coating, including density, adhesion between deposited particles, and particle adhesion, may vary. However, utilizing high processing temperatures for many materials can introduce challenges such as carbon reduction, dissolution and delamination in coatings (Fauchais et al., 2010). Specifically, for materials sensitive to oxygen, the production of coatings may necessitate the use of an expensive vacuum chamber, limiting the broader application of thermal spray in commercial settings (J. R. (Joseph R. . Davis, 2001; Dobler et al., 2000). Traditional thermal spray processes often prove inadequate for temperature-sensitive materials and for repair and manufacturing applications requiring coatings several millimeters thick. These challenges have been successfully addressed by innovative thermal spray methods like CGDS technology (Pathak & Saha, 2017).

A fundamental distinction exists between traditional thermal spray techniques and the CGDS process, as illustrated in Figure 3.2. Traditional thermal spray techniques rely on both thermal and kinetic energy to facilitate coating formation. In contrast, the CGDS process utilizes solely kinetic energy for the same purpose.

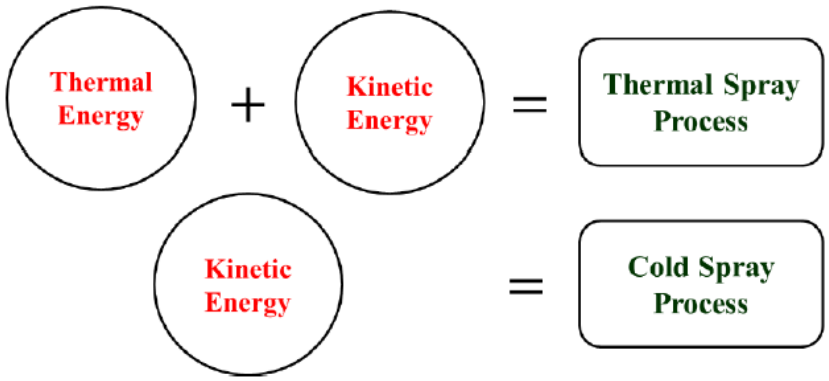


Figure 3.2 Comparison of traditional thermal spray processes and CGDS technology in terms of energy source (Pathak & Saha, 2017).

Table 3.1 Characteristic parameters of various thermal spray processes (Bala et al., 2007).

Parameters	**Thermal spray processes**			
	Wire arc	Plasma	HVOF	CGDS
Temperature (K)	6000	13000	5500	300-900
Velocity (m/s)	50-100	800-1500	1000-2000	1000-2500
Gas	Air, N_2, Ar	Ar, H_2, N_2, He	CH_4, C_3H_6, H_2	Air, N_2, He
Gas flow rates (N/m)	500-3000	40-150	400-1100	1000-3300
Power (KW)	2-5	40-200	150-300	5-10
Feedstock (g/min)	150-2000	10-80	15-50	20-80
Deposit density (%)	80-95	90-95	>95	>95

Thermal spray processes vary in their characteristic parameters, including jet temperature, jet velocity, type of gas, gas flow rates, power, feedstock and deposit density. Table 3.1 presents a comparison of the coating characteristics between wire arc, plasma, HVOF methods and the CGDS process.

Table 3.2 Comparison of CGDS process with competitive technologies (Goyal, 2010).

Process property	**Thermal spray process**			
	CGDS	HVOF	Plasma	Wire arc
Bonding mechanism	Mechanical /Chemical	Mechanical	Metallurgical	Metallurgical
Max. thickness	0.05 -10 mm	< 1.5 mm	< 0.5 mm	0.1 mm
Surface finish	<1 μm Ra	1.3 - 2.0 μm Ra	13.0 μm Ra	2.0 μm Ra
Deposition Rate	1-10 kg/hr	1-5 kg/hr	2-7 kg/hr	5 - 60 kg/hr
Deposition Efficiency	>95 %	50 - 70 %	30 - 60 %	55 - 65 %
Wear resistance	50 mm^3	27 mm^3	10 mm^3	6 mm^3
Bond strength	30-40 MPa	30-70 MPa	30-55 MPa	20-30 MPa
Corrosion rate	0.25 mpy	3.5 mpy	1 mpy	2 mpy
Porosity	0.15 %	1.6-2 %	5%	10-20 %
Oxygen content	0.25 %	3%	9%	5 - 15%
Conductivity	85%	45%	15%	60%
Feedstock size	5-60 μm	5-60 μm	5-20 μm	5-100 μm
Gas consumption	1-5 m3	50 m3	1-5 m3	0.1-5 m3
Power consumption	5 - 15 kW	1 - 2 kW	30 - 100 kW	5 – 10 kW
Powder feed rate	25 - 75 kg/hr	25 kg/hr	15 kg/hr	125-150 kg/hr
Spray velocity	2000 ft/sec	2200 ft/sec	1500- 2000 ft/sec	2300 ft/sec
Feedstock capability	Metallics, polymeric, composites, self-fluxing alloys	Metallics, tungsten carbides, chromium carbides, self-fluxing alloys	Metallics, tungsten carbides, chromium carbides, self-fluxing alloys	Metallics, tungsten carbides, chromium carbides, self-fluxing alloys
Typical Applications	Friction, impact, abrasion, corrosion,	Friction, abrasion, corrosion	Friction, impact, abrasion, corrosion, cavitation	Friction, impact, abrasion, corrosion, cavitation

Thermal spray processes, characterized by diverse energy sources and distinctive parameters, exhibit variations in their process features. These features encompass bonding mechanism, maximum thickness, surface finish, deposition rate, deposition efficiency, wear resistance, bond strength, equipment cost, corrosion rate, porosity, oxygen content, conductivity, feedstock size, gas consumption, power consumption, powder feed rate, spray velocity, feedstock capability, typical applications and more. Table 3.2 offers a comprehensive comparison of the CGDS process against competing technologies, highlighting key process features such as surface roughness, maximum thickness, deposition efficiency, wear resistance, corrosion rate, porosity, oxygen content and conductivity. This analysis underscores the promising results exhibited by CGDS technology (Goyal, 2010).

3.3 Historical Background of The CGDS Process

The development of the cold spraying process can be credited to Professor Anatolii Papyrin and his colleagues at the Institute of Applied and Theoretical Mechanics of the Russian Academy of Sciences in the mid-1980s. Their research initially focused on models subjected to supersonic two-phase flow, involving both gas and solid particles. This exploration led to the successful coating of various materials, including pure metals, metal alloys and composites, onto diverse substrate materials (A. Papyrin, 2007). The cold spray process, considered a significant engineering achievement, has demonstrated its suitability for a wide range of applications (AlMangour, 2017; A. Papyrin, 2007). In the mid-1980s, Russian scientists conducted wind tunnel experiments at the Institute of Theoretical and Applied Mechanics of the Russian Academy of Sciences. These experiments aimed to understand the significance of supersonic two-phase flow for optimal design and safe operations in aviation and space (A. Papyrin et al., 2007).

The studies conducted by Russian scientists in the realm of aerospace engineering aimed to enhance the understanding of the effects of particle flow on fluid dynamics and structural impacts, particularly within the context of supersonic two-phase flows.

These experiments have significantly contributed to aerodynamic investigations using wind tunnels, thereby advancing design and simulation studies in the aerospace field. Notably, the outcomes of these studies marked the first observation of aluminum deposition on an object in a supersonic two-phase flow, with aluminum particle velocities ranging from 400 to 450 m/s and a temperature of 280 K. These pioneering experiments laid the groundwork for discovering the cold spraying process by revealing fundamental physical principles. Wind tunnel experiments have proven invaluable in comprehending the gas dynamics of cold spraying. By scrutinizing the interaction of solid particles with the substrate across a range of particle velocities, these experiments demonstrated that the transition from substrate erosion to coating formation occurs at a specific critical value of the particle velocity (A. Papyrin, 2007). The discovery of the cold spray process was important for science and industry, and it prompted more research to better understand the phenomenon and identify its underlying physical principles. This extensive study includes process modeling, experimental investigations, gas dynamics analysis both inside and outside the supersonic nozzle, nozzle optimization, the effect of the supersonic jet on a substrate, coating properties, particle deformation and bonding mechanisms and equipment and application development (A. Papyrin et al., 2007).

Despite the basic concept of the cold spray process being patented in the early 20th century and discovered in Russia in the 1980s, its commercial development didn't initiate until the early 2000s. The roots of the cold spray process can be traced back to the invention of the thermal spray process by Schoop. However, the notion of using a carrier gas jet to accelerate solid particles for coating formation has been known for over a century. Nevertheless, at that time, the technology required to translate this concept into practical use was complex and needed further development. The first demonstration of the cold injection process occurred during experiments conducted by scientists studying models subjected to supersonic two-phase flow in a wind tunnel in Russia. Through these experiments, it was observed that solid particles precipitated onto the surface following their impact at various sizes, impact angles and velocities, with the condition that the impact velocity exceeded a critical value (H. Singh et al., 2013). It was determined that as the particle velocity increased, there was a swift transition from substrate erosion to coating deposition. At this point, scientists realized

that this phenomenon could be used as a novel coating technique, and they went on to build a cold spray coating machine based on this idea. This device effectively applied a range of metals, alloys, and composites to a variety of substrate materials, demonstrating the adaptability of the CGDS process for a wide range of applications (V. K. Champagne, 2007).

3.4 An Overview of The CGDS Process

CGDS, or simply cold spraying, is the process of applying coatings to a metallic or dielectric substrate by exposing it to a high-velocity jet of small particles the temperature of the gas stream accelerated by a supersonic jet of compressed gas. This process ensures the lowest temperature spraying by carefully selecting a combination of particle temperature, velocity and size. In the CGDS process, powder particles are accelerated by a supersonic gas jet at a temperature lower than the material's melting point, allowing the formation of coatings from solid particles. Consequently, the detrimental effects of high-temperature oxidation, evaporation, melting, crystallization, residual stresses, separation, outgassing, and other common issues in traditional thermal spraying methods are minimized or eliminated. CGDS technology presents significant advantages, opening up new possibilities by mitigating the harmful effects of high temperatures on coatings and substrates. This makes CGDS technology promising for various industrial applications (A. Papyrin, 2007). In the CGDS process, solid powders are accelerated in a Laval nozzle and directed toward a substrate. When the impact velocity surpasses a threshold value, the particles undergo plastic deformation and adhere to the surface. This technology provides ample opportunities for coating different materials, including metals, ceramics, composites and polymers (Moridi et al., 2014). When a particle-laden gas jet interacts with a solid surface, three different events occur based on the particle velocity (V_p). At low V_p, particles are backscattered from the surface. Intermediate V_p values lead to solid particle erosion on the surface, while exceeding a critical value result in particle plastic deformation and adhesion to the substrate, depositing in a manner similar to thermal spray coatings. This scenario is visually depicted in Figure 3.3 using Cu powders (Karthikeyan, 2004). According to the commonly accepted theory, a particle experiences extreme strain rate

deformation upon impact once it reaches the minimum required velocity. A material jet is produced during this process when thermal softening wins out over deformation hardening in the impact zone. This material jet creates metal-to-metal contact between newly exposed surfaces and efficiently removes oxides from the material's surface (Hussain, 2012).

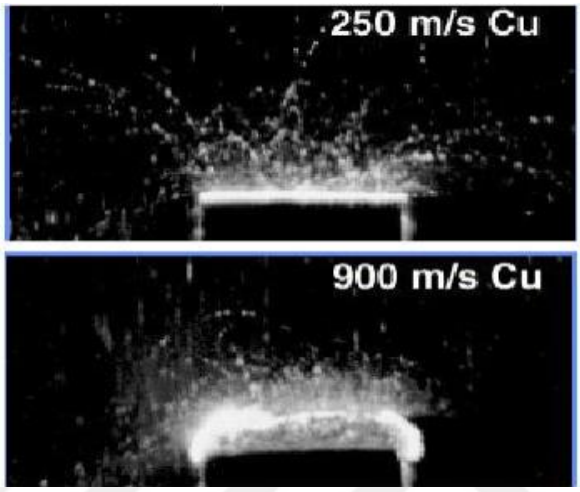


Figure 3.3 Particle behavior depending on velocity in the CGDS process (Karthikeyan, 2004).

The CGDS process utilizes a high-pressure, high-velocity gas jet to accelerate coating particles. In this method, a preheated high-pressure gas jet is transformed into a supersonic gas jet through a convergent/divergent nozzle to counteract adiabatic cooling caused by expansion. Particles carried in a carrier gas are introduced into this supersonic gas jet, resulting in the formation of a high-velocity particle jet due to momentum transfer from the gas jet to the particles (A. Papyrin, 2007). The gas stream's temperature stays below the melting point of the feedstock, and as it expands to supersonic speeds, its pressure and temperature drop. When solid particles come out of the nozzle and hit the surface, they deform plastically and form mechanical or metallurgical bonds with the surrounding material.F This process leads to the creation of a solid-state coating or a free-standing shape. However, material deposition occurs only when the impact velocity of particles exceeds the critical velocity associated with a specific material and temperature (C. J. Li et al., 2010). CGDS produces coatings with advantageous properties as it is a solid-state process. Due to its low-temperature nature, it is well-suited for spray coating phase-sensitive materials like nanophase and

amorphous materials, oxygen-sensitive materials such as aluminum, copper, titanium and carbide composites. Similar to the micro-shot process, the cold spray process produces coatings through compressive stresses, allowing for the production of ultra-thick coatings (5-50 mm) without adhesion failure. Coatings formed through high energy-low temperature exhibit a wrought-like microstructure close to theoretical density values (Karthikeyan, 2004). The coating thickness capabilities of the CGDS process and alternative coating technologies, such as surface transformation/modification and deposition techniques, are contrasted in Figure 3.4. There is a large range of coating thicknesses covered by the CGDS process.

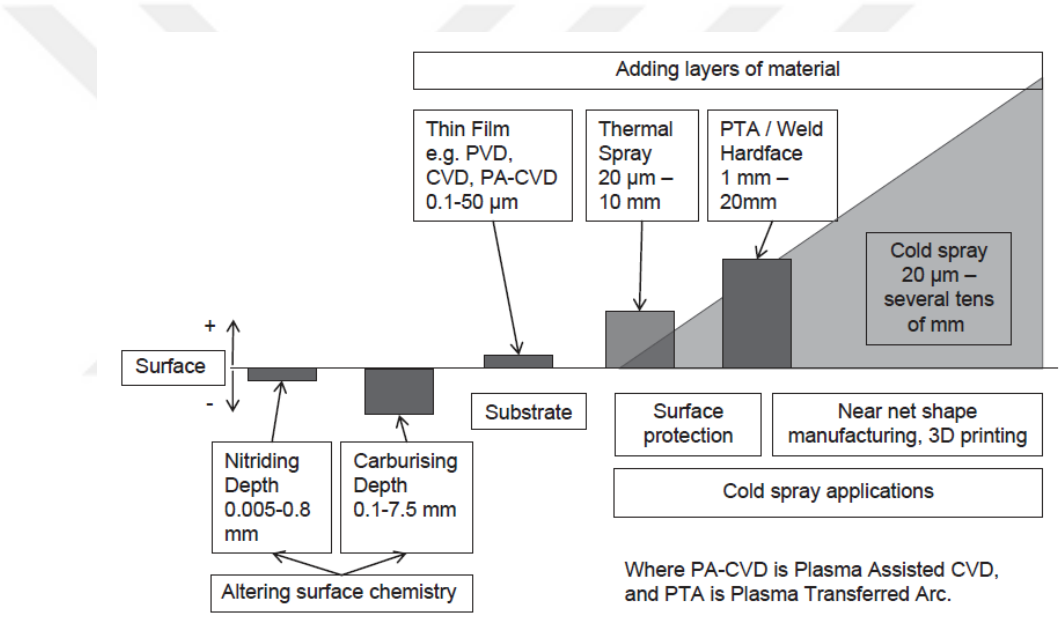


Figure 3.4 Comparison of the CGDS process with other coating technologies in terms of coating thickness ability (Botef & Villafuerte, 2015).

3.4.1 The Physics of CGDS Process

Material deposition in the CGDS process is understood to take place through high-velocity impacts, followed by particle deformation (V. K. Champagne, 2007). The pivotal factor determining bonding is the velocity of the impinging particle. Bonding occurs when the V_p exceeds V_{crit} at the moment of impact (Kosarev et al., 2003). V_{crit} is the minimum velocity that any sprayed particle must attain to adhere to the substrate and is considered a crucial parameter in the CGDS process. In general, achieving a

high particle impact velocity is essential for optimal deposition efficiency and packing density (King et al., 2015).

In the CGDS process, two distinct approaches can be employed to introduce particles into the propellant flow. In the first approach, particles are introduced before the converging-diverging nozzle throat, where the gas pressure surpasses the ambient pressure. This method is known as up-flow injection, necessitating high-pressure compatible powder feeder systems. In the second approach, particles are positioned downstream of the converging-diverging nozzle throat, categorized as downstream injection. In the CGDS process, powder particles are primarily accelerated in the supersonic section of the gas jet. This section operates at a temperature significantly below the material's melting point, ensuring that the particles remain solid throughout their flight, thereby facilitating coating formation (King et al., 2015).

3.4.2 Fundamental Concept of CGDS

The geometry of the nozzle and the characteristics of the feed powders play a crucial role in determining the final temperature and velocity of the sprayed particles. These factors, in turn, directly influence the microstructure as well as the physical and mechanical properties of the coating. It is essential that the temperature of the gas stream remains below the melting point of the particle material. Consequently, CGDS can be accurately characterized as a solid-state precipitation process. The distinctive feature of this technique lies in its achievement of solid-state coating deposition, setting it apart from other conventional thermal spraying methods (Moridi et al., 2014).

In the commercial realm, two types of CGDS systems are available and their classification is based on the method of injecting spray materials into the nozzle. These systems are known as high-pressure cold spray (HPCS) and low-pressure cold spray (LPCS) systems. The primary distinction between these two systems lies in the pressure of the gas used. Specifically, LPCS employs 5-10 bar pressurized gas, whereas HPCS utilizes higher-pressure gas at 25-30 bar. Another differentiating factor is the injection method, where radial injection of the powder is employed in LPCS, while axial injection is utilized in HPCS (Tinashe, 2010; Villafuerte, 2010).

3.4.2.1 LPCS Process

In the LPCS process, accelerator gases such as air or nitrogen are typically utilized. These gases operate at relatively low-pressure levels (5-10 bar) and are pre-heated in a gas heater to enhance their aerodynamic properties, with temperatures often reaching up to 550 °C. This heated gas is subsequently directed through a de-Laval nozzle or a similar converging/diverging nozzle. On the diverging side of the nozzle, the heated gas undergoes acceleration in the range of approximately 300-600 m/s. Solid powder particles are introduced radially into the flow direction of the supersonic nozzle throat section. Subsequently, these particles are accelerated towards the substrate in the LPCS system, as illustrated in Figure 3.5 (H. Singh et al., 2013).

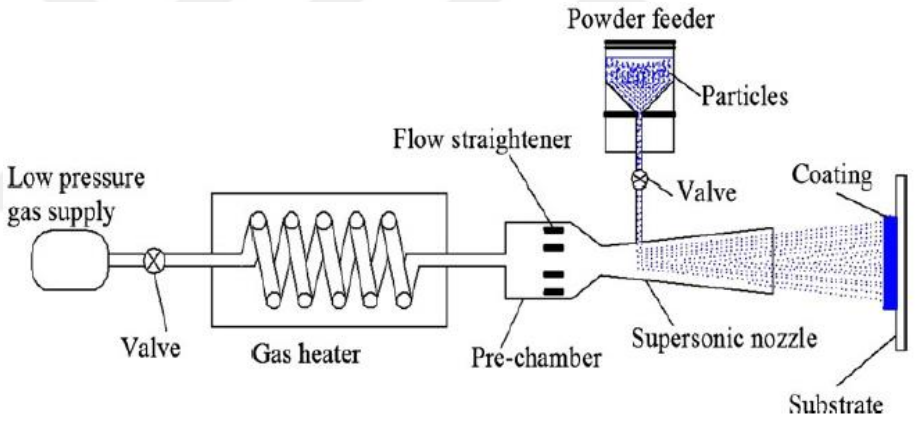


Figure 3.5 Working principle and schematic representation of the LPCS system (H. Singh et al., 2013).

3.4.2.2 HPCS Process

In the HPCS process, the accelerator gas, either helium or nitrogen, is employed. This gas is preheated to 1000 °C under high pressure (25-30 bar) to optimize its aerodynamic properties. Subsequently, the heated gas is directed through a converging-diverging nozzle. Within the nozzle, the gas expansion transforms enthalpy into kinetic energy, propelling the gas flow into the supersonic regime (1200 m/s) while concurrently reducing its temperature. The solid powder feedstock particles

are mixed with the propellant gas in the pre-chamber zone and then introduced upstream of the converging section of the nozzle at a higher pressure compared to the accelerator gas. This design prevents the carrier gas from flowing back into the powder feeder. The arrangement is depicted in Figure 3.6.

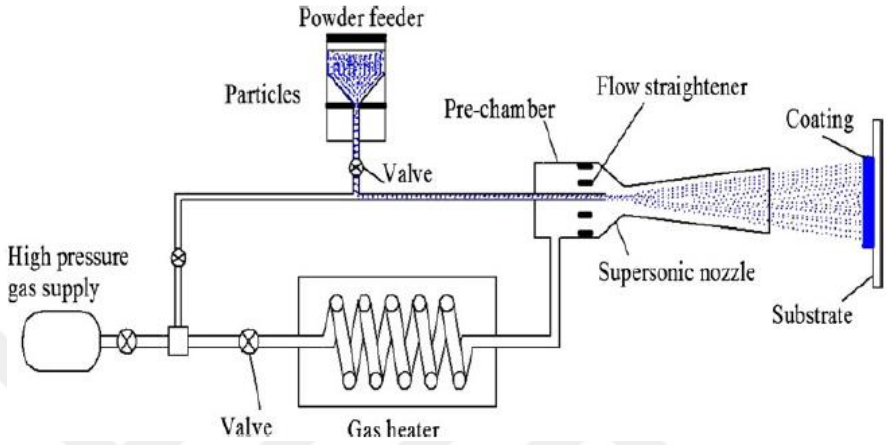


Figure 3.6 Working principle and schematic representation of the HPCS system (H. Singh et al., 2013).

3.4.2.3 Adhesion Mechanism in LPCS and HPCS

Papyrin (2001) conducted depositions of Cu on steel using HPCS and Al / Cu on an Al substrate using LPCS, as illustrated in Figure 3.7. In the case of HPCS, parachute-shaped splats were observed, which were attributed to the high deformation rates experienced by the Cu particles during impact with the substrate (Cavaliere, 2017). The resulting coating produced with CGDS displayed high density with less than 1% porosity. Conversely, in LPCS Cu coatings, lower particle velocities led to relatively smoothly deformed and flattened splats without jet formation. Notably, dark splat boundaries were observed for LPCS, while light splat boundaries were observed for HPCS. This difference in appearance at the splat boundary suggested weak interparticle binding for LPCS and indicated a lower deposition efficiency compared to HPCS. The lower deposition efficiency in LPCS has been linked to the absence of adiabatic shear instability (ASI) contribution to the bonding mechanism (S. Singh et al., 2021).

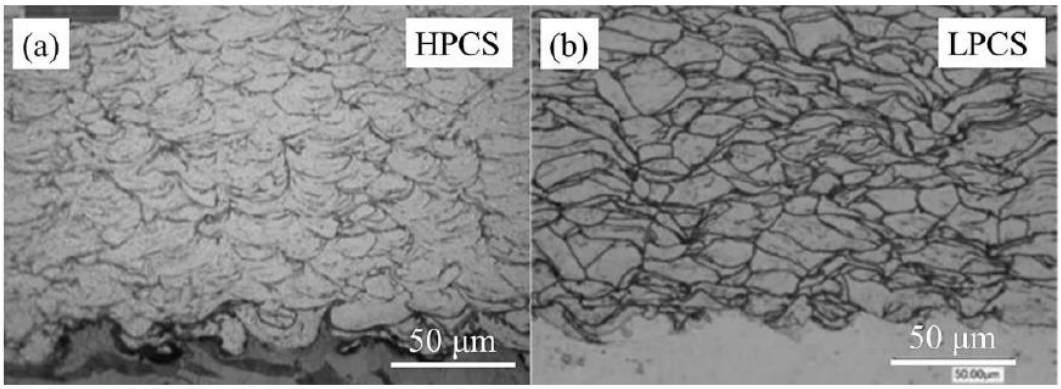


Figure 3.7 Cross-sectional optical micrographs of copper coatings: (a) HPCS system on steel substrate and (b) LPCS system on aluminum substrate (Cavaliere, 2017).

Figure 3.8 depicts the splat formations of coatings for LPCS and HPCS processes. In LPCS, particles may bounce back due to insufficient kinetic energy. This bouncing effect creates a nucleation effect, facilitating the densification of the coating (Assadi et al., 2016; Q. Wang et al., 2012). Consequently, the upper layers of LPCS coatings typically exhibit higher porosity and are less dense than the initially formed coating layers. The phenomenon of shot peening contributes to the flattening of splats in LPCS (Assadi et al., 2003; A. Papyrin, 2001). However, in HPCS coatings, the shot peening phenomenon is absent as the particle velocity surpasses the critical velocity. The high velocity enables incoming particles to interact with previously deposited layers or directly with the substrate. Consequently, the microstructural character of an HPCS coating displays less splat flattening, indicating a higher deposition efficiency (Hussain, 2012; Rokni et al., 2017).

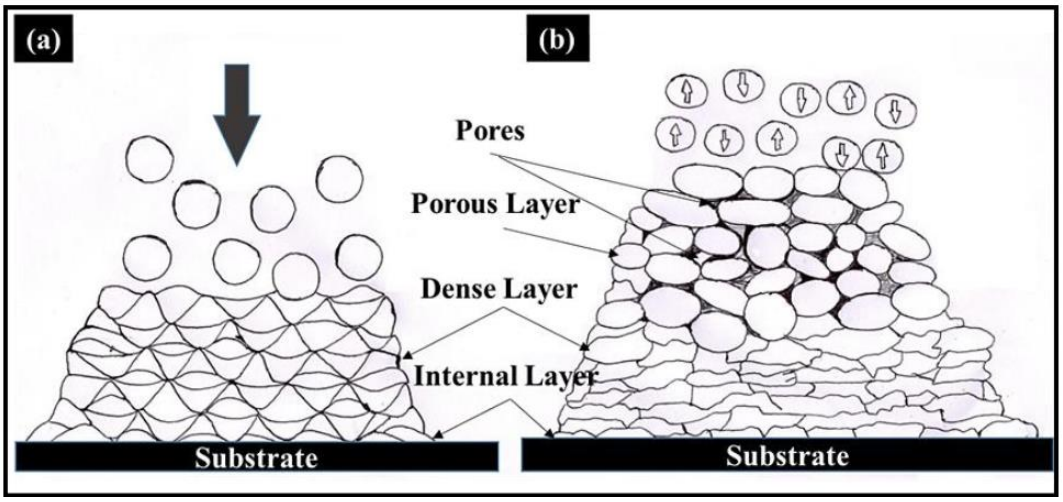


Figure 3.8 Schematic illustration of splat formation in coatings deposited via (a) HPCS and (b) LPCS processes (Cavaliere, 2017).

Table 3.3 presents input parameters that represent the operating capacities of these systems. HPCS has the capability to achieve higher gas temperature and pressure values, leading to higher impact velocities of particles compared to the LPCS process. Consequently, substantial differences in kinetic energies are generated between the two processes (Rokni et al., 2017; Ziemian et al., 2018).

Table 3.3 Operational parameters of HPCS and LPCS systems (Ning et al., 2007).

Parameter	HPCS	LPCS
Process gas	N_2, He, Air	N_2, Air
Gas pressure (MPa)	2.5-6.0	0.5-2.0
Gas temperature (°C)	20-1000	20-500
Gas flow rate (m^3/h)	50-150	15-30

3.4.3 Deposit with a Single Powder Nature: Cold Sprayability of Materials

The deposition method outlined in Table 3.4 covers a broad spectrum of materials. Successful research has encompassed metals, ceramics, polymers and specific compounds such as cermet, stellite and MCrAlY. Positive outcomes have been achieved in studies involving various metals, including copper, aluminum, zinc, nickel, steel, titanium and their alloys (Raoelison et al., 2017). The plastic deformation mechanisms of a metal play a major role in determining its machinability, or how easily

it can be processed using the CGDS method. The dislocation motion and interactions, which are controlled by the crystal structure, are the main factors affecting these mechanisms (Amodeo & Ghoniem, 1990). Metals with a face-centered cubic (FCC) crystal structure, such as aluminum, copper, silver, gold, platinum, nickel and γ iron, are well-suited for the CGDS process due to their high shear planes, providing excellent deformation ability. Metals with a hexagonal structure, namely magnesium, zinc, cobalt, cadmium and titanium, exhibit fewer slip planes and thus lower deformation ability. Body-centered cubic (BCC) metals, including tungsten, tantalum, molybdenum, niobium, vanadium, chromium, alpha iron and gamma titanium, are the least deformable. Lastly, metal-based compounds with a trigonal or tetragonal crystal system are less suitable for the CGDS process due to their low ductility (Raoelison et al., 2017).

Table 3.4 Typical successful deposits with a single powder nature (Raoelison et al., 2017).

Powder feedstock	**Typical successful deposits**	**Main deposition mechanism**
Metals	Al, Ag, Cu, Ni, Ta, Ti, Zn, Fe, Sn, Nb, Mg, Fe	Plastic deformation
Metallic alloys	TiAlV, CuCrAl, CuAgCe, CuAgZr, AlCoCe, SS	Plastic deformation
Bulk metallic glass	NiTiZrSiSn, FeCoCrMoBC, Cu50Ti20Ni30	Viscous deformation
Metal based systems	CoNiCrAlY, MAlCrRe, WC-Co, CrCo stellite	Plastic deformation
Ceramic based phase	SiC, B_4C, WC, TiN	Mechanical interlocking
Oxides	Al_2O_3, TiO_2, WO_3, Y_2O_3, ZrO_2, NiO	Mechanical interlocking
Polymers	PPA, PE	Deformation (+ thermal diffusion)

The CGDS process proves to be an efficient method for processing metals, offering a diverse selection of metal alloys. This versatility is evident in the investigation of various material combinations, as detailed in Table 3.5. Metals exhibit a wide range of functional properties, allowing for the attainment of specific composite properties when used as the component phase in metal matrix composites (MMC). Notably, copper, aluminum, or silver-based coatings are commonly employed in CGDS to enhance electrical conductivity and thermal dissipation, creating materials with a highly effective conductive environment. MMCs produced by CGDS can also feature diverse anti-corrosive properties. For instance, zinc, aluminum, stainless steel, or oxide-based coatings are utilized to prevent chemical surface degradation in ferrous alloys, aluminum alloys and magnesium alloys under normal atmospheric conditions.

Particularly in high-temperature and strongly corrosive environments, these coatings offer crucial anti-corrosive properties by imparting resistance to degradation and oxidation. Superalloy-based coatings contribute to prolonged life through their high mechanical resistance and good creep behavior when exposed to elevated temperatures. The MMCs formed by cold spraying encompass various mixing possibilities, including metal/metal, metal/polymer, metal/oxide, metal/carbide, metal/nitride and metal/ceramic. Oxide, carbide, nitride, or ceramic phases are frequently employed as reinforcement materials to enhance wear resistance (Raoelison et al., 2017).

Table 3.5 Common combinations of MMCs developed through CGDS process (Raoelison et al., 2017).

Phase	**CTE (10^{-6} /°C)**	**E (GPa)**	**Material**	**Material combinations have been explored for CGDS MMCs coatings**											
Ceramic Reinforcement	8-9	420	**Al_2O_3**				O		O	O	O			
	5-6	450	**B_4C**				O			O				
	-	-	**CuO**				O							
	4-5	480	**SiC**				O		O				O	
	9-10	251	**TiN**				O		O					
	5	670	**WC**							O				
Functional metals	23	69	**Al**		O				O			O	O	
	16	124	**Cu**				O							O
	12	196	**Fe**				O							
	13	214	**Ni**	O			O							
	8.5	114	**Ti**			O	O							
	30	78	**Zn**				O							
Metal matrix				**Sn**	**Zn**	**Mg**	**Al**	**Ag**	**Cu**	**Ni**	**SS**	**Fe**	**Ti**	**W**
Melting point (°C)				230	420	650	660	960	1080	1455	1500	1530	1660	3420
CTE (10^{-6} /°C)				23	30	25	23	19	16	13	15-17	12	8.5	4.5
Crystal structure				Tet	HC	H	FCC	FCC	FCC	FCC	-	BCC	HC	BCC

3.5 Parameters of The CGDS Process

In the CGDS process, the deposition growth rate and final coating properties are influenced by several input parameters. These parameters encompass particle impact velocity, gun spray angle, standoff distance, molecular weight of the carrier gas, substrate surface roughness, particle morphology and size distribution, feed rate, gas

temperature and pressure. Each of these factors plays a role in determining the raw material deposition efficiency in cold spray coatings. Similar to cold spray coatings, the efficiency of raw material accumulation is of paramount importance in powder coating methods in general. Raw material deposition efficiency is quantified as the ratio of coating thickness to the number of gun passes (Pathak & Saha, 2017).

3.5.1 Deposition Efficiency

Deposition efficiency (DE) is straightforwardly defined as the ratio of the weight of particles successfully adhering to the substrate (m_s) to the total weight of the initial feedstock particles (M_p). Mathematically, the deposition efficiency can be expressed using Equation 3.1 as follows (A. Papyrin et al., 2006):

$$DE = \frac{m_s}{M_p} \, x \, 100 \tag{3.1}$$

The sandblasting method is commonly employed to enhance adhesion. However, this method comes with drawbacks, particularly the issue of sandblasted particles contaminating the substrate. Particle adhesion is influenced by factors such as contact surface area, plastic deformation, yield stress, processing parameters (especially gas temperature and pressure), particle and substrate temperatures, which can vary depending on various factors (Ghelichi & Guagliano, 2009). Fundamentally, DE fluctuates based on how much the particle velocity exceeds the critical velocity (Gärtner, Stoltenhoff, Schmidt, et al., 2006a; Gilmore et al., 1999).

3.5.2 Critical Velocity

The minimum particle velocity necessary for a material to stick to the substrate is known as the critical velocity (V_{crit}) (A. Papyrin et al., 2006). As depicted in Figure 3.9, when the particle velocity is below V_{crit}, the particle either bounces back upon hitting the substrate, or it hits the substrate, causing surface etching. Particle adhesion, on the other hand, occurs when the particle velocity approaches or surpasses V_{crit}. The types of substrate and feed powder materials, process variables, particle size, and

substrate surface characteristics all affect the variable V_{crit} value (Gärtner, Stoltenhoff, Schmidt, et al., 2006a). Assadi et al., (2003) utilized simulation modeling methods to estimate V_{crit}, which is related to adiabatic shear instability (ASI), and the simulation results are summarized in Equation 3.2:

$$V_{crit} = 667 - 0.014\rho + 0.08(T_m - T_{Ref}) + 10^{-7}\sigma_{uts} - 0.4(T_i - T_{Ref}) \quad (3.2)$$

In Equation 3.2, ρ represents the particle density, T_m is the melting temperature, T_{Ref} is the reference temperature where the ultimate tensile strength is determined, σ_{uts} is the ultimate tensile strength and T_i is the initial particle temperature.

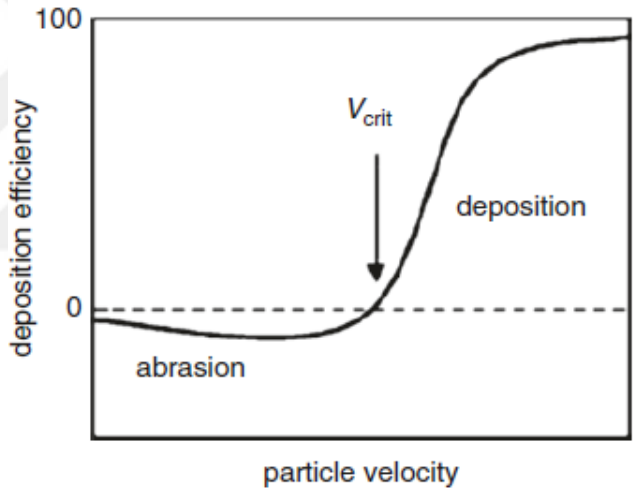


Figure 3.9 The influence of particle velocity on DE in CGDS (Gärtner, Stoltenhoff, Schmidt, et al., 2006a).

Schmidt et al., (2006) formulated an additional correlation for estimating V_{crit} (Equation 3.3). This developed correlation offers a means of estimating the critical velocity with improved precision and accuracy, incorporating considerations for fluids and temperature ranges. This novel method holds applicability in engineering applications and industries where knowledge of critical velocity is crucial.

$$V_{crit} = \sqrt{\left[4F_1\sigma_{uts}\left(1 - \frac{T_i - T_{ref}}{T_m - T_{ref}}\right)\rho_p{}^{-1}\right] + F_2C_p(T_m - T_i)} \quad (3.3)$$

In Equation 3.3, σ_{uts} is the ultimate tensile strength, T_i is the initial particle temperature, T_{Ref} is the reference temperature where the final tensile strength is determined, T_m is the melting point of the particle, ρ_p is the density of the particle and C_p is the specific heat capacity of the particle. F_1 and F_2 are constants serving as material-dependent calibration factors.

When the particle velocity significantly exceeds V_{crit}, not only does this lead to higher DE, as illustrated in Figure 3.9, but it also results in lower porosity (Gärtner, Stoltenhoff, Schmidt, et al., 2006a; Kim et al., 2005b). Porosity plays a crucial role in influencing the mechanical, electrical and thermal properties of CGDS coatings (W. Y. Li et al., 2006; Sudharshan Phani et al., 2007). For instance, a coating with low porosity typically exhibits higher hardness and improved corrosion resistance compared to a more porous coating of the same material. The porosity level in CGDS coatings primarily relies on the feed material and process parameters (S. V. Klinkov et al., 2005; Sudharshan Phani et al., 2007). However, it is feasible to reduce the porosity in the coating after spraying by employing post-treatment methods (Al-Mangour et al., 2014; W. Y. Li et al., 2006). Moreover, post-CGDS heat treatment can bring the mechanical properties closer to the bulk values of the coating material (Sudharshan Phani et al., 2007).

3.5.3 Effect of Particle Impact Velocity

Particle velocity is a crucial parameter in the CGDS process and each material has a specific critical velocity. The capability to adhere to the surface and create a coating is achievable only when particles attain a velocity surpassing this critical velocity. To enhance comprehension of this phenomenon, Figure 3.10 depicts a typical graph illustrating the variation of incubation time (t_i) with particle impact velocity (V_p). Incubation time signifies the duration between the initiation of particle flow for surface treatment and the moment when particles commence adhering to the surface (Pathak & Saha, 2017).

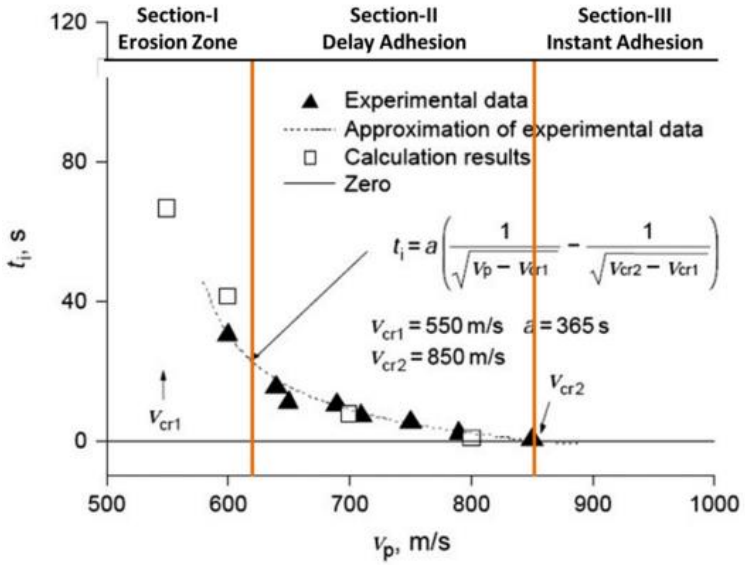


Figure 3.10 Incubation time versus mean particle velocity of aluminum particles on a polished Cu substrate (V. K. Champagne et al., 2005).

As depicted in Figure 3.10, the interaction between particles and the substrate, considering incubation time and two distinct particle velocities (V_{cr1} and V_{cr2}), is delineated into three regions (Section-I, II and III). Section-III corresponds to the region where particle velocity exceeds vcr2 (850 m/s), resulting in immediate adhesion of particles to the initial surface without any delay. When particle velocity is within the range of V_{cr1} and V_{cr2} (Part-II), particles cannot promptly adhere to the initial surface. Adhesion initiates with a delay during which the surface undergoes processing by the first impinging particles. Section-II is commonly denoted as the delayed adhesion region. In Section-I, where velocity values are below vcr1 (550 m/s), only erosion occurs and particles do not adhere to the surface regardless of processing time. This is known as the critical velocity, marking the threshold where the transition from erosion to coating formation commences (V. K. Champagne et al., 2005).

3.5.4 Effect of Particle Morphology

To achieve an appropriately high particle impact rate in the CGDS process, a smaller particle size distribution with lower pitch is considered most suitable. This preference is rooted in the fact that gas/particle momentum transfer, or the travel distance covered by the particle due to the gas, is inversely proportional to the particle

diameter (d) based on Newton's laws of motion, assuming a spherical particle. Consequently, when a powdered substance is utilized and the jet Mach number falls within values close to 3, smaller particle size distribution is expected to result in higher travel and consequently, higher impact velocity. The higher particle velocity is also correlated with the drag force (D) acting on a particle, which can be calculated using Equation 3.4 (A. N. Papyrin et al., 2005):

$$D = \frac{1}{2} \rho \upsilon_{rel}{}^2 A_p C_d \tag{3.4}$$

In Equation 3.4, ρ denotes the propellant mass density and υ_{rel} represents the relative velocity between the propellant and the particle. A_p denotes the projected surface area of the particle and C_d denotes the drag coefficient of the particle. An increased drag coefficient leads to a higher drag force acting on the particle, resulting in an increase in the particle's velocity.

Another crucial aspect concerning powder morphology is that a non-spherical particle with irregular surface and shape characteristics will display different contact behavior upon impact. Ajdelsztajn et al., (2006) demonstrated that localized shear deformation at particle boundaries during impact favors the formation of metallurgical bonds between particles by promoting close inter-particle contact. This effect intensifies as particles with irregular morphology possess a larger surface area, enhancing particle/particle interaction during the deformation process. Furthermore, irregular morphology can heighten stress concentration during impact since the load cannot be distributed evenly, as in the case of spherical particles.

3.5.5 Effect of Powder Feed Rate

The coating thickness is subject to variation based on the mass flow rate of the powder introduced into the carrier gas stream. With an increasing powder feeding rate, the coating thickness exhibits linear growth up to a specific value. However, surpassing this critical thickness value may result in particles striking the substrate surface, inducing excessive stress that can lead to coating delamination. Typically, this

effect is mitigated or alleviated by elevating the gun traversal velocity (Nunthavarawong et al., 2016).

3.5.6 Effect of Spray Angle

When impact occurs at an oblique angle, the particle impact velocity can be resolved into normal and tangential components relative to the surface, as illustrated in Figure 3.11. This is corroborated by studies indicating that the maximum deposition efficiency is achieved with spray angles between 80° and 90° for copper and 70° and 90° for titanium. Information gleaned from Figure 3.12 reveals that within the specified angle range, the spray angle has a significantly lesser impact on deposition efficiency. However, beyond this range, specifically when the spray angle decreases, deposition efficiency declines to a point where particle deposition ceases (40° for copper and 50° for titanium) (Pathak & Saha, 2017).

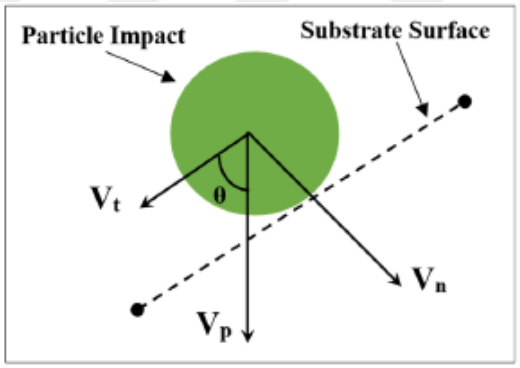


Figure 3.11 Disintegration of particle impact velocity at spray angle θ (Ajdelsztajn et al., 2006).

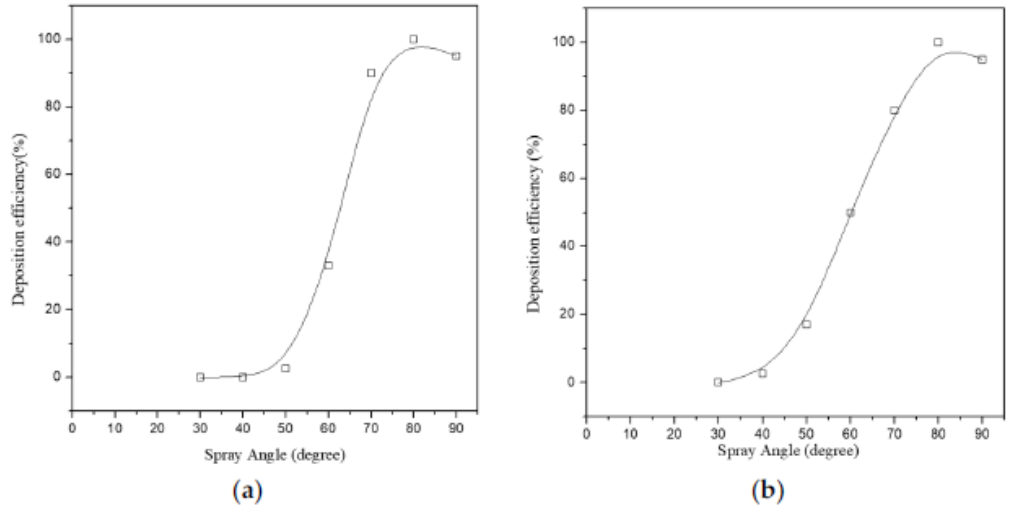


Figure 3.12 Impact of spray angle on DE: **(a)** copper and **(b)** titanium (Ajdelsztajn et al., 2006).

X. Wang et al., (2015) conducted a study modeling the effects of the spray angle on the bonding mechanism of 6061 aluminum alloy. Figure 3.13 depicts the results of their research, leading to the following conclusions. The bonding strength was observed to increase as the spray angle decreased from the normal direction (90°), reaching its maximum at a spray angle of 45°. However, a decrease in deposition efficiency and the strength of the bulk deposit material was noted with a reduction in the spray angle. Moreover, at high spray angles (90° and 75°), jet formation and partial melting events were detected on the substrate surface, while crater formations were observed at low spray angles (60° and 45°).

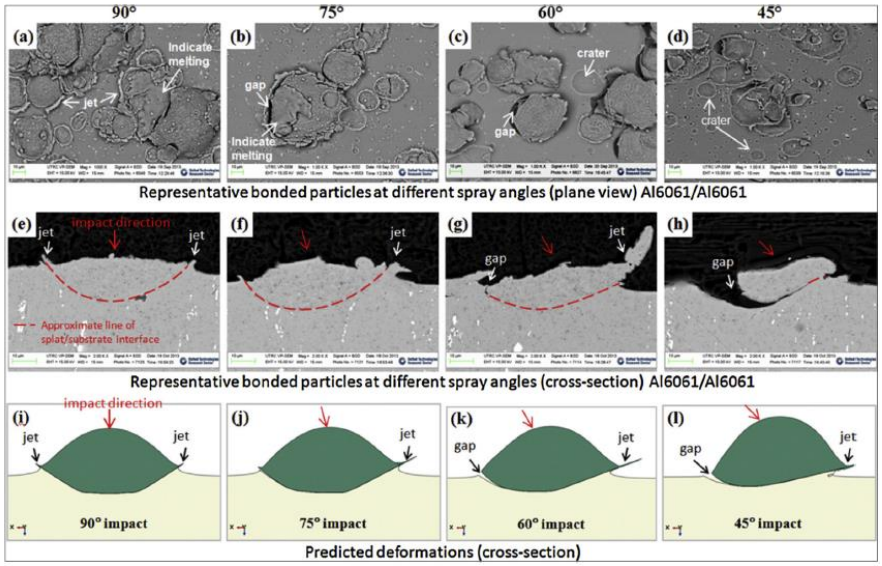


Figure 3.13 Impact of spray angles on particle bonding and associated deformation (X. Wang et al., 2015).

3.5.7 Effect of Standoff Distance

The standoff distance has a notable impact on the impact velocity of powder particles. In the LPCS process, an increase in the standoff distance from 10 mm to 50 mm has been observed to elevate the impact velocity of 10 µm diameter copper particles from 420 m/s to 550 m/s (Jodoin, 2001). A smaller standoff distance leads to a decrease in deposition efficiency due to the intensified power of the curved shock wave. In essence, particle velocity increases outside the nozzle and while particles may lose velocity during flight, the shock wave generated by the impact of preceding particles on the substrate can further diminish their velocity. Conversely, a larger standoff distance allows accumulation to proceed unhindered as the curved shock wave diminishes (Pathak & Saha, 2017).

3.5.8 Effect of Particle and Substrate Temperature

Elevating both the initial temperatures of particles and substrates has a pronounced impact on deposition efficiency, as well as enhancing the physical and tribological-mechanical properties of coatings (Jodoin et al., 2006). This phenomenon is substantiated by the correlation between higher initial particle temperatures and lower

critical velocities. This is attributed to the material's increased softness at higher temperatures, requiring less kinetic energy for plastic deformation on particle surface areas. The higher material temperature enhances thermal softening, a critical aspect of the bonding mechanism and facilitates chemical reactions that contribute to adhesion within the coating-substrate material system (Pathak & Saha, 2017).

3.5.9 Gas Temperature and Pressure

Gas temperature and gas pressure are extensively studied parameters due to their significant influence on particle impact velocity (Gärtner, Stoltenhoff, Schmidt, et al., 2006a; Maev & Leshchynsky, 2008). Research has consistently shown that higher gas temperatures leading to increased particle impact velocities result in coatings with higher DE and improved quality, characterized by lower porosity and enhanced strength (Gärtner, Stoltenhoff, Schmidt, et al., 2006a; Stoltenhoff et al., 2002). Elevated gas temperature has proven beneficial by enhancing plastic deformation through the facilitation of dislocation movement, recovery and recrystallization (Borchers et al., 2008; Gärtner, Stoltenhoff, Voyer, et al., 2006).

For a given gas type and pressure, increasing the gas temperature is necessary to achieve higher particle impact velocities (Meng et al., 2011; Stoltenhoff et al., 2002). However, escalating gas temperature presents technical challenges, including the CGDS gun nozzle's sensitivity to high temperatures, as well as issues related to oxidation and nitridation (V. K. Champagne, 2007). On the other hand, the use of helium gas in the CGDS process has demonstrated a much higher particle impact velocity and lower porosity compared to nitrogen gas under equivalent temperature and pressure conditions (Gilmore et al., 1999; Stoltenhoff et al., 2002). Despite these advantages, nitrogen is typically preferred due to the higher cost associated with helium. Consequently, the CGDS process parameters need careful optimization to produce high-quality coatings using nitrogen gas (AlMangour, 2017).

3.5.10 Role of Surface Preparations

Elevated substrate surface roughness enhances the deposition efficiency of metallic powders by facilitating greater deformation of particles upon impact compared to a smooth substrate. This increased deformation promotes mechanical interlocking, a prominent theory in CGDS coatings supported by particle impingement on the substrate surface. Thus, it can be inferred that augmenting substrate roughness enhances binding by offering more recesses and pits where CGDS particles can lodge. These particles experience additional compression as subsequent particles strike the substrate. In contrast, surfaces with low roughness provide minimal surface area for the initial impinging particles to bond, resulting in weaker bond strength. The challenge for these particles to adhere to the substrate initially causes a reduction in deposited mass (Shockley et al., 2015).

Contrastingly, in an experimental study by Hussain et al., (2009) examining the bonding mechanisms in cold spraying of copper onto an aluminum alloy substrate, various substrate surface preparation methods were explored, including polished, ground and sandblasted surfaces. The study revealed a significant decrease in adhesion between the coating and the substrate, particularly after the sandblasting process. It was proposed that the sandblasted surface prevents jet formation at impact, which leads to a weaker metallurgical bond and less efficient oxide film removal from the interface. Another study by Marrocco et al., (2006) investigated the effects of various surface preparation methods on the strength of the bond of a titanium coating that is cold sprayed onto Ti6Al4V. They proposed that sandblasting induced work hardening in the Ti6Al4V substrate, limiting deformation by the action of titanium particles during cold spraying. This restriction in deformation was hypothesized to lead to lower observed bond strengths.

In a study by Wu et al., (2006) upon examining the application of an Al-Si coating by cold spraying onto mild steel surfaces that had been grit-blasted and polished, it was found that the polished substrate produced a more intimate interface, whereas the sandblasted surface displayed micropores and defects. The observed lower bond strength was associated with the presence of micropores on the grit-blasted surface.

Moreover, higher bond strength was detected with an increase in particle velocity. Conversely, Mäkinen et al., (2007) reported that a copper deposit cold-sprayed onto a sandblasted copper surface exhibited higher bond strength compared to deposition on a similar surface. Table 3.6 examines the bond strength values of coatings obtained through CGDS, comparing reported values from different studies while considering the diversity of coating and substrate materials and their impact on bond strength.

Table 3.6 Overview of bond strength in various substrate/coating combinations (Jeandin et al., 2015).

Coating material	Substrate material	Substrate preparation	Bond strength	Standard	Reference
Al	Al7075	Grit blasting	40	ASTM C633	(Irissou et al., 2007)
Al	Al7075- T651	Polished, grit blasted, shot peening, chemical etching	30–40	ASTM C633	(Irissou et al., 2007)
Al + Al_2O_3	Al7075	Grit blasting	> 60	ASTM C633	(Irissou et al., 2007)
Cu	Aluminum	Grit blasting	24	JIS H 8664	(Fukanuma & Ohno, 2004)
Cu	Aluminum	Grit blasting	> 40	ASTM C633	(Gärtner, Stoltenhoff, Schmidt, et al., 2006b)
Cu	Aluminum	Grit blasting	30–35	ASTM C634	(Taylor et al., 2006)
Cu	Aluminum, copper	Grit blasting	40	EN 582	(Stoltenhoff et al., 2006)
Cu + Al_2O_3	Copper, steel	Grit blasting	20–23	EN582	(Koivuluoto et al., 2008)
Ni	Aluminum	-	> 50	-	(Fukanuma & Huang, 2009)
Ni + Al_2O_3	Copper, steel	Grit blasting	8–9	EN582	(Koivuluoto et al., 2008)
Zn + Al_2O_3	Copper, steel	Grit blasting	33–38	EN583	(Koivuluoto et al., 2008)

Furthermore, the impact of surface preparation on coating efficiency was assessed. Sakaki et al., (2004) noted a slight increase in plating efficiency in the CGDS process of copper and titanium with increased surface roughness on the grit-blasted substrate compared to the polished substrate. Richer et al., (2005) reported an increase in coating efficiency when spraying an aluminum alloy particle onto a coarser grit-blasted surface compared to a finer grit-blasted surface. However, the effect of surface roughness is primarily on the initial layers of the coating and thus, its influence on coating efficiency may be limited, contingent on the significance of the coating formation stage in the overall coating development time.

Table 3.7 provides a comprehensive overview of select process parameters and their impact on the properties of CGDS coatings (Adaan-Nyiak & Tiamiyu, 2023). Notably, while the table suggests that increased particle velocity enhances adhesion and DE, recent research indicates a decrease in these factors at excessively high particle velocities (Tiamiyu et al., 2021; Tiamiyu & Schuh, 2020).

Table 3.7 Summary of the influence of processing parameters on CGDS deposits (Pathak & Saha, 2020).

Parameter	Degree	Deposit strength	Adhesion	Deposit efficiency	Porosity	Residual stress
Gas pressure	↑	↑	↑	↑	↓	↑
Gas temperature	↑	↑	↑	↑	↓	↑
Gas molecular weight	↑	↓	↓	↓	↑	↓
Particle velocity*	↑	↑	↑	↑	↑	↓
Powder feed rate	↑	↓	↓	↓	↑	↑
Stand-off-distance	↑	□	□	□	□	□
Spray angle	↑	↑	↑	↑	↑	↑

↑ = Increase ↓ = Decrease □ = No common view.

3.6. Advantages of The CGDS Process

As illustrated in Figure 3.14, the CGDS process and the ensuing coatings present a multitude of advantages. These benefits encompass high deposition efficiency, rapid deposition rates, minimal thermal energy input to the substrate, preservation of powder material without melting, elevated density, reduced porosity, robust adhesion strength, induction of compressive residual stresses, capacity to generate substantial coating thicknesses, absence of phase transformation, prevention of oxidation and inhibition of grain coarsening. Furthermore, the process results in coatings with high conductivity, superior corrosion resistance and enhanced strength and hardness (Botef & Villafuerte, 2015).

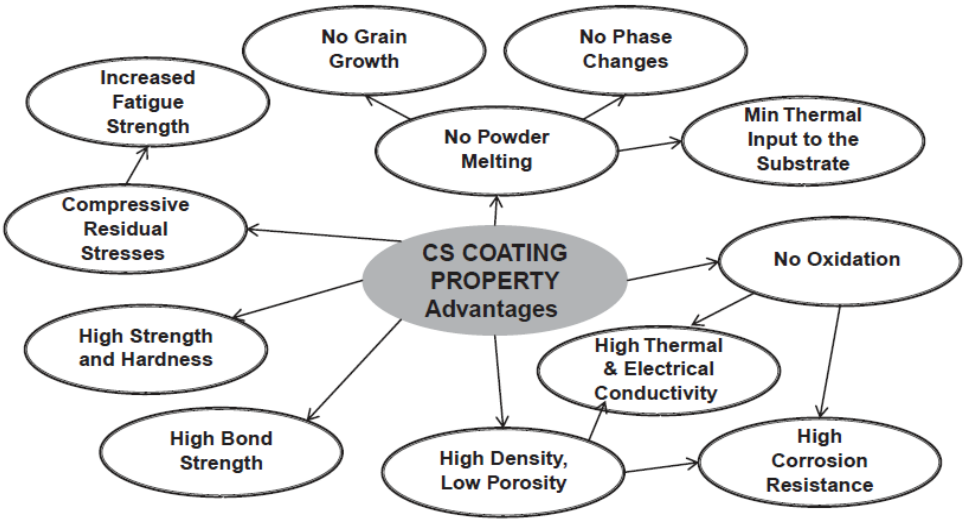


Figure 3.14 Advantages of process properties in CGDS (Botef & Villafuerte, 2015).

3.6.1 High Deposition Efficiency

The CGDS process has demonstrated remarkable success in achieving very high DE values for various metals, alloys and composite materials. Notably, DE values exceeding 95% have been attained for aluminum, copper, and their respective alloys. The key elements contributing to these high DE values involve (a) minimizing the oxygen content of the powder material, (b) alleviating stresses in the powder particles, (c) optimizing particle size distribution and (d) fine-tuning the spraying parameters. Diligent control of these factors has proven effective in achieving exceptional DE values for a broad spectrum of materials, including refractory metals, high-strength materials and other diverse materials (Karthikeyan, 2007).

3.6.2 High Deposition Rate

The cold spray beam exhibits a distinctive narrow and sharply defined structure, typically featuring sharp edges with a diameter around 10 mm. This narrow beam, coupled with a substantial powder feed rate, results in an exceptionally high deposition rate. In a single pass, it is feasible to achieve coatings with a thickness of 1-2 mm for most materials. Notably, CGDS stands out by generating these ultra-thick layers with robust bonding strength, distinguishing it from other coating processes. This

characteristic has been leveraged in advancing CGDS as a tool for the manufacturing of approximate net-shaped products and additive manufacturing (Karthikeyan, 2007).

3.6.3 No or Little Masking

The particle beam employed in the CGDS process is characterized by its narrow structure. While a conventional spray jet may have a diameter of about 10 mm, the use of specialized rectangular nozzles allows for the creation of a spray beam that is 1-2 mm wide, featuring sharp edges. This distinctive attribute eliminates the need for masking in areas where overspray is not permissible, making it highly practical for various applications (Karthikeyan, 2007).

3.6.4 No Grit Blast

The CGDS process can be conceptualized as a triple-process encompassing sandblasting, coating spraying and shot blasting. As anticipated, the velocity distribution within the spray beam exhibits a Gaussian pattern. With optimized parameters, the particles in the core exhibit velocities surpassing the critical velocity, while the surrounding particles have velocities below the critical threshold. As the spray beam is swept, particles at the leading edge impact the surface at velocities below the V_{crit}, inducing solid particle abrasion and creating a micro sandblasting effect. Core particles, hitting the surface with velocities higher than V_{crit}, undergo plastic deformation on the newly cleaned rough surface, forming a coating. Particles at the trailing edge impact at velocities lower than V_{crit}, not only dislodging loosely bound particles but also imparting a shot peening effect on the freshly formed coating. Experimental evidence indicates that for various substrate materials, such as aluminum, copper, titanium, conventional sandblasting is often unnecessary (Karthikeyan, 2007).

3.6.5 High Density

In the cold spraying process, only particles impinging at velocities higher than V_{crit} undergo plastic deformation and agglomeration. This deformation process, characterized by high strain rate deformation, results in the additional conversion of kinetic energy into thermal energy at the moment of impact. These microscopic processes lead to the development of hydrodynamic instabilities, creating metal vapor jets. This vapor jet essentially facilitates vapor deposition of the material at the interparticle interfaces, effectively filling existing pores and cracks. Consequently, the cold spray process can be understood as a combination of particle and microscopic vapor deposition processes. Moreover, loosely bound particles are sprayed and the deposited pieces are subjected to micro-peening due to the effect of trailing-edge particles in the spraying beam. In the final stages, each subsequent pass of the spray beam hits the underlying layer, contributing to an increase in its intensity. The combination of these events results in a cold spray process that produces coatings of near theoretical density (Karthikeyan, 2007). Additionally, with subsequent heat treatments, the deposits become more dense and approach ideal levels due to the closure of pores, splash boundaries and cracks (Chavan et al., 2013).

3.6.6 Flexibility in Substrate-Coating Selection

In numerous engineering applications, there is a demand for substrate-coating combinations involving different materials; This is a problem that is often difficult to solve using traditional processes. Even commonly used materials, such as aluminum versus copper or vice versa, can result in undesirable interfaces. For example, when a molten copper droplet impinges on an aluminum substrate, it can cause the formation of a brittle Cu-Al intermetallic phase, posing a risk of damage to the coated structure in use. Consequently, it becomes imperative to meticulously examine phase diagrams and carefully select substrate-coating pairs to avoid the formation of intermetallic or metastable phases that may contribute to premature damage of the coated system during high-temperature processing. The unique advantage of cold spray lies in its ability to prevent heating and melting of the coating material. This feature prevents the

formation of weak interfaces, providing flexibility in selecting materials according to design requirements (Karthikeyan, 2007).

3.6.7 Minimum Thermal Input to The Substrate

The substrate is heated to varying degrees by the flame in conventional thermal spray processes. When working with temperature-sensitive materials, like polymers and magnesium, among others, this presents challenges. Additionally, heating the substrate in traditional methods can cause temperature-dependent deformation, especially when working with thin samples. The cold spray process, in contrast, does not involve a high-temperature jet to heat the substrate. Instead, the substrate only receives the stagnation enthalpy of the impinging particles. As a result, cold spraying has proven to be a valuable technique for repairing parts and components made of temperature-sensitive materials, as it eliminates problems associated with excessive substrate heating and possible warping (Karthikeyan, 2007).

3.6.8 No Powder Melting

The main physical difference between more conventional thermal spraying techniques and CGDS is that CGDS material bonding takes place exclusively in the solid state. (A. Papyrin, 2007). This requires enough impact energy or particle velocity to cause rapid plastic deformation and joint formation. Therefore, the compressed carrier gas is typically preheated in order to achieve higher gas flow rates in the de-Laval nozzle. On the other hand, even though the CGDS process uses preheating temperatures of up to 800-1000 °C, the hot gas and spray particles only come into contact for a brief period of time, and the gas cools quickly as it expands in the divergent part of the nozzle. This guarantees that the spray material stays below the melting temperature because the temperature of the particles actually stays much lower than the preheating temperature. (Grujicic et al., 2003).

3.6.9 High Bond Strength

Cold-sprayed coatings demonstrate high bond strength on a diverse range of substrate materials, including metals, alloys and composites. It can even be applied to certain materials such as glass and aluminum. The CGDS process employs technology that achieves high particle velocities, enabling the formation of high-strength coatings from various materials. These coatings form without causing deformation in the internal structures of the material and establish a robust bond with the substrate. Consequently, the CGDS process imparts desirable properties such as high temperature resistance and wear resistance (Karthikeyan, 2007). Both adhesive and cohesive strengths play crucial roles in determining the utility of a deposit in any application (Huang & Fukanuma, 2012). It has been observed that incorporating ceramic particles such as Al_2O_3 into pure aluminum can significantly enhance the adhesive/cohesive strength (Irissou et al., 2007; H. Y. Lee et al., 2005).

3.6.10 Compressive Residual Stresses

Most coating processes typically result in coatings with residual stresses in the tensile direction. These stresses, coupled with bonding damage, give rise to microcracks on the coating's top surface. This scenario contributes to diminished fatigue properties of the coating and a deterioration in performance when subjected to real application environments (Maev & Leshchynsky, 2008). In the CGDS process, the coating is formed through plastic deformation in the solid state, resulting in compressive residual stress throughout the entire coating thickness. Industries, particularly those in high-tech sectors like gas turbines, require coatings with compressive residual stresses for enhanced fatigue performance. In certain critical applications, shot peening is applied after spraying to achieve superior fatigue performance. Given that the CGDS process inherently produces coatings with compressive residual stress, these coatings exhibit improved fatigue properties, eliminating the need for additional shot peening steps (Karthikeyan, 2007). Modeling and experimental evidence demonstrate that the CGDS process can generate the desired surface compressive stresses, leading to enhancements in the fatigue life of specific materials. For instance, using the LPCS system, 7075 AA cold-sprayed onto a

5052 AA substrate exhibited an improvement of approximately 30% in fatigue life (Ghelichi et al., 2012).

3.6.11 Ultra-thick Coatings

In most coating processes, tensile stresses are generated during coating formation. As the coating thickness increases, these stresses accumulate at the substrate-coating interface, leading to a reduction in bond strength. When the coating thickness surpasses a critical value, spontaneous delamination of the coating from the substrate occurs. Given that cold spray coatings experience compressive stresses, it becomes feasible to produce ultra-thick layers on various substrates without incurring bond damage. The capability to generate extremely thick coatings that tightly adhere, even on dissimilar materials, opens avenues for applications such as creating high thermal mass layers in thermal insulators and producing challenging-to-machine parts through additive manufacturing (Karthikeyan, 2007).

3.6.12 No Phase Changes

Many problems, including oxidation, decomposition, metastable phase formation, and preferential component loss, are inevitable in high-temperature processes. Phase changes are prevented in the CGDS process by keeping the particles at nearly room temperature (Karthikeyan, 2007). On the other hand, molten species may react during their brief flight from the spray gun to the substrate in high-temperature processes like plasma spraying (Chraska et al., 1992). WC-based powders have been consolidated by researchers using the CGDS method, and XRD analyses have verified that cold spraying did not result in modifications to the chemistry, phase composition, or grain structure (Kim et al., 2005a; M. F. Smith, 2007). Furthermore, nanostructured powder materials have been effectively consolidated into useable forms using the CGDS method without affecting the fine grain sizes (Karthikeyan, 2007).

3.6.13 No Oxidation

Oxidation is a problem when thermal spraying oxygen-sensitive materials like copper, titanium, magnesium, aluminum, and their alloys because it happens at a rate that increases exponentially with temperature. However, the cold spray process circumvents exposure to high temperatures. Additionally, an inert gas is employed to repel particles, effectively retaining spatters formed on the substrate. Consequently, the cold spray process virtually eliminates particle oxidation. Observations indicate that cold-sprayed coatings exhibit slightly lower oxygen content than the starting material. The process of deoxygenation proceeds as follows: A thin oxide layer is present on every fine particle in the raw material. The newly formed metal surface sticks to the substrate surface while the brittle oxide shell breaks apart and is carried away by the gas jet upon impact (Karthikeyan, 2007). The porosity, oxygen content, and thermal characteristics of Cu, Sn, and Al when sprayed using CGDS and conventional thermal spraying are shown in Figure 3.15. The fact that the CGDS process can decrease oxide content instead of increasing it suggests that it has a great deal of potential for a variety of future uses.

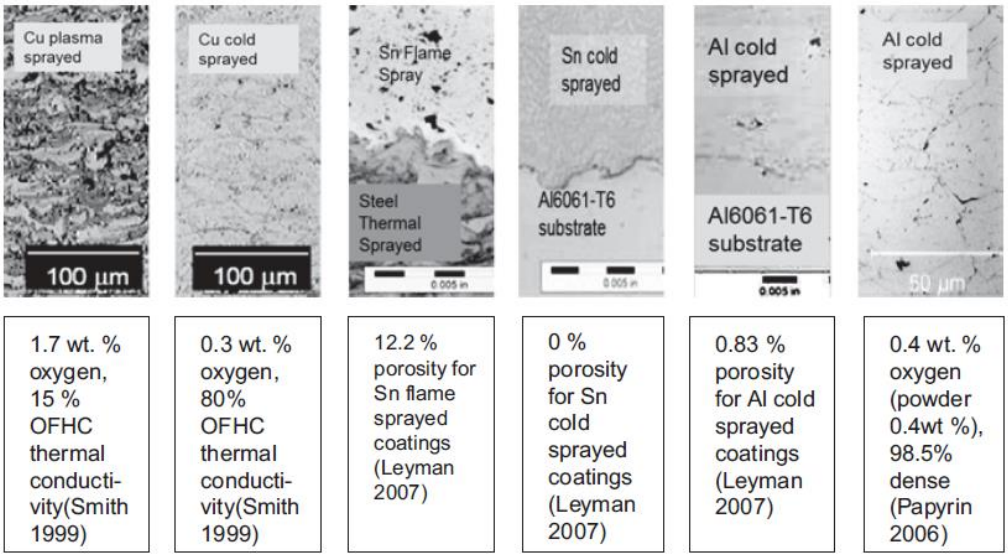


Figure 3.15 Comparing porosity, oxygen content, and thermal properties: Thermal spray vs. cold spray. (*OFHC* oxygen-free high conductivity) (Botef & Villafuerte, 2015).

3.6.14 No Grain Growth

As a low-temperature solid-state bonding technique, CGDS is particularly well-suited for processing temperature-sensitive materials, especially nanomaterials and amorphous materials. Unlike other powder bonding techniques such as pressing, sintering and thermal spraying, CGDS prevents significant grain growth when producing nanostructured coatings. Experiments have demonstrated that unique properties, such as high hardness, can be achieved by combining nano WC powders with CGDS. Similarly, it has been observed that amorphous alloys retain their amorphous state when processed by the CGDS process (Karthikeyan, 2007). Grains will inevitably recrystallize and grow in other material joining processes like powder metallurgy and traditional thermal spraying, which is frequently unacceptable (Kim et al., 2005a). In contrast, the limited heat input during cold spraying generally does not cause grain growth and recrystallization. This is highly advantageous because mechanical and physical properties that strongly depend on surface microstructure and grain size, such as fatigue strength, can be preserved (Al-Mangour et al., 2013).

3.6.15 High Conductivity

CGDS distinguishes itself by producing dense coatings with high interparticle connectivity. Moreover, these coatings exhibit high phase purity and formations such as pores and oxides are minimal or even absent. These properties endow cold spray coatings with excellent thermal and electrical conductivity values (Karthikeyan, 2007).

Electrical conductivity, material density and the presence of dispersed oxide phases serve as key indicators of coating quality (Koivuluoto et al., 2012). Copper, with its exceptional electrical and thermal conductivities, holds significant importance in today's industrialized world due to its commercial availability (Sudharshan Phani et al., 2007). Plasma-sprayed copper coatings containing oxide additives exhibit electrical conductivity values up to 15% lower than oxygen-free high conductivity copper (OFHC) (M. F. Smith, 2007). Conversely, copper coatings obtained through dense CGDS can showcase OFHC copper conductivity exceeding 85% (Karthikeyan, 2007; M. F. Smith, 2007). Comparable copper materials sprayed by conventional

thermal spraying processes typically display OFHC copper conductivity ranging between 40% and 63%. Furthermore, the annealing process applied after CGDS enhances conductivity by facilitating coating densification and recrystallization (Koivuluoto et al., 2012; Sudharshan Phani et al., 2007). Figure 3.16 provides a comparison of the electrical conductivity of copper coatings obtained using high pressure (HP) and low pressure (LP) CGDS systems.

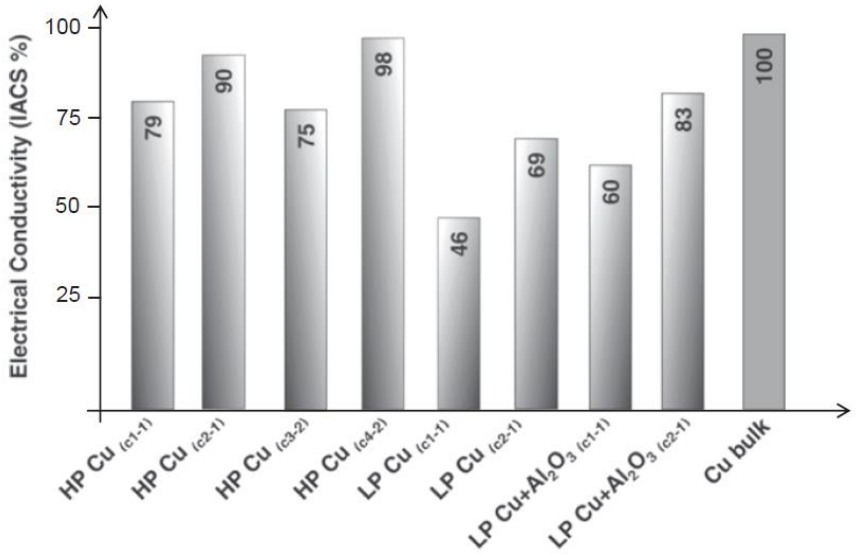


Figure 3.16 Conductivity characteristics of cold-sprayed Cu coatings. (*IACS* International Annealed Copper Standard) (Botef & Villafuerte, 2015).

3.6.16 High Corrosion Resistance

High-density cold spray coatings, characterized by phase purity and a uniform microstructure, exhibit exceptional corrosion resistance properties. Notably, aluminum and other coatings produced through cold spraying demonstrate superior corrosion resistance when compared to their bulk counterparts (Karthikeyan, 2007). Consequently, cold spraying has emerged as a preferred method for localized corrosion repair and protection. Applications of this approach extend to magnesium castings in the defense, aerospace and automotive industries (Suo et al., 2012; Villafuerte & Zheng, 2007).

3.6.17 High Strength and Hardness

Upon evaluating the mechanical properties of coatings generated through the CGDS process, it was consistently observed that the UTS values surpassed those of the corresponding bulk materials. Furthermore, the high plastic deformation experienced by coating particles during the process contributed to elevated hardness values compared to the bulk material properties (Karthikeyan, 2007).

3.7. Limitations of the CGDS process

3.7.1 Near-Zero Ductility

One notable drawback of the CGDS process lies in the necessary plastic deformation experienced by particles, resulting in a reduction of the coating's ductility. According to a study conducted by Ogawa et al., (2008), aluminum coatings produced through CGDS exhibited a higher elastic modulus compared to cold-rolled aluminum substrates. Although no cracks were evident in the aluminum obtained through CGDS under compressive loads, these coatings displayed increased strength in comparison to cold-rolled aluminum. Interestingly, when subjected to the cold spraying method, samples exhibited a capacity to recover their ductility through annealing at relatively low temperatures, up to 270 °C. This finding underscores that a significant amount of plastic deformation energy is retained in cold-sprayed materials and this energy can be harnessed for recrystallization and consolidation upon heating.

3.7.2 Restricted Selection of Sprayable Materials

Although conventional thermal spray techniques are versatile in coating a wide range of materials, one of the main limitations of CGDS at this time is its inability to coat metals or composites that have enough low-temperature ductility. Metals like Al, Cu, Ni, Ti, Ag, Zn, and Ni are notable examples (V. K. Champagne, 2007). CGDS has also been successfully applied to mixtures of these metals with ceramics or other non-ductile materials, such as Al-Al_2O_3 (Irissou et al., 2007), WC-12Co with Ni (Melendez & McDonald, 2013), WC-Co with Cu or Al (J. Wang & Villafuerte, 2009) and even

Al-12Si alloy composites (Yandouzi et al., 2009). Over the years, extensive research has aimed to broaden the applicability of CGDS materials. Studies have explored exotic materials like Al-Ni intermetallic compounds (H. Lee et al., 2010) and efforts have been made to combine CGDS with materials that pose challenges for traditional thermal processes. Original approaches have also been attempted, such as incorporating SiC without a metal matrix binder to enhance oxidation resistance at high temperatures on Ni-Cr-based superalloys (Seo et al., 2012). These endeavors showcase ongoing attempts to expand the range of materials effectively coated by CGDS.

3.7.3 Need for a Substrate Material with Adequate Hardness

In the CGDS process, it is imperative for the substrate material to exhibit adequate hardness in comparison to the spraying material. This requirement ensures that incoming particles undergo significant plastic deformation, facilitating acceptable bonding, as highlighted by Karthikeyan, (2007). Substrates at the extremes of the hardness spectrum pose challenges. Exceptionally soft substrates, like polyethylene, lead to surface cratering, hindering particle accumulation. Conversely, highly brittle substrates, such as carbon, are prone to wear from incoming particles and are susceptible to delamination. In CGDS, the hardness of the substrate material plays a crucial role in providing the necessary plastic deformation for effective bonding. Substrates that are excessively soft or brittle can yield undesirable outcomes, ultimately compromising the integrity of the coating (Botef & Villafuerte, 2015).

3.7.4 Gas Consumption

Gas consumption in CGDS processes is significantly higher than in many thermal spray methods, mostly because higher velocities and flows are required to propel the particles. In this process, nitrogen, helium, and compressed air are frequently used as carrier gases. Due to its high gas velocity and inert nature, which both contribute to improved quality and DE, helium is typically chosen among these. However, the drawback lies in helium being one of the most expensive and rare gases, limiting its

usage to specialized applications (V. K. Champagne, 2007). In recent years, nitrogen and/or air have gained prominence as preferred gases for various CGDS equipment and sprayable materials. The need for high operating parameters when spraying materials that are less ductile at lower temperatures than traditional cold-sprayable metals is what is causing this shift. Superalloys based on nickel, titanium alloys, stainless steels, and tantalum are a few examples. Notwithstanding the benefits, there are considerable capital and operating costs associated with operating in these conditions, including higher gas consumption (Botef & Villafuerte, 2015).

3.8. Mechanism of Coating Formation of The CGDS Process

3.8.1 Impact Phenomena and Bonding Mechanisms in CDGS Process

While the bonding mechanism in thermal spraying is well-explained by the thermal softening due to ASI occurring at the particle–surface and particle–particle interfaces, the exact bonding mechanism in the CGDS process remains incompletely understood (Dickinson & Yamada, 2010; Ghelichi & Guagliano, 2009). A widely accepted model proposes that, during impact, solid particles undergo plastic deformation, disrupting oxides and establishing a tight conformal contact. The resulting high contact pressure facilitates bonding with the target surface (Lima, Karthikeyan, et al., 2002; Lima, Kucuk, et al., 2002). Common observations during spraying onto various surfaces include surface and particle deformation, as well as surface melting, providing evidence for the formation of a metal jet (V. K. Champagne et al., 2005; Ghelichi & Guagliano, 2009). In Figure 3.17, a simulation depicts a copper sphere with a diameter of 20 μm impacting an aluminum plate at a velocity of 650 m/s. The model illustrates that the material near the interface behaves as a viscous fluid, giving rise to interfacial waves, roll-ups and vortexes (V. K. Champagne et al., 2005). Despite these insights, the intricacies of the bonding mechanism in the CGDS process continue to be a subject of ongoing research and exploration.

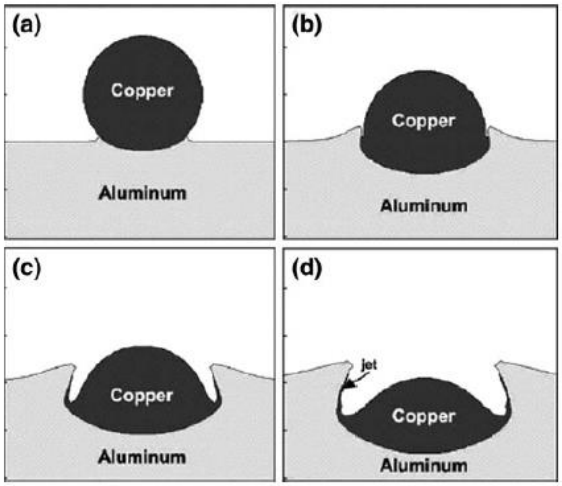


Figure 3.17 Sequential impact of a Cu particle on an aluminum substrate at different time intervals: (a) 5 ns, (b) 20 ns, (c) 35 ns, (d) 50 ns (V. K. Champagne et al., 2005)

The adhesion strength of particles in the CGDS process is proposed to be solely dependent on the kinetic energy they carry upon impact. This kinetic energy is generally much lower than the energy required to melt the particle, establishing cold spraying as a solid-state process (Dickinson & Yamada, 2010; Lima, Karthikeyan, et al., 2002). This concept finds support in research examining the cold spraying deposition of copper onto an aluminum substrate (V. K. Champagne et al., 2005). Moreover, this theory elucidates the significance of the critical particle velocity for deposition to occur, as a sufficient amount of kinetic energy is essential for the solid material to undergo plastic deformation (Lima, Karthikeyan, et al., 2002; Lima, Kucuk, et al., 2002).

In the CGDS method, the initial powder particles in the flow encounter the oxide layer on the substrate, preventing them from reaching the critical velocity (A. N. Papyrin et al., 2005; Steenkiste et al., 2002). Upon impact, these particles create craters and break down the oxide layer. Subsequent particles, in contact with a clean substrate, contribute to the formation of the desired coating (Figure 3.18). The coating formation in the CGDS process involves two stages. In the first stage, a coating layer is established on the substrate and adhesive bonds form through particle-substrate interactions. The selection of suitable substrate and powder materials, along with proper substrate surface preparation, is crucial in this initial stage (A. N. Papyrin et al., 2005). Warming the substrate before spraying is recommended to enhance coating

formation by increasing energy. In the second stage, approaching particles collide with previously deposited particles, undergo deformation, and bond together. As these impacts occur, the particles experience significant deformation, leading to reduced porosity in the coating. Powder preparation, including factors such as its shape, temperature and oxidation level becomes crucial at this stage. Even highly oxidized powder can be successfully deposited on a properly prepared substrate, but coatings formed in this manner may exhibit poor adhesive and cohesive properties (Steenkiste et al., 2002).

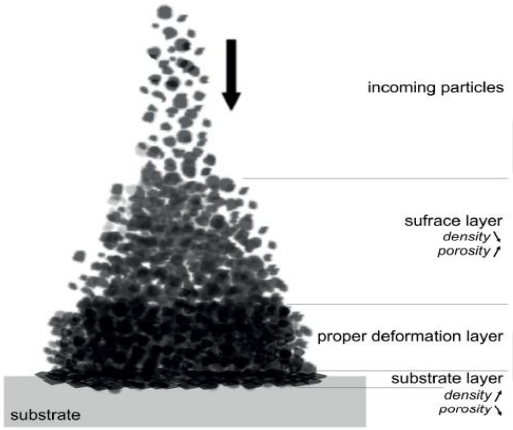


Figure 3.18 Illustration of coating formation in the CGDS process (V. K. Champagne, 2007).

Steenkiste et al., (2002) conducted a study on the formation of aluminum coatings using the CGDS method, focusing on relatively large powder particles (>50μm). They proposed a model to elucidate the coating formation process, outlining four fundamental stages. In the first stage, the substrate surface is activated through substrate cratering, leading to the formation of the initial coating layer as the surface oxide layer breaks. The second stage involves the deformation and realignment of particles due to successive impacts. The third stage is characterized by the formation of metallic bonding, contributing to a reduction in porosity. The final stage sees further concentration of the coating and the occurrence of work hardening. The schematic representation of these four stages in the pavement formation process is depicted in Figure 3.19.

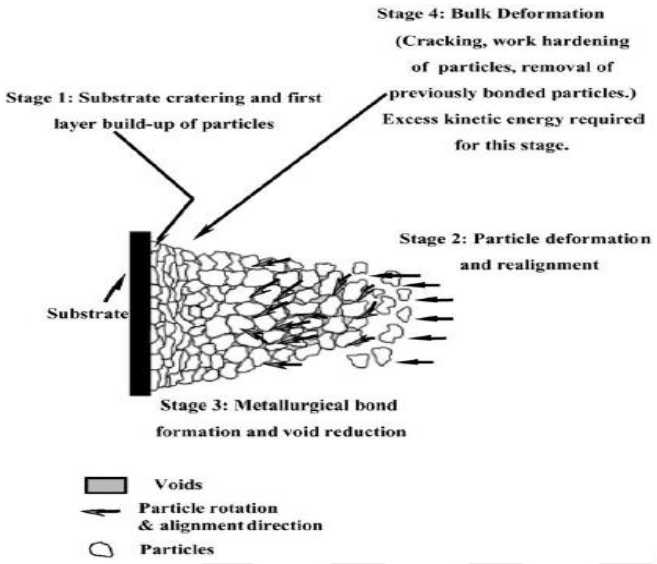


Figure 3.19 Stages of coating development in the CGDS process (Tokarev, 1996)

In the CGDS process, instances may arise where the substrate surface lacks oxides or obstacles. For example, in a pure metal devoid of surface oxides or other barriers, as depicted in Figure 3.20 (a), the excess dissipated energy surpassing the plasticity resulting from particle impact is entirely utilized by the spraying process. This facilitates the establishment of metal-to-metal contact and bonding at a considerably lower critical rate compared to scenarios where a surface oxide layer is present. In the second case, illustrated in Figure 3.20 (b), the excess dispersion energy is initially employed to overcome obstacles like cracking and delamination of surface oxides before metal-to-metal contact and bonding can take place (Adaan-Nyiak & Tiamiyu, 2023).

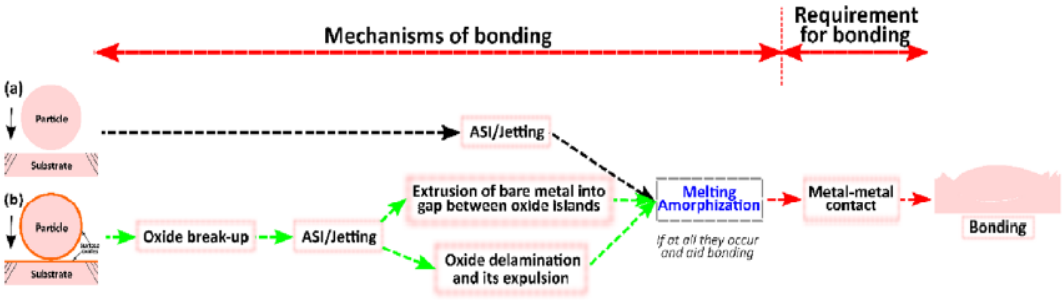


Figure 3.20 Bonding mechanism in a sample case: (a) without and (b) with native surface oxides (Adaan-Nyiak & Tiamiyu, 2023)

In reality, the surfaces of metallic parts are seldom smooth and often coated with an oxide layer. To establish a solid-state bond, it becomes imperative to remove these surface oxide layers and facilitate contact between fresh metallic surfaces. This can be achieved by subjecting the interfacial region to compression and stretching through plastic deformation, as schematically illustrated in Figure 3.21. The relevance to CGDS lies in the recognition of such interfacial deformation, which enables the disintegration of surface oxide layers and the contact of metallic surfaces at the atomic level. Consequently, the oxide layer should be perceived as a geometric constraint rather than an energy barrier to metallurgical bonding (Assadi et al., 2016).

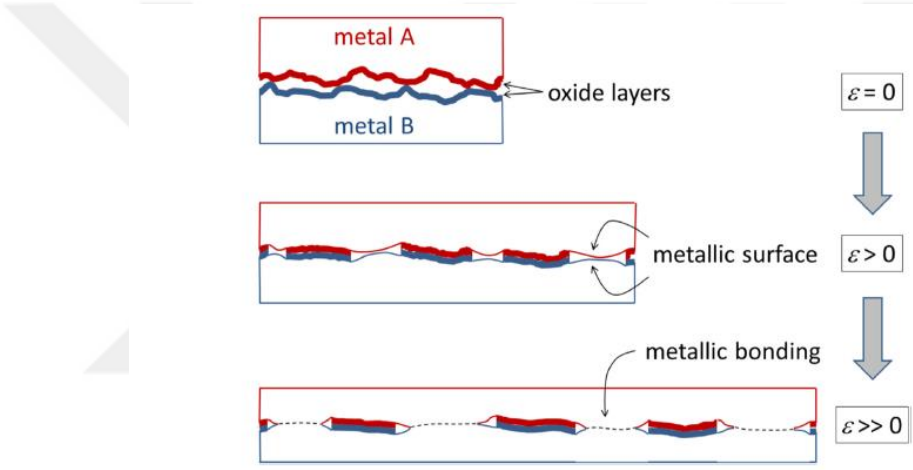


Figure 3.21 Illustration of interfacial plastic deformation in the CGDS process (Assadi et al., 2016)

The interaction between particles and the substrate significantly influences coating properties in the CGDS coating process, primarily due to the bonding mechanism. To gain a deeper understanding of this bonding process, both experimental studies and computational modeling have been conducted. These investigations reveal that adhesion occurs exclusively for powder particles surpassing the critical impact velocity specific to the spray material. In CGDS, the dominant bonding mechanism is associated with atomic-level adiabatic shear instability (ASI) occurring at or above the critical velocity at the particle-substrate interface. When a particle impacts the substrate, a robust pressure field is generated, inducing shear forces that result in lateral acceleration of the material. This localized shear deformation leads to ASI at the atomic level under critical conditions (Moridi et al., 2014). The binding mechanism in

the CGDS process remains a subject of debate, with studies in this field falling into two main categories: mathematical modeling that analyzes the impact on binding and experimental studies utilizing microstructural characterization techniques (Hussain, 2012). Ongoing research in these areas aims to provide further insights into the complex bonding processes during CGDS.

3.8.1.1 Mathematical Modelling Using Numerical Methods

3.8.1.1.1 Numerical Modelling of Copper Single Particle Impact

In the CGDS process, when a spherical particle moving at or above the critical velocity impacts a surface, a robust pressure field is generated, radiating spherically from the point of contact towards the surface. This pressure field induces a shear load that laterally accelerates the material, causing local shear deformation. Under critical conditions, this shear loading gives rise to ASI, where thermal softening prevails over strain and strain rate hardening at a localized level. This results in a discontinuous jump in strain and temperature, leading to the decoupling of flow stress (Schmidt, Gärtner, et al., 2006). The ASI phenomenon triggers a viscous outward flow of material, occurring at temperatures close to the material's melting point. This material ejection phenomenon is reminiscent of the observed material spraying in processes such as explosive welding of materials. Figure 3.22 provides visual evidence of this material ejection phenomenon, showcasing SEM images of a bound particle surrounded by a ring with jet-like morphology at the impact site.

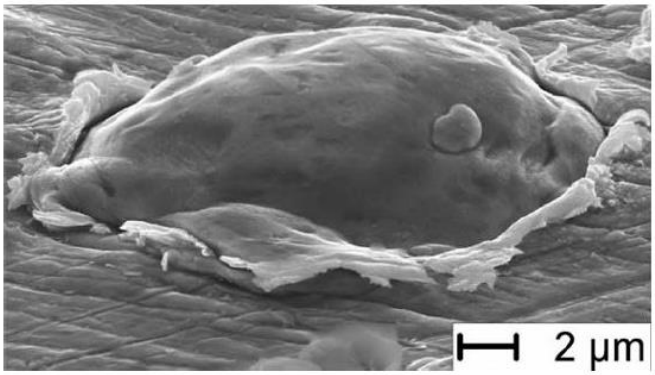


Figure 3.22 SEM of a Cu particle on a Cu substrate (Assadi et al., 2003)

Numerous studies propose that the ASI phenomenon contributes to bond formation in the CGDS process, yet the precise physical mechanism by which ASI promotes bond formation remains unclear. It is suggested that ASI leads to enhanced removal of oxides on contact surfaces, enabling metal-to-metal bonding when two oxide-free surfaces come into contact. Similar metal-to-metal bonding is observed in other solid-state processes like cold welding or roll bonding (Conrad & Rice, 1970). The key criterion distinguishing cold spray bonding from other solid-state processes is the rate of deformation; in CGDS, the deformation rate falls within the range of 10^{6-9} /s. If cold welding or roll bonding occurs, ASI is less likely, although there is substantial plastic deformation at the interface. Theories on cold welding propose that sufficient plastic deformation pressure at the interface ensures conformal contact across a significant portion of the interface. The removal of surface oxides by a material jet produced by ASI can, in principle, provide a clean surface between two mutually conforming regions (Grujicic et al., 2004). It is crucial to have a sufficient number of sliding systems within the material to achieve compliant contact (Buckley & Johnson, 1968). Studies have noted an increase in interfacial bonding when the crystal structure of the metal is FCC instead of HCP or BCC. This is attributed to the greater number of active slip systems present in FCC structures. While numerical models in cold spraying have proven valuable in predicting material deformation behavior, current models often overlook factors such as oxidation removal or the establishment of conformal contact between two surfaces (Hussain, 2012).

3.8.1.1.2 Critical Impact Velocity and Critical Particle Diameter.

ASI occurs when particles move at a specific critical velocity (Assadi et al., 2003; Schmidt, Gärtner, et al., 2006). As illustrated in Figure 3.9, there is a suggested schematic relationship between deposition efficiency and particle velocity. Deposition efficiency is defined as the ratio of the total mass of particles entering the impact area to the mass of deposited particles. Particles traveling below a certain velocity may cause wear on the surface, while particles traveling at or above a certain velocity can induce deposition and coating formation. In this context, the critical velocity, which

represents a shear rate below the erosion event and above the deposition event, is considered crucial (Gärtner, Stoltenhoff, Schmidt, et al., 2006b).

Particle sizes play a role in affecting the critical velocity. The ASI phenomenon, characterized by a rapid increase in local temperature in the bonding region and the rate at which the material loses heat, is crucial in bonding formation. The cooling rate of the material tends to decrease with larger particle sizes. Striking a balance is important; the cooling rate should be low enough to promote shear instability, yet it must be high enough for the interface to solidify and complete the bonding process. In small particles, shear instability can be hindered due to higher temperature gradients and greater strain hardening. Moreover, smaller particles experience higher cooling rates during production, leading to increased strength and they contain higher impurities due to the elevated surface-to-volume ratio (Schmidt, Gärtner, et al., 2006). These factors collectively can impede local deformation at the onset of ASI, potentially increasing the critical velocity. Schmidt et al., (2006) proposed Equation 3.5 for determining the critical size of particles (d_{crit}).

$$d_{crit} = 36\frac{\lambda_p}{C_p.\rho_p.V_p} \tag{3.5}$$

In Equation 3.5, λ_p represents the thermal conductivity, C_p represents the specific heat of the particle, ρ_p represents the density and V_p represents the velocity of the impacting particle. This equation provides insight into the critical particle size at which thermal dissipation is sufficiently slow for ASI to occur. As depicted in Figure 3.23, the critical diameter of various particles can be determined using Equation 3.5 and particles smaller than the critical size will not meet the ASI criterion.

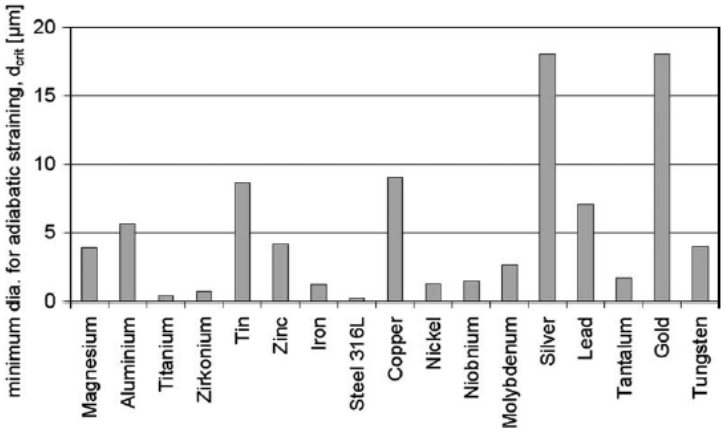


Figure 3.23 Threshold particle diameter for localized ASI in various materials (Schmidt, Gärtner, et al., 2006)

When comparing V_{crit} values reported in the literature, it is essential to consider the effects of particle size distribution and purity. Additionally, the lack of a standardized measurement method introduces some variability among different researchers. Table 3.8 presents seven values for the critical velocity of copper. C. J. Li et al., (2006) reported values ranging from 520 to 610 m/s, with the exception of the measurement at 327 m/s. Initially, the 327 m/s value may seem incompatible with the others. However, it becomes apparent that smaller particle sizes were used in this measurement. Additionally, C. J. Li et al., (2006) employed higher purity copper, a factor shown to be significant in oxidation tests.

Table 3.8 Measured critical velocities for Cu particle (King et al., 2015).

Particle size (µm)	Powder properties	Measurement technique	Critical velocity (m/s)	Reference
5–22	Inert gas atomized, 99.8 % purity	Deposition efficiency, combined with particle velocity distribution by Computational Fluid Dynamics (CFD), verified by laser Doppler anemometry	570	Assadi et al., (2003)
5–25	Spherical morphology, oxygen content < 0.2 %	Deposition efficiency, particle velocity determined by CFD	550	Gärtner, Stoltenhoff, Schmidt, et al., (2006a)
10–33	–	Deposition efficiency, particle imaging	538	Raletz et al., (2006)
		Particle imaging, velocity calculated by 1-D isentropic model	520	

Table 3.8 continues

Average 56	Gas atomized, oxygen content ~0.01 %	Deposition efficiency, particle velocity determined by CFD	327	C. J. Li et al., (2006b)
	As above, oxidized to 0.14 % oxygen		550	
	As above, oxidized to 0.38 % oxygen		610	

3.8.1.1.3 Deposition Window in Cold Spray Process

Figure 3.24 illustrates the proposed relationship between particle velocity and DE at a given temperature. It is argued that at the 50% accumulation efficiency level, the relevant velocity should be identified as the critical velocity. For an appropriate spraying material, deposition efficiency experiences a sharp increase beyond the critical velocity, reaching 100% deposition efficiency at saturation (Schmidt et al., 2009). Optimal coating conditions are anticipated in a region where deposition efficiency is nearly 100%. Beyond the saturation point, the rise in particle velocity results in a decrease in deposition efficiency due to hydrodynamic erosion of particles (S. V. Klinkov et al., 2005; Schmidt et al., 2009). To demonstrate the impact of this phenomenon, cross-sectional images depicting the large-scale impact of a 20 mm copper ball on low carbon steel are presented in Figure 3.36. The particle velocity beyond which accumulation does not occur and only causes erosion is defined as the erosion rate. Furthermore, brittle materials such as ceramics exhibit erosion at any velocity, making deposition through the CGDS process challenging.

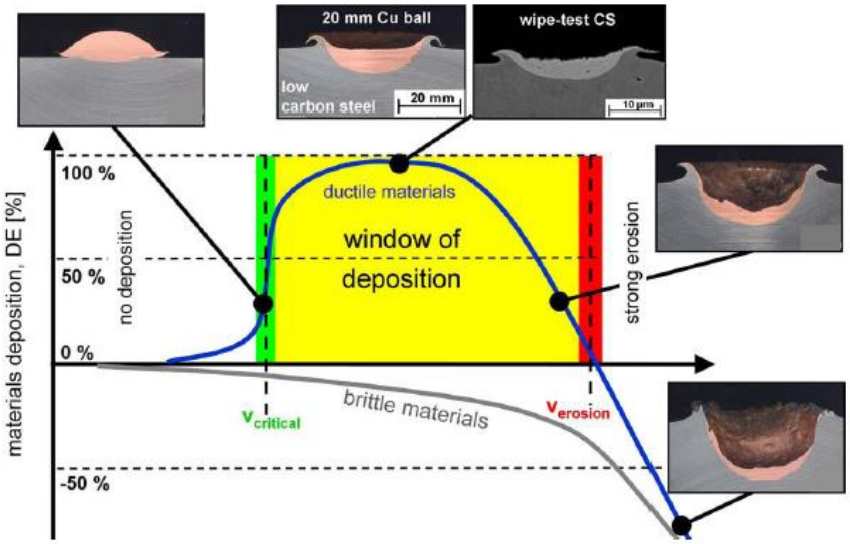


Figure 3.24 Correlating particle velocity, DE and impact effects in a schematic at constant temperature (Schmidt et al., 2009)

3.8.1.1.4 Particle-substrate Impact Behavior

The particle-substrate deformation behavior during the CGDS process can be categorized into four types: soft particle on a soft substrate, soft particle on a hard surface, hard particle on a soft substrate and hard particle on a hard surface (Bae et al., 2008). Figure 3.25 illustrates these four cases, showcasing the effects of particles on substrates. In the soft particle / soft substrate case (e.g., Al/Al), greater deformation was observed compared to the hard particle / hard substrate case (e.g., Ti/Ti) due to lower material strengths. In both cases, higher temperatures were found on the substrate side than on the particle side. In the other two cases, soft particle/hard substrate (e.g., Al/medium steel) and hard particle/soft substrate (e.g., Ti/Al), deformation occurred in the relatively soft counterpart. It is also noteworthy that a significantly higher temperature is attained on the softer side.

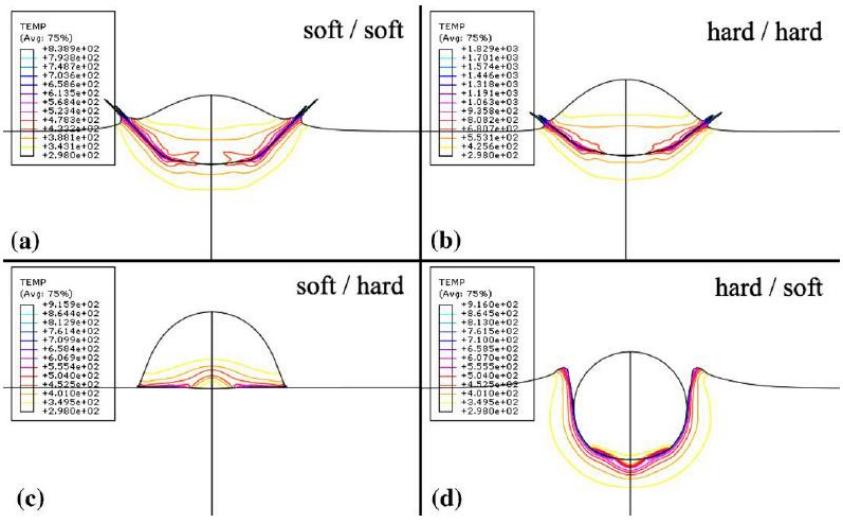


Figure 3.25 Four scenarios of particle impact on substrate: **(a)** soft/soft (Al onto Al), **(b)** hard/hard (Ti onto Ti), **(c)** soft/hard (Al onto Mild Steel), **(d)** hard/soft (Ti onto Al) (Bae et al., 2008)

The choice of feedstock material plays a crucial role in determining the deposition mechanism of particles in the CGDS process. Soft particles tend to undergo more severe deformation compared to hard particles, resulting in better adhesion strength. In contrast, hard particles can cause abrasion on the substrate. On the other hand, soft particles deform without causing abrasion on the substrate (Go et al., 2019). Furthermore, the hardness of the substrate itself is a key factor in the adhesion mechanism. For instance, a soft-soft interface typically provides better adhesion strength, often attributed to the formation of a material jet. Figure 3.26 provides a schematic representation of different particle-substrate hardness combinations (Rokni et al., 2017).

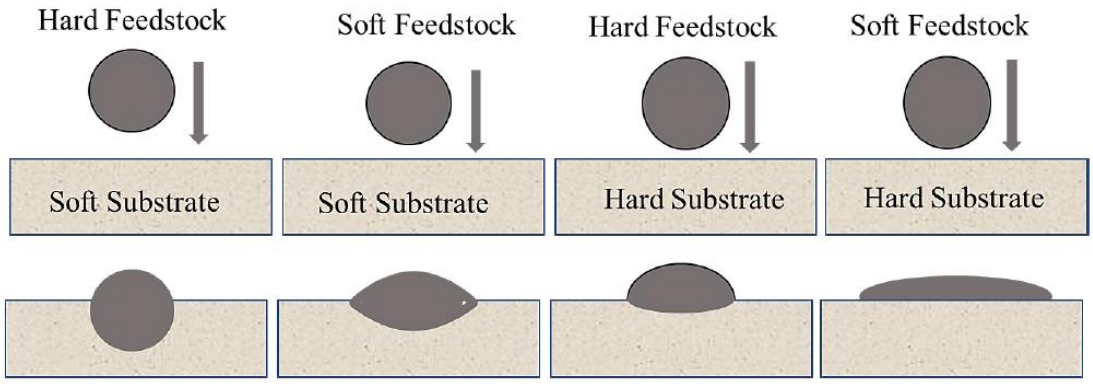


Figure 3.26 A diagram illustrating the impact behavior of various particle-substrate hardness combinations (Rokni et al., 2017).

A similar phenomenon is observed during the deposition of powder mixtures containing both soft metal and hard metal particles, as illustrated in Figure 3.27 under two different scenarios. The impact energy of soft metal particles is sufficiently high to facilitate bonding on the substrate surface as well as on previously adhered soft or hard metal particles. Conversely, the impact energy of hard particles is only adequate for bonding to a surface pre-coated with soft metal. Scenario 1 depicts the mechanical embedding of hard particles into a soft matrix. However, if hard particles reach a surface covered with previously bonded hard particles, the impact energy is insufficient for bonding, causing the hard particle to bounce back (scenario 2). As a result, the deposition efficiencies of hard and soft mixture components exhibit significant differences. The deposition efficiency of soft metal particles remains constant, whereas the deposition efficiency of hard metal particles depends on the type of surface the hard particles encounter upon impact. Consequently, if the spray mixture contains a low percentage of hard metal particles, scenario 1 predominates. Increasing the percentage of hard particles in the mixture shifts the formation probability towards scenario 2 (Lapushkina & Sova, 2019).

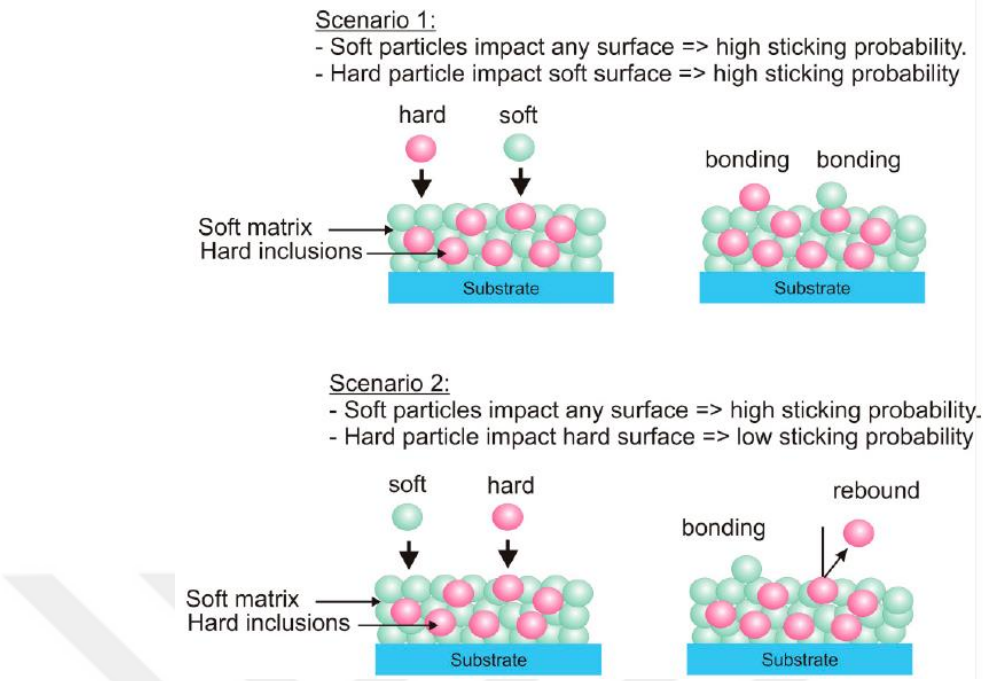


Figure 3.27 Potential particle dynamics upon impact in the context of CGDS using a two-component powder blend with hard and soft components (Lapushkina & Sova, 2019)

3.8.1.1.5 Adhesion and Rebounding Energy

In the cold spray literature, there exists a bonding model that incorporates adhesion energy and recoil energy (J. Wu, Fang, et al., 2006). In this model, bonding is conceptualized as the outcome of the competition between adhesion energy and recoil energy. Experimental studies have been conducted to observe the impact of velocities on deposition across a wide range, encompassing velocities both below the critical velocity and above the erosion rate. Adhesion energy (Ad) is defined as the energy required for an attached particle to detach from the substrate. Ad is calculated using Ad_{max} (maximum adhesion energy) and a% (percentage of bonded atoms per unit at the adhesive interface) with the formula Ad = a% Ad_{max}. Kurochkin et al., (2002) proposed Equation 3.6 to calculate a%.

$$a\% = 1 - exp\{-\upsilon t_c \exp[\frac{-E_a}{kT_c + \frac{(1-e_r)M_a V_p^2}{2}}]\} \quad (3.6)$$

In Equation 3.6, υ represents the natural frequency of specific oscillations of the atoms in the lattice, t_c represents the contact time, E_a represents the activation energy, T_c represents the contact temperature, k represents the Boltzmann constant, e_r represents the recoil coefficient, M_a represents the atomic mass value and V_p represents the velocity of the impacting particle.

$$Ad_{max} = S_c N_a E_1 \tag{3.7}$$

Ad_{max} can be calculated using Equation 3.7. In this equation, S_c refers to the contact area of a single particle to the surface, N_a refers to the total number of atoms in the unit plane and E_1 refers to the single bond energy between two atoms.

Rebounding energy refers to the energy required for a particle to bounce back as soon as it leaves the surface. The rebounding energy (R_e) is expressed using Equation 3.8 as:

$$R_e = \frac{1}{2} e_r m_p {V_p}^2 \tag{3.8}$$

In Equation 3.8, m_p and V_p refer to the mass and velocity of the particles respectively and e_r refers to the rebounding coefficient.

Figure 3.28 illustrates the calculated adhesion energy and recoil energy for Al-Si particles in three different sizes (25 μm, 30 μm and 50 μm) at various velocities. The particle can successfully attach to the substrate only if the adhesion energy surpasses the rebounding energy. When the particle velocity is below the critical velocity but exceeds the erosion rate, the rebounding energy surpasses the adhesion energy, hindering the occurrence of any deposition.

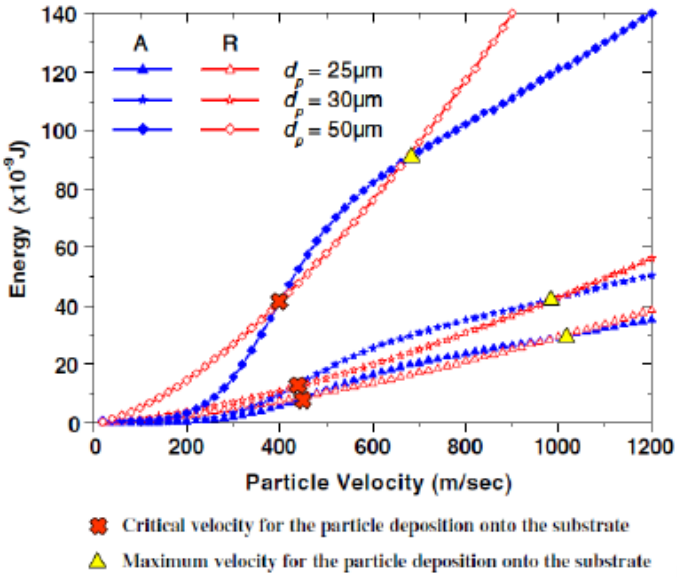


Figure 3.28 Computed adhesion energy and rebounding energy for Al-Si feedstock of different sizes impacting mild steel (J. Wu, Fang, et al., 2006)

3.8.1.2 Experimental Investigations

3.8.1.2.1 Shear Lips and Craters Formation

In the early stages of cold spraying, investigations into particle–substrate interactions revealed the formation of slip lips at the interface of deposited particles and the creation of craters in the substrate from particles bouncing back. A. Papyrin et al., (2006) conducted a study on the interaction between individual aluminum particles and a copper substrate at different velocities, with the aim of understanding the transition from particle recoil to adhesion. At lower particle velocities, individual craters formed upon particle impact and no particles were deposited. As the particle velocity increased, particles began to adhere to the substrate. These experiments demonstrated that beyond the critical rate threshold, a transition from substrate erosion to sedimentation occurs. Assadi et al., (2003) reported the morphology of jet-type cutting lips around copper particles deposited on a copper substrate. Hussain et al., (2009) investigated the deformation behavior of particles in copper-aluminum and titanium-steel systems, attributing particle and substrate deformation to high strain rate material properties. Figure 3.29 illustrates that aluminum particles deposited on a copper substrate result in particle jetting, while copper particles deposited on an aluminum substrate cause spraying of the aluminum substrate. Jet-type morphology was not observed in the craters left by non-adhesive particles in the substrate.

Additionally, Dykhuizen et al., (1999) stated in a study on cold spraying of copper particles onto a steel substrate that crater formation depends on particle velocity and pointed out that an increase in velocity leads to an increase in crater depth.

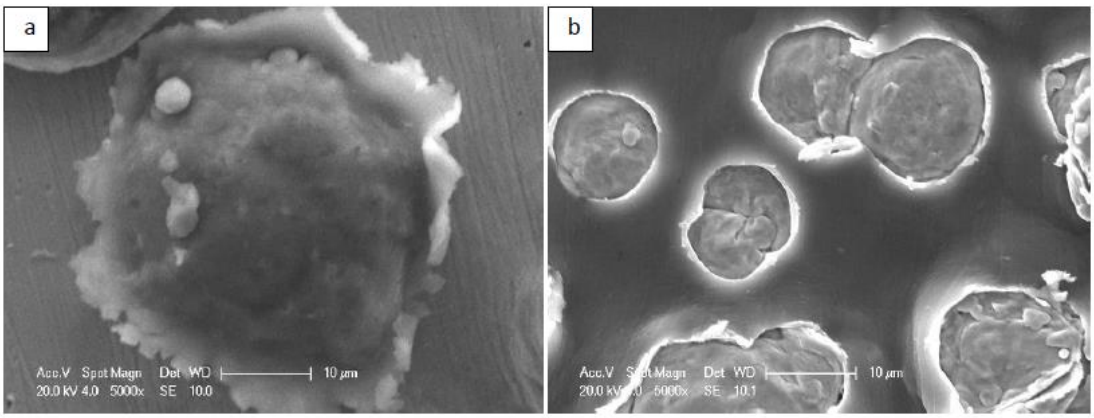


Figure 3.29 Views of **(a)** Al particle on Cu substrate and **(b)** Cu particles on Al substrate (Hussain et al., 2009)

3.8.1.2.2 Bonding in Low Pressure CGDS Process

In the context of LPCS, the particle velocity remains significantly below the critical velocity required for deposition. It is widely acknowledged that for metal particles to be successfully deposited on the substrate surface, they must undergo substantial plastic deformation. In contrast, in the HPCS system, the particle's velocity surpasses the critical velocity, enabling intense plastic deformation to generate the necessary kinetic energy. The shear flow at the interface results in the dissipation of kinetic energy, diminishing rebound flow and promoting close surface coupling. Plastic deformation, following shear flow, is influenced by material properties and impact pressure. To facilitate impact, the material can be softened through thermal softening, or the impact pressure can be increased by enhancing the impact force or reducing the contact area. At velocities below critical velocities, the impact force is often insufficient to induce shear flow. Therefore, achieving the desired state can frequently be accomplished by minimizing the contact area. A rough surface with numerous peaks at the powder scale can induce extensive plastic deformation compared to a smooth surface (Hussain, 2012).

In the production of coatings using the LPCS system, ceramic powder components such as alumina are combined with metallic powder. The primary purposes of incorporating ceramic powder are to activate the sprayed surfaces and to enhance the substrate/sprayed layers through the shot-peening method (Koivuluoto et al., 2008; Shkodkin et al., 2006). When metal mixtures containing both soft and hard metals or ceramic powders are sprayed at a low gas stagnation temperature to deposit the soft metal, a composite coating comprising a soft matrix with embedded hard particles can be formed (Guo et al., 2009; S. V. Klinkov et al., 2008). Simultaneously, using the same hard powder, the same equipment and the same low gas stagnation temperature, if soft particles are not added, the coating cannot be formed because the coalescence efficiency is zero (Lapushkina & Sova, 2019). The presence of ceramic particles in the feedstock introduces a compression effect, leading to improved coating properties. Moreover, ceramic particles contribute to the cleaning of the nozzle. It has been observed that increasing the proportion of ceramics in the feedstock enhances the bond strength and density of the coating, albeit at the expense of decreased DE (Hussain, 2012).

3.8.1.2.3 Removal of Surface Oxides

The initial layer of coating deposition, involving the deposition of particles onto the substrate, includes surface activation through cratering of the substrate surface and the removal of surface contamination (A. Papyrin et al., 2006; Tokarev, 1996). According to A. N. Papyrin et al., (2005), the first impinging particles enhance the chemical activity of the surface by increasing dislocation concentrations in the uppermost layer. During particle deformation events, oxide shells on interacting surfaces are broken and clean surfaces are brought together, facilitating bonding. Moreover, it has been suggested that the interfacial material jet produced by the ASI phenomenon assists in removing oxide films on the surface, ensuring the establishment of an intimate metal-metal contact (Assadi et al., 2003; Schmidt, Gärtner, et al., 2006).

Kang et al., (2008) and C. J. Li et al., (2010) investigated the influence of powder oxide content on the critical rate for deposition. It has been proposed that the critical velocity of the material depends not only on its material properties but also on its oxidation state. The studies indicated that increasing the oxide content of copper

powder from 0.02 wt.% to 0.38 wt.% raised the critical velocity from 300 m/s to 610 m/s. Additionally, Kang et al., (2008) explored the impact of aluminum feed powder oxide content on critical velocity. The findings revealed that increasing the oxide content of the powder, with the same size distribution, from 0.001 wt.% to 0.045 wt.% resulted in an increase in the critical velocity from 742 m/s to 867 m/s. Conversely, it was mentioned that the critical velocity is influenced by oxide thickness. Thicker oxide layers were found to require more energy for removal, leading to less dissipation of plastic deformation energy into the particle. Moreover, the increase in oxide content led to a decrease in the particle flattening rate. Although ASI at the particle-substrate interface can disrupt the oxide film, it is suggested that some oxide may remain at the interface, hindering particle-substrate adhesion (J. F. Li et al., 2010).

3.8.1.2.4 Contributions of Mechanical and Metallurgical Components on Adhesion

In the CGDS process, adhesion is linked to metallurgical bonding and mechanical interlocking (Hussain et al., 2009). The dominance of each mechanism is largely contingent on the properties of the particle/substrate and the conditions of particle impact (Drehmann et al., 2014; Huang et al., 2014). Robust mechanical interlocking is commonly observed at the coating-substrate interface when particles are considerably harder than the substrate. In such instances, the impact of incoming particles leads to metal jetting, forming lips of soft substrate material that partially cover the impacting particles (Hussain et al., 2009). Additionally, if the hardness of the impacted surface is significantly lower than the hardness of the powder, particles may adhere to the surface even below the critical impact velocity (Bray et al., 2009). The contributions of these two bonding mechanisms, as applied in CGDS technology, are explained in terms of modified composite theory. It has been noted that, when applying cold-sprayed copper coatings to aluminum substrates, mechanical interlocking can predominantly contribute to the total bond strength, while metallurgical bonding becomes significant only when the substrate is softened before spraying (Hussain, 2012).

Hussain et al., (2009) introduced a connection mechanism termed "mechanical locking" when applying the CGDS method to spray copper particles onto aluminum

surfaces. They explained that the impact of copper particles on the aluminum surface resulted in the formation of lips on the aluminum surface, partially enclosing the copper particles. This led to a mechanical locking effect between the substrate and the impacting particles, as depicted in Figure 3.30.

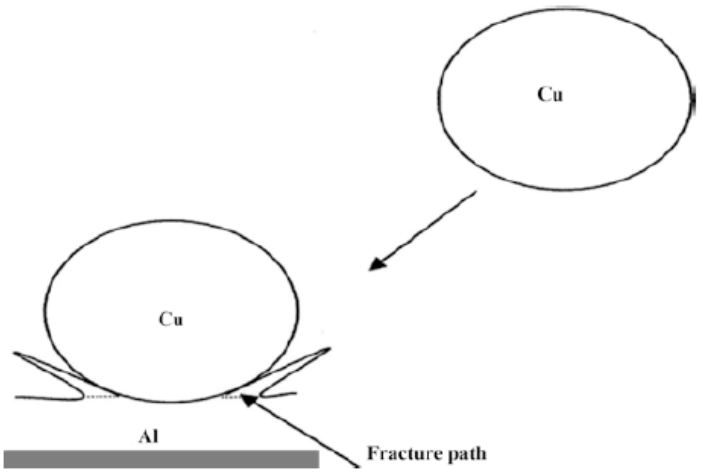


Figure 3.30 Illustration of jet formation on an aluminum substrate induced by an approaching Cu particle (Hussain et al., 2009)

CHAPTER FOUR
APPLICATIONS OF COLD GAS DYNAMIC SPRAY PROCESS

4.1. Background

CGDS technology holds significant potential across various industries (Kumar et al., 2020). Widely utilized as a coating technology, the CGDS process finds application in diverse sectors, including defense, aerospace, automotive, electronics-electromagnetics, energy, biology-medicine, marine and more (Yin et al., 2018). Among thermal spraying technologies, the CGDS process stands out as the most widely employed, thanks to its ability to be sprayed onto any substrate due to its low heat input. Notably, CGDS technology enables the deposition of cermets, ceramic mixtures and complex metals onto diverse substrates. This process facilitates the production of thick coatings characterized by low porosity, minimal oxide content and crack-free properties (Kumar et al., 2020). Coatings generated through the CGDS process provide effective protection against high temperatures, corrosion, abrasion, oxidation, and chemical exposure (V. Champagne & Helfritch, 2016). Furthermore, CGDS has evolved into an additive manufacturing technology, demonstrating success in the production of free-standing metal parts and the repair of damaged metal components in recent years (W. Li et al., 2018; Yin et al., 2017).

The CGDS technique was initially applied in the last decade of the previous century (V. K. Champagne, 2007). Presently, this process finds widespread use across various industries, contributing to the enhancement of product value and improving the functionality and performance of numerous commercial products. Recent successful applications of the CGDS process encompass coatings, repairs, and the creation of freestanding structures. These coatings exhibit a wide range of functionalities, from corrosion protection films to catalytic surfaces. In the realm of component repairs, aviation materials and castings take a leading role. Structural applications include the manufacturing of heat exchangers, pipes and gears using CGDS (Kumar et al., 2020).

CGDS demonstrates its versatility in various electrical applications, including the creation of coherent antennas, circuits and electromagnetic shielding. Furthermore, in the realm of biology and medicine, CGDS proves invaluable for applications such as the development of self-cleaning surfaces and the repair of bones. The CGDS process

stands out as a prominent technology, particularly in defense industry applications. To facilitate its implementation and standardize repair processes, a military standard known as MIL-STD-3021, titled "Material Deposition, Cold Spraying," has been established and approved by all departments and agencies of the US Department of Defense (DOD). This standard outlines CGDS processing procedures and test methods, significantly contributing to the acceptance and standardization of CGDS technology in defense industry applications and repair processes (V. Champagne & Helfritch, 2016).

The CGDS process has transformed the landscape of component repairs, making a substantial contribution to lowering sustainability costs, particularly in the aerospace industry. Comparable savings can be realized across various crucial sectors, including petrochemical and nuclear energy industries. A report highlights the significant role of the CGDS process in diminishing maintenance frequencies and cutting costs for the DOD and the defense industry. The aviation industry, particularly in the production of aircraft components, faces challenges related to corrosion and wear in materials like magnesium alloys. Critical components such as transmission and gearbox housings, especially in large and expensive rotorcraft, are particularly susceptible to these issues. CGDS technology emerges as a promising solution with the potential to enhance operational continuity in the industry. Specifically, CGDS applications in aviation, with a focus on large and valuable components, present an opportunity to prolong aircraft life and enhance operational efficiency by mitigating maintenance costs. This represents a noteworthy advancement in securing comparable benefits for the defense industry and other sectors (V. K. Champagne et al., 2017).

4.2. Potential industrial applications of CGDS

The CGDS process offers a large number of deposits solutions summarized briefly in Table 4.1. In this table various functional features, materials researched for the CGDS process and typical application areas are discussed. In general, the CGDS process has at least four potential usage areas: surface functionalization, restoration, art/decoration and bulk production that provides certain material properties (Raoelison et al., 2017).

Tablo 4.1 Current perspectives on the capabilities of the CGDS process (Raoelison et al., 2017).

Functional properties of CGDS deposit	Metals and alloys	Metal/Polymer	MMCs : Metal/Ceramic	MMCs : Metal/Metal	Intermetallics (IMCs)	Oxides	Ceramics	WC cermets	MMCs/Cermets	MAlCer	MCrAlY	Stellites	Carbides	Polymers	Thermites	Nanomaterials	Typical application area
Corrosion resistant	O	O	O	O	O				O	O	O	O	O			O	Aerospace, automobile, electronics, defense, petrochemical , oil industry, energy
Oxidation resistant	O	O		O	O	O			O	O	O						
Erosion resistant	O		O					O				O	O			O	Aerospace, naval, electric contact applications
High specific strength	O	O	O		O		O									O	Variety of industrial sectors
Wear resistant	O		O	O	O	O	O	O	O							O	Automobile, aerospace, machining, decoration
Abrasive	O							O				O				O	Variety of industrial sectors
Anti-friction	O			O								O					Automobile, aerospace, naval, civil engineering
Specific bonding layer	O									O	O						Variety of industrial sectors
Restoration	O		O														Aerospace, defense, petrochemical
Bulk material	O													O		O	Variety of industrial sectors
Biocompatibility	O					O								O		O	Biomedical (dental and orthopedic implants)
Anti-bacterial	O	O				O								O			Biomedical
Conductive/insulation	O		O	O		O	O			O						O	Electronic, aerospace, energetic, electric contact
Photovoltaic performance	O		O			O										O	Energy generation industry
Photocatalytic performance	O					O										O	Energy generation industry
Energetic materials	O				O	O									O		Energy generation industry, energetic

4.2.1. Coatings

Surface engineering involves research aimed at enhancing the surface properties of materials to extend the functionality and lifespan of components. Coatings confer functional properties by forming a thin film layer on the surface. These coatings are applied to impart thermal and corrosion resistance, enhance wear resistance, reduce the friction coefficient, or improve the aesthetic and decorative qualities of the material surface. The proper implementation of surface engineering and coatings markedly enhances the performance and durability of components, leading to lower energy consumption, extended service life and reduced maintenance costs (Dobler, 2006).

CGDS has undergone significant enhancements, evolving into a dependable process for surface functionalization. This progress can be attributed to three primary advantages: the ability to bond the coating to a surface that is metallurgically incompatible in traditional techniques, the deposition of diverse materials, and the capability to preserve initial properties during solid-state deposition. These factors facilitate the development of various functional properties. For metallic structures, notable advancements have been achieved in terms of special resistance performances (corrosion resistance, oxidation resistance, erosion resistance and wear resistance), special durability performances (high specific strength and anti-friction ability) and other distinctive properties (such as interconnection functions, heat dissipation, or abrasive properties) (Raoelison et al., 2017).

Coatings are typically applied to surfaces to provide protection or enhance functionality and they often consist of layers no thicker than 1 mm, occasionally even thinner than 0.1 mm. The CGDS process is a commonly favored technique for applying coatings, particularly when dealing with temperature-sensitive substrates and/or coating powder. CGDS mitigates the adverse impacts that may arise from high temperatures by preventing the thermal effects on both the coating material and the substrate. This method is particularly well-suited for alloys and materials sensitive to heat. Furthermore, the adhesion strength and surface properties of coatings produced through the CGDS process surpass those achieved by alternative coating methods, contributing to its growing popularity within the industry (V. Champagne & Helfritch, 2016). Surface coatings play a crucial role across various manufacturing and

engineering industries, enhancing the surface properties of components crafted from economical, lightweight, or sustainable materials. These coatings have paved the way for innovative technologies in diverse products, including gas turbine engines, drill bits, architectural glass, orthopedic implants and more. Surface engineering and advanced coatings serve to predictably extend the service life of components or confer properties that the original substrate material may lack, ensuring optimal performance in specific applications. The need for diverse material attributes and the economic repercussions of material loss due to surface degradation have driven the development of efficient and cost-effective surface treatment processes (Khan et al., 2010; Schmidt, Gaertner, et al., 2006). Table 4.2 succinctly outlines the primary advantages and application areas of CGDS coating materials.

Table 4.2 Applications of CGDS coating materials in manufacturing and engineering industries (Kumar et al., 2020).

Coating Material	Primary Property Benefit	Application
Ceramic coatings	Improved corrosion resistance and wear resistance	Solar cells, sterilization, cancer therapy, condenser, machining tool protection, engine exhaust manifolds, photo electrodes, oxidation resistance at elevated temperature, Furnace components, heat treating equipment, chemical processing equipment, heat exchangers, rocket motor nozzles, exhaust manifolds, jet engine parts and nuclear power plant components etc.
Zinc-aluminum alloys	Sacrificial galvanic protection for corrosion resistance, oxidation and sulfidation resistance	Covering material for roofs, steam generators, corrosion protection of steel and other high- temperature applications, bridges, ships, and other large structures power boilers and other high-temperature uses etc.
Nickel based alloys	Good resistance to wear, oxidation and high temperature corrosion	Used where corrosion free life is required for a long period. It can also be used for dimensional restoration and repair, wear resistance application, mill rolls, gas turbine, pumps and chemical plants. medical equipment's, heat exchanger, etc. piston extruders and glass mold industry. Aerospace, automotive, oil refining industries medical devices, agriculture, wearing plates and pump bushing etc.
Copper, silver, aluminum and titanium alloys	Excellent electrical conductivity or superior corrosion resistance	Applications that require excellent electrical conductivity or superior corrosion resistance are the two areas of greatest interest to motive and electronics, in aerospace and military application etc.

4.2.1.1 Corrosion protection

The CGDS technology represents a highly effective strategy for corrosion mitigation, providing a protective shield to the material or substrate against adverse environmental factors. The primary function of the coating produced through the CGDS process is to envelop the material surface, serving as a barrier to hinder the substrate's interaction with water, oxygen, chloride ions and other corrosive agents. The widespread adoption of zinc and aluminum coatings on steel attests to their prevalence in safeguarding various structures, including pipelines, bridges, towers, tanks and large steel constructions exposed to corrosive elements like seawater and humid atmospheres. This innovative CGDS process demonstrates versatility in corrosion protection and finds application across a spectrum of industries, encompassing the defense sector, automotive, aerospace, glass manufacturing, paper and pulp, chemical, cement, metal processing and printing industries (Fauchais et al., 2010).

4.2.1.2 Wear protection

In the cold spray deposition process, the effective deposition of powders is contingent upon inducing deformation in the particles upon impact. Consequently, the deposition of hard and wear-resistant materials poses challenges. To address this limitation and create abrasion-resistant coatings through cold spray, a prevalent approach involves the concurrent spraying of a composite mixture comprising hard particles and softer, more pliable particles. In this method, the softer material tends to accumulate upon contact with the substrate, forming a ductile layer. Simultaneously, the hard and wear-resistant particles become embedded within this ductile layer. The resultant deposition manifests as a composite structure, characterized by a matrix composed of hard particles, typically ceramics, embedded within a metal binder (V. Champagne & Helfritch, 2016).

4.2.2. Restoration/Repair

Presently, a substantial expansion is evident in the domain of restoration and repair applications, owing to the utilization of the cold spray method. The growing interest in this field aligns with the advancement of novel "green techniques and methods,"

contributing to ecological advancements. Beyond material recycling, the process of repair and refurbishment presents a dependable alternative in the product life cycle assessment. This approach not only facilitates savings in terms of raw material and energy consumption associated with the production of an entire product but also yields favorable outcomes in various dimensions, including ecological efficiency improvement, reduction in waiting time for product replacement, mitigation of stock shortages and alleviation of budget constraints. This underscores the economic viability of restoration and repair processes employing cold spraying (Raoelison et al., 2017).

The application of CGDS for repair purposes is primarily directed towards achieving dimensional restoration. The metal powder employed in the restoration of a component may or may not be identical to the metal constituting the repaired part. In certain instances, the use of a different metal may offer superior properties compared to the original part, particularly in cases of corrosion damage, where employing a more corrosion-resistant metal can enhance the repair. The aviation industry stands out as a prominent beneficiary of CGDS repair methodologies. Notably, certain magnesium alloy aviation materials, integral to the manufacturing of aircraft components, face significant corrosion challenges. Prior to the advent of CGDS technology, the recovery of numerous components was rendered impractical due to the absence of a suitable technology for dimensional restoration. The ability to apply the repair metal at a relatively low temperature is often crucial for successful application. A proficient repair must meet diverse service requirements, encompassing dimensional integrity, bond strength, porosity, corrosion resistance and strength (V. Champagne & Helfritch, 2015).

4.2.3. Additive manufacturing

Additive manufacturing (AM) stands as an advanced technological approach wherein three-dimensional objects are constructed through the sequential deposition of materials such as metal, plastic, or concrete, layer by layer. This innovative technology presents numerous advantages over traditional manufacturing methods, including reduced material waste, facile production of components, heightened precision, enhanced quality and expedited production times (Rejeski et al., 2018). The

CGDS method offers a distinctive capability in additive manufacturing, where there exists no theoretical constraint on the thickness of coatings. Utilizing the cold spray method and powders derived from diverse raw materials, substantial deposits, reaching several centimeters in thickness, can be achieved. Consequently, the CGDS process demonstrates the ability to generate three-dimensional shapes featuring various geometries. To achieve this, the cold spray nozzle is strategically directed towards a suitably shaped mandrel onto which the feed powder is applied. The robotic control of the nozzle enables it to traverse the contours of the intended shape, facilitating the deposition of multiple layers until the desired thickness is attained. Subsequently, the mandrel is removed and machining operations are executed (V. Champagne & Helfritch, 2016).

Cold Spray Additive Manufacturing (CSAM) emerges as a novel member in the additive manufacturing family, harnessing the inherent advantages of cold spray technology. Distinct from extensively explored fusion-based additive manufacturing methods like laser beam melting (LBM), electron beam melting (EBM) and laser metal deposition (LMD), CSAM boasts unique attributes. Table 4.3 delineates a comparative analysis of CSAM and other prevalent additive manufacturing technologies, showcasing its distinctive merits and drawbacks. Notably, CSAM excels in shorter production cycles, accommodating unlimited product sizes, offering heightened flexibility and proving adept at repairing damaged components. Additionally, CSAM stands out as an optimal choice for working with high-reflectivity metals such as copper and aluminum, presenting a superior capability compared to laser-based additive manufacturing processes (Yin et al., 2018).

Table 4.3 Comparison of advantages and disadvantages between CSAM and other fusion-based additive manufacturing (Yin et al., 2018).

Parameter	**CSAM**	**SLM**	**EBM**	**LMD**
Powder feed mode	Direct deposition	Powder bed	Powder bed	Direct deposition
Feedstock limitations	Difficulty processing high hardness and strength metals	Difficulty processing high reflectivity and poor flowability metals	Unsuitable for non-conductive and low melting-temperature metals	Difficulty with high reflectivity metals
Powder melting	No	Yes	Yes	Yes
Product size	Large	Limited	Limited	Large
Dimensional accuracy	Low	High	High	Medium

Table 4.3 continues

Mechanical properties	Low	High	High	High
Mechanical properties	High	High	High	High
Production time	Short	Long	Long	Long
Equipment flexibility	High	Low	Low	Low
Suitable for repair	Yes	No	No	Yes

4.2.4. Biological applications

4.2.4.1 Antimicrobial

The presence of bacterial contamination on surfaces that are frequently touched elevates the risk of infection. To address this concern, various antibacterial agents have been explored, including zinc oxide, calcium oxide, magnesium oxide, silver and chitosan-copper, with some of these agents being applied in conjunction with CGDS (Raoelison et al., 2017). Over the past decade, investigations have been undertaken to assess the antimicrobial efficacy of copper and its alloys against diverse microorganisms that pose public health risks in sectors such as food processing, healthcare and air conditioning applications. Despite these efforts, the optimal method for depositing copper onto surfaces and the resulting mass structure have not been conclusively determined (V. Champagne & Helfritch, 2016; Kumar et al., 2020).

V. K. Champagne & Helfritch, (2013) undertook a study to evaluate the disinfection efficacy of three copper surfaces, aiming to ascertain optimal deposition methods and deposit properties. The research investigated the antimicrobial effectiveness of various copper surfaces, with copper-based deposits generated through three distinct thermal spraying methods: plasma spraying, wire arc spraying and CGDS. The surfaces were subsequently inoculated with methicillin-resistant *Staphylococcus aureus* (MRSA) and after a 2-hour exposure to the bacteria, surviving MRSA samples were analyzed and the outcomes were compared. The findings revealed that CGDS technology exhibited superior effectiveness compared to other techniques, achieving microbial destruction exceeding 99.9% after a two-hour exposure. It was deduced that the deformation hardening induced by high-speed particle effects during the CGDS process contributes to increased ionic dissipation within the copper microstructure, thereby enhancing antimicrobial activity.

4.2.4.2 Antifouling

Biofouling is a problem affecting underwater surfaces. Marine biofouling has major economic impacts on shipping, offshore oil and gas platforms, energy and water treatment plants and aquaculture. Copper and copper-based coatings have been shown to have long-term antifouling effectiveness on marine surfaces (V. Champagne & Helfritch, 2016). Therefore, Vucko et al., (2012) developed a cold spray method to embed copper particles on the surface of polymer structures as an alternative to copper plates and copper-containing paints.

4.3. Cold Spray Applications in the Defense Industry

The cold spray process has evolved from being an emerging technology to becoming a practical alternative to thermal spray for specific applications (A. Papyrin et al., 2006). Extensive research and development investigations have substantiated that CGDS technology represents a cost-effective and environmentally friendly approach for surface protection and the restoration of dimensional tolerances in components made from magnesium, aluminum and titanium alloys within both helicopter and fixed-wing aircraft applications. A prevalent issue faced by both the DOD and the commercial aircraft industry pertains to the corrosion of magnesium helicopter gearboxes. It has been underscored that the application of cold spray coatings offers a viable means to mitigate corrosion damage in gearboxes, particularly when employed in conjunction with enhanced protective systems such as Tagnite coatings (V. K. Champagne, 2007).

The reparative attributes of the CGDS process contribute to enhanced performance, facilitating feature recovery and dimensional restoration. Notably, the infrequency of necessary alterations also results in reduced logistical costs. This manifests in a decreased demand for gearboxes both in the operational field and during transportation between warehouses and operating bases. The implementation of the CGDS process holds considerable potential for cost reduction through the mitigation of defects, thereby improving operational readiness and security. This underscores the economic

advantages associated with the CGDS process in bolstering efficiency and reliability within the relevant operational contexts (V. K. Champagne et al., 2017).

Research findings presented by Fernandes Barbosa et al., (2009) indicate that the cold spray method exhibits the capability to generate dense pure titanium coatings on aluminum 7075 substrates, achieving thicknesses exceeding 300 μm without inducing undesirable microstructural changes. The study concludes that the CGDS process can be refined for optimal performance, yielding coatings superior to those produced by conventional thermal spray techniques. Notably, this optimization is achieved with economic efficiency and a heightened deposition rate, rendering the CGDS method particularly well-suited for aviation applications. The implications for the aerospace industry are significant, as such coatings have the potential to extend material lifespan and concomitantly reduce maintenance and repair costs. The heightened corrosion resistance afforded by these coatings positions the CGDS method as an advantageous technological solution in enhancing the durability and cost-effectiveness of materials within the aerospace sector.

Stoltenhoff & Zimmermann, (n.d.) showcased the potential of cold spraying as a repair technology by employing three distinct precipitation-hardened aluminum alloys, namely AA2224, AA6061 and AA7075. These alloys were utilized for critical components such as CH-53 helicopter landing gear shock pylons and C-160 aircraft rotor blades. Concurrently, an enhancement in fatigue resistance was observed in select coated samples. This improvement is attributed to the mitigation of crack formation and propagation, attributable to the beneficial compressive residual stresses generated within the coating during the CGDS process. The study establishes the efficacy of the CGDS process as a viable technology for the repair of critical aviation components like helicopter landing gear and aircraft rotor blades. It has been substantiated that coatings obtained through CGDS contribute to the extension of material life by augmenting fatigue resistance, thereby enabling the safe utilization of components over an extended period. This outcome carries the potential to substantially diminish maintenance and repair costs while concurrently bolstering safety and operational continuity in the aviation industry.

Kumar & Chavan, (2011) have applied the CGDS process across various applications, particularly in the repair of gas turbine components where the imposition of high thermal processes, such as welding, is impractical. Notably, the repair of 6061 aluminum fan housings, susceptible to damage, has been successfully addressed using this method. Additionally, in the manufacturing of titanium compressor body isogrids, the implementation of titanium cold spraying has proven effective in minimizing starting stock material and reducing machining waste. This successful approach extends beyond titanium and encompasses materials such as copper, aluminum and zinc. Furthermore, diverse components, including diffusers, combustion chambers, turbines and exhaust nozzles, have been effectively repaired using the CGDS process. Dr. Kumar's reported successes also extend to the repair of aluminum and magnesium aviation components, exemplified by the repair of S-70 Seahawk and C-160 Transall propeller blades. These studies collectively demonstrate the effectiveness of CGDS technology in repairing gas turbines and aerospace components, particularly in situations where thermal processes are unsuitable or demand high precision.

4.3.1. Cold Spray Application Examples in the Defense Industry

4.3.1.1 Cast Magnesium Transmission and Gearbox Housings

Magnesium alloys have been developed, exhibiting favorable mechanical properties and low densities, enabling the casting of intricate shapes. These alloys, known for their good machining characteristics, find particular utility in weight-sensitive applications, such as in helicopters like the UH-60 helicopter (V. K. Champagne, 2008; V. K. Champagne et al., 2010). However, one drawback of magnesium alloys is their high anodic index, making them highly susceptible to galvanic corrosion when coupled with other metals. Notably, magnesium alloys utilized in transmission and gearbox housings display poor resistance in wet, salt-laden environments (V. K. Champagne & Barnett, 2012; Leyman & Champagne, 2008). Detailed insights into the repair of magnesium gearbox housings for military helicopters, presented by V. K. Champagne, (2008), are noteworthy. The repair process involved the removal of corrosion damage from surfaces and meticulous surface preparation before coating application. Various aluminum alloy powders, including

commercially pure aluminum (CP-Al), high-purity aluminum, Al-6061, Al-4047 and Al-5056, are available for repairs. For this specific repair, CP-Al was selected. A coating was applied to damaged areas and machined to original dimensions. Typically, the final coating thickness exceeds 0.4 mm to ensure a continuous environmental barrier. In cases requiring high hardness and adhesion strength, Al-6061 is employed, often applied with helium as the primary process gas (V. K. Champagne, 2008; DeForce et al., 2007; Rooy, 1990).

4.3.1.2 Fretting Damage on an A357 Transmission Housing.

A significant number of gearboxes and transmission housings utilized in aircraft are crafted from A356 or A357 aluminum-silicon alloys, originally developed as casting alloys (J. R. Davis, 1996b). Their unique combination of strength, hardness, density and the capability to be cast into intricate shapes make them particularly well-suited for aerospace applications. Despite their advantageous properties, these alloys can incur damage during operation, be it from wear, impact, or corrosion. For instance, in fighter jet aircraft, the mounting pad surface for a hydraulic pump on an externally mounted auxiliary transmission housing is prone to fretting-a phenomenon where two metal surfaces undergo repeated contact, leading to degradation through oxidation and mechanical wear (Bock & Whitley, 1999). Attempts to rectify the damage using conventional thermal spray processes proved unsuccessful, as the thermal spray coatings suffered damage during the final machining process intended to create a smooth surface.

Subsequently, a cold spray process was developed to address the fretting damage on the hydraulic pump pad. The repair necessitated excellent adhesion strength, hardness equal to or greater than A357, a similar coefficient of thermal expansion (CTE) and good machinability. Various commercially available alloys were considered and Al-4047 and Al-6061 emerged as the two alloys offering the best combination of properties. Al-6061 was chosen for its high hardness and adhesion strength (Eden et al., 2016).

4.3.1.3. B-1 Forward Equipment Bay Panel.

Wear caused by chafing around fastener holes in skin panels is a common issue on military aircraft, leading to skin panels exceeding fit tolerances at fastener locations. In the case of a B-1 bomber left upper aft forward equipment bay (FEB) panel, chafing damage to the fastener holes resulted in an out-of-tolerance fit. This panel is removed during aircraft maintenance and the repeated removal and installation of fasteners contribute to wear and elongation of the panel holes. As wear progresses, fasteners sit increasingly below the panel surface, leading to turbulent flow, panel vibration and eventually pull-through with the potential loss of fasteners during flight (Eden et al., 2016).

The FEB panel is an internally stiffened, bonded composite-metal hybrid structure with Al-2024-T6 skin. To avoid damage to the hybrid composite structure, the panel's temperature must not exceed 100 °C during repair. Before the introduction of cold spray, there was no approved method for repairing damage to the Al-2024-T6 skin. Due to its low-temperature input, cold spray was chosen as a potential repair process (C. Widener et al., 2013).

4.3.1.4. TD-63 Hydraulic Actuator Body. (Navy Valve Actuator Repair)

The internal bore of an Al-6061-T6 hydraulic actuator body experienced exfoliation and pitting corrosion damage due to exposure to seawater. Traditional repair options such as tungsten inert gas welding, metal inert gas welding and laser cladding were considered, all of which could generate strengths and porosities meeting or surpassing the repair requirements for aluminum actuator coupon test samples (C. A. Widener et al., 2015). Porosity, adhesion and tensile testing results demonstrated that the cold spray process could yield deposits meeting the required performance parameters. The maximum allowable porosity in the deposited material was set at 5%. The porosity in the initial mockup's deposited material exceeded the acceptable limit, while the cold-spray-deposited material exhibited an average of 3% porosity based on 14 measurements (Eden et al., 2016).

4.3.1.5. 2024AA and 7075AA Aircraft Components

Due to their high strength-to-weight ratios, 2024AA and 7075AA find widespread use in aerospace applications (Rooy, 1990). These alloys are typically subjected to heat treatment to achieve the desired combination of strength, ductility and corrosion resistance. Conventional repair processes like welding or cladding, involving exposure to high temperatures, can alter the temper of these alloys, leading to diminished mechanical properties. Extensive repair may necessitate reheat treatment, introducing additional challenges. The low heat input associated with the cold spray process offers a solution by enabling the repair of tempered aluminum alloys without adversely affecting their properties (Eden et al., 2016).

4.3.1.6. B-1 Nose Landing Gear False Axle

The nose landing gear false axle is responsible for attaching complete wheel assemblies to the main landing gear axle, essentially creating a quick-change tire system. This component features two locations where bearings ride. Over extended service periods, the bearings gradually wear down the false axle, reaching a point where replacement becomes necessary. The axle itself is constructed from Al-2024. In an effort to enhance the wear performance of the component, nickel-blended powders were chosen as the candidate materials for deposition. Pure nickel powder was specifically selected due to its excellent deposition characteristics, particularly the work hardening that occurs during deposition and its favorable machinability. Studies have demonstrated that the hardness of nickel deposited through the cold spray process can be up to 60% higher than conventionally cold-worked nickel (Kaur et al., 2015; Kim et al., 2005b).

4.3.1.7. LAU-128 Missile Rail

The LAU-128, a guided missile launcher commonly employed on fighter aircraft, is mounted to a standard rail launcher. These launchers are affixed to each of the aircraft's underwing pylons, carrying one payload per rail. Throughout takeoff and flight, the aircraft carries the missiles and during landing, it accommodates any

missiles that have not been utilized during the flight. The rail tracks, experiencing chafing and wear due to vibration and loading, particularly during takeoff and landing, are subjected to potential damage. To establish the process parameters and develop repair methods, a series of cold spray samples were created using 7075 AA powder (Eden et al., 2016).

4.3.1.8. Aging Aircraft Hinge Fitting

Hinge fittings utilized on the cargo bay door of a military transport aircraft are crafted from Al-7075-T6. Over the course of operating the bay door and during flight, these hinge fittings are susceptible to wear and corrosion damage. To address this issue without the need to remove the fittings from the aircraft, a cold spray process was developed for depositing Al-7075 powder to effect repairs on the damaged hinge fittings (Eden et al., 2016).

4.3.1.9. B-1B Chafing.

A primary focus within the DOD, Federal Aviation Administration (FAA) and National Aeronautics and Space Administration (NASA) is the extension of the operational life of currently deployed aircraft. In order to address maintenance challenges and repair damaged components, effective repair processes are essential. Hydraulic tubing chafing represents a persistent issue across a wide range of Air Force, Army and Navy aircraft, leading to significant costs in maintenance man-hours and a reduction in operational readiness rates. Notably, the B-1 aircraft grapples with one of the most significant and chronic maintenance problems related to the chafing of titanium hydraulic lines. To tackle this challenge, a cold spray repair method was developed. This approach not only addresses chafing damage on existing tubing but also applies an additional coating to mitigate chafing on new tubing (Eden et al., 2016).

CHAPTER FIVE
CORROSION AND TRIBOLOGICAL PROPERTIES OF ALUMINIUM ALLOYS

5.1 Corrosion of Aluminum and Its Alloys

Aluminum alloys (AAs) find extensive utilization across various industries, including aerospace, defense, automotive, shipbuilding and chemical sectors, owing to their commendable specific strength, thermal conductivity, corrosion resistance and favorable processing characteristics. Consequently, aluminum stands as the predominant non-ferrous metal material in industrial applications (Arrabal et al., 2013; Reboul & Baroux, 2011). From a thermodynamic perspective, aluminum exhibits pronounced reactivity, possessing a significant affinity for oxygen as indicated by its position in the electromotive force series. Despite this reactivity, aluminum demonstrates high resistance to a variety of atmospheres and chemicals, a quality attributed to the formation of an aluminum oxide film on the metal surface. Notably, this protective film swiftly re-establishes itself when compromised. Consequently, under typical environmental conditions, the corrosion rate of aluminum experiences a marked reduction over time (Birbilis & Hinton, 2010). Under natural conditions, aluminum alloys (AAs) have the capability to develop a passivation film predominantly composed of Al_2O_3, with a thickness ranging from approximately 10 to 100 nm. This film imparts a protective effect on the underlying base material, facilitating the stable existence of AAs in natural environments (Fan et al., 2021). The growth of oxide layers is subject to modification through impurities and alloying additions, while elevated temperature and humidity accelerate this process. The mitigation of corrosion is facilitated by the presence of a protective oxide film, which serves a dual role as a resistant barrier against dissolution and an effective insulator. This inhibitory mechanism restricts the involvement of electrons, generated during the oxidation of the metal, from participating in any concurrent cathodic reactions associated with the oxidation process (Birbilis & Hinton, 2010).Nevertheless, the passivation film, while present, is characterized by its thin, porous and discontinuous nature. When subjected to demanding environmental conditions, such as high temperatures, elevated salinity and increased humidity during service, the passivation

film becomes susceptible to breakage, leading to a compromise in its protective efficacy. The rupture of the oxide film exposes the matrix material to the atmosphere, consequently instigating corrosion damage (Fan et al., 2021). In a broader context, most AAs utilized in airframes are highly susceptible to severe corrosion when exposed to moderately strong acids. While alkalis generally exhibit lower corrosiveness compared to acids, aluminum is notably vulnerable to the corrosive impact of various alkaline solutions unless they incorporate a corrosion inhibitor (Staley, 2017).

The corrosion morphology observed in AAs predominantly manifests as localized corrosion, encompassing various common forms such as stress corrosion cracking (SCC), pit corrosion, crevice corrosion, galvanic corrosion and microbiologically influenced corrosion (MIC) (Fan et al., 2021). Noteworthy areas of corrosion research pertaining to AAs include investigations into the localized corrosion of magnesium-containing aluminum alloys, the phenomenon of SCC in alloys employed in aerospace applications, galvanic corrosion of aluminum in both atmospheric and automotive settings and the occurrence of filiform corrosion in aluminum sheets (Birbilis & Hinton, 2010). In addition, the susceptibility of aluminum materials to localized corrosion makes them particularly vulnerable to MIC. The MIC phenomenon involves the acceleration and/or alteration of corrosion processes caused by the presence and activity of microorganisms by forming a biofilm on the metal surface (Rajasekar & Ting, 2010). MIC is not a new type of corrosion, it is accompanied by degradation of the metal substrate, resulting in an increase in the kinetics of the corrosion process by the presence and metabolic activity of microorganisms. These effects can be critical, so it is important to consider the roles and conditions of microorganisms in corrosion (Beech et al., 2000). The consequences of MIC phenomenon are pitting corrosion, crevice corrosion and de-alloying corrosion and correspond to localized corrosion type (Nelson et al., 2017).

5.2 Types of Corrosion

5.2.1 General Corrosion

The corrosion of aluminum constitutes an electrochemical process wherein metal atoms undergo dissolution. This phenomenon exclusively occurs when the oxide film either dissolves or suffers damage. The oxide film of aluminum exhibits stability in neutral conditions; however, it becomes soluble in strongly acidic and strongly alkaline environments. The thermodynamic stability of aluminum oxide films is elucidated by the potential versus pH (Pourbaix) diagram provided in Figure 5.1 (Pourbaix, 1966). According to this diagram, under ideal conditions, aluminum: (1) undergoes corrosion, (2) achieves passivity owing to the formation of a hydrargillite film at approximately neutral pH values and (3) attains immunity to corrosion at negative potential values (Birbilis & Hinton, 2010).

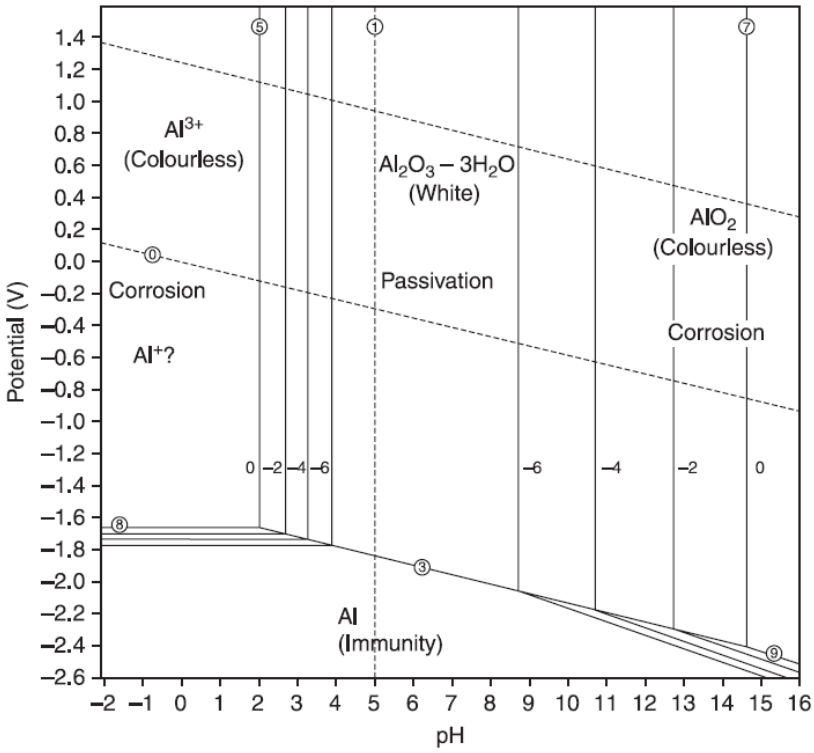


Figure 5.1 Pourbaix diagram for pure aluminum (Pourbaix, 1966).

Considering that corrosion is an electrochemical process, the corrosion potentials occurring on the surface of different aluminum alloys are of great importance. The

difference between the potential of AAs and the potential of other metals is as important as the relationship between the potential of the microstructural components of an alloy (Birbilis & Hinton, 2010).

5.2.2 Bimetallic or Galvanic Corrosion

Aluminum exhibits an anodic nature relative to numerous metals and when immersed in an electrolyte, the resultant potential difference induces a flow of current and leading to pronounced corrosion. In specific instances, the moisture film formed on surfaces due to aggressive atmospheres can instigate galvanic corrosion. Notably, in marine environments, copper, brass and bronze pose significant challenges in terms of galvanic corrosion. Table 5.1 provides a series of corrosion potentials for unheat-treated wrought, heat-treated wrought and cast aluminum alloys, alongside standard corrosion potentials for select metals based on ASTM G69-97 standard measurements. The bimetallic corrosion of aluminum stands as a prevalent cause of corrosion damage in service, as the majority of other engineering metals exhibit noble potentials markedly higher than those of aluminum (Birbilis & Hinton, 2010).

Table 5.1 Comparison of measured corrosion potentials in 1M NaCl containing H_2O_2 (Birbilis & Hinton, 2010).

Material	**Corrosion potential (V_{SCE})**
Al (99.999)	-0.75
Cu (99.999)	+0.00
Fe	-0.55
Mg	-1.64
Zn	-0.99
1100	-0.74
2014-T6	-0.69
2024-T3	-0.60
3003	-0.74
5052	-0.76
5154	-0.77
6061-T4	-0.71
6061-T6	-0.74
6063	-0.74
7039-T6	-0.84

Table 5.1 continues

7055-T77	-0.75
7075-T6	-0.74
7075-T7	-0.75
7079-T6	-0.78
8090-T7	-0.75

5.2.3 Crevice Corrosion

In the event that a crevice forms between two aluminum surfaces or between aluminum surfaces and a non-metallic material, such as a polymer, the presence of electrolyte can instigate localized corrosion within the crevice. Crevice corrosion arises due to a disparity in oxygen concentration between the mouth of the crevice and its interior, resulting in a localized cell effect. The higher oxygen concentration at the crevice mouth compared to the oxygen-depleted zone within the crevice establishes a difference in local corrosion potentials. Consequently, corrosion predominantly occurs in the less noble area, namely, the oxygen-depleted region within the crevice. Simultaneously, the oxygen-rich region at the crevice mouth serves as the cathode (Birbilis & Hinton, 2010).

Crevice corrosion poses significant challenges in engineering applications, as the locations susceptible to this form of corrosion are frequently challenging to circumvent in practical constructions. Such sites include welded lap joints, riveted areas, valve seats and deposits that may accumulate during service (Roberge, 1999). Notably, in the context of aluminum, the presence of narrower crevices tends to accelerate the initiation of corrosion attacks.

5.2.4 Pitting Corrosion

Pitting represents the predominant form of corrosion observed in aluminum alloys. In certain near-neutral aqueous solutions, the initiation of a pit triggers its ongoing propagation into the metal, a phenomenon driven by the acidification of the solution within the pit. Acidic conditions impose limitations on the formation of protective alumina films, which typically serve as a deterrent to pit development (Frankel, 1998).

Pitting corrosion arises when localized or aggressive environments compromise the integrity of the passive and corrosion-resistant film on a metal surface. Such environments typically harbor halide ions, with chlorides being particularly predominant. Solutions containing chloride ions pose significant threats, creating localized corrosion potential gradients between the metal surface and areas where chloride concentrates or accumulates. Pits may initiate at various sites such as scratches, mechanical defects, second phase particles or stochastic local discontinuities in the oxide film. The interaction between the matrix and second phase particles is the primary catalyst for pit initiation. Given the bulk instability of the oxide film under acidic or alkaline conditions, pitting occurs exclusively within the near-neutral pH range. Chlorides play a crucial role in undermining the film by forming $AlCl_3$, often present in solution alongside the pits. As aluminum ions disperse from the pits, aluminum hydroxide species precipitate as a membrane, perpetuating the isolation and concentration of local acidity, thereby sustaining continuous pitting. While the morphology of pits varies depending on the alloy type and environmental factors, the cavities typically assume a hemispherical shape. This characteristic distinguishes pits as localized corrosion initiation sites from other corrosion forms involving propagation modes like intergranular or exfoliation corrosion (Birbilis & Hinton, 2010).

5.2.5 Localized Corrosion: Intergranular and Exfoliation

Intergranular corrosion (IGC) represents a distinctive manifestation of microstructurally influenced corrosion, wherein the electrochemical characteristics of the grain boundary region in the alloy differ from those of the bulk or adjacent microstructure of the alloy (Hunter et al., 1963). Corrosion activity can emerge as a consequence of heterogeneities in the grain boundary structure. In aluminum-copper alloys, the precipitation of Al_2Cu particles at grain boundaries renders the neighboring solid solution anodic, heightening its susceptibility to corrosion. In the case of aluminum-magnesium alloys, a contrary scenario arises, given that the precipitated phase Mg_2Al_3 exhibits a lower nobility compared to the solid solution. Nevertheless, the occurrence of severe intergranular attack can be averted in these two alloys by adhering to proper manufacturing and heat treatment conditions. In the context of the

aluminum-magnesium system, nearly all commercially utilized alloys are in a supersaturated state, attributable to the fact that the solubility of magnesium at ambient temperatures is below 1 wt.%. This condition implies that alloys containing over 3 wt.% magnesium may experience grain boundary precipitation and the consequential sensitization of grain boundaries to susceptibility to intergranular corrosion when subjected to elevated service temperatures. The degree of sensitization can be estimated by examining the continuity of Mg_2Al_3 precipitation at the boundaries. Continuous boundaries are indicative of a heightened susceptibility to IGC (Birbilis & Hinton, 2010). In aluminum-zinc-copper alloys with a highly anodic precipitated phase, the initiation of IGC occurs with relative ease. Nevertheless, the susceptibility to IGC is intricately linked to the specific heat treatment conditions and their impact on grain boundary solute segregation, the morphology and composition of the grain boundary precipitate and the characteristics of the surrounding alloy matrix (Knight et al., 2003).

IGC manifests distinct characteristics from pitting corrosion. Although intergranular corrosion may originate from a pit, its progression along susceptible intergranular pathways outpaces the rate of propagation observed in pitting corrosion. Both phenomena exert detrimental influences on fatigue crack initiation and serve as pronounced stress concentrators, consequently diminishing the cyclic loading cycles to failure. Despite pitting corrosion having the capacity to commence in neutral bulk conditions, the localized environment at the corroding metal undergoes substantial differentiation from the bulk electrolytic environment once pitting stabilization occurs or when corrosion propagation ensues through mechanisms such as intergranular corrosion. Notably, electrolytes in pit bases or occluded regions can exhibit either acidic or alkaline attributes, thereby fostering heightened rates of localized attack (Birbilis & Hinton, 2010).

Aluminum alloy exfoliation corrosion, as documented by Zhao & Frankel, (2007), results from intergranular corrosion processes. This phenomenon typically manifests in areas where the alloy microstructure has undergone significant deformation, leading to the flattening and elongation of the grain structure along the working direction. Intergranular corrosion initiates from transverse edges and pits, progressing along

grain boundaries parallel to the alloy. Exfoliation is characterized by the elevation of layers of relatively uncorroded intragranular metal due to the expansion of corrosion products within intergranular corrosion layers. Notably, instances of exfoliation are observed in aircraft components surrounding rivet or bolt holes, where the end grain of the microstructure is exposed. (Birbilis & Hinton, 2010).

5.2.6 Environmentally Assisted Cracking

In a broader context, the term Environmentally Assisted Cracking (EAC) encompasses various mechanisms including SCC, corrosion fatigue (CF) and hydrogen embrittlement (HE) (Birbilis & Hinton, 2010).

5.2.6.1 Stress Corrosion Cracking

SCC represents a time-dependent intergranular fracture mode necessitating the simultaneous presence of continuous tensile stress and a corrosive environment in aluminum alloys. Such stresses can manifest due to various factors, including (1) the operation of components, (2) residual stresses stemming from the heat treatment process and cold working or (3) the application of stresses during the assembly process (Birbilis & Hinton, 2010).

The minimum tensile stress required to induce SCC in susceptible alloys is typically significantly lower than the macroscopic yield stress, as indicated by studies by Scamans et al., (1987); Scamans & Holroyd, (1986). The susceptibility to SCC has imposed constraints on the application of aluminum alloys, particularly those in the 7xxx series, limiting their use in certain contexts. Various theories have been proposed to elucidate the mechanism of SCC, with two primary contenders. The first posits that corrosion plays a dominant role, wherein cracking results from preferential corrosion with anodic dissolution, akin to IGC along grain boundaries. The second theory suggests that hydrogen is the primary driver, with cracking along grain boundaries being intensified by absorbed atomic hydrogen. This hydrogen is sourced from the IGC process itself, generated by corrosion within acidified cracks. The presence of absorbed hydrogen is believed to weaken grain boundaries. Moreover, the corroded

metal is exposed to a microenvironment that is aggressive and distinct from the unique and bulk electrolytic environment, rendering SCC a particularly insidious form of damage (Birbilis & Hinton, 2010). Aluminum alloys characterized by low strength and high purity exhibit a diminished susceptibility to SCC. Conversely, alloys with heightened susceptibility to SCC include those within the 7XXX, 2XXX and higher strength 5XXX series, distinguished by grain boundaries laden with precipitates. The SCC phenomenon in 7XXX alloys manifests in both water and water vapor, along with chloride-containing electrolytes. In contrast, the majority of other vulnerable alloys succumb to SCC when exposed solely to environments containing chloride ions (Birbilis & Hinton, 2010). Table 5.2 provides a comparative assessment of the relative resistance of various AAs against SCC.

Table 5.2 Qualitative SCC resistance of aluminum alloys (J. R. (Joseph R. . Davis, 1999).

Alloy and temper	**SCC resistance**
2014-T3	Poor
2024-T3, T4	Poor
2024-T8	Good
2124-T851	Good
2219-T6, T8	Excellent
6061-T6	Excellent
7049-T73	Good
7 × 75-T6	Poor
7 × 75-T73	Excellent
7 × 75-T76	Intermediate
7079-T6	Poor

5.2.6.2 Corrosion Fatigue

CF denotes the interaction involving irreversible cyclic plastic deformation and localized corrosion activity. In structures subjected to fatigue loading, corrosion pits have consistently been observed to initiate crack growth (Van Der Walde et al., 2005). An aerospace alloy, 7075-T6, investigated in a fatigue study, disclosed that all samples experienced fracture stemming from cracks associated with pitting (Jones & Hoeppner, 2005). Numerous studies, underscore the pivotal and detrimental impact of the pitting phenomenon on fatigue life (J. R. (Joseph R. . Davis, 1999). CF events

manifest in diverse forms, contingent upon the specific environment and application. However, the variables influencing the progression of CF crack growth encompass stress intensity, loading frequency, stress ratio, alloy composition, microstructure (electrochemical potential) and environmental composition (temperature) (Birbilis & Hinton, 2010).

5.2.6.3 Hydrogen Embrittlement

Hydrogen exhibits a pronounced propensity to dissolve readily in both aluminum and its alloys, a phenomenon observed in both the molten state and at elevated temperatures proximate to the alloy's melting point, particularly in environments containing water vapor or abundant hydrocarbons. While the presence of hydrogen in molten aluminum gives rise to porosity in cast products, it does not exert any discernible influence on the corrosion performance or subsequent susceptibility to HE (Birbilis & Hinton, 2010). However, recent investigations have presented experimental evidence indicating that hydrogen generated during corrosion has the capability to permeate grain boundaries, thereby inducing embrittlement (Osaki et al., 2006; Thakur et al., 2007).

5.2.7 Microbiologically influenced corrosion

Aluminum alloys 7075 and 2024 find extensive application in both the structural components and brittle parts of aircraft. The inclusion of alloying elements in these metals renders them prone to localized corrosion, concurrently heightening their susceptibility to bacterial adhesion. Multiple documented instances of aircraft degradation are attributed to microbial proliferation arising from contamination within fuel storage tanks and aircraft wing tanks, constituting the phenomenon known as MIC (Nelson et al., 2017). The phenomenon that induces corrosion in materials through the metabolic activities of various microorganisms is termed MIC (Emde et al., 1992; Lv & Du, 2018). Research indicates that approximately 20% of global corrosion losses are attributed to MIC, underscoring its significance as a substantial contributor to corrosion damage in structural materials (Castaneda & Benetton, 2008; Dursun &

Soutis, 2014). MIC operates as a mechanism linked to the corrosion of metal surfaces influenced by the physiological processes of microorganisms (Vaughn-Thomas, 2011). Additionally recognized as bio-corrosion, MIC, as outlined by Shi et al., (2011), can induce corrosion in a spectrum of materials, including stainless steel, carbon steel, aluminum, zinc and copper alloys. Importantly, MIC has the capacity to expedite various forms of corrosion, encompassing uniform corrosion, pitting corrosion, crevice corrosion, galvanic corrosion, IGC, dealloying and SCC (Rawat et al., 2016). In the contemporary aviation landscape, aluminum alloys remain the predominant choice for manufacturing fuel tanks in civil aircraft, constituting approximately 80% of the materials used in civil aviation aircraft (Dursun & Soutis, 2014). Microorganisms gain entry into fuel tanks through airborne contaminants and water ingress (R. N. Smith, 1991). The presence of water inside fuel tanks serves as a catalyst for microbial growth, potentially leading to MIC in the tank structures (Nelson et al., 2017). Notably, historical incidents underscore the severity of MIC in aviation. In 1958, microbial contamination resulted in the blockage of a bomber plane's fuel system, leading to a crash in the United States. In 1996, numerous aircraft fuel tanks in China experienced corrosion, marking one of the most significant MIC incidents in Chinese history (Fan et al., 2021). Consequently, MIC has evolved into a critical form of corrosion that is increasingly acknowledged, particularly within the aviation industry.

Specifically, within the aviation industry, the microbial contamination of jet fuel systems has been identified as a persistent issue for over four decades. This contamination encompasses diverse groups of microorganisms, including anaerobic sulfuric-reducing bacteria, iron-oxidizing bacteria, manganese-oxidizing bacteria and acid-producing bacteria (Dexter, 2003; Muthukumar et al., 2003). Hagenauer et al., (1994), conducted a comprehensive investigation into the impact of microorganisms on aircraft corrosion damage in collaboration with various aircraft manufacturers. The study revealed that a total of 208 microorganisms, comprising 158 bacteria, 36 yeasts and 14 fungi, were isolated from corroded areas on seven distinct aircraft. The findings indicated that microorganisms isolated from the *genera Micrococcus, Enterococcus*, *Staphylococcus*, *Aerococcus*, *Bacillus*, *Aspergillus* and *Penicillium* exhibited pronounced corrosive effects, particularly against 7075 aluminum alloy.

In the aerospace industry, main body structures such as fuselage skins, stringers, frames, as well as wing and empennage skins, spars and ribs, mechanical systems including landing gear legs, cylinders, forks and struts and fluid systems encompassing fuel tanks, pressure vessels and connectors extensively utilize high-strength aluminum alloys from the 2XXX and 7XXX series. The susceptibility of these materials to corrosion is of paramount importance for ensuring the structural integrity of aircraft (Staley, 2017). Specifically, 7075 aluminum alloy holds significant prominence as a specialized material, particularly in aircraft manufacturing, often employed for critical components such as actuators (Matuszak et al., 2019; Yang et al., 2022). 7075 AA is extensively employed in the aviation sector due to its notable advantages, including high strength, good toughness and favorable formability, aligning with the imperative of achieving lightweight structures in the defense industry (Lourenço et al., 2015; Lukiyanchuk et al., 2004). However, the aerospace industry's requisites for aluminum alloys extend beyond mechanical properties, encompassing critical considerations for surface properties, particularly corrosion resistance (Cao & Song, 2018; Sun et al., 2010). The application of 7075 aluminum alloy is significantly constrained by its susceptibility to corrosion, wherein the protective oxide film on the alloy is prone to damage (X. Li et al., 2022). This concern is particularly exacerbated in prolonged humid environments, such as cloudy and rainy conditions, amplifying the corrosion damage to aviation aluminum alloys (Xuewu et al., 2022). Consequently, this corrosion susceptibility poses risks to the safe operation of aircraft, thereby negatively impacting human life and property safety. Addressing this challenge and effectively enhancing the corrosion resistance of Actuator AAs constitutes a crucial scientific problem within the realm of aerospace research (T. Shi et al., 2022).

5.3 Corrosion Protection in Aluminum Alloys

The natural passive oxide on AAs is insufficient to provide adequate protection against corrosion during service. Consequently, various technologies and multi-layered protection schemes are employed to mitigate the degradation of these components in demanding operational environments. An effective approach for components made of sheet metal involves the use of a coating known as Alclad. The

coating thickness typically ranges between two percent and ten percent of the sheet thickness. The clad alloy used in 2XXX series alloys is typically around 99.5% Al, while for 7XXX series alloys, it is 99% Al with 1% Zn. The clad alloy, lacking microstructural phases such as intermetallic particles present in the core alloy, exhibits superior corrosion resistance. Alclad sheets find widespread use in the aircraft industry for exterior surfaces like fuselage skins (Birbilis & Hinton, 2010). Alclad was innovated by Edgar Dix of Alcoa Laboratories in 1927 to address corrosion issues in 2XXX alloy aircraft plates. Even today, Alclad continues to be extensively employed in the aircraft industry. The inclusion of pure aluminum as a sacrificial cladding to these 2XXX alloys enhances their resistance to corrosion (Staley, 2017).

In aircraft, the prevailing protection scheme typically incorporates a primer and a topcoat, with an inorganic coating primarily serving as a pre-treatment or surface preparation step. The primary objective of pre-treatment is to impart corrosion protection capabilities and enhance adhesion for subsequent paint coatings. Within the aircraft industry, two prevalent pre-treatment processes are conversion coatings and anodizing (Birbilis & Hinton, 2010).

Chromate conversion coatings have been extensively employed in the aircraft industry for more than 80 years. These coatings are generated through immersion, spraying, or swabbing in an acid solution containing hexavalent chromate salts. The process yields a film primarily composed of hydrated chromium oxide (Hughes et al., 1997). This film also retains some soluble hexavalent chromate ions, known for their potent corrosion inhibition capabilities. For AAs, these ions can effectively inhibit both the cathodic and anodic reactions (Frankel & McCreery, 2001). However, due to their intrinsic toxicity, carcinogenicity and associated environmental, health and safety concerns, regulations restrict and discourage the use of chromates. Numerous alternatives to chromate conversion coatings have been explored, but many have proven ineffective on corrosion-prone alloys, particularly those in the 2xxx and 7xxx series, especially under conditions like Neutral Salt Spray testing. Apprehensions about chromates spurred the development of boric-sulfuric acid anodizing as a substitute for chromic acid anodizing and this process is now employed for certain aircraft components (Hinton, 1991).

Anodized coatings are created through electrochemical polarization in an electrolyte containing chromic acid, phosphoric acid, or sulfuric acid. The anodizing process yields an oxide film, with thicknesses reaching up to 10 μm, contingent on the specific acid anodizing bath used (Biestek & Weber, 1976). In contrast, native oxide films on aluminum typically range down to 0.05 nm. While anodized films offer superior corrosion protection compared to chromate conversion coatings, they may be more susceptible to fragility. Consequently, the choice between conversion coatings and anodized coatings for different sections of an aircraft structure depends on structural and loading considerations (Birbilis & Hinton, 2010).

Primer paint coatings designed for aluminum alloys serve the dual purpose of enhancing the adhesion of subsequent topcoats and acting as a barrier against moisture infiltration. Additionally, they incorporate a substantial amount of corrosion-inhibiting pigments, making the primer the primary source of corrosion protection in the overall protective scheme. The prevalent primer utilized in aircraft construction is a two-component epoxy polyamide, comprising an epoxy resin binder and a polyamide resin hardener. Titanium dioxide is incorporated for durability and opacity, while extenders like silica are added to fill the coating. The corrosion inhibition additive employed is strontium chromate, known for providing robust hexavalent chromate inhibitor ions. These ions have the capacity to permeate through the coating, offering protection, particularly at locations where the coating is compromised or exhibits damage such as cracks (Birbilis & Hinton, 2010).

On external aerodynamic surfaces such as fuselages, tails, wings and in landing wheel bays, a polyurethane topcoat is applied over the primer. This topcoat constitutes a two-part system comprising an isocyanate resin and a hydrolated polyester hardener. The primary functions of the topcoat are to shield against ultraviolet radiation, provide chemical resistance and exhibit durability and flexibility. Over time, exposure to weather, temperature fluctuations from high-altitude flight, soil accumulation and mechanical stress can lead to the deterioration of topcoats. This deterioration manifests as discoloration, chalking and cracking, particularly in structural areas prone to stretching (Birbilis & Hinton, 2010).

A crucial aspect of the aircraft component protection strategy involves the utilization of sealants. Over time, all paint coatings eventually harden and develop cracks, which permit moisture to infiltrate the alloy substrate. Protective sealants serve as an additional layer of defense, particularly in critical areas such as joints and fastener holes. These sealants are formulated from organic compounds like polysulphides and polythioesters, possessing attributes such as excellent adhesion and high elasticity at low temperatures. Capitalizing on these properties and the ability to be applied at thicknesses of approximately 200 μm, sealants serve as an effective supplementary barrier against moisture ingress at joints and holes. They also play a vital role in corrosion prevention and mitigating galvanic corrosion by isolating dissimilar metals. Sealants are applied to mating surfaces of joints and fastener holes during assembly while the sealant is still in the curing process. This approach facilitates the compression of excess sealant into the joints, creating a barrier against moisture infiltration. This construction method, known as wet assembly, is employed for corrosion protection. Flexible sealants are typically employed in both interior and exterior locations within an aircraft structure to safeguard against moisture accumulation, complementing the protective role of paint coatings (Birbilis & Hinton, 2010).

Conventional surface treatment methods of aluminum and its alloys include electrodepositing (Abdel-Gawad et al., 2019; da Silva Savonov et al., 2019), electroplating (Xu et al., 2019), anodizing (Ding, 2019; Kikuchi et al., 2015) and PVD/CVD (Bashir et al., 2017). Various methods have been proposed to prevent aluminum corrosion, such as electrodeposition of cerium or silane films, cathodic protection using a Mg-rich coating, organic coating, conversion coating and polymer coating (Diggle et al., 1969; L. K. Wu et al., 2010). Anodizing is considered one of the most practical methods for corrosion protection. Anodizing creates a nano porous oxide layer on top of the aluminum surface (Hwang et al., 2002; Masuda & Fukuda, 1995). The mentioned methods are gradually disappearing from use due to the unfriendly environment or the disadvantages of high equipment requirements. The rise of ceramic materials offers important ideas for material protection, such as thermal spraying (Naimi et al., 2012) and laser cladding (Y. X. Li et al., 2018). This type of technology is limited only to cases where film substrate adhesion and uniformity of film thickness are not particularly strict. However, there is a risk of changing the

microstructure of the substrate material due to thermal effects caused by thermal and laser processes (Birbilis & Hinton, 2010).

5.4 Sliding Wear of Aluminum and Its Alloys

Given the extensive utilization of aluminum and its alloys in structural applications within the aerospace, defense and automotive industries, there is a heightened importance in investigating the tribological properties of these alloys (Rooy, 1990).

The predominant tribological applications associated with AAs are primarily centered around sliding wear or metal-to-metal contact. Sliding wear is evident when one solid surface undergoes frictional contact with another solid, commonly referred to as adhesive wear. The term "adhesive" implies surface adhesion, albeit oversimplifying the complex array of potential mechanisms at play. Rigney, (1988) has proposed substituting the term "adhesive wear" with "sliding wear" to better encapsulate the nuanced nature of this phenomenon. This form of wear is alternatively characterized as metal-on-metal wear, particularly prevalent when sliding occurs between two metallic surfaces. The sliding interface may exhibit variations in lubrication, ranging from an unlubricated (dry) state to partial or full lubrication, contingent upon the specific application context. The sliding wear characteristics of aluminum alloys are subject to the influence of several factors, encompassing material considerations such as chemical composition, microstructural attributes and hardness, as well as system-related variables like the nature of the counterface and prevailing temperature conditions (Subramanian, 2010).

5.4.1 Chemical composition

AAs employed in wear-related applications incorporate alloying elements such as silicon, copper, magnesium, zinc and nickel. Additionally, these alloys may include other elements like modifiers, grain refiners and impurities (Subramanian, 2010).

Al and Si undergo eutectic formation at approximately 12.5 wt.%. In wear-centric applications, AAs predominantly feature silicon as the principal alloying element. Cu, possessing a maximum solubility threshold of 5.7 wt.%, holds significance as an

alloying element. The inaugural manifestation of age hardening was noted in an Al-Cu alloy characterized by exceptionally fine $CuAl_2$ precipitates. Concurrently, as the hardness of AAs elevates through precipitation, their wear resistance attains a zenith at the peak hardness point (Subramanian, 1992). It has been reported that the inclusion of copper, up to 4 wt.%, in Al–Si alloys has demonstrably enhanced their wear resistance (Beesley & Eyre, 1976). The Mg content in Al-Si alloys typically hover around 1 wt.% due to compromised mechanical properties observed at higher concentrations, attributable to the emergence of brittle, acicular-shaped intermetallic compounds. The enhancement in the wear characteristics of Al-Si alloys, incorporating Mg, is achieved through solid solution hardening. A systematic investigation into the incorporation of Zn in AAs has revealed that elevated Zn concentrations adversely impact the wear characteristics of aluminum alloys, primarily attributable to compromised mechanical properties at elevated temperatures. Ni undergoes a reaction with Al, resulting in the formation of Ni_3Al precipitates, which contribute to heightened hardness and elevated temperature resistance. The inclusion of Ni in Al-Si alloys, ranging from 1 to 3 wt.%, is associated with a concurrent enhancement in wear resistance (Beesley & Eyre, 1976).

5.4.2 Microstructure

Si, along with other secondary phases embedded in the Al matrix, governs the mechanical properties, including the wear behavior, of Al-Si alloys. For instance, Vandelli, (1968) observed that an AA with 17 wt.% Si exhibited enhanced wear resistance compared to alloys containing either 14.5 or 25 wt.% Si. It is noteworthy, however, that the levels of other alloying elements, including Cu and Ni, were not kept constant. The alloy demonstrating superior wear resistance also manifested higher hardness, likely attributed to solid solution strengthening facilitated by the presence of copper. Observations have been made regarding the impact of microstructural refinements on the wear performance of AAs. Reports indicate that the alteration of the eutectic Al-Si alloy results in an augmentation of wear resistance in both the alloy and its composites (Subramanian et al., 1986).

5.4.3 Hardness

If there exists a singular mechanical property that governs wear, it is hardness. As posited by Archard, (1953), the wear rate of a material exhibits an increase with applied load and conversely decreases with hardness. The hardness of aluminum alloys can undergo augmentation through various methods. Nevertheless, it is crucial to consider that the approach employed for increasing hardness holds significance. For instance, while work hardening enhances material hardness, it does not necessarily result in a proportional increase in wear resistance. Among this category of alloys, it has been demonstrated that those in the peak-aged condition present the most favorable wear resistance (Subramanian, 1992). The durability of the secondary phase may play a crucial role in regulating the wear characteristics of AAs.

5.4.4 Counterface

The counterface materials exhibit distinct interactions with the Al pin, encompassing variations in asperity size, adhesion of asperities within the wearing surfaces and the dynamics of heat generation and dissipation at the wearing interface. In essence, the impact of the counterface on the wear of AAs is mediated by its characteristics such as hardness, solid solubility and thermal conductivity (Subramanian, 2010).

5.4.5 Temperature

The ambient temperature exerts an influence on the wear characteristics of AAs and their composites. With an elevation in test temperature, there is a decrease in the material's hardness, leading to an expansion of the true contact area. At elevated temperatures, the resistance to crack propagation diminishes, consequently accelerating the formation of debris. Abrasive wear holds industrial significance; however, the inherently low hardness values of AAs render them unsuitable for such applications. Nevertheless, the incorporation of rigid abrasive particles, achieved through liquid metallurgy or powder metallurgy methods, enhances their hardness sufficiently to impart suitable resistance to abrasion for specific purposes. Viable options encompass matrix hardening, the nature and loading of hard particles and

interface engineering. Additionally, the application of MMC overlay coatings presents an alternative strategy (Subramanian, 2010).

5.5 Corrosion and Wear Behavior of Cold Gas Dynamic Sprayed Coatings

Numerous surface treatments and multi-layer protection strategies are employed to safeguard aluminum and its alloys against corrosion. However, these methods carry drawbacks such as environmental and health concerns, potential alterations to the microstructure due to thermal effects, the necessity for periodic maintenance, the requirement for sophisticated equipment and the need for additional protective layers. Despite these challenges, the CGDS process emerges as a promising technique in various industrial applications by minimizing or eliminating adverse effects associated with conventional thermal spraying processes. The CGDS technique and the resultant coatings offer advantages, including high deposition efficiency, elevated deposition rates, minimal thermal energy input to the substrate, non-melting of powder material, high coating density, low porosity, robust adhesion strength, compressive residual stresses, capacity for producing substantial coating thicknesses, absence of phase transformation, no oxidation, prevention of grain coarsening, high conductivity, superior corrosion resistance, and elevated strength and hardness. This section includes studies on the corrosion and wear behavior of coatings produced using CGDS technology.

da Silva et al., (2018) conducted a comprehensive investigation on the morphological, mechanical and corrosion resistance characteristics of WC-12Co and WC-25Co coatings applied to 7075 AA-T6 using the CGDS process. The high-pressure CGDS procedures for applying WC-Co coatings were executed at a maximum working pressure of 40 bar, at a temperature of 800 °C and utilizing nitrogen as a carrier gas. Cross-sectional analysis of the coatings revealed dense structures with low porosity. The determined coating thicknesses were 65 μm for WC-12Co and 118 μm for WC-25Co. XRD analysis indicated the absence of brittle phases in the coatings. SEM images and electrochemical test results following a 700-hour exposure to a NaCl solution demonstrated superior corrosion resistance for WC-25Co. Both WC-12Co and WC-25Co coatings exhibited resilience during salt spray testing, withstanding

1000 and 3000 hours, respectively. Extended immersion times, however, resulted in the dissolution of the cobalt phase and the loss of WC particles, permitting electrolyte access and substrate corrosion, ultimately leading to interconnected pore formation. The study concluded that the inferior performance of the WC-12Co coating could be attributed to its lower thickness, higher porosity and consequently, a greater number of defects.

da Silva et al., (2020) employed CGDS to deposit aluminum coatings on 7075 AA-T6, exploring the impact of the porous outer layer on various coating properties, including corrosion resistance. The coatings were meticulously prepared in five layers through high-pressure CGDS, utilizing 25 bars of pressure and a gas temperature of 350°C. Microstructural, morphological, mechanical, wear and corrosion properties of the coating were evaluated using both as-prepared and polished samples. Cross-sectional analysis revealed a dense structure with low porosity (0.8%) and a thickness of up to 300 μm for the coating. In sliding wear tests, a volume loss of 3.2×10^{-4} mm^3/Nm was observed, predominantly influenced by the adhesive wear mechanism. In the abrasive wear test, the wear rate was determined as 1.1×10^{-4} mm^3/Nm for the as-prepared coating and 0.8×10^{-4} mm^3/Nm for the polished coating. The polished coating exhibited a reduced wear rate attributed to fewer pores, interparticle spaces and a higher hardness value. Electrochemical test results and SEM images, acquired after immersing the as-prepared and polished coatings in a 3.5% NaCl solution, revealed electrolyte penetration to the coating/substrate interface after 900 hours. The porous nature of the top layer in the as-prepared coating did not enhance corrosion resistance, leading to initial accelerated corrosion through pores. This process increased chemical attack, enlarged small defects and allowed significant attack at the coating/substrate interface.

Chen et al., (2020) conducted an investigation into the microstructure, mechanical properties and tribological behavior of tin bronze-alumina coatings generated through LPCS within an artificial seawater environment. CuSn5–Al_2O_3 composite coatings were deposited onto a 7075 AA-T651 substrate. The study utilized commercial CuSn5 (5.0 wt.% Sn) and angular Al_2O_3 powders as feedstock. CuSn5–Al_2O_3 composite coatings were produced using the DYMET 423 LPCS equipment in four layers at 8

bar pressure and approximately 500°C gas preheating temperature. As the Al_2O_3 content in the feedstock increased from 0 to 30 wt%, the work-hardening effect of Al_2O_3 particles amplified the plastic deformation of CuSn5 particles, concurrently reducing the coating porosity from 0.95% to 0.41%. However, this led to a decrease in the deposition efficiency of the coatings from 22.3% to 18.6%. The hardness of CuSn5–Al_2O_3 composite coatings exhibited an increase from 154.7 to 194.2 HBW with the rising Al_2O_3 content. Furthermore, the bonding strength of the coatings saw an elevation from 11.2 MPa to 32.5 MPa. The findings indicated that the work hardening of Al_2O_3 particles positively influenced the density, hardness and bonding strength of the coatings. In a simulated seawater environment, coatings with diverse Al_2O_3 contents, in conjunction with their Al_2O_3 counterparts, manifest lower friction coefficients within the range of 0.24 to 0.33, as compared to those interacting with the 316L steel ball, where friction coefficients range from 0.57 to 0.81. Furthermore, as the Al_2O_3 content increases, the wear rate of the coatings decreases when in contact with the two counterparts. Coating the substrates results in a substantial reduction in the wear rate, on the order of approximately four magnitudes. The wear mechanisms observed predominantly involve abrasive and corrosive wear.

Chen et al., (2019) applied a copper-graphite solid lubricating coating onto 7075 AA-T651 using LPCS. The coating was prepared using electrolytic copper powder and Cu-coated graphite powder containing 50 wt.% graphite. The DYMET 423 LPCS equipment facilitated the production of copper-graphite coatings under 8 bar pressure and a gas preheating temperature of approximately 500°C. The study focused on the microstructure, deposition efficiency, mechanical properties and dry sliding wear behaviors of the copper-graphite coatings. The results indicated that the incorporation of Cu-coated graphite particles mitigated the plastic deformation of adjacent copper particles in the coatings. As the Cu-coated graphite content in the feedstock increased from 0 wt.% to 20 wt.%, the deposition efficiency, hardness and bonding strength of the copper-graphite coatings decreased by 49%, 21% and 70%, respectively. Notably, the copper-graphite coating with 20 wt.% Cu-coated graphite content exhibited the lowest friction coefficient (0.15) and wear rate (6.00×10^{-5} mm^3/Nm). Compared to 7075 AA-T651, this coating demonstrated a 57% reduction in the friction coefficient and a 78% reduction in the wear rate.

Miroslaw et al., (2020) investigated the deposition of cold-sprayed Al/Al_2O_3 and Cu/Al_2O_3 coatings on various substrates, including stainless steel (AISI 304), aluminum alloy (AlCu4Mg1), copper (Cu110) and brass (CuZn40Pb2), aiming to enhance resistance against cavitation erosion (CE) and sliding wear (SW). The study conducted a comparative analysis of these coatings. The LPCS process was employed to deposit coatings using Al (40 wt.%) and Cu (50 wt.%) blended with Al_2O_3 feedstocks at 60 wt.% and 50 wt.%, respectively. The raw material powder morphologies were examined, revealing spherical aluminum, dendritic copper and crushed alumina. Dymet 413 LPCS equipment was utilized to produce Al/Al_2O_3 and Cu/Al_2O_3 composite coatings under 9 bar pressure, with preheating temperatures of 200°C (Al/Al_2O_3) and 600°C (Cu/Al_2O_3). Results showed that the Cu/Al_2O_3 coating exhibited a denser structure than Al/Al_2O_3 but had lower adhesion and microhardness. While the cavitation resistance of both Al/Al_2O_3 and Cu/Al_2O_3 was found to be lower than bulk alloys, these coatings demonstrated higher sliding wear resistance compared to AlCu4Mg1, CuZn40Pb2 and AISI 304. The addition of Al_2O_3 effectively reduced material loss in LPCS composite coatings but led to an increase in the friction coefficient. The wear mechanism of the coatings exhibited an adhesive-abrasive mode. In both cavitation erosion and sliding wear environments, Cu/Al_2O_3 demonstrated more promising behavior than Al/Al_2O_3. Cavitation erosion resistance (CER) was observed in the order $Al/Al_2O_3 < Cu/Al_2O_3 <$ Cu110 < AlCu4 < CuZn40Pb2 < SS 304, with bulk alloys showing higher CER values than LPCS coatings. The addition of alumina reinforcing particles increased sliding wear resistance by reducing material loss and wear factor (K) in the composites.

H. Chen et al., (2022) conducted a study investigating the corrosion behavior and microstructure of Cu-based composite coatings produced by cold spraying. The findings revealed that all coatings exhibited a dense microstructure and a noticeable negative correlation between thickness and hardness was observed, with coatings exceeding 290 μm in thickness. Commercial dendritic Cu powder, spherical Zn powder and spherical Al powder were used as feedstock materials, with 6061AA chosen as the substrate material. The substrate was sanded with 600# sandpaper before spraying to enhance the bonding between the coating and substrate. Cu-based coatings were produced using a commercial P800Q2-II cold spray system under 18 bar

pressure, 450°C gas temperature and a nitrogen gas environment. Surface investigations showed relatively rough coating surfaces and porosity values varied between 0.68% and 1.21%. All coatings exhibited high microhardness due to strong work hardening during particle deposition. Changes in feedstock composition influenced particle deposition behavior, resulting in different coating microhardness. Potentiodynamic polarization curves confirmed that the corrosion current density of coatings was associated with the elemental content and microstructure, with low porosity beneficial in reducing the corrosion rate. Open circuit potential (OCP) monitoring and electrochemical impedance spectroscopy (EIS) test results demonstrated that different feedstock materials significantly impacted the corrosion behavior of Cu-based coatings. The coating with the lowest Zn content (Coating 4) exhibited the best corrosion resistance.

Zhang et al., (2020) conducted a study on the mechanical and corrosion properties of cold-sprayed Al-based coatings in a 3.5% NaCl solution. The application involved the use of pure (CP) Al, 2024 AA and 5083 AA powders, along with supplementary spherical Al_2O_3 particles. The substrate material chosen was 2024 AA-T3, and the substrate surface was sandblasted with 24 mesh silica sand at 0.7-0.8 MPa pressure to enhance bond strength. Coatings were produced using DYMET 423 LPCS equipment and process parameters were optimized, revealing that deposition efficiency increased with higher preheating temperatures (200°C to 600°C) and gas pressures (6 bar to 8 bar). The coatings exhibited a dense microstructure with low porosity (< 1.7%) and high adhesion strength (> 45 MPa). Among the coatings, the 5083 AA coating demonstrated the best overall mechanical properties, including the highest microhardness, cohesive strength and residual compressive stress. Conversely, the CP Al coating exhibited the weakest mechanical properties. E_{OCP} observations indicated that all coatings had lower E_{OCP} values than the 2024 AA-T3 substrate. Cyclic polarization measurements revealed that pitting corrosion was the predominant form for the tested coatings. The CP Al coating exhibited the highest pitting resistance and repassivation ability, while the 2024 AA coating showed the weakest performance. In conclusion, the 5083 AA coating demonstrated a favorable combination of mechanical and anti-corrosion properties.

Triantou et al., (2015) investigated the microstructure and tribological behavior of Cu and Cu+Al_2O_3 cold spray coatings. The feedstock materials for coating deposition included commercially available Cu and Al_2O_3 powders. Cu particles exhibited a spherical morphology, while the Al_2O_3 particles had an angular shape. The substrate material chosen was 2017 AA and the coatings were produced using HPCS equipment at 30 bar pressure, 450°C gas temperature and a N_2 carrier gas environment. Cross-sectional examination revealed the production of thick and dense coatings without evidence of oxidation or phase transformation during cold spraying. The addition of 10 wt.%, 20 wt.% and 30 wt.% Al_2O_3 in the powder mixtures resulted in Al_2O_3 content of 1.2%, 2.4% and 3.3% in the coatings, respectively. The incorporation of Al_2O_3 particles caused a slight increase in the microindentation hardness values of composite coatings compared to pure Cu coatings. Microindentation hardness values were influenced by the Al_2O_3 percentage in the coating but were independent of the Al_2O_3 particle size. Non-lubricated pin-on-disc sliding friction and wear tests were conducted using alumina pins. The sliding friction coefficients were found to be in the range of 0.4-0.5 for all coatings. The friction coefficient increased with the addition of Al_2O_3, reflecting the increased friction force of the ceramic particles. However, the specific wear rates of all composite coatings were lower than the specific wear rate of the Cu coating, indicating superior wear resistance of the composite Cu+Al_2O_3 coatings. The dominant wear mechanism identified was microabrasion-microploughing, with wear traces showing microgrooves and plastic deformation in Cu particles.

Ngai et al., (2018) investigated the corrosion behavior of 7075 AA coatings in a saltwater environment. Coatings on 7075 AA-T651 substrates were prepared by cold spraying of 7075 AA powder using He and N_2 as carrier gases. The coatings were produced using the HPCS system and the coatings deposited with N_2 and He were named N-CS and He-CS, respectively. He (28 bar and 375 °C) was utilized to produce dense coatings, while N_2 (35.6 bar and 480 °C) was used to produce more porous coatings. Differences in the fundamental corrosion behavior of 7075 AA bulk, N-CS and He-CS cold spray deposited samples were examined through electrochemical and immersion test techniques. The results indicated that microporosity played a role in corrosion properties and corrosion degree. N-CS coatings exhibited limited particle deformation and had a high degree of porosity, whereas materials sprayed in a He gas

environment showed extensive microstructural deformation and almost no porosity. Electrochemical experiments conducted on the coatings revealed that both coatings exhibited less corrosion resistance than the 7075 AA substrate. The occurrence of localized corrosion varied qualitatively, with irregular pitting/intergranular corrosion in the bulk material, microscale crevice corrosion in the N-CS coating and more limited pitting in the He-CS coating.

Meydanoglu et al., (2013) conducted a study on the microstructural evolution, mechanical properties and corrosion performance of coatings produced from B_4C or SiC reinforced 7075 AA matrix on 6061 AA-T6 using the CGDS process. In this study, B_4C and SiC powder particles were separately mixed with 7075 AA. The volume ratios of ceramic particles in the feedstock powder mixtures were determined as 10% and 20%. While 7075 AA particles exhibited a spherical morphology, B_4C and SiC particles were observed to have an angular morphology. The coating production was carried out at 9.8 bar pressure, 300 °C gas temperature and a helium carrier gas environment. Microstructural studies revealed that fine-grained coatings without discontinuities at the interface were obtained and the addition of ceramic particles increased the coating density. XRD patterns of the coatings showed the presence of Al, B_4C and SiC phases, with no other phases detected, indicating no phase transformation during spraying. The addition of ceramic particles to the 7075 AA matrix significantly increased the hardness and wear performance of the cold-sprayed coatings. However, the effect of the amount of ceramic particles in the coating on wear performance was found to be less significant, suggesting that the presence of more than 8% by volume ceramic particles in the coating structure does not contribute to wear resistance. Among the composite coatings, B_4C reinforced coatings exhibited higher wear resistance than SiC reinforced coatings, attributed to differences in elastic modulus and particle size. Potentiodynamic polarization tests revealed that the corrosion potential (E_{corr}) of cold-sprayed coatings was nobler, but the corrosion current densities (i_{corr}) of the coatings were much higher than those of the 6061 AA substrate. This indicated that the corrosion of the coatings started later but spread faster compared to 6061 AA. The addition of ceramic particles to 7075 AA particles resulted in an increase in i_{corr} compared to an unreinforced 7075 AA coating.

In the investigation conducted by Zhu et al., (2020), the study focused on the production and characterization of Al-Zn-Cu composite coatings featuring varying Cu contents through the cold spraying process. The composite powder utilized consisted of spherical Al powder, Zn powder and Cu powder, each possessing an average particle diameter of 20 μm. The application of coatings was carried out using LPCS equipment, with a 6063 AA chosen as the substrate. Compressed air served as the medium for transporting the coating powders. The coatings were fabricated under specific conditions, namely 8 bar pressure, a gas preheating temperature of 500°C, resulting in three distinct coatings labeled as 25Cu, 30Cu and 35Cu, corresponding to the varying Cu content in the coating. The primary focus of the study centered on assessing the impact of different copper concentrations on the microstructure and properties of Al-Zn composite coatings. Notably, all three coatings exhibited a dense structure with porosity levels below 2%. As Cu content increased, both coating porosity and dislocation density decreased. The uniform composition of the coatings was maintained and no discernible phase changes were observed. The addition of copper was found to enhance the plastic deformation of the coating, leading to increased density in grain dislocation and promoting grain refinement. Furthermore, the hardness of the coatings surpassed that of the substrate material, with the addition of copper proving effective in elevating coating hardness. It was established that an increase in the Al-15Zn content in the coating correlated with a proportional rise in i_{corr} and corrosion rate. Notably, the 35Cu coating demonstrated superior properties in terms of electrical conductivity and corrosion resistance.

Dzhurinskiy et al., (2012) conducted a comprehensive study on the electrochemical behavior of protective metal coatings, which were fabricated using LPCS. The coatings were applied onto commercially available 2024AA-T3 Alclad, which also served as the reference material for corrosion tests. The production parameters included a preheating temperature of 500 °C and a pressure of 6.2 bar. Five distinct coating compositions were investigated: CP1 (100 vol.% Al), CP2 (75 vol.% Al - 25 vol.% Al_2O_3), CP3 (50 vol.% Al - 50 vol.% Al_2O_3), CP4 (30 vol.% Al - 50 vol.% Al_2O_3 - 20 vol.% Zn) and CP5 (35 vol.% Al - 40 vol.% Al_2O_3 - 25 vol.% Zn). The electrochemical behavior and performance of these coatings were assessed using techniques such as OCP and potentiodynamic polarization. Results from accelerated

corrosion tests indicated that the corrosion severity of the sprayed composites heightened with an increased concentration of alumina particles in the coating. The E_{corr} values for all coatings were found to be anodically oriented compared to the substrate material. Over time, E_{corr} values decreased for CP4 and CP5, while they increased for CP2 and CP3. Furthermore, i_{corr} values for all coatings exceeded those of the substrate material, with the highest i_{corr} values observed in coatings containing zinc (CP4 and CP5). It was noteworthy that the degradation process in Al-Zn-Al_2O_3 composite coatings was accelerated by the galvanic coupling of Al-Zn.

Winnicki et al., (2017) conducted an investigation into the impact of different copper powder morphologies and ceramic additions on the porosity, corrosion resistance and electrical conductivity behavior of coatings fabricated using LPCS. Two types of commercially available copper powders were employed: Electrolytic copper (E-Cu) and spherical copper (S-Cu). Additionally, each copper powder was blended with Al_2O_3 in a 50:50 weight ratio before the deposition process. S-Cu powder, generated through gas atomization, exhibited a spherical morphology, while E-Cu powder, produced via electrolysis, displayed a dendritic morphology. The ceramic reinforcement (Al_2O_3) was prepared by crumbling and its particles exhibited an irregular morphology. The substrate material chosen for the study was 1350 AA and its surface underwent activation through sandblasting at 6 bar pressure, achieving a surface roughness of Ra = 9.5 μm. The coatings were generated using DYMET 413 LPCS equipment, with process parameters set at 9 bar pressure and a preheating temperature of 600 °C. Four distinct coatings were created based on the variation in powder morphology and alumina addition. Microstructure analysis revealed that the deposited composite coatings exhibited lower porosity compared to pure metal coatings. Coatings produced with dendritic copper powder exhibited the highest porosity, attributed to reduced particle deformation. The introduction of ceramics to the metal powder led to an increase in the hardness of the coatings. Corrosion protection of the coatings was assessed through polarization measurements. All coatings demonstrated higher E_{corr} values in the cathodic direction compared to the substrate. However, the incorporation of ceramics significantly reduced the E_{corr} values for both coatings. The findings indicated that E-Cu+Al_2O_3 and S-Cu coatings offered effective corrosion protection for 1350 AA.

Y. J. Li et al., (2017) conducted an investigation to assess the influence of Cu feedstock morphology and microstructure on the deposition behavior and microstructure of cold-sprayed coatings. The study involved a comparative examination of DE, coating porosity, electrical conductivity and corrosion behavior for coatings produced using conventional gas-atomized Cu (GA Cu) powder and electrolytic Cu (E Cu) powder. Notably, GA Cu particles exhibited a spherical morphology with a dense cross-section, while E Cu particles displayed a dendritic morphology and a porous microstructure. The substrate material utilized was 1100 AA, which underwent sandblasting with 24-mesh alumina particles prior to the coating deposition process. The DWCS-2000 cold spray system was employed for coating deposition, with process parameters set at 30 bar pressure, a gas temperature of 400 °C and N_2 as the processing gas. The findings revealed that the composition, oxygen content, particle size, feedstock morphology and porosity significantly influenced DE, coating microstructure and properties. Under identical conditions, E Cu powder demonstrated a high DE of 70.5%, whereas GA Cu powder exhibited a lower DE of only 34.4%. In corrosion tests involving four different samples (AA substrate, Bulk Cu, GA Cu and E Cu) all Cu-based coatings displayed higher corrosion potential in the cathodic direction compared to the AA substrate. The bulk Cu sample exhibited the highest E_{corr}. Interestingly, while the AA substrate demonstrated the highest i_{corr}, the lowest i_{corr} was observed for bulk Cu. In comparison to Cu-based coatings, E Cu, with its nobler E_{corr}, exhibited a lower i_{corr}.

L. Zhang et al., (2019) endeavored to enhance the performance of magnesium alloys by employing cold spray deposition to create Cu-Ni/Al_2O_3 and Cu-Zn/Al_2O_3 metal-ceramic coatings. These coatings were compared with Cu-Al_2O_3 coatings in terms of microstructures, microhardness, tribological behavior and corrosion resistance. High purity Cu, Ni and Zn metal powders, along with irregular Al_2O_3 ceramic powder averaging 20 μm in size, were chosen as starting powders. The substrate material was AZ31B magnesium sheet. The coatings were produced using commercial LPCS equipment (DYMET-423), utilizing compressed air as the carrier gas with a driving pressure of 6 bar. During the spraying process, the stand-off distance was set at 10 mm, the traverse speed at 500 mm/min. and the preheated temperature of the carrier gas at 500°C. Results indicated that the incorporation of Ni or Zn into a Cu-Al_2O_3

coating contributed to the formation of a denser composite coating with reduced porosity. The addition of Ni increased the microhardness of the Cu-Al_2O_3 coating but did not enhance antifriction performance or wear resistance. Conversely, the addition of Zn improved antifriction performance, wear resistance and microhardness of the Cu-Al_2O_3 coating. It was concluded that the primary reason for this discrepancy is that the addition of Ni does not alter the adhesion wear mechanism of the Cu-based coating, whereas the addition of Zn weakens this mechanism. Furthermore, the corrosion resistance of the Cu-Al_2O_3 coating was found to increase with the addition of Ni, attributed to the improved compactness and corrosion resistance of Ni. However, the incorporation of Zn did not improve the corrosion resistance of the Cu-Al_2O_3 coating due to the rapid corrosion of Zn and the formation of loose corrosion products lacking protective effects.

Certain bioactive metals, such as Ag, Cu and Zn, as well as naturally occurring products, have shown promise in preventing or delaying MIC phenomena, making them viable options for advanced biomaterials with antibacterial properties. Among these, Cu and Cu-based alloys, often applied as coatings, emerge as commonly employed solutions. Various coating methods can be utilized for this purpose (Ghosh et al., 2020). In a study by Jing et al., (2008), Cu porous materials were prepared through electrodeposition on the substrate. The antibacterial efficacy of Cu was explored, specifically against *Escherichia coli*. The results demonstrated that Cu porous materials exhibited potent and persistent antibacterial activity against *Escherichia coli*. Nie et al., (2010) evaluated the effectiveness of a Cu-plated surface and a superhydrophilic Cu-dotted oxide coating in inactivating *Escherichia coli*, methicillin-resistant *Staphylococcus aureus* (*MRSA*) and *Enterococcus faecium*. Plasma electrolytic oxidation of Al was employed to produce the oxide surface, followed by the electroplating of Cu metal on top of the oxide layer. The findings indicated that the antibacterial performance of the Cu-dotted oxide surface surpassed that of the Cu plate surface and remained effective even in humid/wet environments. In the work by Wrona et al., (2017), Cu, Cu alloys (CuNi35, CuSn10) and a Cu composite coating (Cu-TiO210) were deposited on substrate surfaces through plasma spraying. All coatings demonstrated substantial antibacterial activity, particularly against Gram-negative bacterial species and on satin surfaces. Y. Chen et al., (2008)

observed a remarkable antibacterial effect against *Escherichia coli*, *Pseudomonas aeruginosa* and *Staphylococcus aureus* with hydroxyapatite (HAP) coatings. Meininger et al., (2018) electrochemically deposited $Ca(OH)_2$ (Portlandite) coatings on substrate surfaces. The addition of Ag^+ and Cu^{2+} ions to the hydroxide led to reduced bacterial growth against *Staphylococcus epidermidis*.

Metals characterized by low melting points and mechanical strength, such as copper, zinc, and aluminum, prove highly suitable for the CGDS process (Moridi et al., 2014). In a study by Sanpo et al., (2008), the deposition properties of Al/ZnO coatings produced through CGDS at room temperature using Al/ZnO powder at various ratios were investigated. It was observed that the antibacterial activity significantly increased with the rising concentration of ZnO nanopowder in the composite powder feedstock and CS coating. Another study by Sanpo et al., (2009) explored the antibacterial behavior of cold-sprayed Cu (chitosan-copper complex) powder and its deposits against *Escherichia coli*. The results demonstrated an enhanced antibacterial activity with increasing Cu/Al powder concentrations in the composite powder feedstock and cold-sprayed coating. This study also highlighted the feasibility of cold spraying biopolymer complexes. In a related investigation, Sanpo & Tharajak, (2017) examined the antimicrobial properties of HA/PEEK coatings with different transition metals, including silver, nickel, zinc and copper. Successful deposition occurred through cold spraying at preheating temperatures of 150–160°C and pressure of 10–14 bar. Evaluation of the lethal effect against *Staphylococcus aureus* revealed a trend of HA-Ni/PEEK < HA-Cu/PEEK < HA-Zn/PEEK < HA-Ag/PEEK, with HA-Ag/PEEK displaying the highest antibacterial tendency. In a study by Jin et al., (2015), the antibacterial properties of a Ti-Cu coated layer were examined, revealing that almost all bacteria placed on the Ti-Cu coated layer were killed within 6 hours. The coatings exhibited excellent antibacterial abilities attributed to the release of copper ions. Furthermore, Sanpo et al., (2011) investigated the biocompatibility and antibacterial properties of cold-sprayed ZnO/Ti composite coatings on an Al 6061 substrate using the CGDS process. The ZnO/Ti coatings, produced under helium gas at temperatures between 300-400 °C and pressure of 13-15 bar, demonstrated significant antibacterial effects against *E. coli*. Biocompatibility results indicated a

decrease in cell viability with increasing ZnO concentration in the coating composition.

In a study conducted by Champagne & Helfritch, (2013), Cu deposition on AA was performed using three distinct thermal spraying methods: Plasma spray, wire arc spray and cold spraying. Subsequently, the treated surfaces were exposed to *MRSA* and maintained at room temperature for approximately 2 hours. Upon evaluating the results based on the *MRSA* quantity, a ranking of cold-sprayed < wire arc-sprayed < plasma-sprayed was established. Notably, the cold spraying method exhibited the lowest amount of surviving *MRSA* after a 2-hour contact period compared to the other thermal spraying methods.

In a study conducted by Hutasoit et al., (2021), Cu coatings were applied to both stainless steel and aluminum substrates through the cold spraying process. The coated samples, in both as-deposited and heat-treated states, underwent exposure to *Escherichia coli* and *Staphylococcus aureus* bacteria. The HPCS equipment was utilized for coating production, employing 30 bar pressure and 500°C compressed air conditions. Cu coatings on stainless steel were tested in two conditions: In the as-deposited state and after annealing at 400°C for 10 minutes to induce the formation of an oxide layer on the Cu deposits. Antibacterial tests and bacterial attachment tests were conducted on four different samples, including bulk Cu and as-deposited Cu coatings on aluminum. The results indicated that as-deposited Cu coatings exhibited the inactivation of both types of bacterial cells under a 30-minute exposure. However, on heat-treated Cu-coated surfaces, both *E. coli* and *S. aureus* were not completely eliminated even after 60 minutes of exposure. The presence of Cu oxides (Cu_2O and CuO) on the surface of heat-treated samples was detected. This result suggested a decrease in antibacterial activity due to the presence of Cu(I) and Cu(II) ions and lower concentrations of Cu(0)-metallic Cu ions. Moreover, Cu ions on the bulk Cu surface were found to react more aggressively with Gram-negative *E. coli* bacterial cells compared to Gram-positive *S. aureus* cells, leading to faster inactivation of *E. coli*. In the case of bimetallic galvanic coupling with negative potential, as observed in the Cu/Al coating/substrate configuration, Cu ions exhibited more aggressive reactions against Gram-positive *S. aureus*, resulting in a shorter inactivation time compared to

E. coli. Conversely, the copper coating/substrate configuration (Cu/SS) with positive galvanic coupling potential produced fewer Cu ions compared to bulk copper samples, resulting in higher inactivation times for both types of bacterial cells. The study demonstrated that different coating/substrate galvanic coupling configurations respond differently to various types of bacteria.

Sundberg et al., (2019) explored the impact of corrosion on surfaces treated with conventional and nanomaterial Cu through the cold spray process, with a focus on antimicrobial applications. The cold-sprayed samples were compared with bulk wrought pure Cu. The study involved heat treatment (HT) applied to the samples and oxidation was conducted on 99% pure bulk Cu. HT (annealing) of the bulk, conventional and nanomaterial Cu surfaces was carried out through surface combustion. Corrosion tests were conducted on seven different samples (bulk Cu, conventional Cu CS, nano Cu CS, CuO, bulk Cu HT, Conventional Cu HT and Nano Cu HT). Various corrosion tests, including EIS, Linear Polarization (LP) and ion release analysis, consistently demonstrated that nanomaterial Cu exhibited a higher corrosion rate compared to conventional Cu. The nanomaterial Cu, characterized by a smaller grain size and larger grain boundaries than conventional Cu, resulted in increased ion release and contributing to the elevated corrosion rate. Despite the higher corrosion rate, nanomaterial coatings demonstrated an enhancement in antimicrobial efficiency compared to conventional Cu, particularly in the context of contact killing of the Influenza A Virus. Microscopic analyses substantiate corrosion findings, revealing that nanomaterial Cu possesses markedly smaller grains compared to conventional Cu, suggesting a higher proportion of grain boundaries available for the release of Cu ions into the surrounding environment. Given that the primary antimicrobial mechanism of Cu resides in contact killing, the elevated ion release and corrosion rate observed in nanomaterial Cu directly contribute to its heightened antimicrobial efficacy in the contact killing of the Influenza A Virus when juxtaposed with conventional Cu.

CHAPTER SIX
EXPERIMENTAL DETAILS

6.1 Specimen Preparation

In the experimental investigations, 7075 AA-T651 was employed as the substrate material, characterized by a chemical composition denoted as (0.29% Fe, 0.08% Si, 0.22% Mn, 0.20% Cr, 0.042% Ti, 1.68% Cu, 2.37% Mg, 5.79% Zn and balance Al) and mechanical properties denoted as (yield strength: 521-544 MPa, tensile strength: 579-604 MPa and elongation: % 9.5-12.4). The 7075 AA in sheet form, measuring 500x500x10 mm, was supplied by Seykoç Aluminum Ltd. To facilitate proper mounting of the specimens on the coating bench, the initially supplied sheet of 7075 AA was subjected to laser cutting, conforming to the technical drawing depicted in Figure 6.1, to approximate dimensions. Subsequently, precision was achieved by employing wire-cut electrical discharge machining (EDM) to bring the material to its final specified dimensions.

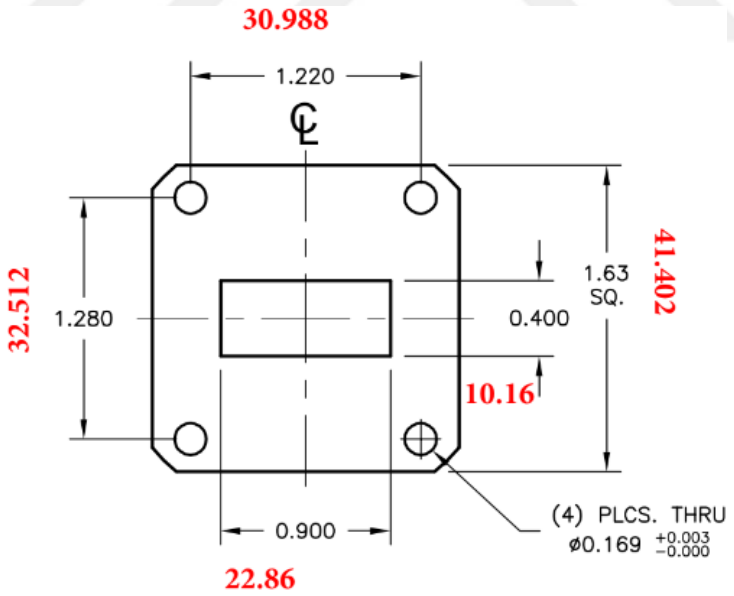
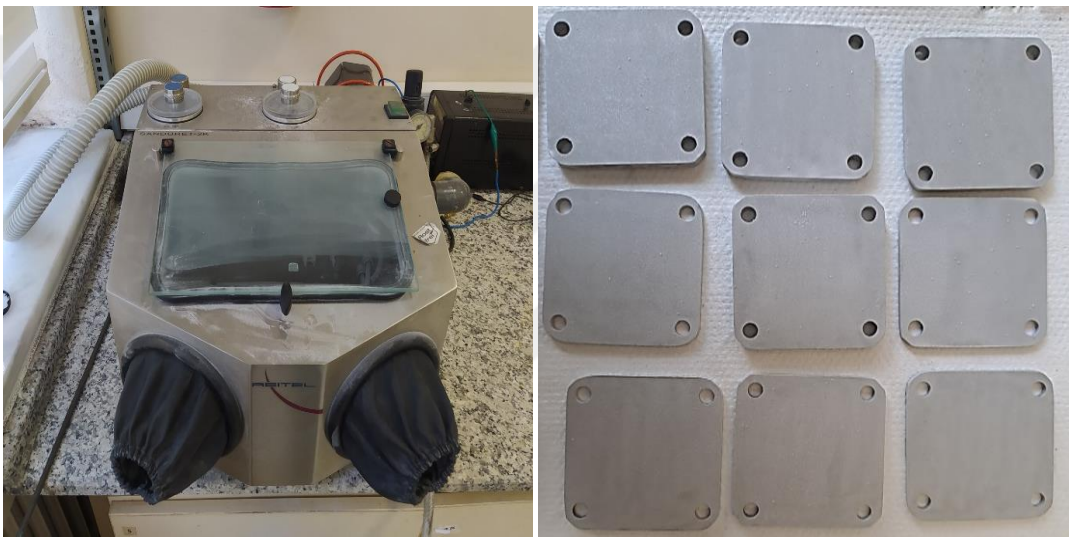


Figure 6.1 Technical drawing of the specimen

To ensure consistent surface quality among all specimens and to enhance mechanical bonding through surface activation before the coating process, sandblasting was

executed utilizing the Reitel Sanduret-2K sandblasting device (Megadental Gmbh), depicted in Figure 6.2 (a). The sandblasting operation was conducted at a pressure of 3.5 bar, employing alumina particles with a size of 250 µm. Following the sandblasting procedure, comprehensive surface roughness measurements were conducted on the specimens. The results revealed values of Ra: 1.90 µm and Rz: 14.4 µm. Figure 6.2 (b) illustrates the final state of the specimens, which were precisely cut to conform to the required dimensions and subjected to the sandblasting process before the coating application.



(a) **(b)**

Figure 6.2 **(a)** Reitel Sanduret-2K sandblasting device and **(b)** images of specimens following sandblasting process

6.2 Coating Powders and Characterization

In the fabrication of coatings, commercially available Cu-Al_2O_3 (CA), Ni-Zn-Al_2O_3 (NZA) and Cu-Zn-Al_2O_3 (CZA) coating powders, featuring particle diameters within the range of approximately 5-70 µm, were employed. These coating powders were procured from DYMET (Obninsk Center for Powder Spraying, Russia) and exhibit a purity exceeding 99%. Throughout the coating production process, CA and CZA powders were utilized individually. Additionally, powder compositions of 85% Cu-Al_2O_3 + 15% Ni-Zn-Al_2O_3 (CNZA15) and 70% Cu-Al_2O_3 + 30% Ni-Zn-Al_2O_3 (CNZA30) were prepared by mechanically blending CA and NZA powders in specific

weight ratios. This systematic approach ensured the formulation of diverse coating compositions to meet specific requirements and applications.

The characteristics of the coating powders employed in the CGDS process play a crucial role in influencing both the process parameters and the ultimate properties of the coatings, as extensively discussed in the literature. Therefore, a comprehensive examination of the particle size distributions, morphologies, phase structures and phase ratios of the powders was conducted. Particle size distributions of the powders were assessed using a laser particle size distribution device (HORIBA LA-950). The ZEISS GeminiSEM 560 scanning electron microscope (SEM) equipped with an array of secondary electron (SE) and backscattered electron (BE) detectors, along with an energy dispersive X-ray spectrometer (EDS) attachment, was employed to determine powder morphologies. The SEM analyses were carried out using SE and BE methods at magnification levels of 500x-1000x-2500x. To mitigate electron charging resulting from the low electrical conductivity of the powders, a thin gold-palladium conductive film was applied to the specimens using the Quorum SC7620 sputter coater before SEM analysis. Low accelerating voltages were utilized during SEM analysis. Furthermore, powder morphologies were corroborated by conducting semi-quantitative elemental analysis through point EDS and EDS mapping. The crystal phase components and their relative proportions in the powders were ascertained through X-ray diffraction (XRD) using the Rigaku D/max-2200/PC series X-ray diffractometer equipped with an SA-HF3 model X-Ray tube (Cu-Kα radiation). Peak fitting was applied to identify the crystalline phases by comparing the angular positions of the peaks with reference models in the International Center for Diffraction Data (ICDD) Powder Diffraction File (PDF2). Concurrently, the composition of the coating powders was cross-referenced with the specifications provided by the supplier company using X'pert High Score Plus software. This multi-faceted analytical approach ensured a comprehensive understanding of the coating powder characteristics for optimized CGDS processes and enhanced coating properties.

6.3 Low Pressure CGDS Equipments and Design of Spray Process Experiments

Prior to commencing the coating production process, a semi-automated coating bench was designed and developed. This bench comprises essential components, including a servo motor, a spray table, a connecting rod, a misaligned connection apparatus, a linear rail system, wheels and a laboratory-type elevator. The bench's structural and functional details are depicted in Figure 6.3. The coating bench serves as a specialized platform, offering the capability to uniformly spray a predetermined quantity of powder onto a designated surface within a specific time frame. It is equipped to effectively control and maintain the distance between the nozzle and the substrate. Additionally, the bench enables precise adjustments to the movement of both the substrate and nozzle along the x and y axes. This functionality is instrumental in preventing the overlap of coatings and ensuring consistent repeatability in the coating process. The semi-automated nature of the bench enhanced efficiency and precision in coating applications.

The coatings were generated using the commercially accessible DYMET-423 (Obninsk Center for Powder Spraying, Russia) low-pressure CGDS equipment. The DYMET-423 device is equipped with two distinct powder feeders, facilitating seamless transitions between different powders throughout the coating process. The conveyance of powder particles is achieved through compressed air generated by a dedicated compressor. Designed to be compatible with robotic and automated systems, the DYMET-423 device is versatile and well-suited for the production of diverse metal-based (Al, Zn, Cu, Ni, Sn, Pb etc.) coatings. Additionally, it offers the option of manual operation. Figure 6.4 presents an illustrative depiction of the DYMET-423 CGDS equipment along with its associated components.

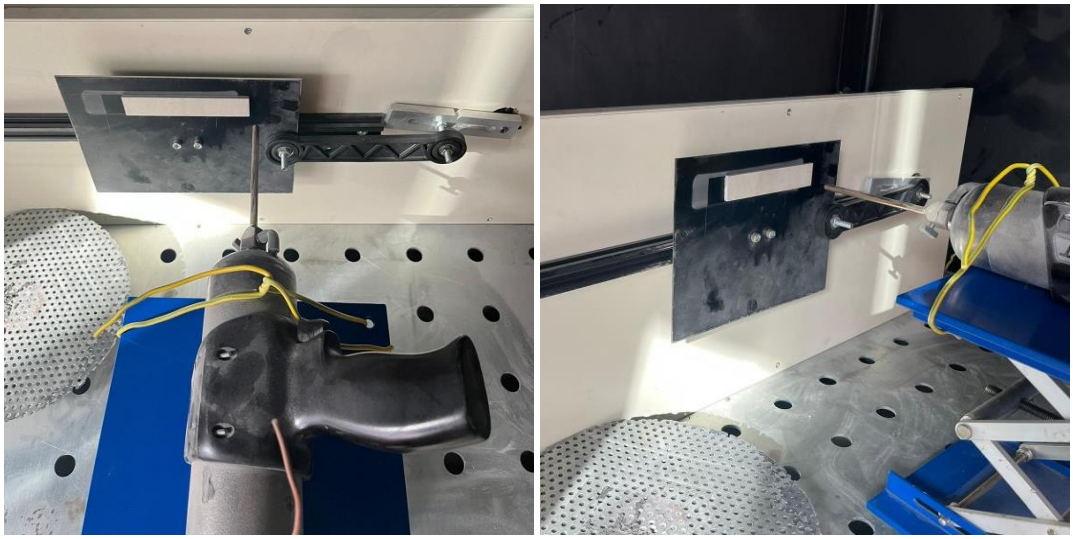


Figure 6.3 Images of semi-automated coating bench

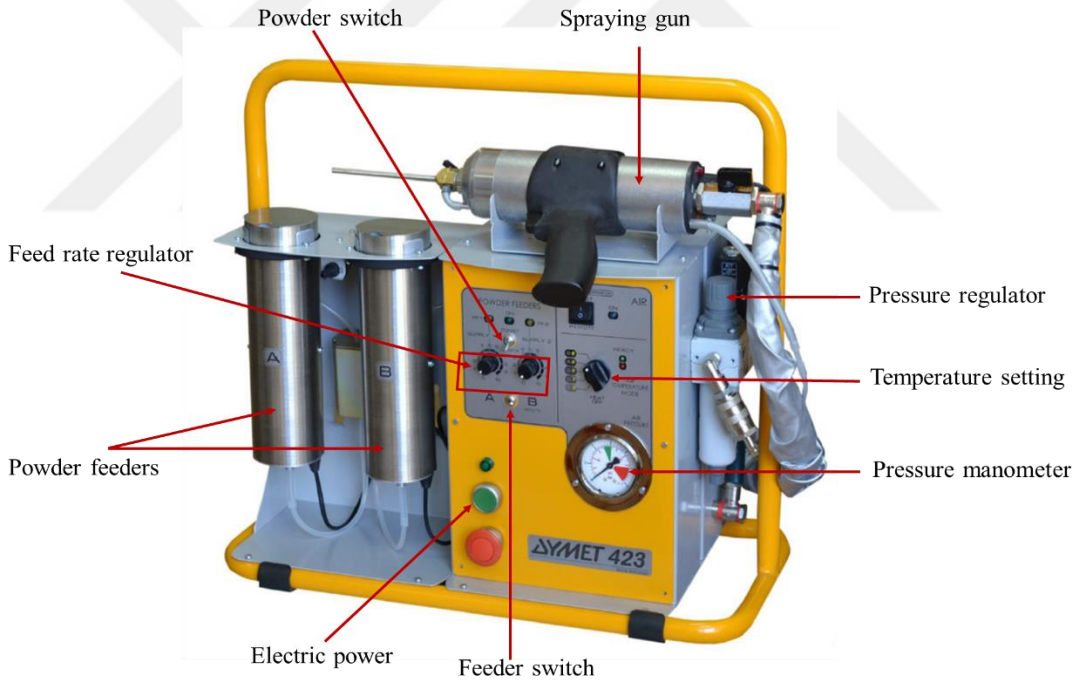


Figure 6.4 Schematic of DYMET-423 low pressure CGDS equipment and its components

Process parameters that are important in the production of coatings were determined depending on the nature of the method, the surface quality and mechanical properties of the substrate material, the crystal structure and mechanical properties of the powder material and were optimized as a result of repeated trials. Based on these data, the

following parameters were determined to be applied similarly in all experimental sets: compressed air pressure 8 bar, preheating temperature 300 °C, powder feeding rate 0.3 g/s, traverse speed 10 cm/s, stand-off distance 15 mm, The number of spraying steps was determined as 10 passes and 20 passes, respectively. Spraying operations were carried out using a stationary spray gun, and the specimen moved in the x direction. The movement of the specimen in the x direction is in the form of going and returning and 1 going or 1 returning movement of the specimen is considered as 1 pass (spraying step). Experimental sets in which powder composition, number of spraying steps and coatings are included as variables are given in Table 6.1 and CGDS processes were completed in line with these experimental sets. Macro-scale images of 8 different Cu-based coatings obtained as a result of the CGDS process are presented in Figure 6.5.

Table 6.1 Experimental sets considered in the production of coatings on 7075 AA.

Experiment Set	**Powder composition**	**Number of spraying step (passes)**	**Coating**
1	CA	10	CA 10p
2	CA	20	CA 20p
3	CNZA15	10	CNZA15 10p
4	CNZA15	20	CNZA15 20p
5	CNZA30	10	CNZA30 10p
6	CNZA30	20	CNZA30 20p
7	CZA	10	CZA 10p
8	CZA	20	CZA 20p



Figure 6.5 Images of Cu-based coatings produced with the CGDS process

6.4 Coating Characterization

This section encompasses a comprehensive examination of various aspects of Cu-based coatings, including microstructure, thickness, hardness, adhesion strength, phase analysis and surface roughness.

6.4.1 Preparation of Cross-Section of Coating

To investigate the microstructure throughout the thickness of the coatings, substrates coated through the CGDS process underwent a sequential process involving sectioning, resin encapsulation and final polishing. Sectioning was executed using a SiC precision cutting disc from Cloeren Technology GmbH, affixed to a Struers Labotom-5 manual cutting machine. The coated specimen was securely clamped in a vise and the cutting disc was positioned to initiate contact with the coated side and exit through the substrate side. This approach significantly mitigated the risk of coating detachment from the substrate during the cutting process. Subsequently, the sectioned specimens underwent ultrasonic cleaning in ethanol to eliminate residues from the cooling liquid.

Following sectioning, a cold mounting process was conducted using epoxy resin (EpoFix from Struers) at room temperature without the application of vacuum. Epoxy resins, distinguished by their reduced shrinkage compared to cold mounting acrylic resins, were employed. The low viscosity of the epoxy resin facilitated penetration into the coating's pores and cracks, meeting stringent edge retention requirements during subsequent grinding and polishing stages. Fine grinding was executed using diamond-coated composite thin grinding discs, known for maintaining flatness and ensuring an effective material removal rate. The final stage of fine grinding involved the use of 2000 grit SiC paper. Subsequently, polishing was carried out utilizing 3 μm diamond paste in an alcohol-based lubricant. The concluding polishing step employed a 50 nm colloidal silica suspension. The orientation of the specimen throughout the grinding and polishing processes holds significant influence on the preparation outcomes. To prevent adhesive damage to the coating, the abrasive direction was meticulously controlled to proceed from the coating to the substrate.

6.4.2 Microstructural Investigation and Coating Thickness Measurement

Microstructural investigations were conducted using the Nikon Eclipse ME600 optical microscope (OM) and the ZEISS GeminiSEM 560 SEM. The optical microscope is equipped with a Nikon DS-Fi1 CCD camera, enabling high-resolution image capture at 2560 x 1920 pixels. Given that the produced coatings featured a rough upper surface with open pores, only polished sections of the coatings were subjected to examination using both OM and SEM. To eliminate electron charging resulting from the coatings' low electrical conductivity, the specimens underwent a thin gold palladium conductive film coating using the Quorum SC7620 sputter coater before analysis. Moreover, SEM analysis employed low accelerating voltages. The surface morphology of the coatings was scrutinized in the SE mode, while the BE mode was employed to discern contrasts between areas with distinct elemental compositions and to unveil sub-surface features and surface topography defects. Furthermore, semi-quantitative elemental analysis was carried out for the produced coatings through point EDS and EDS mapping techniques.

Within this investigation, microstructure images were acquired at magnifications of 100x, 200x and 500x during OM examinations. Additionally, SEM examinations were conducted at magnifications of 500x and 1000x. In the context of coating thickness analyses, measurements were meticulously obtained from seven distinct regions. To guarantee measurement accuracy, both OM and SEM were employed in these analyses.

6.4.3 Measurement of Hardness

The Shimadzu HMV microVickers hardness tester was employed to acquire the through-thickness hardness profile of the coatings. Hardness scanning was conducted from the coating towards the substrate, taking into consideration the trace width in cross-section measurements. Out-of-plane indentations were executed on the coating oriented parallel to the substrate surface, employing a peak load of 0.025 kg (245.2 mN) ($HV_{0.025}$) and an application time of 10 seconds. The chosen loading value was determined based on the maximum indentation depth obtained during indentation. To prevent the hardness value from being influenced by the substrate's properties, it was ensured that the maximum indentation depth did not exceed 10% of the entire coating thickness, measured from the free surface. Moreover, for each specimen, a minimum of 5 measurements were conducted from different regions and the hardness values were derived by averaging these individual measurements.

6.4.4 Scratch Test

The scratch test serves as a widely adopted method for assessing the adhesion quality of coatings on various substrates. In this test, a diamond stylus with a spherical tip geometry is employed to exert a normal force onto the surface of the coated specimen. Concurrently, the coated specimen undergoes displacement at a constant rate, while the normal force is incrementally increased. Stresses induced in the coating by the applied normal force at a specific point lead to coating damage such as cracking, spalling, or chipping. The normal force that results in a specific level of coating damage is defined as the critical scratch load (Lc). Precise determination of critical scratch loads is achieved by analyzing fluctuations in tangential force data or acoustic

emission signals. Additionally, specific surface deformations can be observed through OM or SEM. It is noteworthy that one or more distinct critical scratch loads may be defined to represent progressive levels of coating damage, as applicable to a particular substrate/coating combination.

This study employed the CSM Instruments micro scratch test device, capable of applying a maximum load of 150 N, to assess the practical adhesion strength of the coatings. Prior to baseline measurements, a preliminary scan was conducted on the coated surface to identify surface slope. Subsequently, to investigate the progressive damage characteristics in the coating, the normal load on the diamond Rockwell stylus with a 200 μm tip diameter was linearly increased from 1 N to 150 N at a normal loading rate of 149 N/min. Simultaneously, the coated specimen underwent displacement at a constant speed of 6 mm/min. The total scratch track length was determined as 6 mm. After scratch test, a final scan was performed on the surface to evaluate the elastic recovery of the coating-substrate system. Throughout the scratch test, the normal load, penetration depth and acoustic emission signals were recorded to identify the critical scratch loads corresponding to specific observed damage.

6.4.5 X-Ray Diffraction Measurement

In this investigation, coating powders were sprayed onto the substrate in an ambient atmosphere, subjected to the preheating temperature of the compressed air employed as a carrier gas and subsequently used to produce coatings. Concurrently, plastic deformation energy was released as the coating powders impacted each other and the substrate. Therefore, it is critical for the phase content of the powder material and the resulting coating phase content produced from the same powder, to closely resemble each other and for undesired phase transformations and oxide formations to be avoided. Given the substantial impact of crystal phase structure on the electrochemical and mechanical properties of the coating, the crystal phase components and their relative proportions were investigated utilizing XRD. In this study, the phase composition of the coating was analyzed using the Rigaku D/max-2200/PC series X-ray diffractometer equipped with the SA-HF3 model X-Ray tube (Cu-Kα radiation). Following the recording of the XRD spectrum, peak fitting was applied to discern the

crystalline phases present, by comparing the angular positions of the peaks with reference models from the International Center for Diffraction Data (ICDD) Powder Diffraction File (PDF2).

6.4.5.1 Through-Thickness Phase Profile

XRD analyses were conducted after coating production; however, certain components of the coating powder remained undetected within the bulk coating. This limitation was attributed to backscattering inherent in the CGDS method or the capacity constraints of the XRD device detector. Consequently, in order to elucidate the phase structure of all components, the prepared coatings underwent sanding on 1200 grit silicon carbide sandpaper using an automated grinding machine rotating at 150 rpm. Subsequently, the sanded coatings were subjected to XRD analysis once again. To enhance signal detection from thin coatings and minimize interference from the substrate, a modified approach utilizing a low grazing incidence angle in 2θ/θ scanning methods was employed. This adjustment aimed to mitigate the overwhelming signal contribution from the substrate, thereby accentuating the signal strength originating from the porous coating. In the context of this study, Grazing Incidence X-ray Diffraction (GIXRD) was implemented, wherein only the detector underwent movement while maintaining a fixed X-ray tube at a low incidence angle of 3°. Experimental parameters included an X-ray tube voltage of 40 kV and a current of 36 mA. The scanning range spanned from 5° to 90°, with a narrow sampling width of 0.02° and a deliberate scan speed of 2°/min. To optimize data acquisition, divergence and scattering slits of 1° were utilized, complemented by a receiving slit set at 0.3 mm. This configuration ensured precision in capturing the diffraction pattern, particularly from the coating of interest, while minimizing the influence of signals originating from the underlying substrate.

6.4.5.2 Quantitative Phase Analysis

Quantitative phase analysis was executed on a set of coating powders, namely CA, NZA, CNZA15, CNZA30 and CZA. XRD scans were carried out employing the 2θ/θ scanning method. Experimental conditions encompassed an X-ray tube voltage of 40

kV and a current of 36 mA. The scanning range extended from 5° to 90°, with a sampling width of 0.02° and a deliberate scan speed of 2°/min. Precise control over the experimental setup was maintained through the utilization of divergence and scattering slits set at 1° each, accompanied by a receiving slit of 0.3 mm. This configuration was instrumental in optimizing the diffraction pattern resolution and signal-to-noise ratio. For the subsequent phase proportion calculations, Rietveld refinement was employed and the analysis was conducted using the X'Pert Highscore Plus software. This refinement process allowed for accurate determination of the quantitative distribution of phases within the coating powders, contributing to a comprehensive understanding of their crystalline composition.

6.4.6 Surface Profilometry

Stylus surface profilometry involves the use of an instrument that amplifies and records the vertical displacements of a stylus moving at a constant speed across the surface under examination. In our current investigation, the Ambios Technology XP-2 surface profilometer is employed, incorporating an optical deflection height measurement mechanism and a magneto-static force control system. This design results in a low-force stylus assembly, accommodating loads as minute as 0.05 mg and a stylus tip with a radius of 2 μm. The instrument's capabilities extend the measurement of vertical features from less than 10 Å to approximately 400 μm, with a specified vertical resolution of 1.5 Å at the 10 μm setting and 15 Å at the 100 μm setting. The stylus arm is pressed against the specimen surface and traversed at a constant speed using a traverse unit. As the stylus moves over the specimen, it detects surface deviations, generating a signal proportional to the vertical stylus movement. This signal is subsequently amplified, conditioned and digitized. The acquired surface profile data are then utilized to assess specimen roughness in accordance with the ISO 4287:1997 standard. This standard delineates the roughness sampling lengths pertinent to the measurement of roughness parameters in non-periodic profiles, offering a standardized approach for evaluating surface characteristics.

6.5 Electrochemical Corrosion Tests

6.5.1 Experimental Setup

Within this investigation, electrochemical tests were conducted utilizing a standard three-electrode electrochemical cell configuration. The cell featured an Ag/AgCl reference electrode, a platinum mesh as the counter electrode and the test specimen as the working electrode, as illustrated in Figure 6.6. The electrochemical behaviors of both the 7075 AA and Cu-based coatings were explored employing cyclic polarization and EIS techniques. Prior to the initiation of cyclic polarization and EIS tests, the open circuit potential (OCP) of the test specimens underwent a stabilization period of 30 minutes. Corrosion tests were performed at ambient temperature in a 3.5 wt.% NaCl solution and electrochemical measurements were carried out using a research-grade Gamry Reference 600 potentiostat/galvanostat/ZRA.

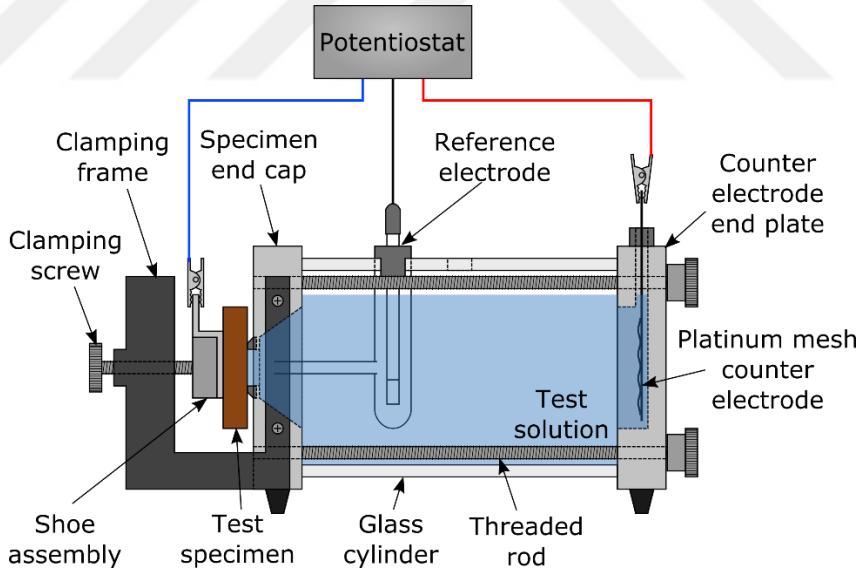


Figure 6.6 Three-electrode electrochemical cell configuration utilized in corrosion tests (Tekin, 2016)

6.5.2 Cyclic Polarization

Potentiodynamic polarization scanning is a valuable technique for extracting crucial insights into electrode processes. This method furnishes information about the cathodic behavior of an electrochemical system, corrosion rate, pitting sensitivity and passivity. All DC electrochemical techniques designed for determining corrosion rates aim to measure the i_{corr}, providing information on corrosion intensity and penetration rate. The Tafel extrapolation method represents the fundamental approach for experimentally evaluating the i_{corr} value. In this study, cyclic polarization was applied to both bare and coated test specimens to comprehensively assess localized corrosion sensitivity and the formation of pits, especially critical for 7075 AA. The cyclic polarization scan resembles the potentiodynamic scan, with the distinction that the voltage is swept over a range and then returned to the initial potential. Due to surface alterations caused by reactions during the scan, data from the return voltage scan often does not overlap with data obtained from the forward scan Accordingly, cyclic polarization test parameters were configured to simulate an aggressive corrosion environment. These parameters are designated as Initial E (V): -0.25 (E_{ocp}), Apex E (V): 3 (E_{ocp}), Final E (V): 0 (E_{ocp}), Forward Scan (mV/s): 0.3, Reverse Scan (mV/s): 0.3, Specimen Area (cm^2): 1, Apex I (mA/cm^2): 5. Using the data derived from the tests, the corrosion rate is determined in accordance with Faraday's law, incorporating Equation 6.1.

$$Corrosion\ rate\ (mg/dm^2.day) = 0.0895.i_{corr}(\mu A/cm^2).EW \qquad (6.1)$$

In the provided equation, EW denotes the equivalent weight of the alloy employed in the corrosion test. The polarization resistance (R_p) of the alloy is determined using the Stern-Geary Equation as presented in Equation 6.2.

$$R_p = \frac{\beta_a.\beta_c}{2.303.i_{corr}.(\beta_a.\beta_c)} \qquad (6.2)$$

In this equation, β_a and β_c represent the anodic and cathodic Tafel slopes, respectively.

6.5.3 Electrochemical Impedance Spectroscopy (EIS)

The EIS technique employs a diverse range of low-magnitude polarizing voltages, which cycle between peak anodic and cathodic magnitudes through a spectrum of alternating current (AC) voltage frequencies, as opposed to utilizing a series of single-magnitude and polarity direct current (DC) voltages. The polarizing voltage amplitudes in EIS typically span from 5 to 20 mV and are centered around the OCP. The AC voltage amplitude is set at 5 mV (± 5 mV from OCP), constituting a complete cycle that involves polarizing to a 5 mV peak anodic potential, discharging (to OCP = 0), polarizing to a -5 mV peak cathodic potential, discharging and then polarizing again to a 5 mV peak anodic potential. EIS employs voltage frequencies ranging from 100 kHz to several mHz in its measurements. At each frequency, resistance and capacitance values are recorded. These recorded values offer insights into corrosion behavior and rates, as well as properties of the coating under investigation. By analyzing the impedance response across a range of frequencies, EIS provides valuable information on the electrochemical characteristics of materials, contributing to a comprehensive understanding of corrosion processes and coating performance. EIS data is commonly analyzed through fitting it to an electrical equivalent circuit model, which typically involves the utilization of resistors, capacitors and inductors. These equivalent circuit elements are chosen to construct a model that accurately reflects the physical structure of the electrochemical system. For instance, the electrical behavior of an electrical double layer on a corroded bare metal surface can be effectively modeled using a simple electrical circuit comprising resistors and a capacitor. EIS data can be presented graphically in various ways, incorporating component vector magnitudes, total impedance magnitudes, or phase angles. Three prevalent types of EIS plots include complex plane plots (commonly known as Nyquist graphs), Bode magnitude plots and Bode phase plots. Complex plane graphs portray real and imaginary impedance quantities for each polarization frequency (Tait, 1994).

Accordingly, EIS measurements were conducted under both OCP and aggressive corrosion conditions. The tests were executed within the 10^{5}-10^{-2} frequency range, applying ±10 mV AC signal amplitude, with DC Voltage (V) set to 0 (E_{ocp}) and Points/decade set to 10. To simulate aggressive corrosion conditions, the only

alteration made to the aforementioned test parameters was adjusting the DC voltage (V) value, which was designated as 0.1 (E_{ocp}).

6.6 Microbiologically Influenced Corrosion Tests

6.6.1 Preparation of Test Specimens

For MIC tests, specimens measuring 1x1 cm and comprising 7075 AA, bulk Cu, CA, CNZA15, CNZA30 and CZA coatings were prepared. These specimens underwent sterilization using UV light before being utilized in the tests. Notably, for the specific objectives of this study, a relative comparison of corrosion resistance between coating and bulk configurations was designed. This involved the inclusion of bulk Cu in MIC tests, alongside Cu-based coatings produced through the CGDS process.

6.6.2 Preparation and Revitalization of Microorganisms

Several reports documenting corrosion-induced deterioration in military or civilian aircraft have indicated an association with microbial growth stemming from contamination within fuel storage tanks and aircraft wing tanks (Nelson et al., 2017). Hence, organisms that perceive the environment within jet fuel as a source of nourishment and habitat were considered. In the study conducted by Graef, (2003), prevalent microorganisms thriving in the jet fuel environment are enumerated in Table 6.2.

Table 6.2 Microorganisms commonly observed in the jet fuel environment (Graef, 2003).

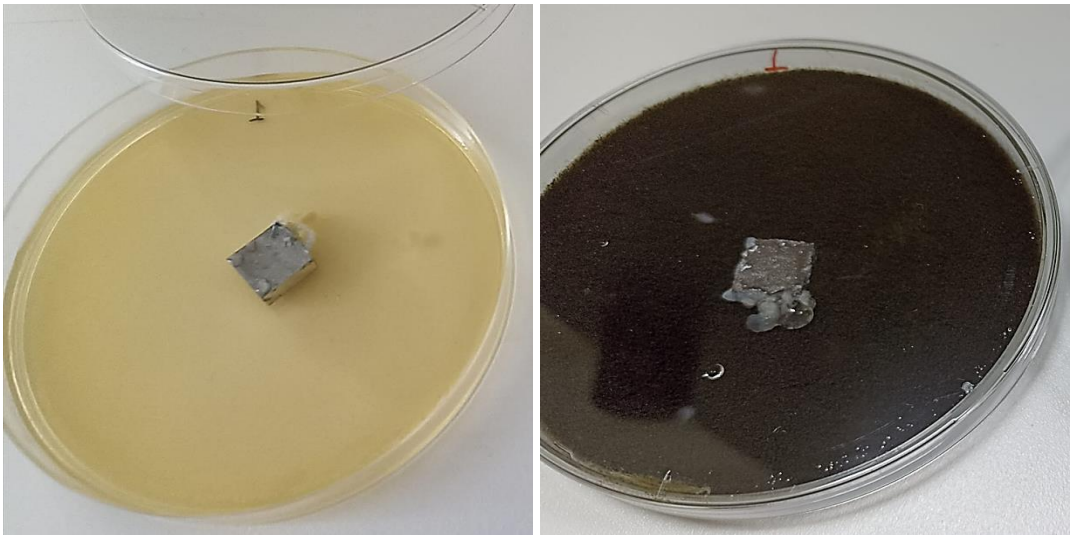
Bacteria	**Fungi**	**Yeast**
Bacillus	*Hormoconis resinae*	*Candida*
Micrococcus	*Aspergillus*	
Pseudomonas	*Fusarium*	
Arthrobacter	*Penicillum*	

Taking into account the bacteria and fungi listed in Table 6.2, reference strains were selected for the corrosion tests: *Pseudomonas aeruginosa* ATCC 15442, a gram-

negative bacterium and *Aspergillus niger* ATCC 6275, a fungus species. *P. aeruginosa* was cultivated in Trytic Soy Agar (TSA, Merck, pH: 7.3) medium at 37 °C for 24 hours, and the suspension was prepared using phosphate buffer (PBS, pH: 7.2). The suspension density was adjusted to a 0.5 McFarland value using a densitometer. *A. niger* was cultured on Malt Extract Agar (MEA, Merck, pH: 5.6) medium at 25 °C for 7 days and a spore suspension was prepared using a hemocytometer at a concentration of 10^6 spores/mL.

6.6.3 Assessment of Microbiologically Influenced Corrosion Tests

From the *P. aeruginosa* suspension, 100 µL was transferred to previously poured and solidified TSA plates, while from the *A. niger* spore suspension, 100 µL was transferred to MEA plates using an L-spreader. The suspensions were left at room temperature for 30 minutes to allow for diffusion into the medium. Subsequently, sterile specimens were placed at the center of the plates and the plates containing bacterial samples were incubated at 37 °C, while those containing fungus samples were incubated at 25 °C for a period of 4 weeks. After incubation, the specimens were cleaned of organism and medium residues. The presence and severity of MIC were evaluated visually. The bacterial and fungus containing plates used during these tests are illustrated in Figure 6.7.



(a) **(b)**

Figure 6.7 Petri dish specimens: **(a)** *P. aeruginosa* growth medium and **(b)** *A. niger* growth medium

6.7 Wear Tests

The investigation into the wear characteristics of both uncoated and coated substrates employed a linear reciprocating ball-on-flat configuration, as illustrated in Figure 6.8. In this experimental setup, a spherically ended upper specimen, typically in the form of a ball-shaped specimen, interacts with a flat lower specimen as it slides against the ball specimen. The ball is securely affixed and a vertical load is applied through the ball specimen onto the horizontally oriented flat specimen. The latter undergoes a reciprocating motion, moving back and forth under predetermined conditions such as sliding velocity, sliding distance and stroke length. During the test, the friction force is determined by measuring the deflection of the elastic arm through an inductive displacement transducer. This friction force data is essential for calculating the friction coefficient. The obtained friction coefficient data play a crucial role in evaluating transitions in wear behavior, as these transitions are often correlated with variations in friction. This experimental approach provides valuable insights into the dynamic interplay between the sliding surfaces, contributing to a comprehensive understanding of wear mechanisms and behavior in both uncoated / coated substrates.

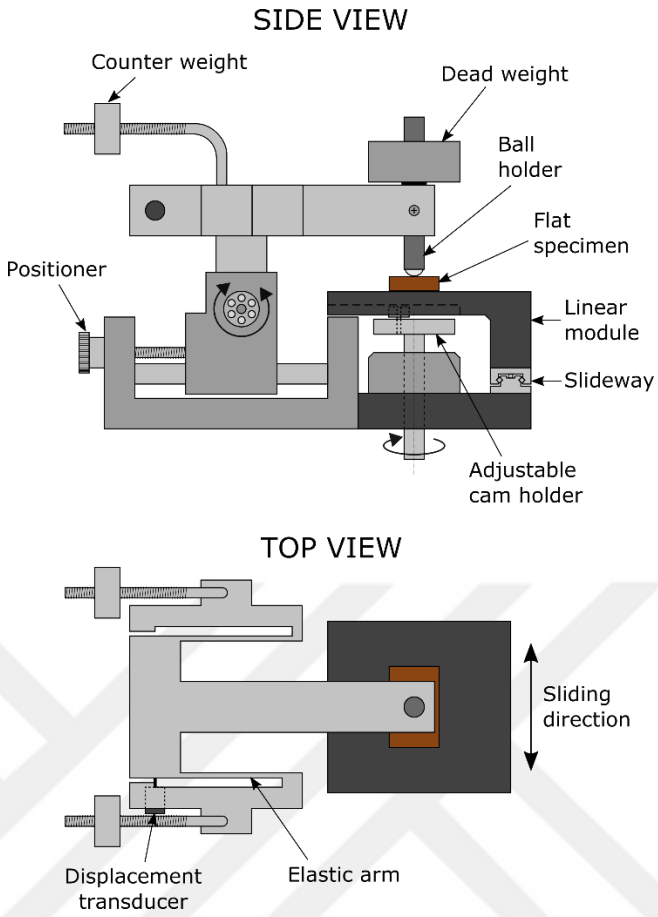


Figure 6.8 CSM instruments standard tribometer configuration utilized in wear tests (Tekin,2016)

In this investigation, the CSM Instruments standard tribometer was employed for conducting linear reciprocating wear tests. Prior to the wear test, the specimens underwent ultrasonic cleaning in ethanol for ten minutes, followed by drying in hot air. Dry sliding wear tests were conducted with a constant sliding speed of 0.04 m/s under a 1 N load. The stroke length and total sliding distance were set at 10 mm and 100 m, respectively. Wear tests utilized 6 mm diameter balls made of AISI 52100 (100Cr6) steel. To assess the wear behavior of coated and uncoated substrates under lubricating conditions, sliding wear tests were repeated using Lubcon Turmotemp II/400 KL, a high-temperature grease containing PTFE and perfluorinated polyether, under similar test conditions. After wear tests, the specimens were once again ultrasonically cleaned in ethanol for ten minutes and dried in hot air. Following the wear tests, material loss for both coated and uncoated substrates was estimated from the wear track profile using a stylus profilometer. The wear volume of the ball

specimen exhibiting flat wear marks was calculated using equations 6.3 and 6.4, where d represents the wear scar diameter and r represents the ball radius.

$$Volume\ Loss, V_p = \left(\frac{\pi h}{6}\right) . \left(\frac{3d^2}{4} + h^2\right) \tag{6.3}$$

$$h = r - \left(r^2 - \frac{d^2}{4}\right)^{\frac{1}{2}} \tag{6.4}$$

CHAPTER SEVEN
RESULTS

7.1 Characterization of Coating Powders

The parameters such as particle size, morphology and the percentage composition of components within coating powders play a crucial role in both the CGDS process and the final product properties. These parameters and the effects induced by coating powders are comprehensively elucidated in the literature section titled "Surface Modification by Cold Gas Dynamic Spray Process." This study meticulously focuses on the properties of powders used in coating production, conducting particle size distribution analysis, as well as SEM and XRD analyses. The obtained results and findings are systematically evaluated within the framework of the following headings.

7.1.1 Particle Size Distribution Analysis

Particle size distribution analyses were conducted through a minimum of three repeated measurements and the particle size distribution graphs for coating powders are presented in Figure 7.1. The average particle size values for CA, NZA, CNZA15, CNZA30 and CZA coating powders were determined as 25.30 μm, 27.28 μm, 25.68 μm, 26.81 μm and 22.33 μm, respectively. These results indicate that the coating powders exhibit particle size distribution ranges consistent with the requirements of the CGDS process. Additionally, it was observed that the highest particle size was measured in NZA powder, while the lowest was in CZA powder.

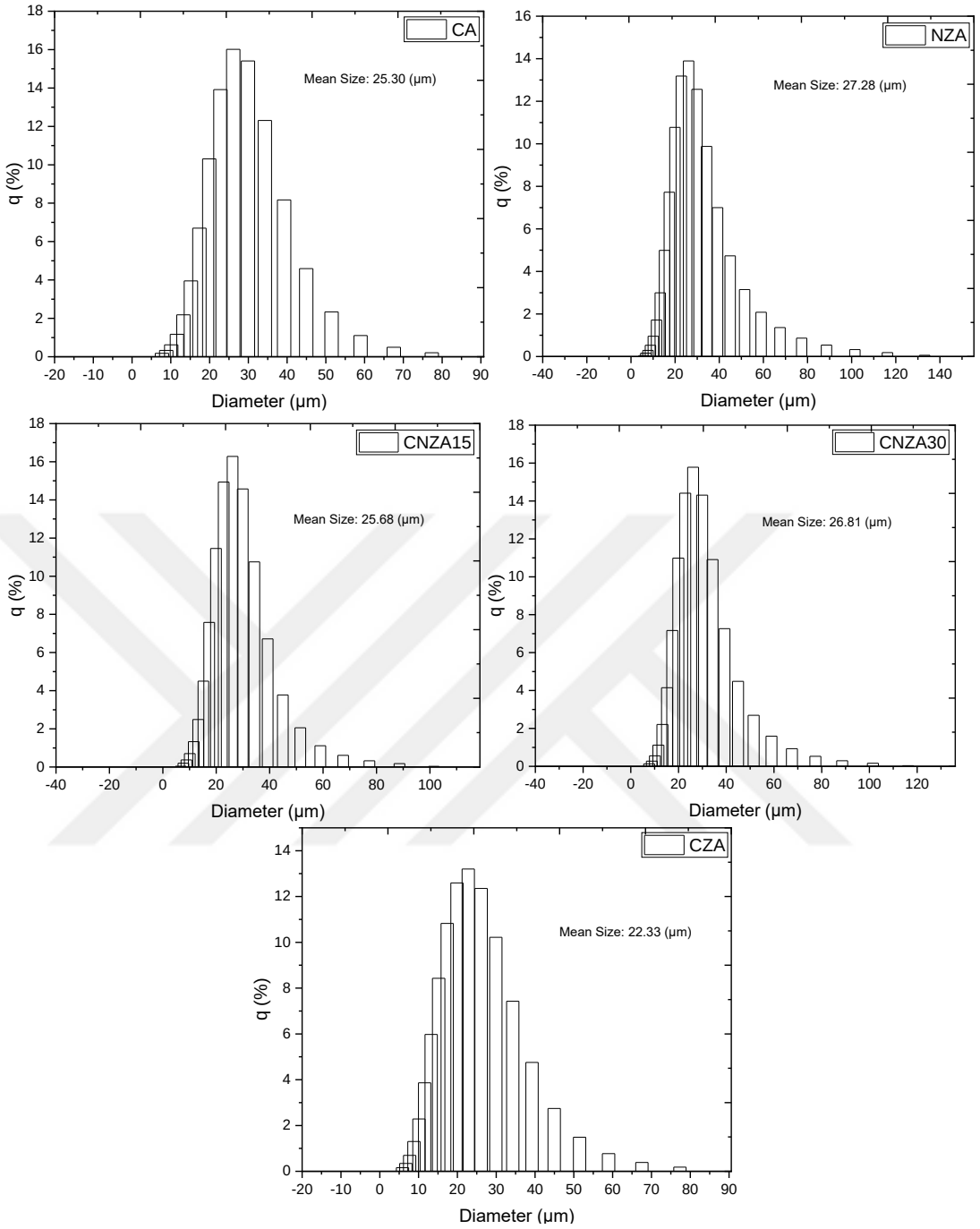
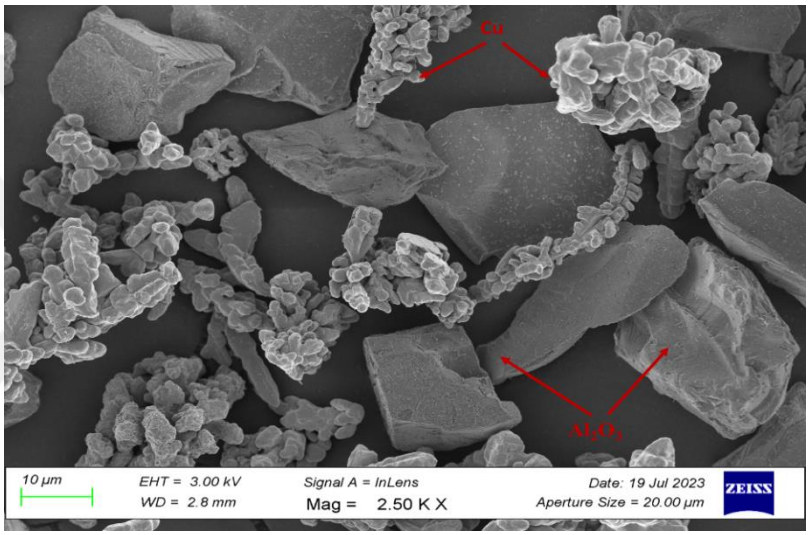


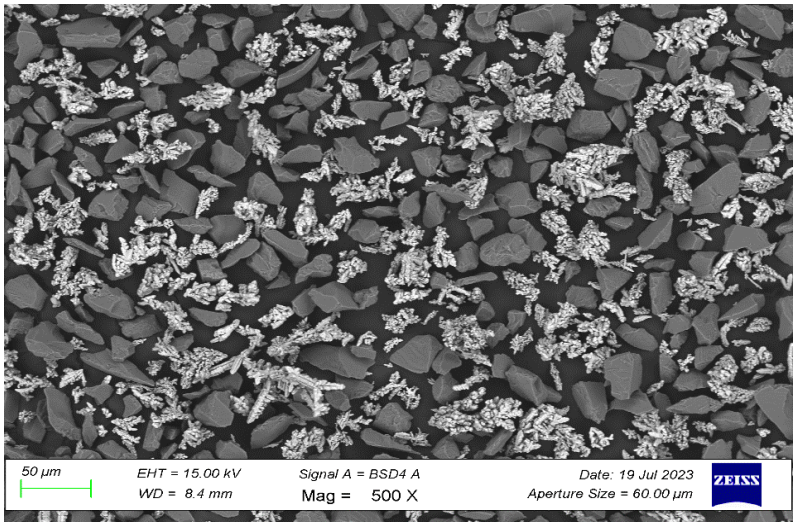
Figure 7.1 Particle size distribution graphs of coating powders

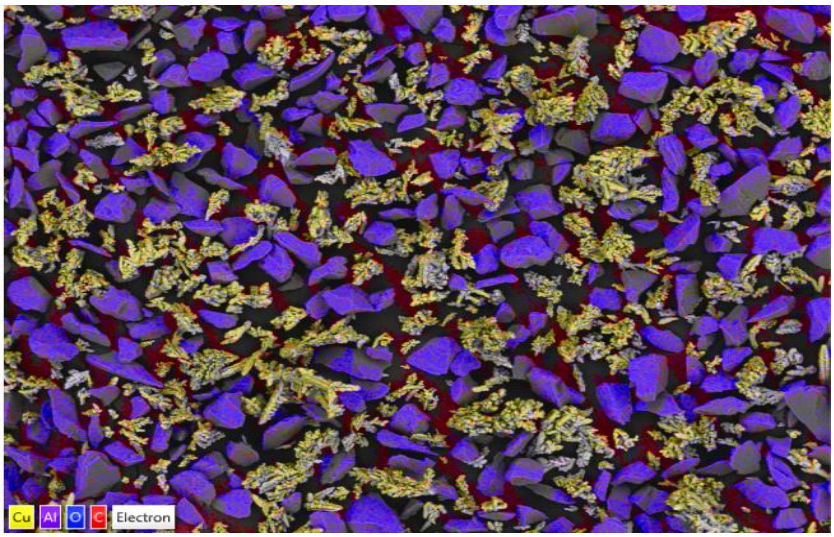
7.1.2 SEM Analysis

The morphologies of coating powders were determined through SEM examinations using SE and BE methods. Additionally, semi-quantitative elemental analysis was performed through EDS analyses, allowing for the approximate determination of the

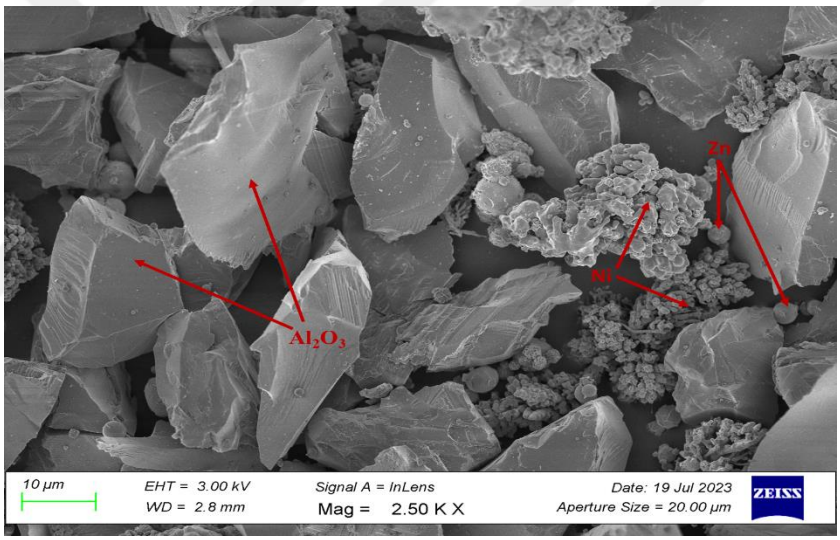
distribution ratios of components within the composition, thereby confirming the powder morphologies. Images from SEM analyses and EDS mapping outputs are presented in Figure 7.2. The conducted studies revealed that each coating powder component possesses a distinct morphology and material types were identified through EDS analyses. In this context, it was determined that copper exhibits a dendritic morphology, alumina displays an angular morphology, nickel features a spongy morphology and zinc possesses a spherical morphology.

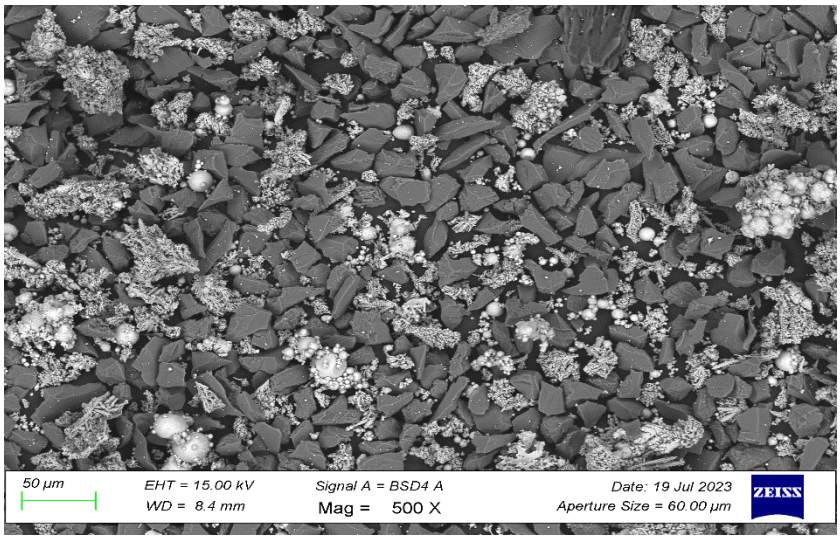


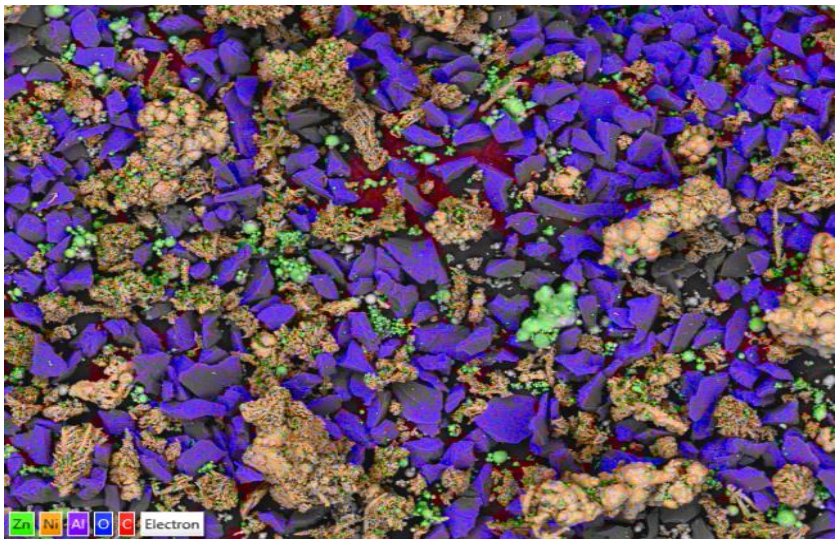



Cu
Al
O
C
Electron

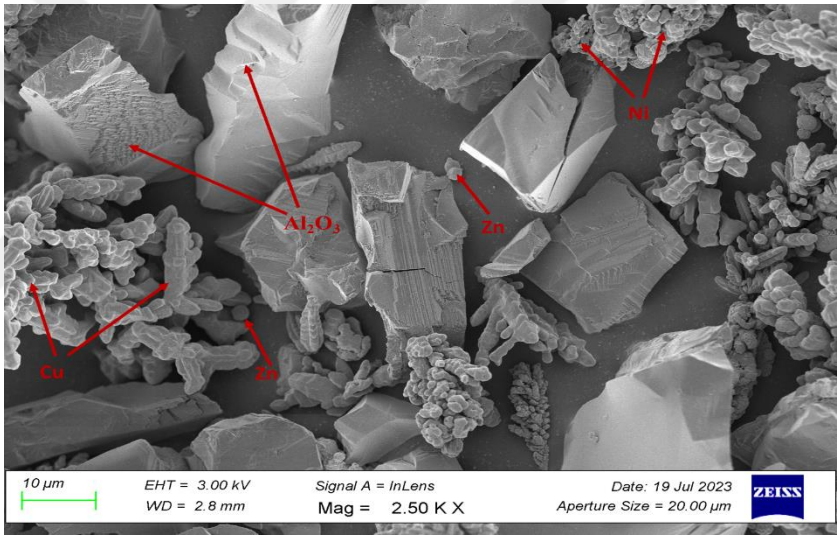
(a)

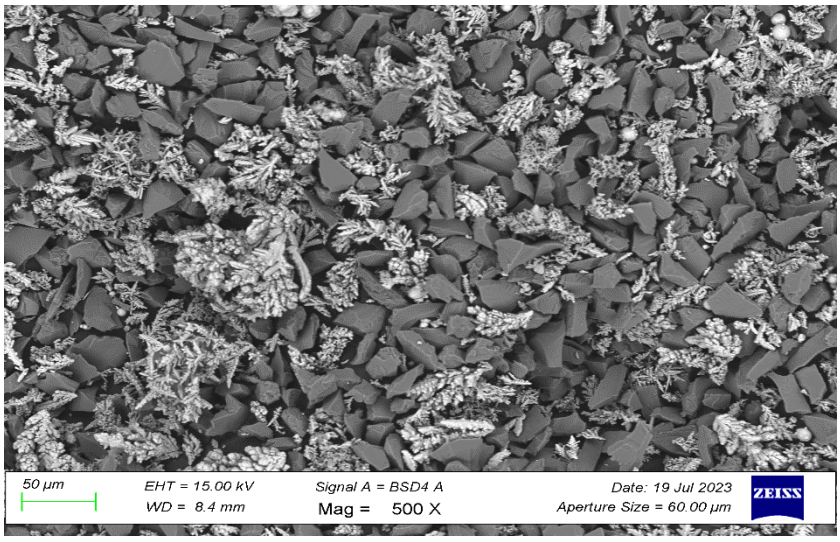

Zn
Ni
Al_2O_3
10 µm
EHT = 3.00 kV
WD = 2.8 mm
Signal A = InLens
Mag = 2.50 K X
Date: 19 Jul 2023
Aperture Size = 20.00 µm
ZEISS

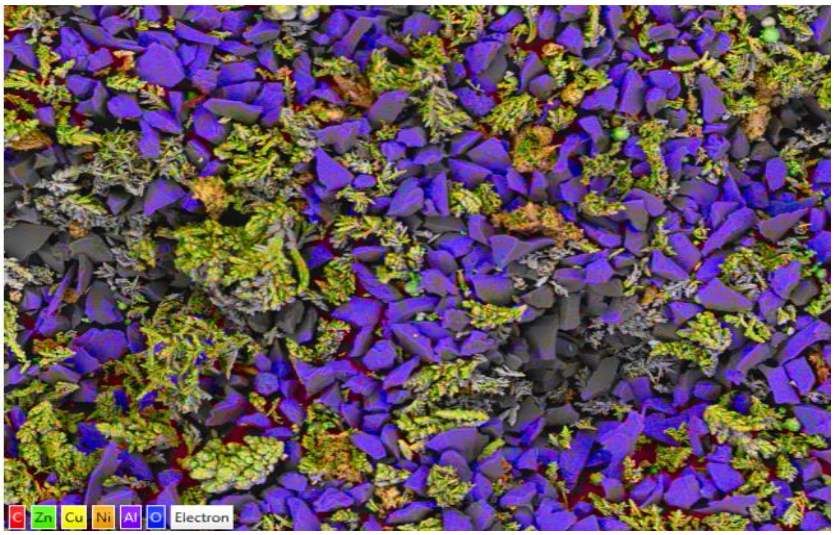

50 µm
EHT = 15.00 kV
WD = 8.4 mm
Signal A = BSD4 A
Mag = 500 X
Date: 19 Jul 2023
Aperture Size = 60.00 µm
ZEISS


Zn
Ni
Al
O
C
Electron

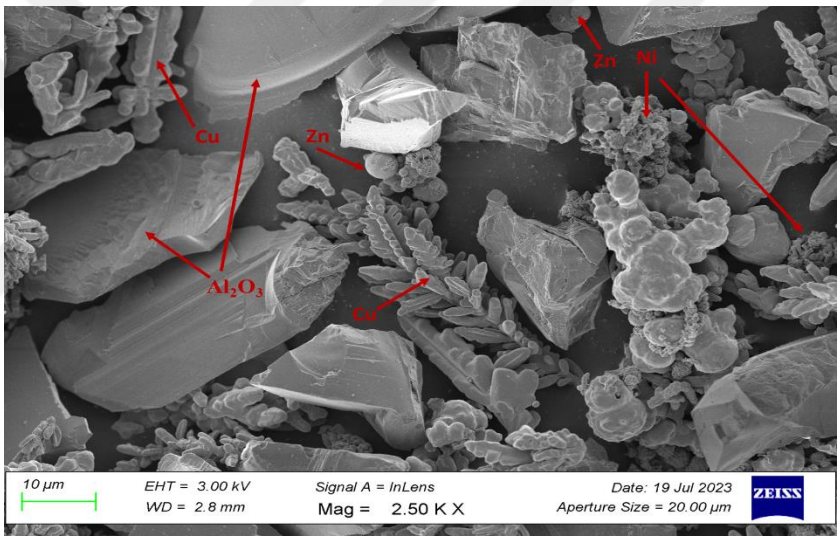
(b)

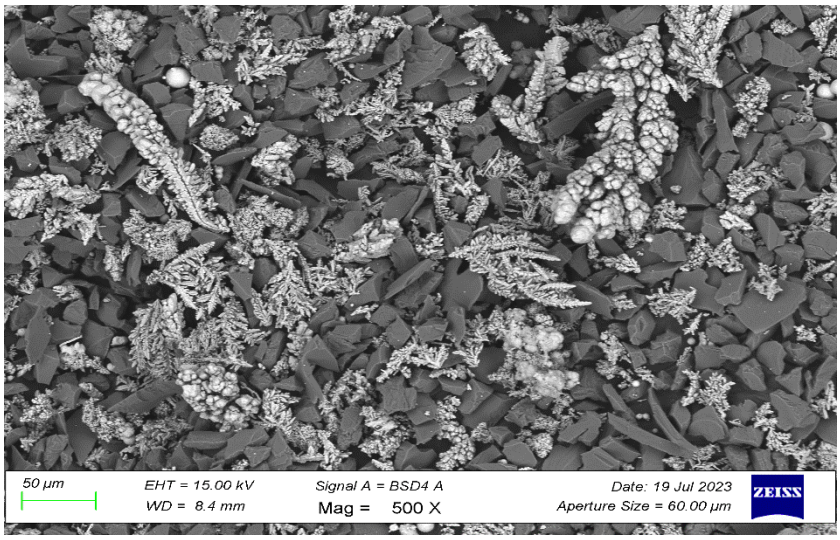

Ni
Al_2O_3
Zn
Cu
Zn
10 µm
EHT = 3.00 kV
WD = 2.8 mm
Signal A = InLens
Mag = 2.50 K X
Date: 19 Jul 2023
Aperture Size = 20.00 µm
ZEISS

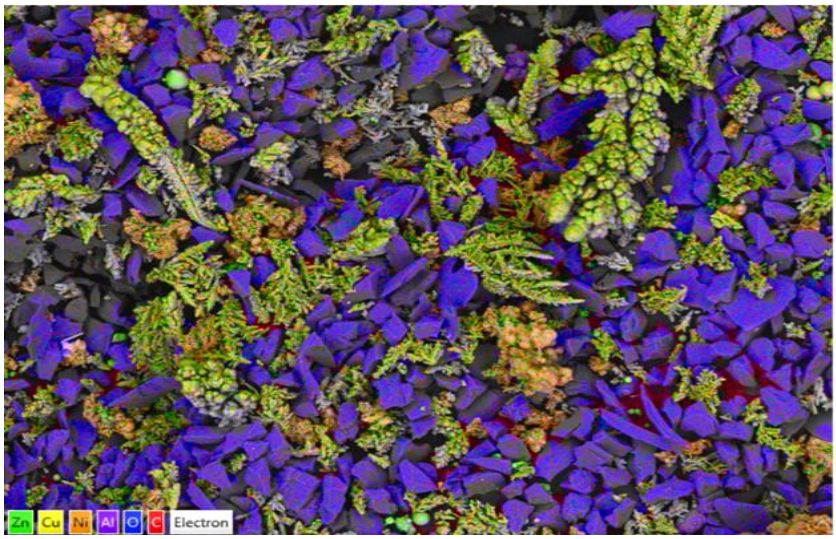

50 µm
EHT = 15.00 kV
WD = 8.4 mm
Signal A = BSD4 A
Mag = 500 X
Date: 19 Jul 2023
Aperture Size = 60.00 µm
ZEISS


C
Zn
Cu
Ni
Al
O
Electron

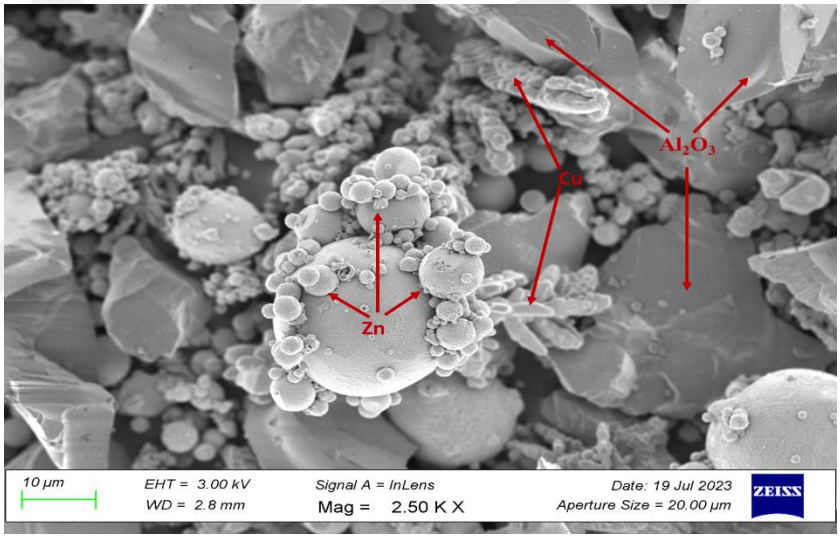
(c)

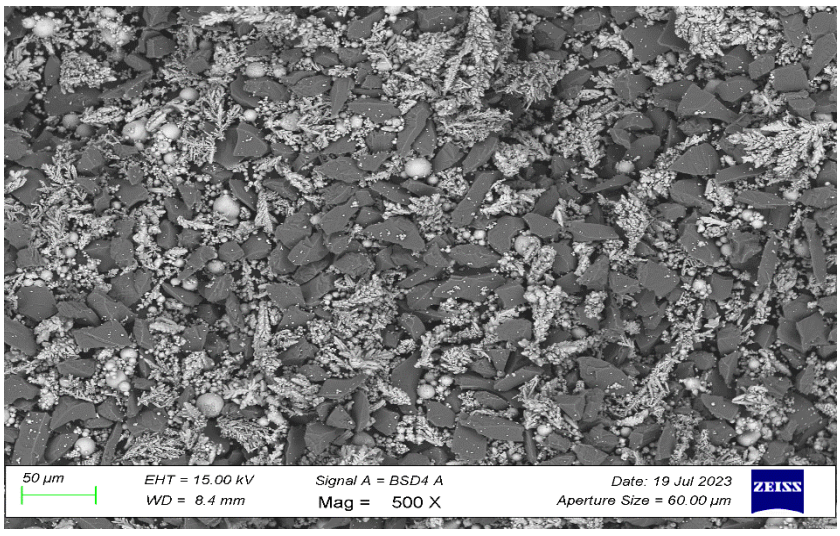

Zn
Ni
Cu
Zn
Al_2O_3
Cu
10 µm
EHT = 3.00 kV
WD = 2.8 mm
Signal A = InLens
Mag = 2.50 K X
Date: 19 Jul 2023
Aperture Size = 20.00 µm
ZEISS

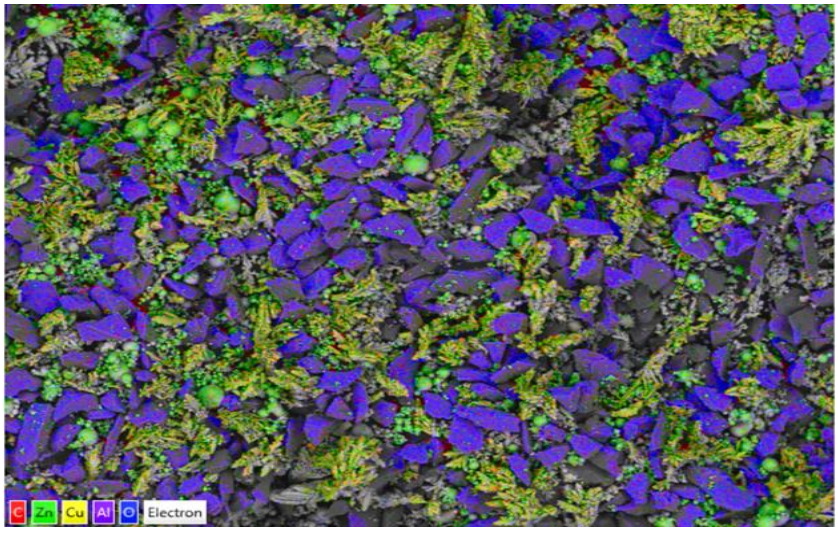

50 µm
EHT = 15.00 kV
WD = 8.4 mm
Signal A = BSD4 A
Mag = 500 X
Date: 19 Jul 2023
Aperture Size = 60.00 µm
ZEISS


Zn
Cu
Ni
Al
O
C
Electron

(d)


Al_2O_3
Cu
Zn
10 µm
EHT = 3.00 kV
WD = 2.8 mm
Signal A = InLens
Mag = 2.50 K X
Date: 19 Jul 2023
Aperture Size = 20.00 µm
ZEISS


50 µm
EHT = 15.00 kV
WD = 8.4 mm
Signal A = BSD4 A
Mag = 500 X
Date: 19 Jul 2023
Aperture Size = 60.00 µm
ZEISS



(e)

Figure 7.2 SEM images and EDS mapping outputs of coating powders: **(a)** CA, **(b)** NZA, **(c)** CNZA15, **(d)** CNZA30 and **(e)** CZA

The results of point EDS studies conducted on coating powders have confirmed the morphology of each component present in the powder compositions. The analysis output for the CNZA30 powder, encompassing all components, is presented in Figure 7.3 for illustrative purposes.

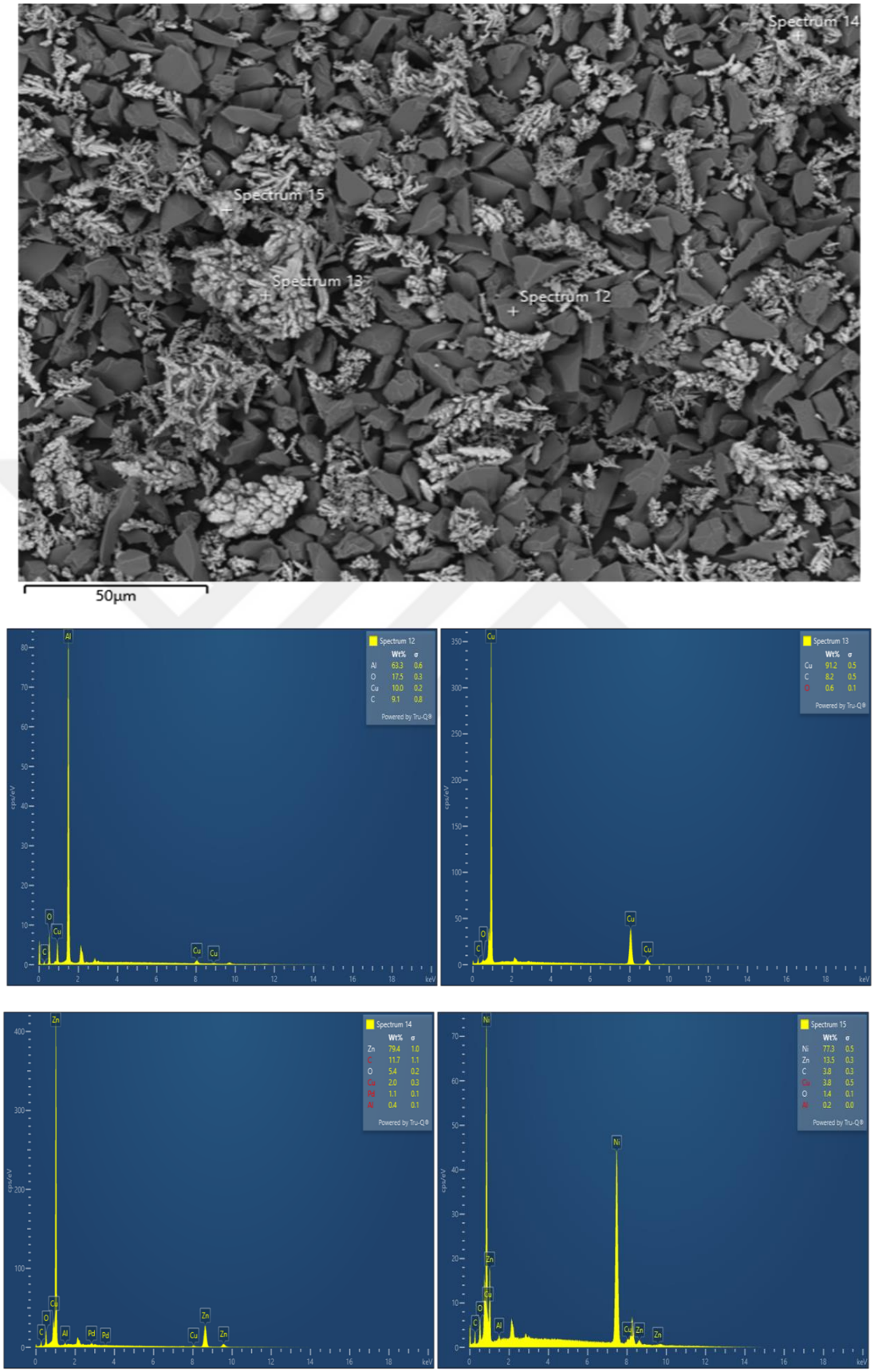


Figure 7.3 Results of point EDS analysis for CNZA30 powder

7.1.3 Phase Analysis

The XRD patterns of coating powders are presented in Figure 7.4. All patterns exhibited matches consistent with the analyzed composition and no unexpected phases were detected. Dominant phases in all coating powders, except for NZA powder, were identified as Cu and Al_2O_3. In NZA powder, the dominant phases were found to be Ni and Al_2O_3. Additionally, as anticipated, Ni phase was detected in CNZA15 and CNZA30 powders, while Zn phase reached significant intensity values in CZA powder.

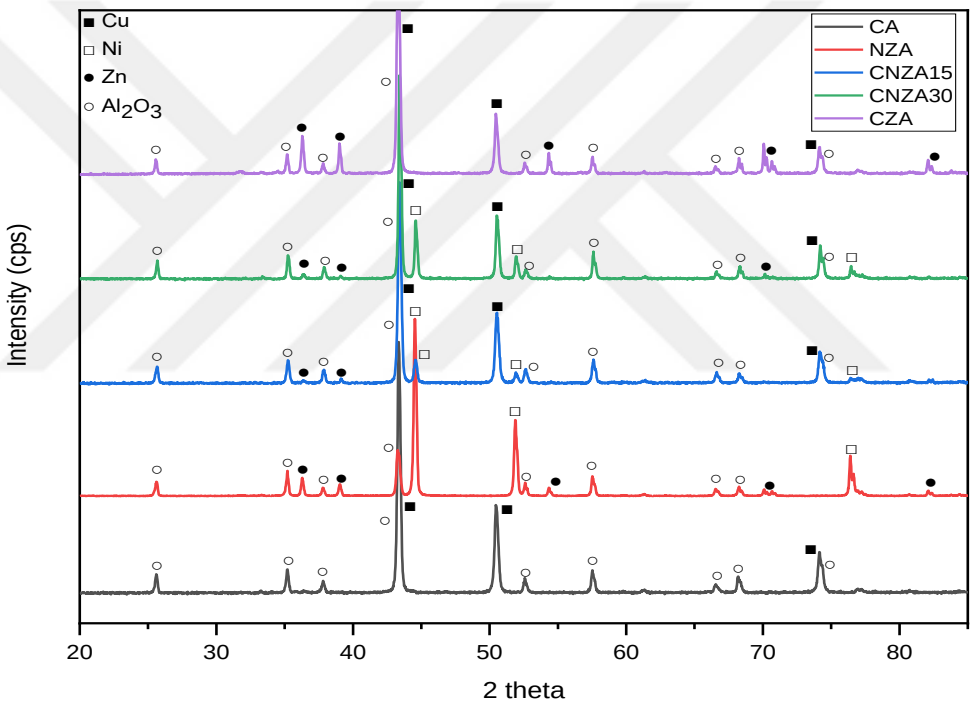


Figure 7.4 XRD patterns of coating powders

Quantitative analyses were conducted on coating powders to compare with the manufacturer's specifications. The percentage ratios of components within the powder composition were determined and presented in Table 7.1. The obtained results indicate that the ingredients and their percentage ratios in the coating powders are consistent with the manufacturer's specifications.

Table 7.1 Quantitative analysis results for coating powders.

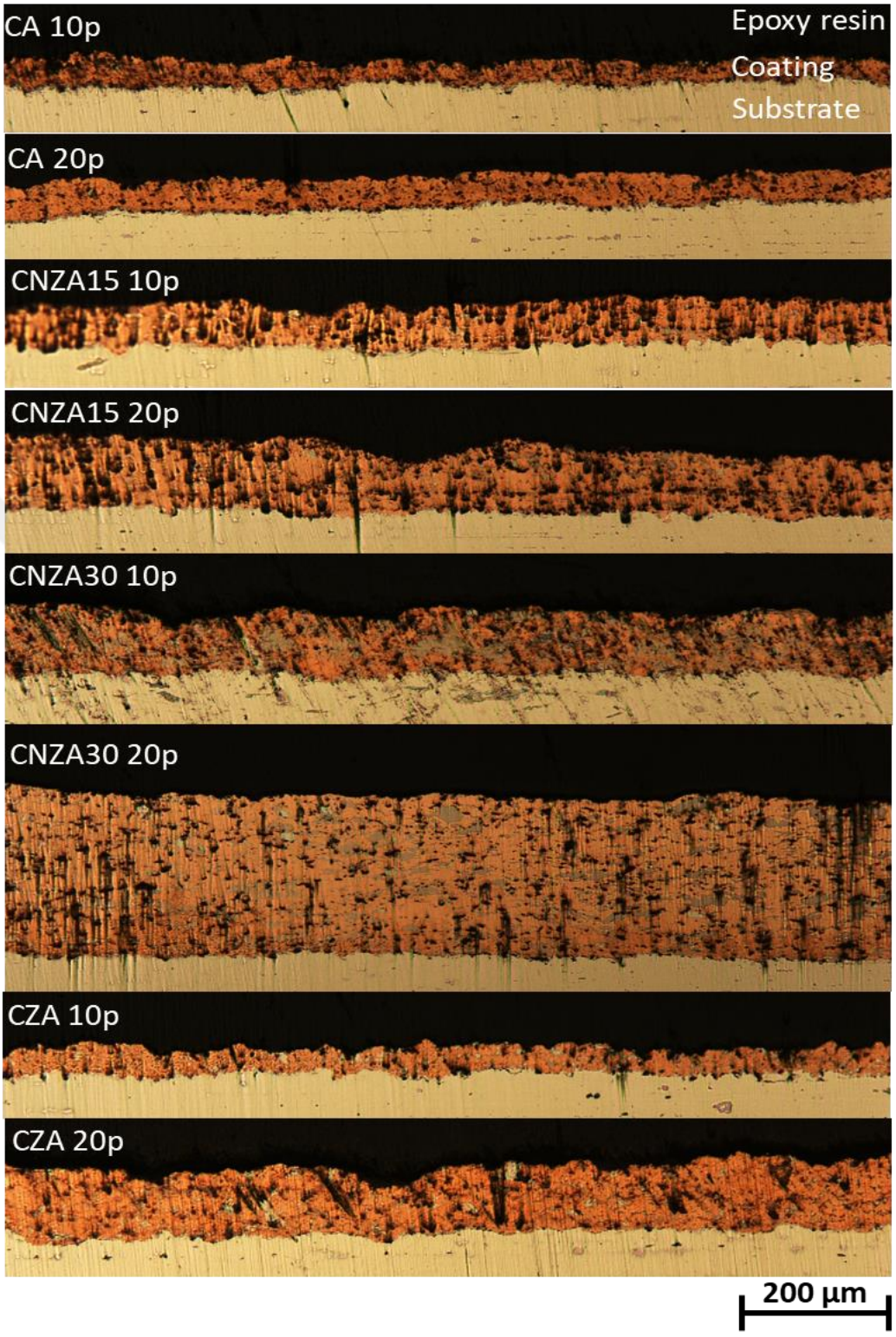
Coating powder	Powder ingredient (%)			
	Cu	Ni	Zn	Al_2O_3
CA	50	-	-	50
NZA	-	50	10	40
CNZA15	42.5	6	1.7	49.8
CNZA30	37.7	14.7	2.3	45.3
CZA	35	-	25	40

7.2 Characterization of Cu Based MMC Coatings

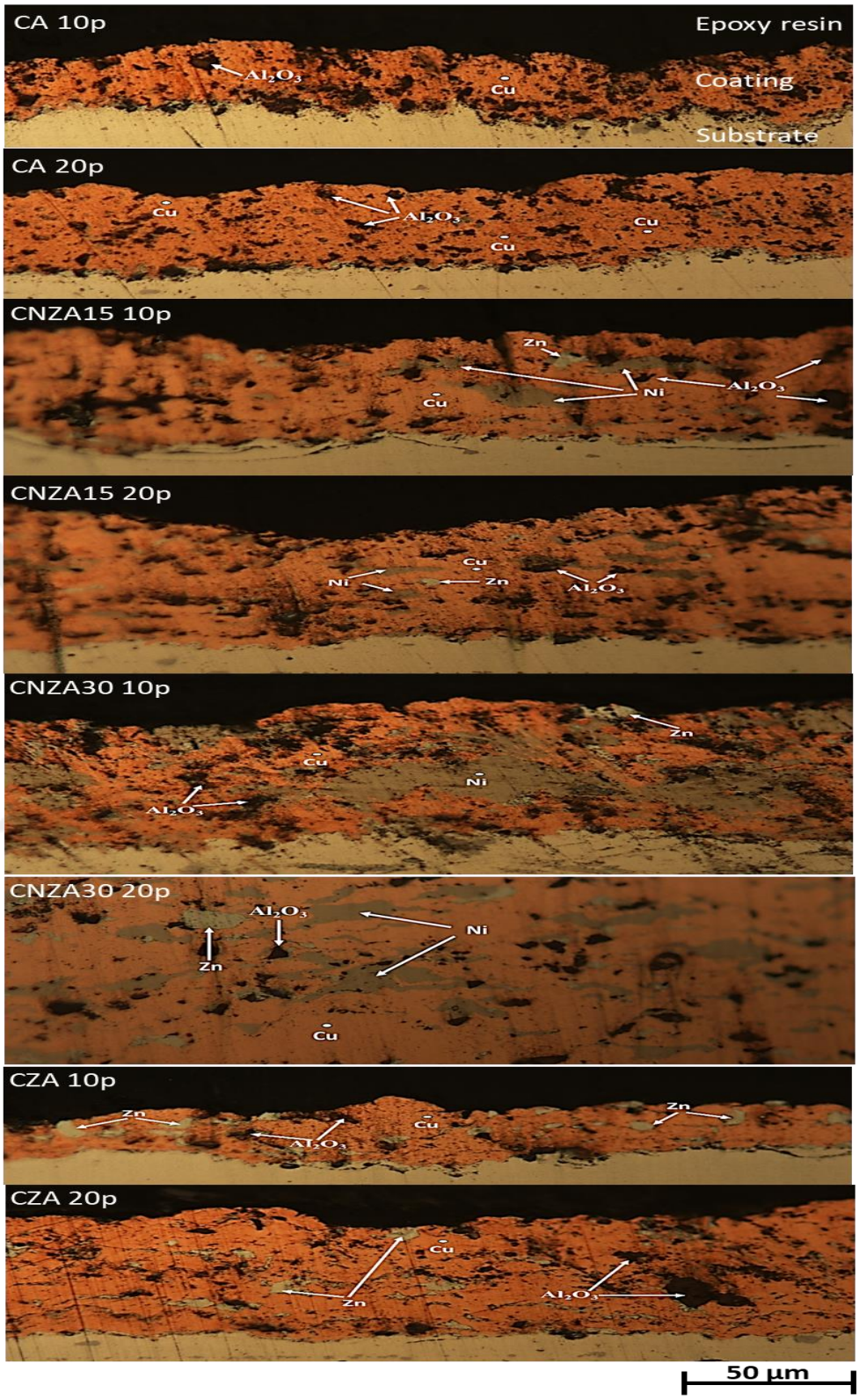
In this section, the results and findings of analyses, including OM, SEM, Vickers Hardness, Scratch Test, XRD and Surface Profilometry, conducted on 8 different Cu-based MMC coatings produced within the scope of the thesis, have been thoroughly examined under the following headings.

7.2.1 Microstructural Investigation and Coating Thickness Measurement

In this study, OM examinations were conducted at magnification ratios of 100x, 200x and 500x, while SEM examinations were performed at magnification ratios of 500x, 1000x and 2500x. For illustrative purposes, images at 100x and 500x magnification ratios for OM examinations and at 1000x magnification ratio for SEM examinations are presented in Figures 7.5 and 7.6, respectively. Microstructure formations of metal and ceramic components in the coating powder were identified based on regions of different colors in the images. The results indicated that the dominant metal matrix in the coating microstructures is copper and Al_2O_3 particles are uniformly distributed in the metal matrix. Furthermore, microscopic examinations of cross-sections revealed that the lowest surface porosity was observed in CA coatings, while the highest surface porosity was observed in CZA coatings. Zhu et al., (2020) conducted research on Al-Zn-Cu composite coatings with varying Cu content and found that increasing Cu content reduced coating porosity. Additionally, it was determined that with an increase in the number of spraying steps, surface porosity in coatings decreased due to the peening effect.


CA 10p
Epoxy resin
Coating
Substrate
CA 20p
CNZA15 10p
CNZA15 20p
CNZA30 10p
CNZA30 20p
CZA 10p
CZA 20p
200 µm

(a)



(b)

Figure 7.5 Cross-sectional OM images of Cu-based coatings **(a)** 100x and **(b)** 500x magnification

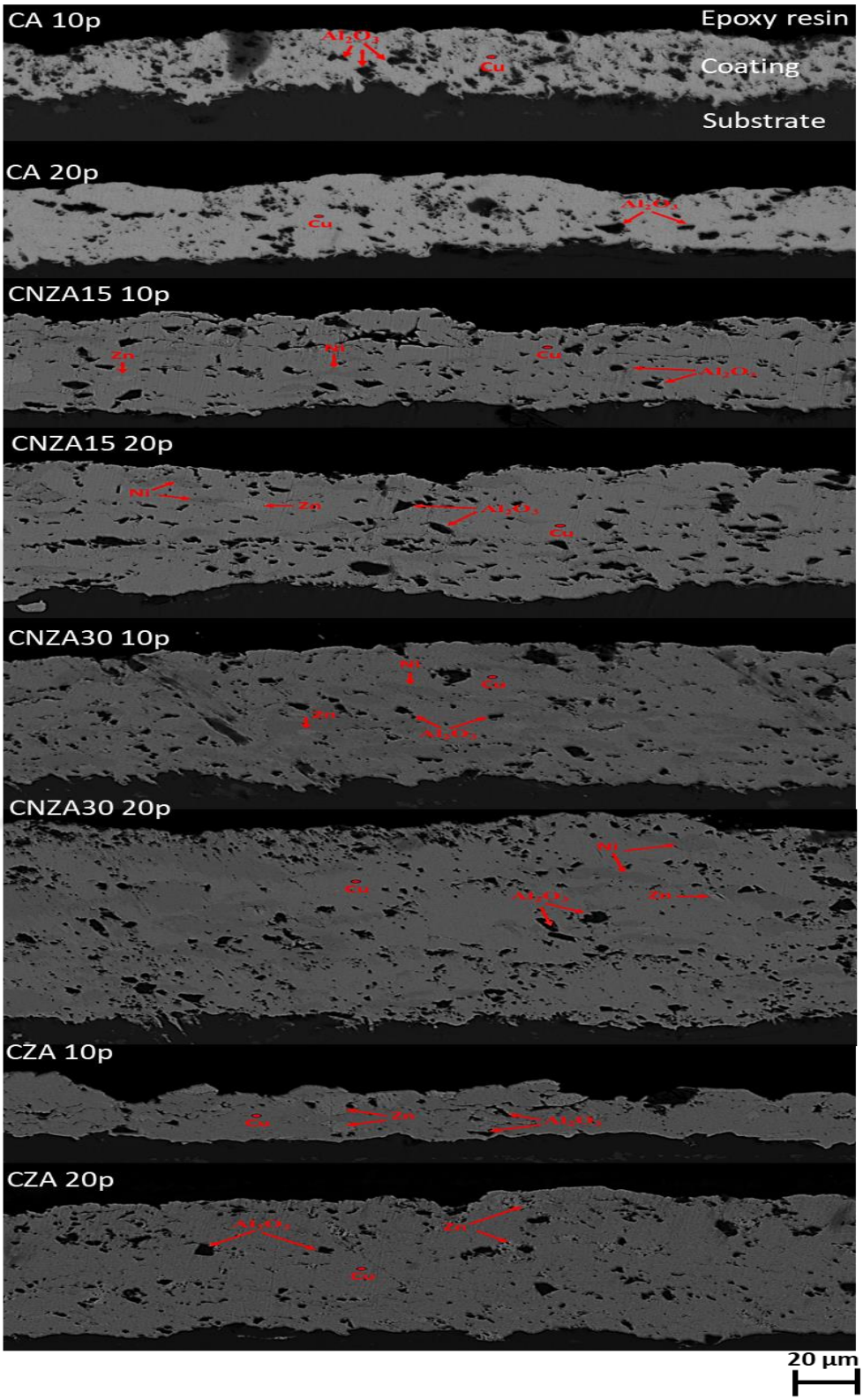
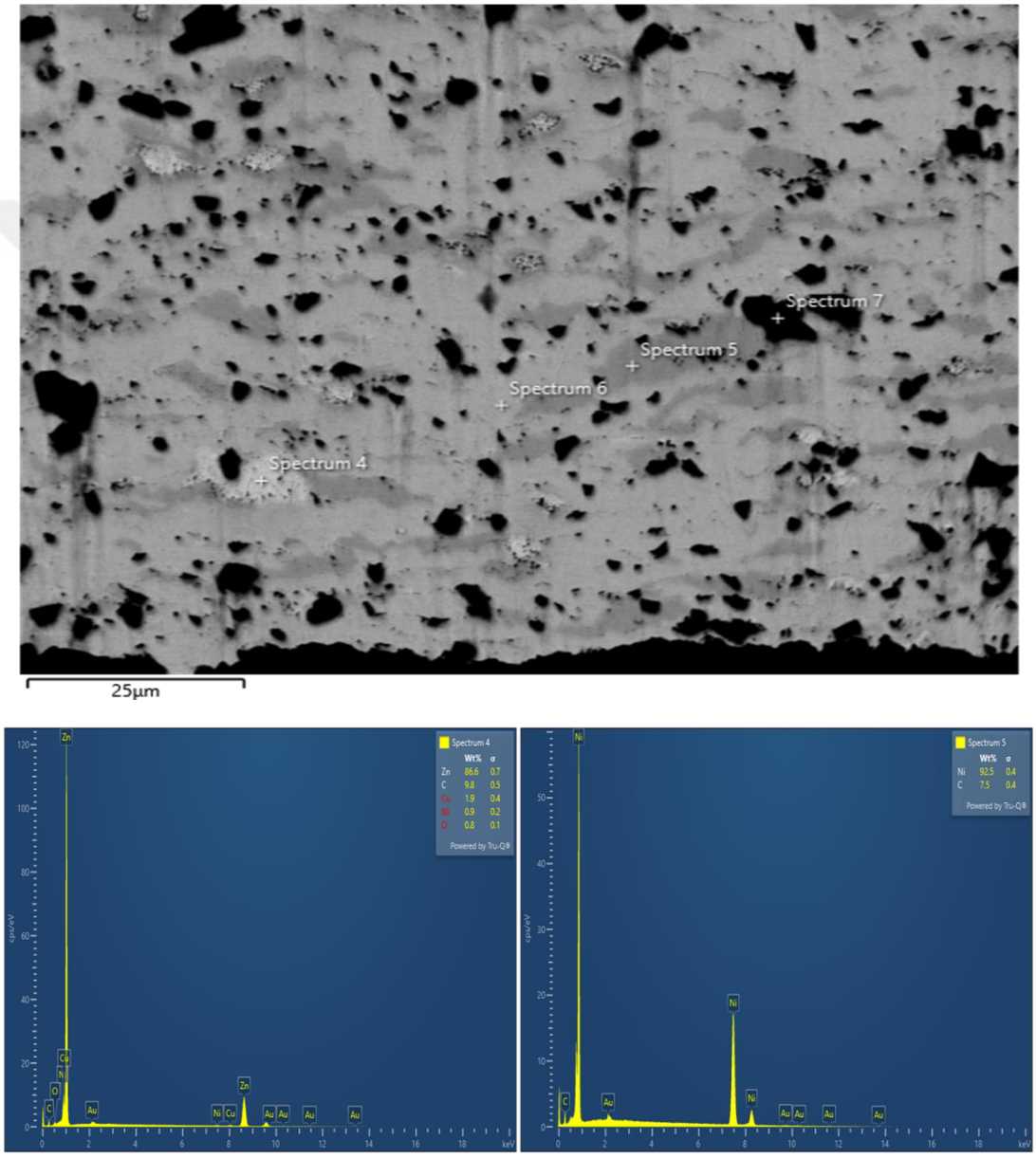


Figure 7.6 Cross-sectional SEM images of the Cu-based coatings at 1000x magnification

Furthermore, point EDS studies were conducted concerning the characterized coatings and the components corresponding to different colored regions observed in the microstructure examinations were identified. For illustrative purposes, the analysis output for the CNZA30 20p coating, encompassing all microstructure components in different colors, is presented in Figure 7.7.



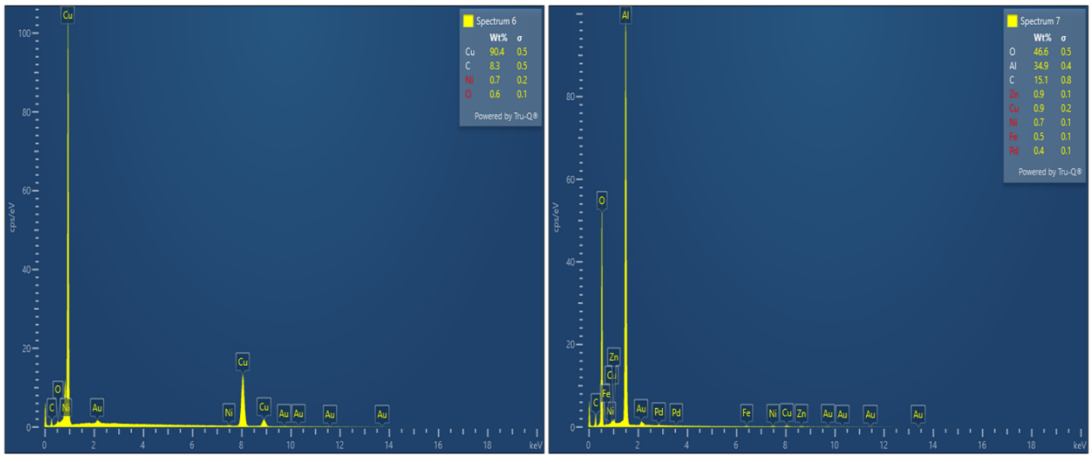


Figure 7.7 Results of point EDS analysis for CNZA30 coating

Concerning coating thicknesses, measurements were taken from 7 different regions in both OM and SEM examinations and the results of these measurements are presented in Table 7.2, including maximum, minimum and average values. When evaluating the coating thicknesses, it was observed that the highest coating thicknesses were obtained in CNZA coatings. This observation is particularly associated with the positive contribution of nickel in the NZA powder added to the CA powder, which, during coating production, embeds into the Cu matrix with relatively lower hardness, thereby contributing to an increase in coating thickness. Additionally, it was determined that the coating thickness varies proportionally with the number of spraying steps and similar findings have been reported in the literature (Celotto et al., 2007; Xiong et al., 2015).

Table 7.2 Thickness measurement results for Cu-based coatings.

Coating	**Thickness Measurements (µm)**		
	Min.	Max.	Avg.
CA 10p	32.0±1.3	49.0±1.2	38.5
CA 20p	46.5±1.6	54.7±1.3	51.0
CNZA15 10p	54.0±1.8	76.0±1.5	70.0
CNZA15 20p	86.1±2.3	116.9±2.5	100.1
CNZA30 10p	79.2±1.9	99.9±1.9	92.2
CNZA30 20p	273.4±2.9	284.0±2.7	277.4
CZA 10p	30.2±0.9	49.6±1.2	37.4
CZA 20p	79.8±2.1	96.8±1.7	89.3

7.2.2 Measurement of Hardness

One of the significant mechanical properties of cold-sprayed coatings is their hardness and these hardness values are closely related to the durability of coatings in tribological applications. The hardness of materials is determined by intrinsic material properties such as grain size, porosity, purity and phase composition, as well as other experimental factors like applied load and temperature. In this study, cross-sectional microhardness values were determined using a Vickers hardness testing machine based on measurements taken from at least 5 different regions. The most significant challenge encountered during hardness measurements was identified as the difference in distribution of the soft metal matrix and the hard ceramic particle, where the indentation hit. Therefore, it was observed that dramatic regional changes could occur in the measurement values. The minimum, maximum and average values for these measurements are provided in Table 7.3. The highest hardness values were obtained in CNZA coatings, attributed to the presence of the Ni component in the coating; the lowest values were found in CZA coatings. Hardness values for all coatings except CNZA30 coatings were below the hardness value of the 7075 AA used as the substrate material. When examining theoretical hardness values found in the literature for Cu-based cold-sprayed coatings, it was observed that the hardness values varied between 110-180 HV. These results confirm that Ni-containing coatings exhibit higher hardness values (H. Chen et al., 2022; L. Zhang et al., 2019).

Table 7.3 Vickers hardness values for the substrate and Cu-based coatings.

Specimen	**$HV_{0.025}$**		
	Min.	Max.	Avg.
7075 AA	179±4.1	186±4.5	183
CA 10p	141±2.7	150±3.3	145
CA 20p	146±2.6	154±3.5	150
CNZA15 10p	145±2.6	157±3.5	151
CNZA15 20p	144±2.1	173±4.1	158
CNZA30 10p	165±3.1	210±4.8	187
CNZA30 20p	166±3.3	218±4.7	192
CZA 10p	82±1.5	92±1.6	87
CZA 20p	95±1.7	103±1.9	99

7.2.3 Scratch Test

In the scratch test, the critical load value representing a specific, well-defined and recognizable damage event, is determined through the analysis of scratch tracks under an optical microscope. The bright regions observed in the optical microscope images of scratch tracks correspond to the spallation of the coating. In conjunction with image analysis, data graphics such as tangential force, acoustic emission and penetration depth are also employed to ascertain the critical load values. Data graphs and optical microscope images of scratch tracks created on coatings with incremental loading up to a maximum of 150 N are presented in Figures 7.8 and 7.9, respectively. When data graphs and OM examinations of Cu-based coatings are simultaneously evaluated, it is observed that the coatings either stripping, chipping or partial tearing at a certain distance. Based on this information, distance and critical load (Lc) values were determined for each coating and indicated in the data graphs with vertical lines.

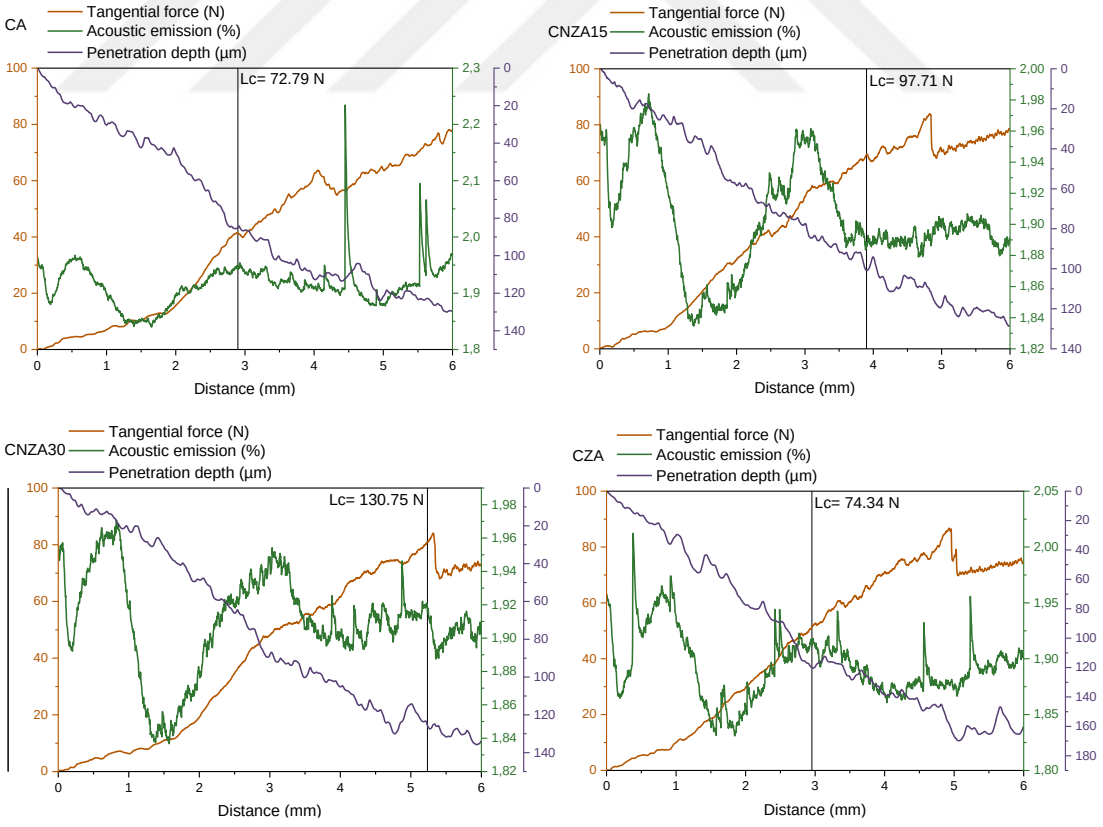


Figure 7.8 Graphical presentation of data obtained from scratch tests on Cu-based coatings

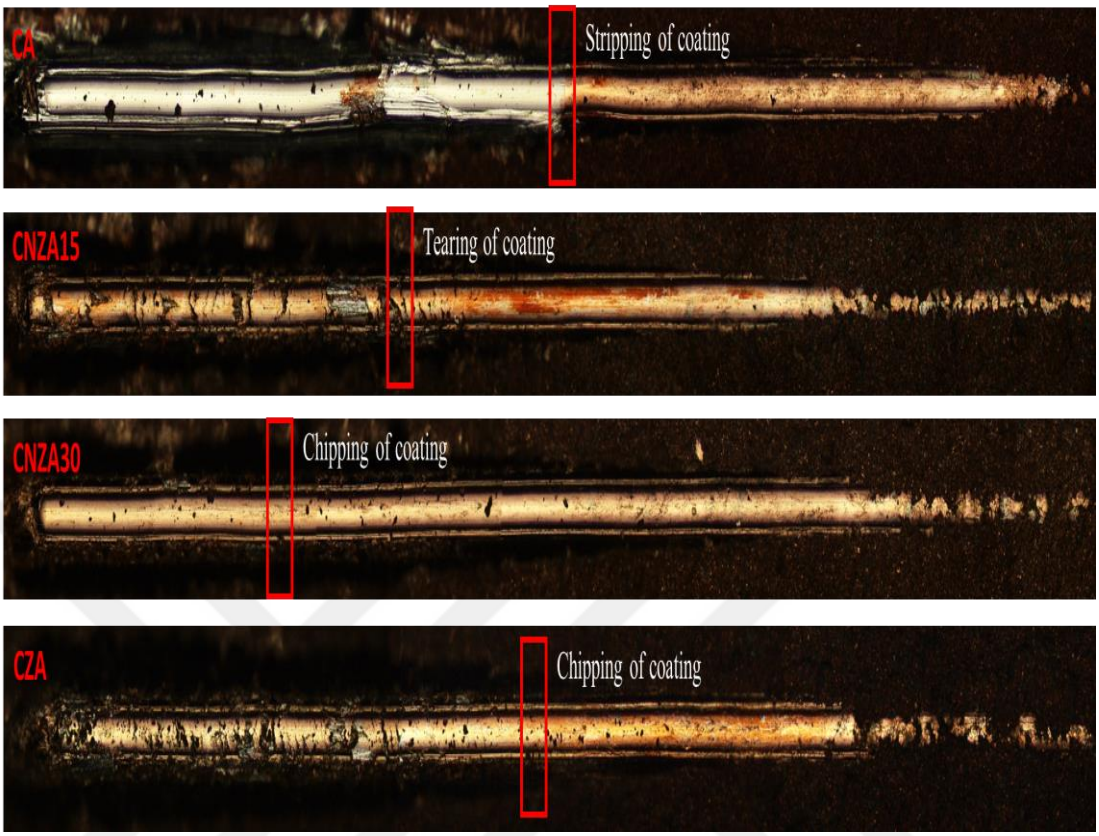


Figure 7.9 OM images of scratch tracks on Cu-based coatings

Upon a detailed examination of OM images of scratch tracks, it was observed that for CA, the coating peeled off, for CNZA15 partial tearing occurred, for CNZA30, the coating maintained its presence parallel to high adhesion strength and for CZA chipping occurred. The Lc values for Cu-based coatings are provided in Table 7.4. The highest Lc values were observed in CNZA15 and CNZA30 coatings, which contain Ni. The observed high scratch resistance in CNZA15 and CNZA30 coatings was associated with increased load-carrying capacity due to higher coating hardness and thickness compared to other Cu-based coatings. Additionally, it is believed that the effective plastic deformation associated with the higher hardness of Ni particles during the CGDS process contributes to increased adhesion strength compared to other powder components. On the other hand, considering that micro-pores in the coating structure act as stress concentrators and initiate micro-cracks leading to coating fragmentation, it can be said that CNZA15 and CNZA30 coatings have the lowest

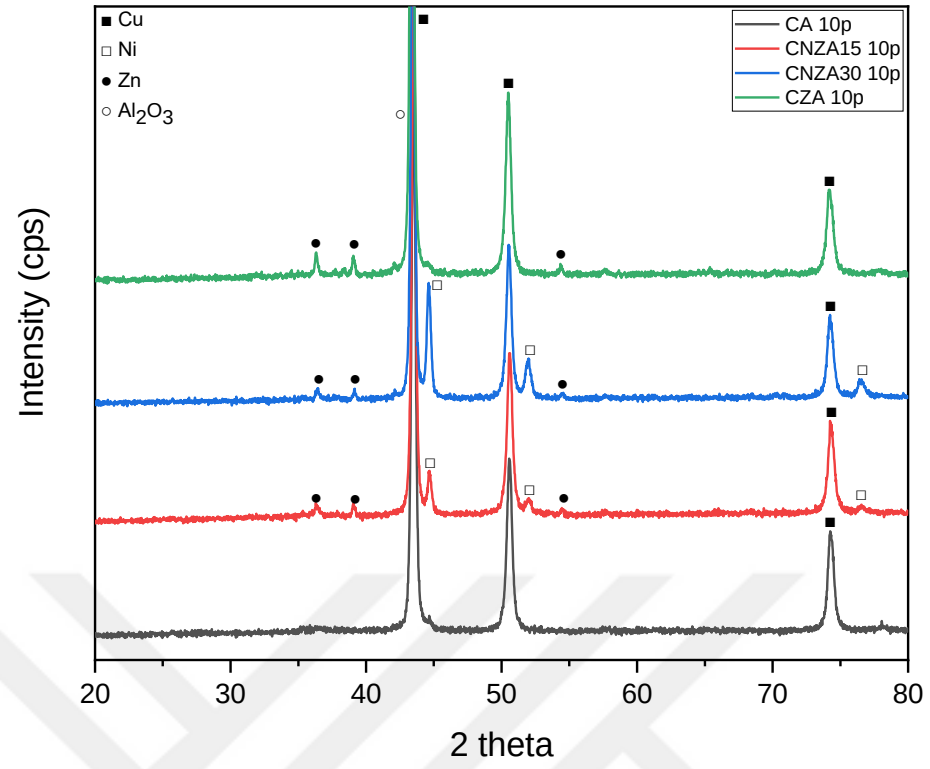
micro-porosity due to the influence of Ni and Zn. CA and CZA coatings exhibited similar L_c values and the slight increase in L_c value for CZA was associated with its relatively low friction coefficient and low micro-porosity attributed to Zn. Zhang et al., (2019) in their study on Cu-based coatings, demonstrated that the presence of Ni and Zn in the coating composition is effective in obtaining coatings with low porosity, dense and compact structures.

Table 7.4 Critical load values of Cu-based coatings.

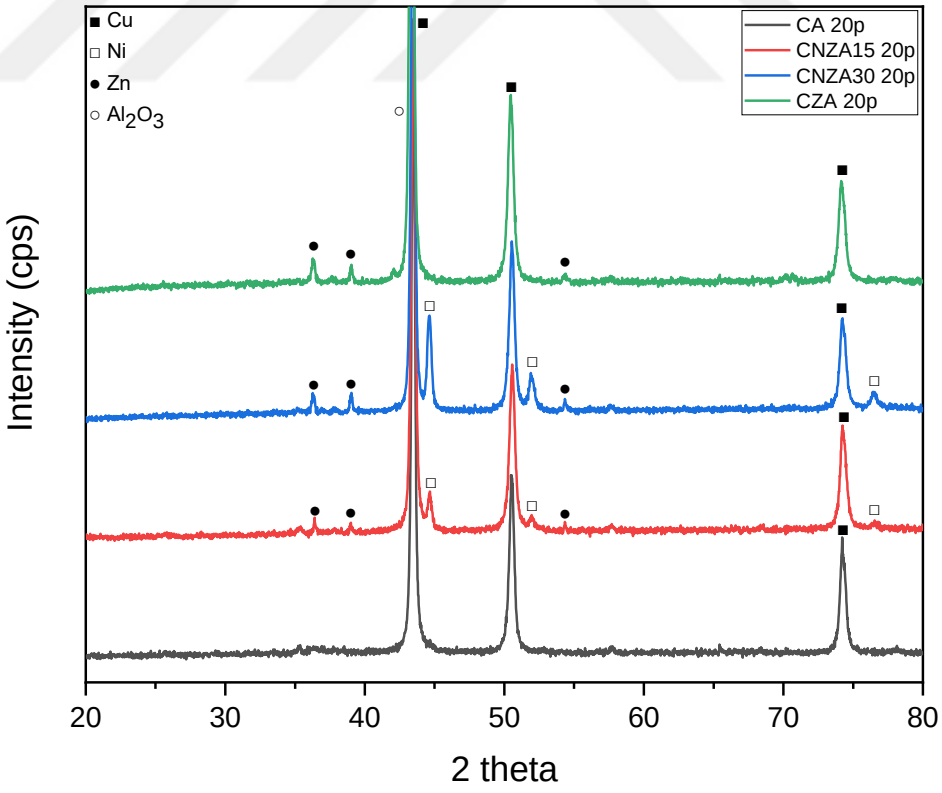
Coating	**L_c (N)**
CA	72.79
CNZA15	97.71
CNZA30	130.75
CZA	74.34

7.2.4 Phase Analysis

XRD diagrams for CA, CNZA15, CNZA30 and CZA coatings are presented in Figure 7.10. XRD patterns were shown separately, grouped by the number of spraying steps, either 10 passes or 20 passes. The examined XRD patterns indicated that the phase contents of the powder material and the coating produced with the same powder were similar, with no peaks corresponding to any phase other than the components present in the feed powders. Therefore, it was concluded that, due to the nature of the CGDS process, the powders do not experience high temperatures during the spraying process and there is no thermal effect causing any phase transformation. Additionally, no diffraction peaks indicating oxidation or chemical reactions were detected. XRD patterns showed that the dominant phase content for all coatings was Cu and Al_2O_3 and the number of spraying steps had no effect on the phase contents of the coatings. Ni phase was distinctive and identified for CNZA15 and CNZA30 coatings. Additionally, considering the intensity values of the peaks, it was observed that the Ni phase in the CNZA30 coating and the Zn phase in the CZA coating were more pronounced in parallel with the amounts in the feed powder. XRD results corroborated the microstructure analyses and EDS findings.



(a)



(b)

Figure 7.10 XRD patterns of Cu-based coatings: **(a)** 10 passes **(b)** 20 passes

7.2.5 Surface Roughness Analysis

7075 AA aluminum alloy and coating surface roughness values were obtained using Ambios Technology XP-2 surface profilometer with a 4 mm measurement distance and 0.4 mm/s scanning speed. Average R_a and R_z values from measurements taken in at least 3 different regions are presented in Table 7.5. The measurements indicated that the surface roughness values of the coatings produced by CGDS, dependent on the deformation of powder materials and the deposition process of different metal/ceramic components, were higher than those of the sandblasted 7075 AA. When the coatings were evaluated among themselves, the lowest surface roughness values were observed in CA and the highest surface roughness values were found in CZA coatings. Additionally, it was found that the number of spraying steps affected the surface roughness values and lower surface roughness values were obtained with 20 passes coatings, along with the peening effect.

Table 7.5 Surface roughness values for the substrate and Cu-based coatings.

Specimen	**Surface Roughness (µm)**	
	R_a	R_z
	Avg.	Avg.
7075 AA	1.90±0.11	14.40±1.3
CA 10p	2.42±0.17	12.89±1.1
CA 20p	1.99±0.11	11.51±1.2
CNZA15 10p	3.38±0.27	19.59±1.8
CNZA15 20p	2.38±0.19	15.31±1.6
CNZA30 10p	3.62±0.29	20.81±1.8
CNZA30 20p	2.77±0.21	17.58±1.7
CZA 10p	5.35±0.39	31.74±2.9
CZA 20p	5.25±0.33	29.66±2.7

7.3 Electrochemical Corrosion Properties

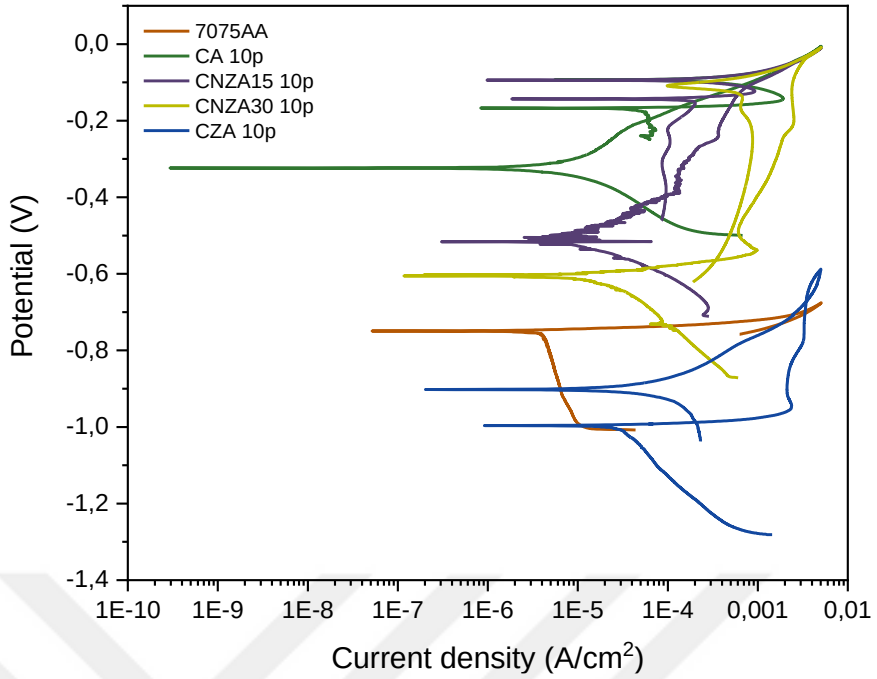
7.3.1 Cyclic Polarization

Within the scope of accelerated corrosion tests, cyclic polarization method was applied in a 3.5 wt.% NaCl solution according to ASTM G59 and ASTM G102 standards and corrosion parameters were determined through Tafel extrapolation. The

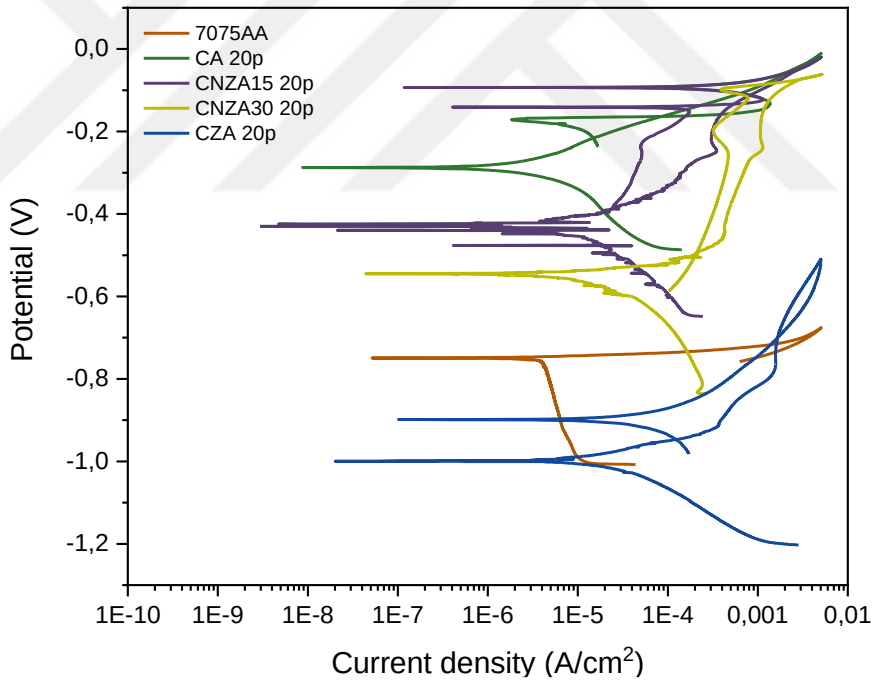
cyclic polarization curves of tested 7075 AA and coatings are presented in Figure 7.11. The curves are grouped separately based on the number of spraying steps, 10 passes and 20 passes. Under OCP conditions, corrosion parameters such as E_{corr}, i_{corr} and corrosion rate (CR) were determined using the Tafel extrapolation method and are shown in Table 7.6. In cyclic polarization tests, excessive voltage was applied in the anodic direction to the specimens to reach a current of 5 mA and the passivation capabilities of the specimens under aggressive corrosion conditions were evaluated. The excessive voltage required to reach 5 mA (E_{5mA} - E_{corr}), primary passivation potential (E_{pp}), breakdown potential (E_b), passive region (E_b - E_{pp}), re-passivation potential (E_{rp}), (E_{rp} - E_{corr}), passive current density (i_p) and the final current density after cyclic polarization (i_f) values for the specimens were determined and presented in Table 7.7.

Table 7.6 Corrosion parameter values of specimens that were obtained by Tafel extrapolation.

Specimen	**E_{corr} (V)**	**i_{corr} (A/cm^2)**	**CR (µm/year)**
7075 AA	-0.702	4.40x10-6	46.07
CA 10p	-0.324	8.35x10-6	87.43
CA 20p	-0.288	5.15x10-6	53.92
CNZA15 10p	-0.516	13.10x10-6	137.16
CNZA15 20p	-0.430	12.80x10-6	134.02
CNZA30 10p	-0.606	17.60x10-6	184.28
CNZA30 20p	-0.545	15.60x10-6	163.34
CZA 10p	-0.998	29.20x10-6	305.74
CZA 20p	-1.023	26.40x10-6	276.42



(a)



(b)

Figure 7.11 Cyclic polarization curves of specimens: **(a)** 10 passes and **(b)** 20 passes

E_{corr} explains a material's tendency to corrode and is primarily related to the material's chemical composition (material type). I_{corr} is associated with the structural properties of the material. In addition to this information, the positions of materials in

the galvanic series are also important and reflect their active or noble character against corrosion. The standard electrode potentials of coating components (Cu, Ni and Zn) are known to be 0.342 V, -0.257 V and -0.761 V, respectively. When examining Figure 7.11 and Table 7.6 and considering the components present in the coating, it is observed that the corrosion potentials of the coatings change in the anodic direction due to the influence of ceramic particles (Al_2O_3). Some literature studies have similarly found that the addition of ceramic particles to the coating matrix leads to a change in corrosion potential in the anodic direction (Dzhurinskiy et al., 2012; Y. J. Li et al., 2017; Meydanoglu et al., 2013). When evaluating the coatings among themselves, all coatings except CZA shifted the E_{corr} value of 7075 AA in the cathodic direction (Y. J. Li et al., 2017; Winnicki et al., 2017). The highest corrosion potential was observed in CA, while the lowest corrosion potential was identified in CZA coatings. Therefore, it can be stated that CZA coatings are more active in terms of corrosion reactions. Dzhurinskiy et al., (2012) in their study on 5 different coatings, reported that coatings containing Zn showed a change in corrosion potential in the anodic direction compared to those without Zn and indicating that they are more active in terms of corrosion reactions. The influence of Zn on the E_{corr} value can also be observed by examining CNZA15 and CNZA30 coatings. The E_{corr} values of CNZA30 coatings, which contain proportionally more Zn in the coating matrix, is lower compared to CNZA15 coatings.

The i_{corr} values of the coatings were confirmed to be associated with the elemental composition, microstructures and porosity of the coatings through cyclic polarization curves. The results indicated that different powder components significantly altered the corrosion behavior of Cu-based coatings. While Tafel extrapolation suggested that all coatings, except CZA, exhibited a higher E_{corr} in the cathodic direction compared to 7075 AA, the i_{corr} values of Cu-based coatings were much higher than that of 7075 AA under OCP conditions. This suggests that the corrosion of the coatings started later compared to 7075 AA but spread more rapidly (Meydanoglu et al., 2013). Additionally, the top layer of the coatings, with its porous nature and the presence of irregular and small defects along the cross-section, did not contribute to enhancing corrosion resistance. As a result, it was found that the initial accelerated corrosion passing through the pores increased chemical attack and expanded small defects. When the coatings were compared, the lowest i_{corr} value and CR were observed in CA coatings,

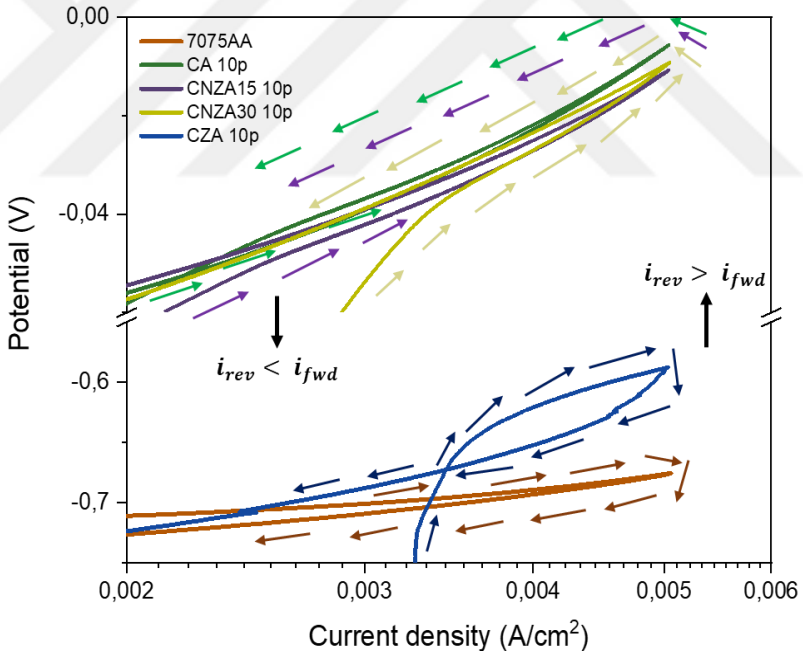
while the highest values were found in CZA coatings. It was determined that as the amount of Ni and Zn in the coating increased, both i_{corr} and CR increased dramatically. This phenomenon was associated with the formation of Cu-Ni-Zn and Cu-Zn galvanic couples in CNZA and CZA coatings respectively, contributing to the acceleration of the degradation process (H. Chen et al., 2022; Dzhurinskiy et al., 2012). The formation of the Cu-Zn galvanic couple, resulting in the most significant difference in standard electrode potential for CZA coatings, confirmed the highest i_{corr} value and CR. Additionally, 20 passes coatings with a more intense structural morphology, attributed to the peening effect, exhibited lower i_{corr} and CR values. This result was associated with a slight reduction in the amount of surface porosity due to the increase in the number of spraying steps (H. Chen et al., 2022).

Table 7.7 Passivation parameter values of specimens that were obtained by cyclic polarization.

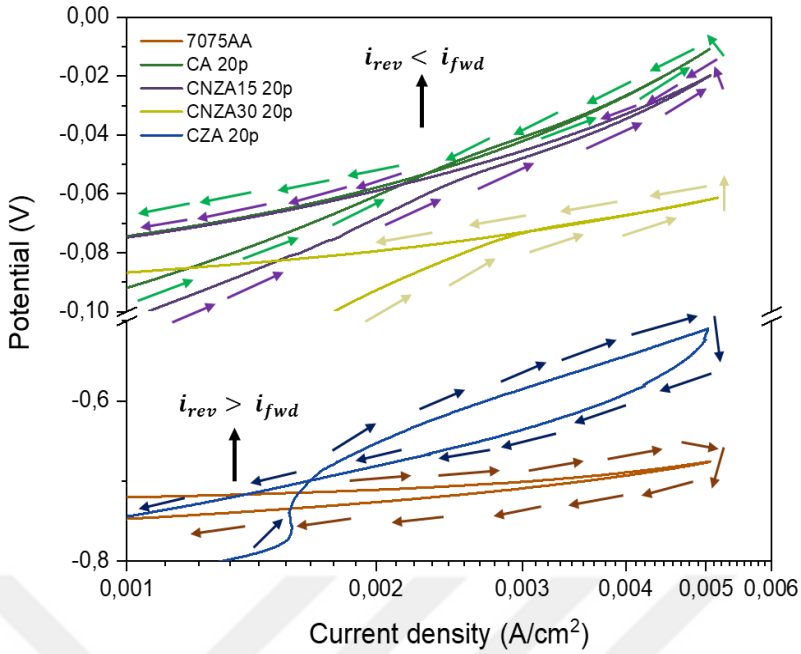
Specimen	E_{5mA}-E_{corr} (mV)	E_{pp} (mV)	E_b (mV)	E_b-E_{pp} (mV)	E_{rp} (mV)	E_{rp}-E_{corr} (mV)	i_p (µA)	i_f (µA)
7075 AA	73.7	-701.6	-701.6	0.0	-	-	-	627.6
CA 10p	317.5	-277.4	-210.5	66.9	-93.73	229.97	26.7	62.1
CA 20p	276.5	-252.9	-216.9	36.0	-93.26	194.34	8.7	16.8
CNZA15 10p	505.6	-235.6	-112.9	122.7	-94.07	422.23	134.6	85.1
CNZA15 20p	410.0	-241.9	-133.9	108.0	-93.20	336.90	121.9	21.7
CNZA30 10p	595.7	-204.7	-92.5	112.2	-109.60	495.90	609.7	190.7
CNZA30 20p	483.7	-233.4	-116.0	117.4	-99.34	445.66	424.9	102.4
CZA 10p	408.2	-765.3	-638.4	126.9	-902.20	95.90	2113.0	230.1
CZA 20p	512.0	-767.2	-666.0	101.2	-898.50	124.50	1560.0	171.6

The evaluation of the corrosion behavior and passivation capabilities of the substrate and coatings under aggressive conditions was conducted by examining Figure 7.11 and Table 7.7. Upon detailed examination of cyclic polarization curves, it was observed that 7075 AA rapidly activated, anodic reactions dominated, the current increased rapidly upon the application of the lowest overpotential in the anodic direction, reaching a critical level (5mA) and pitting corrosion initiation was detected. For the substrate material 7075 AA, it was determined that OCP, E_{pp} and E_b values were equal, passivation did not occur, reverse scan current density was higher than the forward scan current density and positive hysteresis occurred. However, in all Cu-based coatings, it was observed that anodic reactions were suppressed and the critical

current level (5mA) could only be reached by applying a higher overpotential. When evaluating the coatings, it was found that the reverse scan current density was lower than the forward scan current density and all coatings exhibited negative hysteresis. However, there was an exceptional case for CZA, where initially the reverse scan current density increased compared to the forward scan current density and then the current decreased, reaching lower levels than the forward scan current density. Additionally, all coatings demonstrated re-passivation and it was observed that the E_{rp} value was greater than the E_{corr} value. However, 7075 AA did not exhibit re-passivation. At this point, the difference in ($E_{rp} - E_{corr}$) values indicated the potential for re-passivation in the order of CZA < CA < CNZA15 < CNZA30 for the coatings. It was particularly understood that the presence of Ni in the coating significantly contributed to the ability of re-passivation.



(a)



(b)

Figure 7.12 Transition regions from forward to reverse scans for cyclic polarization curves of the specimens: **(a)** 10 passes and **(b)** 20 passes

The transition regions from forward to reverse scans for cyclic polarization curves of the specimens have been grouped based on the number of spraying steps (10 passes and 20 passes) and presented separately in Figure 7.12. Negative hysteresis occurs when the reverse scan current density is lower than the forward scan and positive hysteresis occurs when the reverse scan current density is higher than the forward scan. Cyclic polarization curve hysteresis provides information about the rates of pitting corrosion and how easily the passive film can self-repair. Positive hysteresis occurs when the passive film damage cannot be repaired and/or pit formation begins; negative hysteresis occurs when a damaged passive film can self-repair and/or pit formation has not started. Additionally, when E_{corr} is greater than E_{rp}, it indicates that pits will continue to grow and when E_{corr} is less than E_{rp}, it suggests that pits will not grow. Based on this information, it can be stated that pit formation begins, continues to spread and the passive film does not form for 7075 AA. Nevertheless, it can be understood that pit formation has not started for CA, CNZA15 and CNZA30 coatings, and the damaged passive film can self-repair. For the CZA coating, it can be stated that even if pit formation starts, these pits do not grow and the damaged passive film can

self-repair. When Table 7.7 is examined, since passivation did not occur in 7075 AA under aggressive corrosion conditions, the i_p value could not be determined. However, among the specimens, 7075 AA exhibited the highest i_f value. When coatings are evaluated among themselves, the lowest i_p and i_f values are proportional to the i_{corr} values determined by Tafel extrapolation and are observed in CA coatings, while the highest values are found in CZA coatings. This situation is also evident from the passive region width values presented in Table 7.7. The lowest passive region width among the specimens was observed in 7075 AA. The low passive region width observed in CA coatings is associated with the pseudo-passive cyclic polarization curves observed in CA coatings. A pseudo-passive cyclic polarization curve has a transpassive and passive region in the pseudo-passive region, but it may not have distinct E_b or E_{pp} potentials. The current in the pseudo-passive region may increase slightly, but the magnitude of the slope is not a unique feature of the metal-electrolyte system. Additionally, estimating the E_b and E_{pp} values of pseudo-passive curves can be challenging and therefore, somewhat subjective (Tait, 1994; Z. Zhang et al., 2020).

7.3.2 Electrochemical Impedance Spectroscopy

The Nyquist plots and equivalent circuits that were used for fitting EIS spectra of 7075AA and Cu-based coatings are shown in Figure 7.13 and Figure 7.14, respectively. For CA and CNZA coatings, an equivalent circuit model with one time constant was used for fitting EIS spectra (Figure 7.14b). In this model, R_s is the solution resistance, R_1 is the charge transfer resistance (or polarization resistance) and CPE_1 is the capacitance of double layer. In case of bare 7075AA, the Nyquist plot shows a depressed semicircle at high-medium frequency range and an inductive loop at low frequencies. Therefore, the EIS spectrum of 7075AA was fitted using an equivalent circuit that included one-time constant with an additional inductive circuit element as shown in Figure 7.14a. In this model, R_2 is the inductive resistance and L is the inductance connected in series with R_2. The high-medium frequency capacitive semicircle was related to the double layer relaxation because it is a rapid charging and discharging process. The inductive loop at low frequencies was attributed to the localized corrosion and hydrogen evolution. It has been reported that an inductive behavior is clearly seen in the EIS spectra only when the oxide layer is locally broken

as a result of the combined presence of chlorides and the availability of an anodic current and there is a generation of superfluous hydrogen (Yang et al., 2019). For CZA coatings, the Nyquist plots showed two depressed semicircles at high and low frequencies, therefore, two time constants were used to fit impedance spectra (Figure 7.14c).

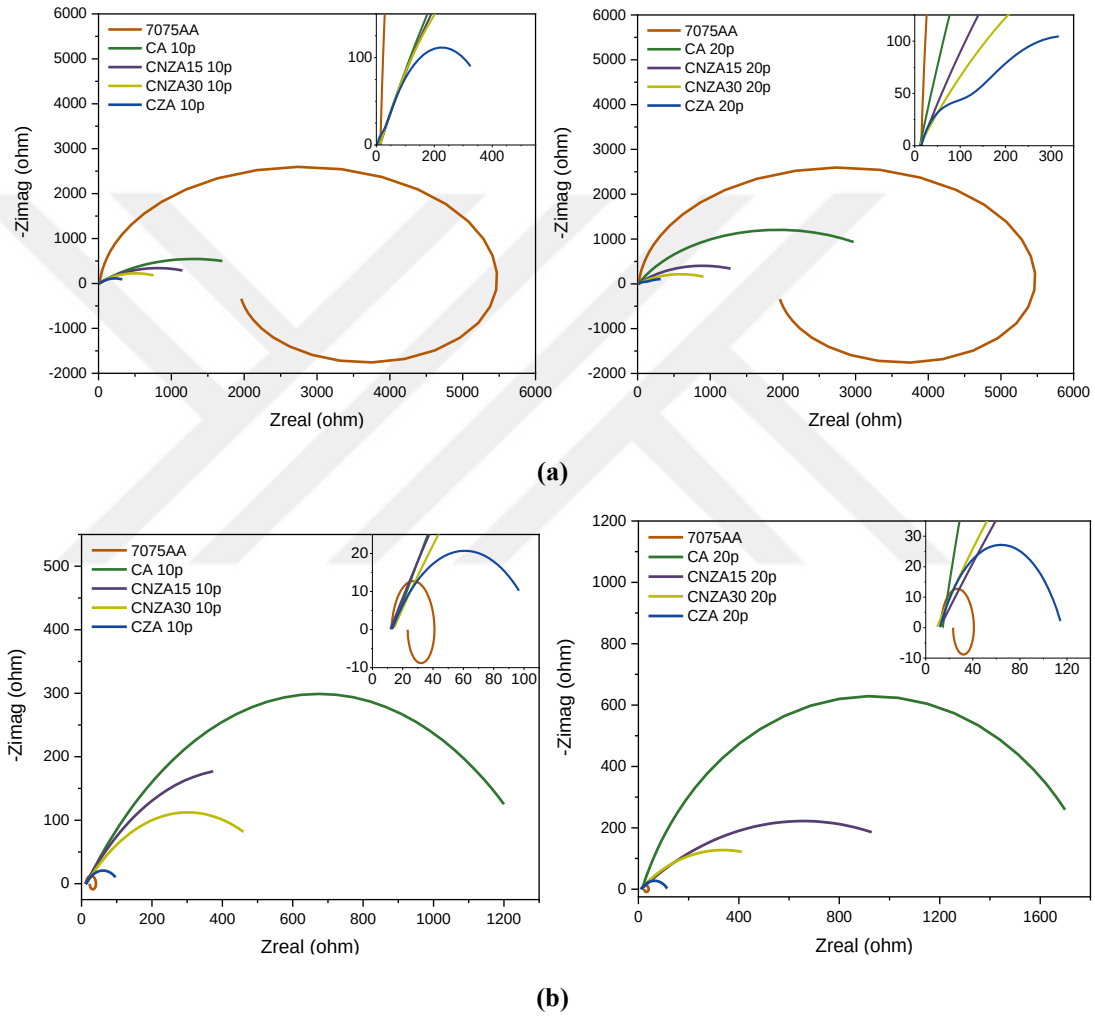


Figure 7.13 Nyquist plots of specimens: DC Voltage **(a)** 0 V (vs OCP) and **(b)** 0.1 V (vs OCP)

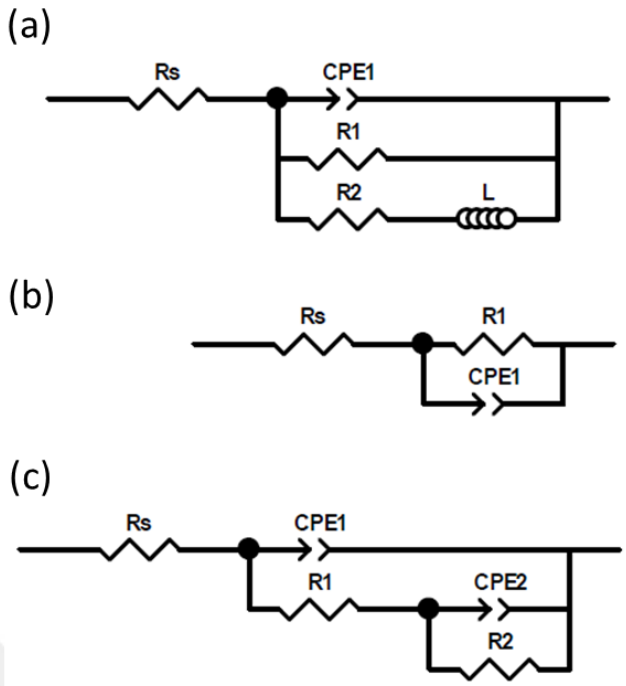


Figure 7.14 Equivalent circuit models that were used in fitting the impedance spectra of **(a)** 7075 AA, **(b)** CA and CNZA coatings, **(c)** CZA coatings

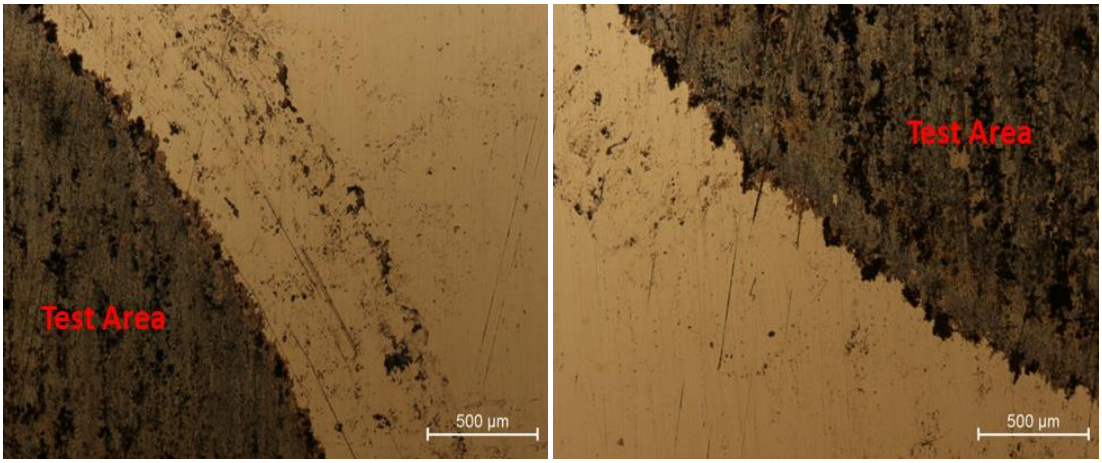
Table 7.8 The equivalent circuit element values obtained by fitting the EIS curves of specimens.

Specimen	DC Voltage	R_s ($\Omega \cdot cm^2$)	R_1 ($\Omega \cdot cm^2$)	$(CPE\text{-}T)_1 \times 10^{-6}$ (F)	$(CPE\text{-}P)_1$	R_2 ($\Omega \cdot cm2$)	$(CPE\text{-}T)_2 \times 10^{-6}$ (F)	$(CPE\text{-}P)_2$	L ($H \cdot cm^{-2}$)
7075 AA	0 V (vs OCP)	14.2	5590	10.9	0.954	2910	-	-	12800
	0.1 V (vs OCP)	12.5	28.9	22.7	0.923	17.1	-	-	1.214
CA 10p	0 V (vs OCP)	11.7	2576	921	0.510				
	0.1 V (vs OCP)	13.7	1320	523	0.541	-	-	-	-
CA 20p	0 V (vs OCP)	11.4	3840	775	0.714	-	-	-	-
	0.1 V (vs OCP)	14.4	1830	795	0.766	-	-	-	-
CNZA15 10p	0 V (vs OCP)	12.6	1600	1200	0.513	-	-	-	-
	0.1 V (vs OCP)	11.7	853	6210	0.510	-	-	-	-
CNZA15 20p	0 V (vs OCP)	13.3	1770	1180	0.544	-	-	-	-
	0.1 V (vs OCP)	12.0	1290	1110	0.423	-	-	-	-
CNZA30 10p	0 V (vs OCP)	13.1	990	1824	0,540				
	0.1 V (vs OCP)	13.8	576	2170	0.474	-	-	-	-
CNZA30 20p	0 V (vs OCP)	10.6	1175	1024	0.444	-	-	-	-
	0.1 V (vs OCP)	9.5	653	3780	0.470	-	-	-	-
CZA 10p	0 V (vs OCP)	9.6	394	5660	0.627	31.9	1000	0.74	-
	0.1 V (vs OCP)	12.9	96	8300	0.519	-	-	-	-
CZA 20p	0 V (vs OCP)	14.5	435	11200	0.535	115.1	1100	0.67	-
	0.1 V (vs OCP)	11.7	129	2000	0.553	-	-	-	-

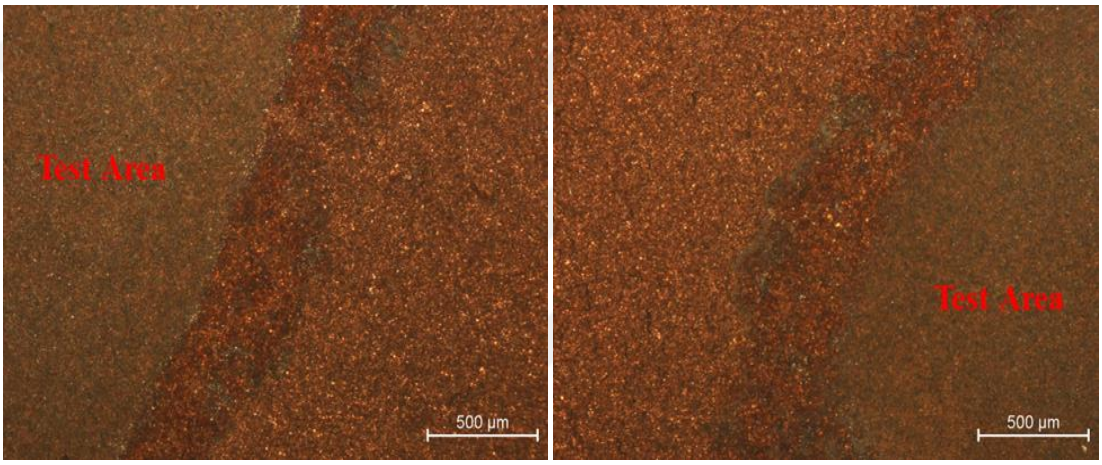
The EIS fitting results are listed in Table 7.8. As can be seen from the table, bare 7075AA has higher resistance value than Cu-based coatings when the impedance spectra were taken at 0V (vs OCP). However, the resistance value of 7075AA was decreased dramatically when the EIS test was conducted at an anodic potential of 0.1V (vs. OCP). This may be explained by the increased anodic current at 0.1V which can facilitate the localized corrosion and hydrogen evolution. On the other hand, with increasing anodic potential, the decrease in resistance of Cu-based coatings appears to be much less than that of bare 7075AA. This could be explained by the increased polarization resistance of Cu-based coatings exhibiting trans-passive behavior in cyclic polarization tests whereas 7075AA showed much higher anodic current values indicating the localized corrosion. When the coatings compared each other, CA coatings have higher resistance values than CNZA and CZA coatings, indicative of higher corrosion resistance of CA coatings. It has also been observed that the resistance of coatings was increased with increased coating thickness (number of spraying steps). The lowest resistance values were obtained with CZA coatings which also have higher corrosion rates than other coatings.

7.3.3 Optical microscopy examinations after corrosion tests

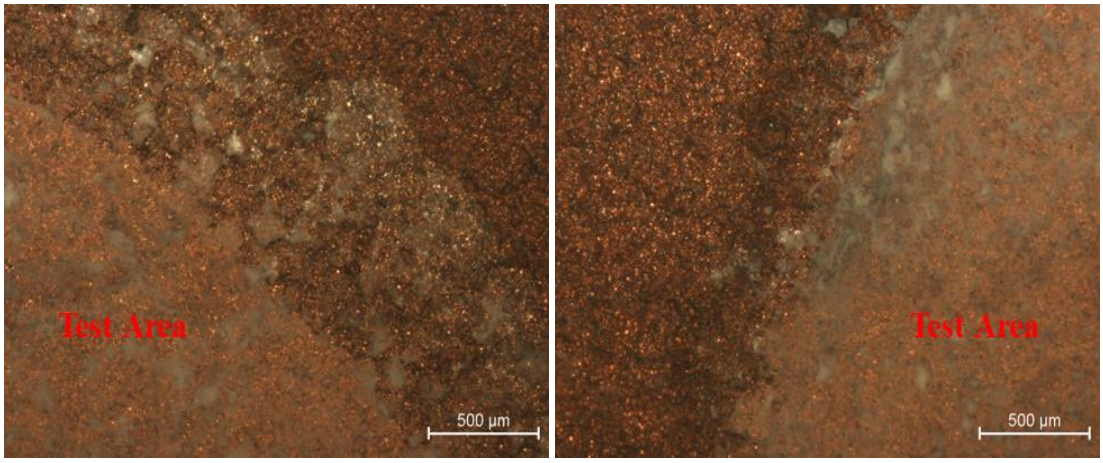
In order to facilitate a comprehensive analysis of the numerical values associated with corrosion parameters presented in Table 7.6, Table 7.7 and Table 7.8, OM examinations were conducted. The primary objective was to assess the corrosion formations and their intensities in the specimens following corrosion tests. Surface images (50x magnification) and cross-sectional images (100x and 200x magnification) were obtained through OM examinations. During these investigations 7075 AA, coatings exhibiting the best (CA) and worst (CZA) results in terms of corrosion parameters were selected as exemplary cases. Figure 7.15 and 7.16 depict the surface and cross-sectional images, respectively.



(a)

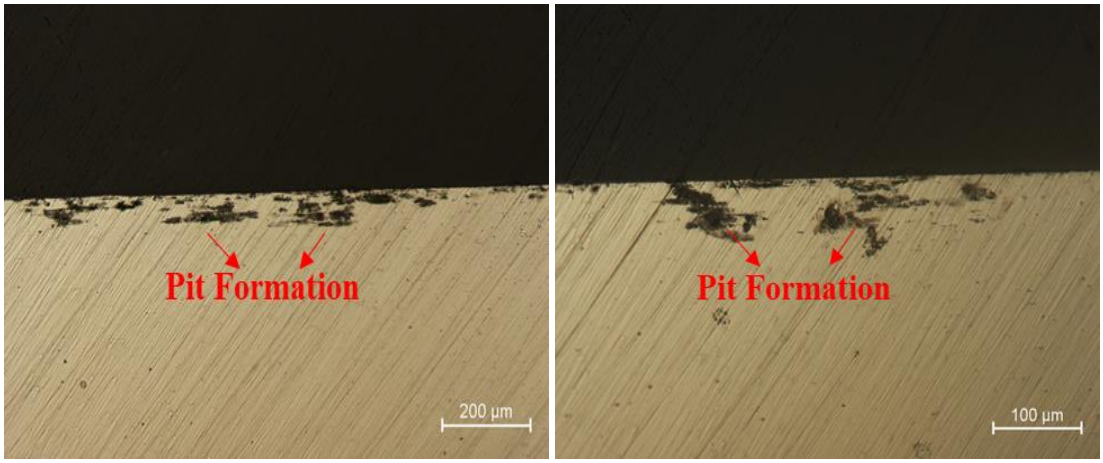


(b)

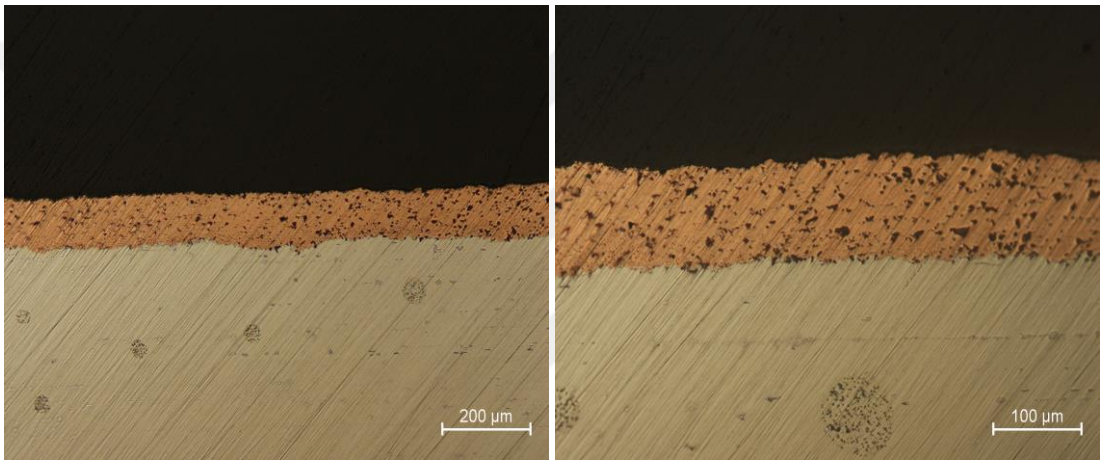


(c)

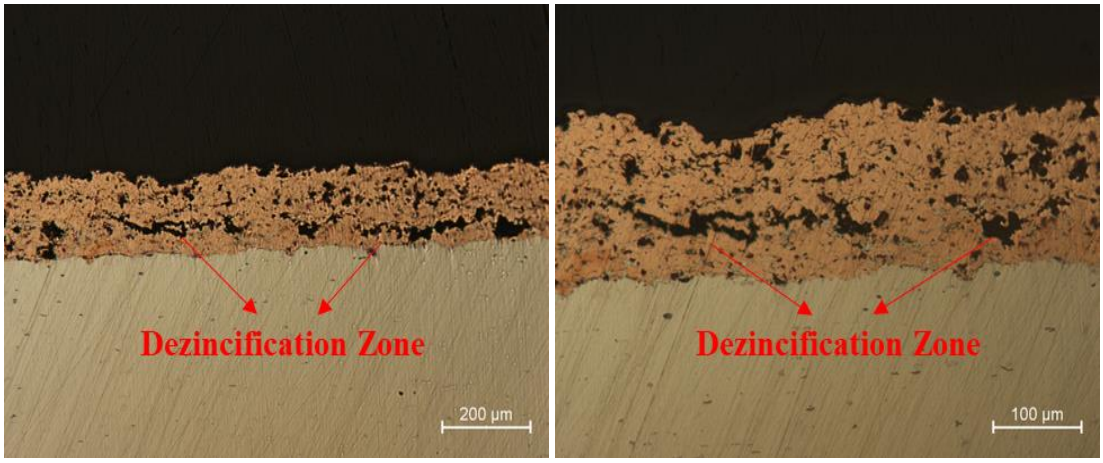
Figure 7.15 Surface images of specimens after corrosion tests: (a) 7075 AA (b) CA and (c) CZA



(a)



(b)

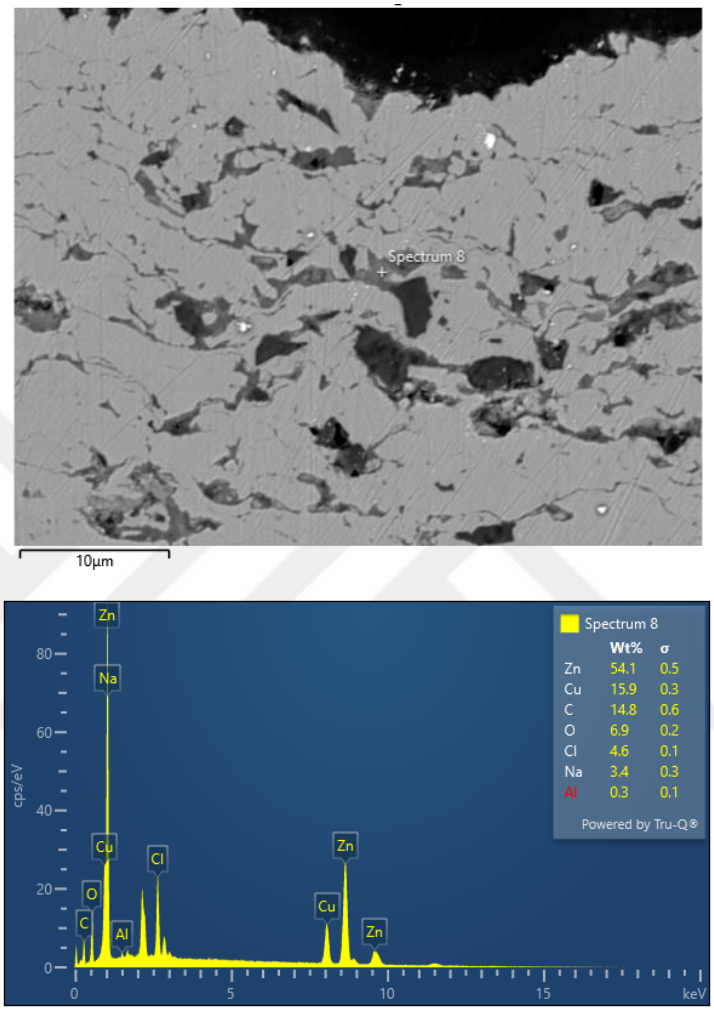


(c)

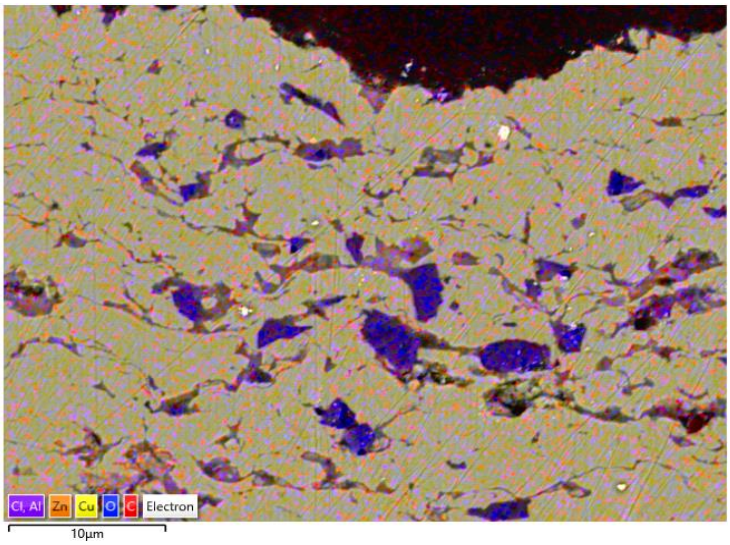
Figure 7.16 Cross-sectional images of specimens after corrosion tests: (a) 7075 AA, (b) CA and (c) CZA

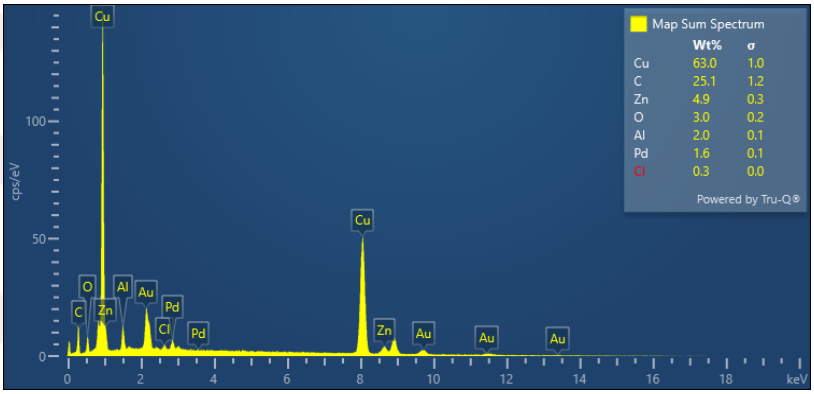
After a meticulous examination of the surface and cross-sectional images for 7075 AA, CA, and CZA, results consistent with the corrosion parameters provided in Table 7.6, Table 7.7 and Table 7.8 were obtained. For 7075 AA, the initiation of pit formation and its extensive spread across a significant portion of the surface were observed. Pit formation and its propagation were also identified through cross-sectional examinations provided in Figure 7.16 (a), revealing that the pits originating on the surface expanded toward the substrate. In the case of the CA coating, general corrosion and corrosion product formation on the surface were evident, but no evidence of pitting corrosion was found. Additionally, cross-sectional examinations presented in Figure 7.16 (b) confirmed that there was no pit formation on the coating-substrate interface; the substrate remained unaffected. For the CZA coating, relatively sparse white/gray corrosion products in small fragments were observed on the test surface. These white/gray corrosion products were further clarified through cross-sectional examinations in Figure 7.16 (c) and revealing signs of dezincification in the coating microstructure. Regions where zinc was depleted had aggregated, forming microscopically visible black-colored capillary. These findings suggest a localized dezincification process, leading to the formation of intricate black-colored capillary within the microstructure. Furthermore, SEM examinations were undertaken to validate the dezincification regions, accompanied by point EDS and EDS mapping analyses. The EDS analysis results depicted in Figure 7.17 confirmed that in the dezincification regions, where zinc had migrated away from the structure, Na and Cl ions had penetrated into the vacated spaces. L. Zhang et al., (2019) in their study on Cu-based cold-sprayed coatings, reported similar findings. According to their observations, the corrosion current density (i_{corr}) of the Cu/Zn-Al_2O_3 coating was higher than that of the Cu-Al_2O_3 coating. They concluded that Zn accelerated the corrosion of the Cu-Al_2O_3 coating, highlighting Zn as a highly reactive metal with a lower electrode potential than Cu. The study proposed that in the Cu/Zn-Al_2O_3 coating, Zn and Cu formed a corrosion couple, with Zn acting as an anode compared to Cu, thereby accelerating the corrosion process. Corrosion tests conducted by Zhang and colleagues revealed on the surface of the Cu/Zn-Al_2O_3 coating numerous, albeit not very dense, white corrosion products in small fragments. These corrosion products were identified as $Zn_5(OH)_8Cl_2.H_2O$ and ZnO. The significant potential difference

between Cu and Zn was suggested to induce rapid corrosion of Zn, similar to the dezincification phenomenon commonly observed in brass.



(a)



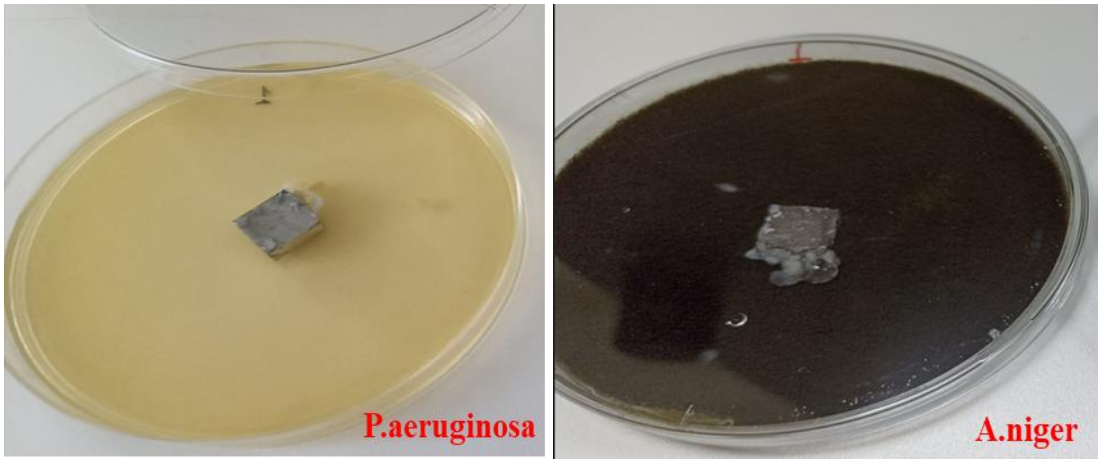


(b)

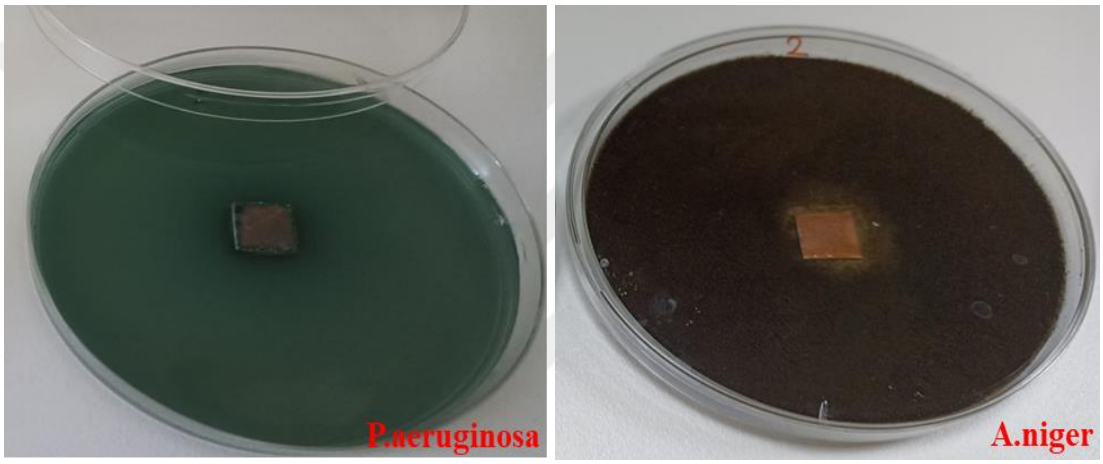
Figure 7.17 SEM analysis outputs for the dezincification region: **(a)** point EDS **(b)** EDS mapping

7.4 Microbiologically Influenced Corrosion Properties

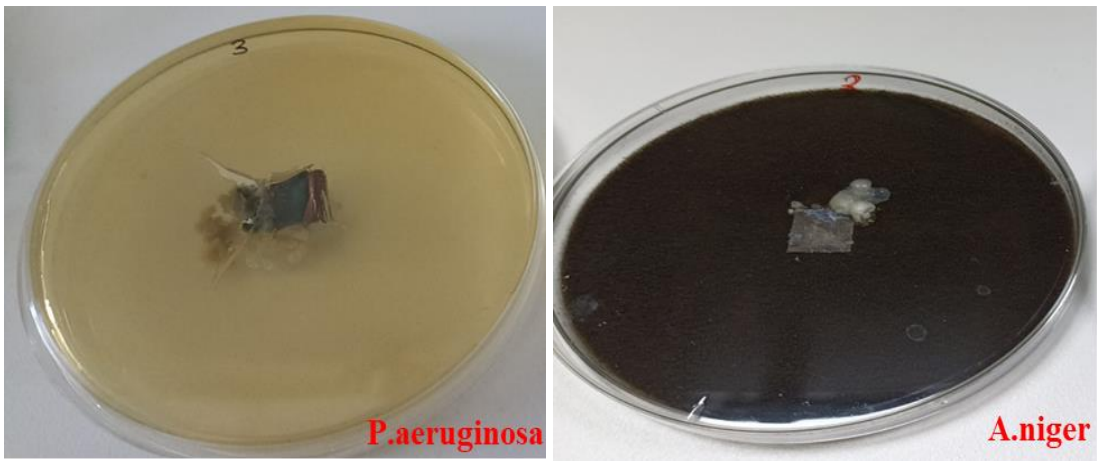
The incubation period for 7075 AA, bulk Cu, CA, CNZA15, CNZA30 and CZA specimens in petri dishes containing Gram-negative bacteria (*Pseudomonas aeruginosa*) and a fungus species (*Aspergillus niger*) was concluded after four weeks. Visual representations of the petri dishes before the removal of specimens at the end of the incubation period are provided in Figure 7.18.


P.aeruginosa
A.niger

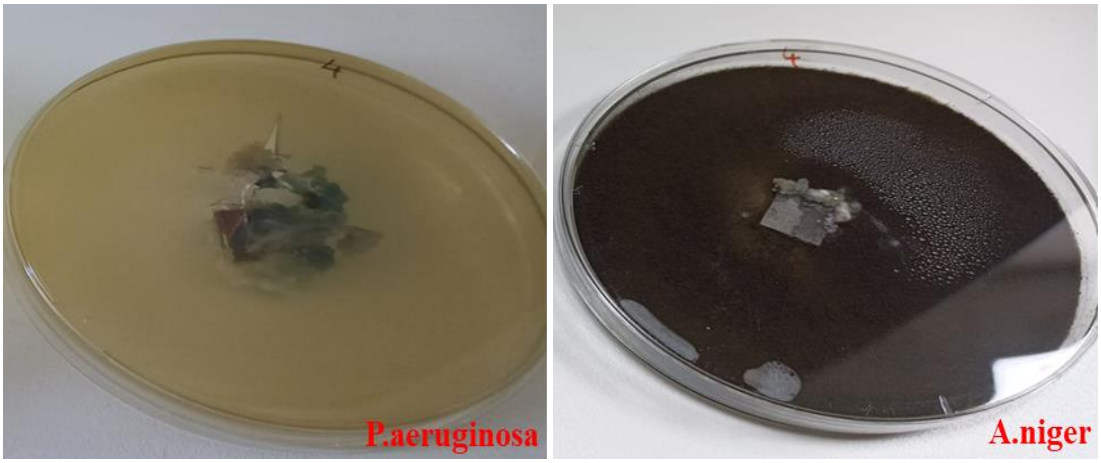
(a)


P.aeruginosa
A.niger

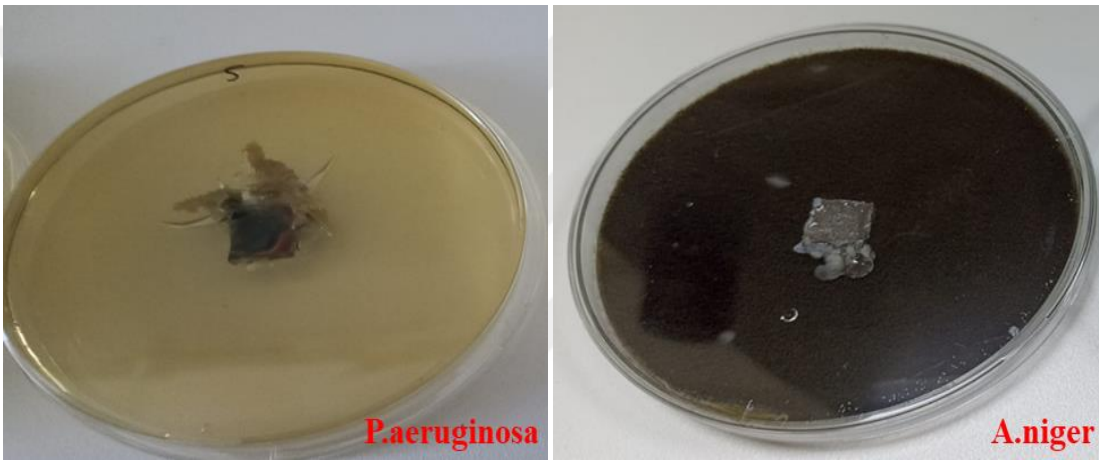
(b)


P.aeruginosa
A.niger

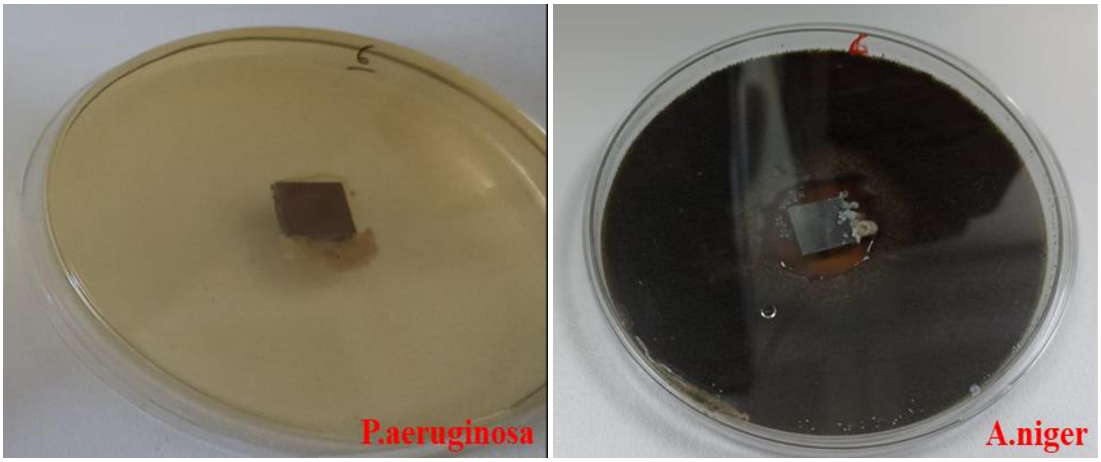
(c)



(d)



(e)



(f)

Figure 7.18 Petri dish images containing specimens at the end of the incubation period: **(a)** 7075 AA, **(b)** Bulk Cu, **(c)** CA, **(d)** CNZA15, **(e)** CNZA30 and **(f)** CZA

Upon examining the petri dish specimens after the incubation period, it was observed that blue-green (patina) $Cu_2CO_3(OH)_2$ (copper II carbonate hydroxide) formation occurred in the bulk Cu, CA, CNZA15, and CNZA30 specimens on the TSA growth medium containing *Pseudomonas aeruginosa*. Particularly, in the petri dish where bulk Cu was present, the color of the growth medium shifted from yellow to blue-green. For CA, CNZA15 and CNZA30 specimens, there was no noticeable change in the growth medium color, but oxide formation initiated on the specimen surfaces without spreading to the entire growth medium. No significant changes were observed for the 7075 AA and CZA specimens and despite the presence of Cu in the CZA specimen, there was no apparent sign of $Cu_2CO_3(OH)_2$ formation.

When evaluating the specimens on the MEA growth medium containing *Aspergillus niger*, intense fungus growth was observed around all specimens except for bulk Cu. Otherwise, an antifungal effect and inhibition zone were identified in both bulk Cu and CZA specimens. The antifungal effect and inhibition zone were limited for bulk Cu, while notably impressive results were obtained for the CZA coating. A detailed visual representation of the prominent inhibition zone detected in the CZA specimen is provided in Figure 7.19, with a measured zone diameter of 7 mm.

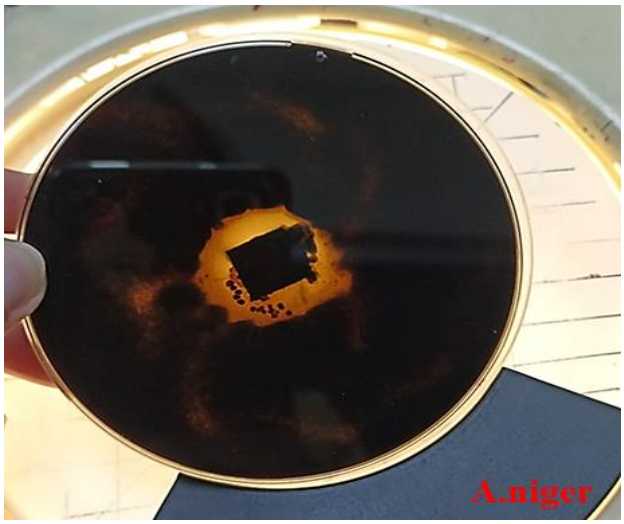
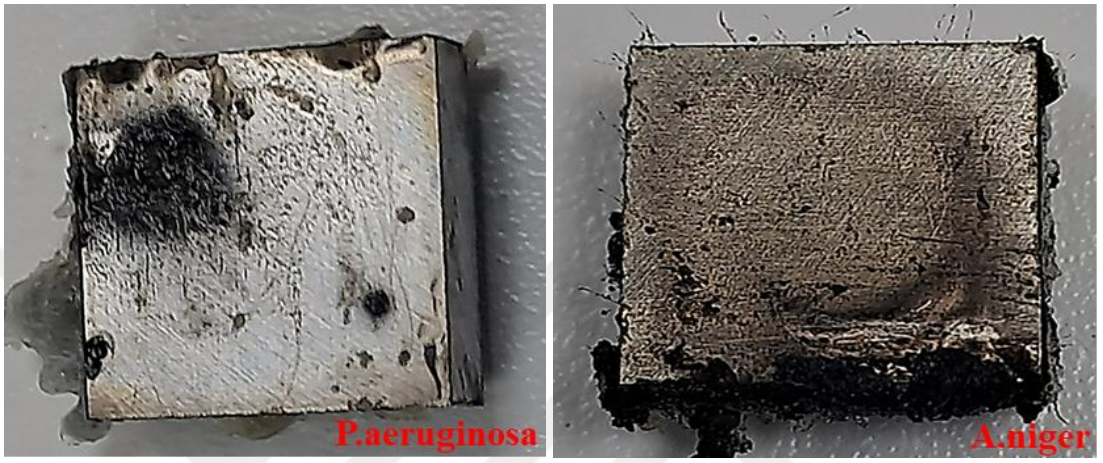
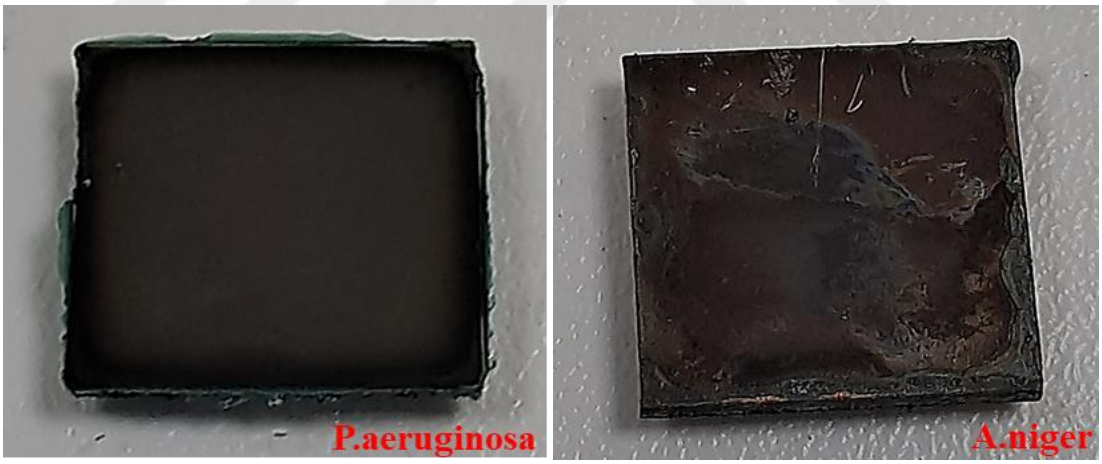


Figure 7.19 Inhibition zone identified in the *A. niger* medium for the CZA coating

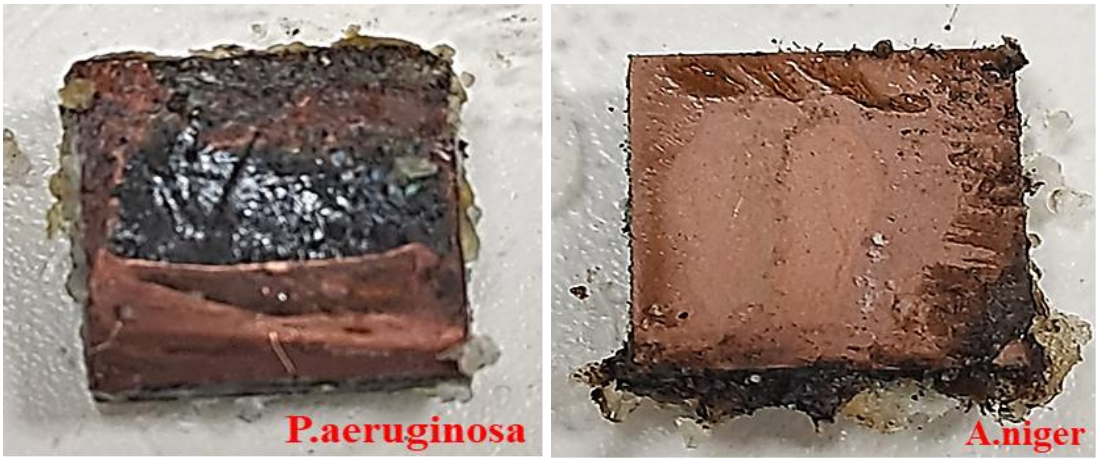
Following the initial visual examination, the specimens were thoroughly cleaned of microbial residues and growth medium remnants to investigate the effects and severity of the MIC phenomenon in detail. Visual representations of the specimens after the incubation period, removed from the petri dishes, are presented in Figure 7.20.



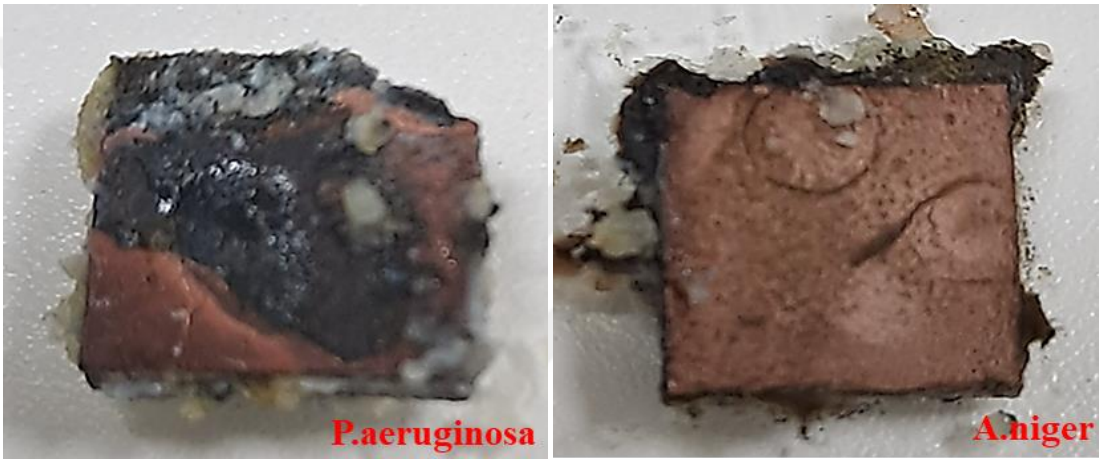
(a)



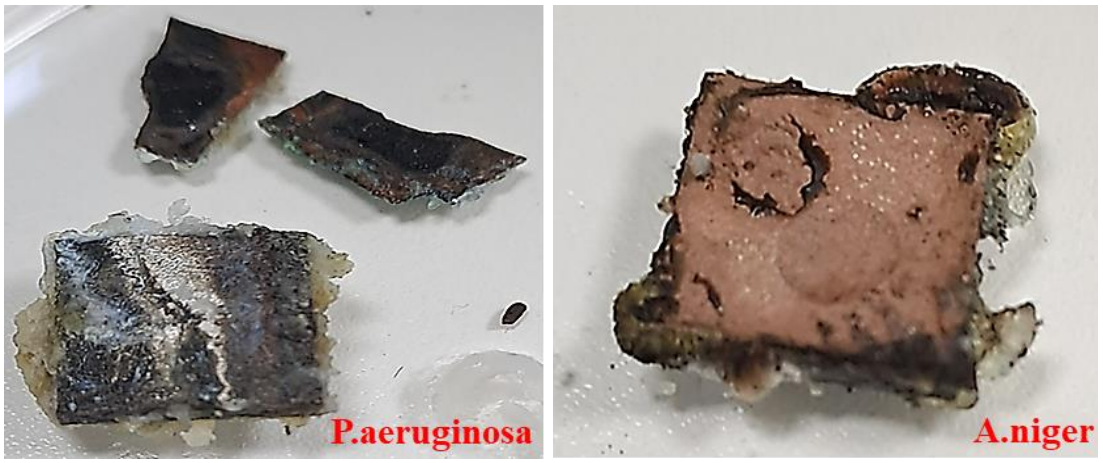
(b)


P.aeruginosa
A.niger

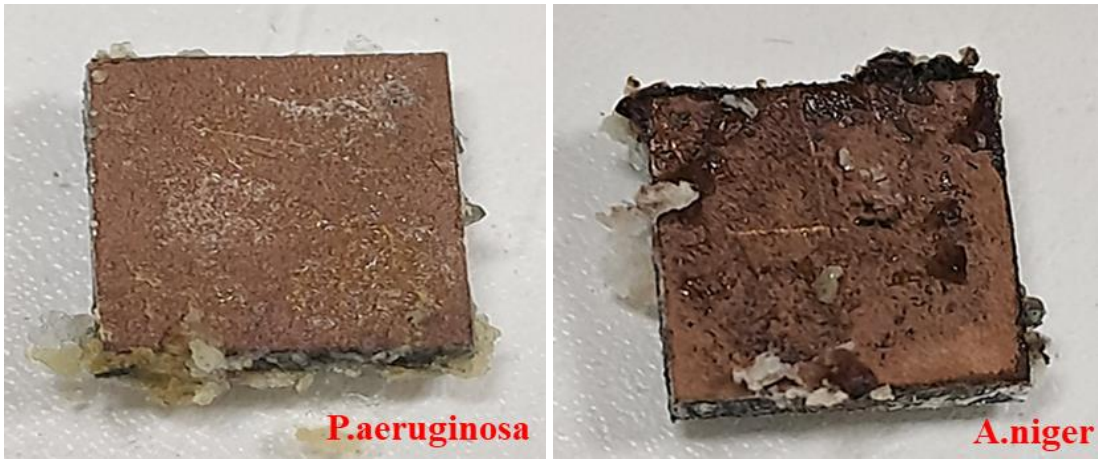
(c)


P.aeruginosa
A.niger

(d)


P.aeruginosa
A.niger

(e)



(f)

Figure 7.20 Images of specimens removed and cleaned from the growth medium: **(a)** 7075 AA, **(b)** Bulk Cu, **(c)** CA, **(d)** CNZA15, **(e)** CNZA30 and **(f)** CZA

Upon evaluating the specimens removed from the *Pseudomonas aeruginosa* and *Aspergillus niger* growth mediums, the initial impression was that the specimens were more affected by the MIC phenomenon in the growth medium inoculated with *P. aeruginosa* compared to the growth medium inoculated with *A. niger*. In the *P. aeruginosa* environment, MIC effects were observed in all specimens except CZA. In this context, pits were observed on the surface of 7075 AA, oxidation was identified in bulk Cu and general corrosion effects were noted. In CA, CNZA15 and CNZA30 specimens, along with galvanic interaction, the substrate-coating interface became susceptible to corrosion, leading to a breakdown in substrate-coating integrity and delamination in the coatings. In the CNZA30 specimen, the coating separated completely from the substrate, exposing the 7075 AA substrate surface. The MIC resistance exhibited by the coatings in the *P. aeruginosa* environment was determined in the order of CNZA30 < CNZA15 < CA < CZA. These findings were consistent with the antibacterial activity hierarchy determined in the literature as Ni < Cu < Zn.

In the *A. niger* environment, general corrosion effects were observed on the surfaces of the 7075 AA and bulk Cu specimens. However, for Cu-based coatings no signs of corrosion were detected, the coating-substrate interface remained unaffected by corrosion and coating integrity was preserved. Additionally, the superior antifungal effect exhibited by Cu-based coatings in the *A. niger* environment compared to the

bulk Cu specimen was attributed to the presence of Al_2O_3 in the coatings (Gudkov et al., 2022).

The fact that CZA showed no signs of MIC in both bacterial and fungal environments and exhibited the best performance among the coatings was attributed to the significant presence of Zn within the coating. In a study conducted by Pasquet et al., (2014), it was found that zinc ions (Zn^{2+}) demonstrated antimicrobial activity against various bacterial and fungal species. The partial dissolution of ZnO particles released Zn^{2+} ions into the aqueous suspension, contributing to the antimicrobial activity of ZnO. Sanpo et al., (2011) conducted a study on the biocompatibility and antibacterial properties of a cold-sprayed ZnO/Titanium composite coating. The results indicated that ZnO/Ti coatings exhibited significant antibacterial effects against *E. coli.* Additionally, biocompatibility results demonstrated a decrease in cell viability with an increase in the concentration of ZnO in the coating composition. Sanpo & Tharajak, (2017) investigated the antimicrobial properties of coatings containing different transition metals such as silver, nickel, zinc and copper against *Staphylococcus aureus* in another study. The study evaluated the lethal effect of cold-sprayed specimens on the control solution. This assessment resulted in the order Ni < Cu < Zn < Ag, indicating that the maximum antibacterial tendency was observed in the coating containing silver, as the surviving bacterial population was the lowest. In another study, the impact of corrosion on conventional and nanomaterial copper cold-spray surfaces for antimicrobial applications was investigated. Nanomaterial copper, having a smaller grain size and consequently larger grain boundaries compared to conventional copper, contributed to an increased ion release rate, leading to enhanced corrosion. The increased ion release for nanomaterial copper directly contributed to its antimicrobial effectiveness. When comparing the average particle size distributions of the coating powders used in this thesis study, the lowest average particle size was determined for CZA. Therefore, it is believed that the increased ion release due to the small particle size contributes to the antimicrobial effectiveness of CZA (Sundberg et al., 2019).

Following the MIC tests, the specimens were decontaminated through autoclave sterilization at 121°C and 1.5 Atm pressure for 30 minutes, as a compulsory

requirement. Consequently, this process induced changes in the surface morphologies of the specimens, made it impractical to conduct OM or SEM examinations and prevented a meaningful interpretation.

7.5 Tribological Properties

7.5.1 Wear Behavior

Wear tests were conducted under both dry sliding and lubricated conditions using high-temperature grease with PTFE additives and perfluoropolyether base (Lubcon Turmotemp II/400 KL-LUBRICANT CONSULT GmbH) and wear tracks were obtained. To determine the exact final shape of the wear surfaces and calculate the volume of material lost due to wear, an Ambios Technology XP-2 surface profilometer was employed. Sectional area measurements of the wear tracks were carried out using the TrueSurf program and volume losses were calculated. Volume losses for the specimens were separately calculated under dry sliding and lubricated conditions, as presented in Table 7.9. Moreover, the porous nature of Cu-based coatings has facilitated the retention and presence of the grease on the surface by adhering to these pores, thereby minimizing wear to a great extent. The solid lubricating layer remained within the wear tracks and pores throughout the duration of the wear test, mitigating frictional forces and protecting the coating from wear damage. Consequently, it was not feasible to conduct sectional area measurements of wear tracks or measure volume losses for Cu-based coatings under lubricated conditions.

Table 7.9 Volume loss values of specimens that were obtained by TrueSurf program.

Specimen	**Volume loss (mm^3)**	
	Dry condition	Lubricated condition
7075 AA	0.171	0.153
CA 10p	0.065	-
CA 20p	0.046	-
CNZA15 10p	0.053	-
CNZA15 20p	0.033	-
CNZA30 10p	0.027	-
CNZA30 20p	0.021	-
CZA 10p	0.141	-
CZA 20p	0.114	-

The wear rates and wear profiles of bare 7075 AA (under dry sliding and lubricated conditions) and Cu-based coatings (under dry sliding conditions) are presented in Figures 7.21 and 7.22, respectively.

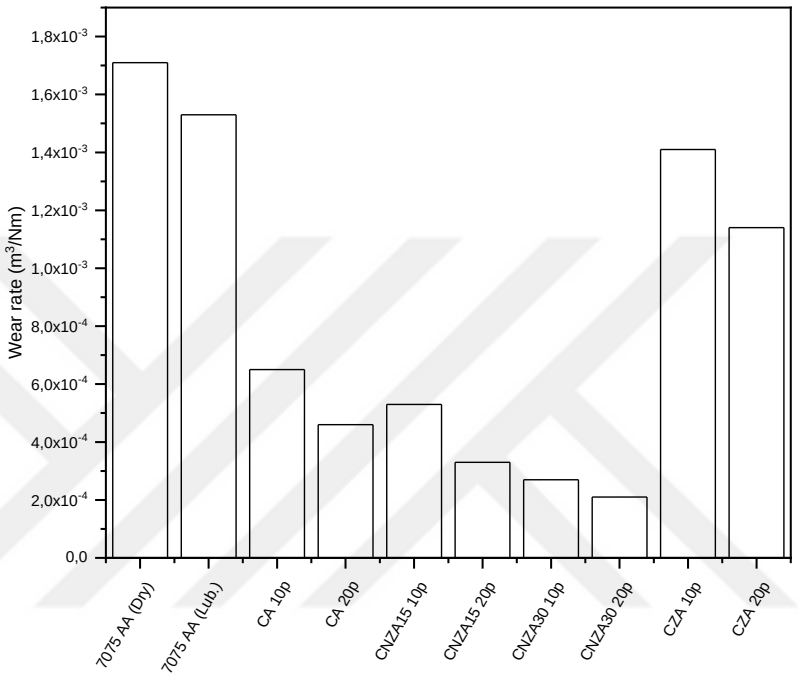
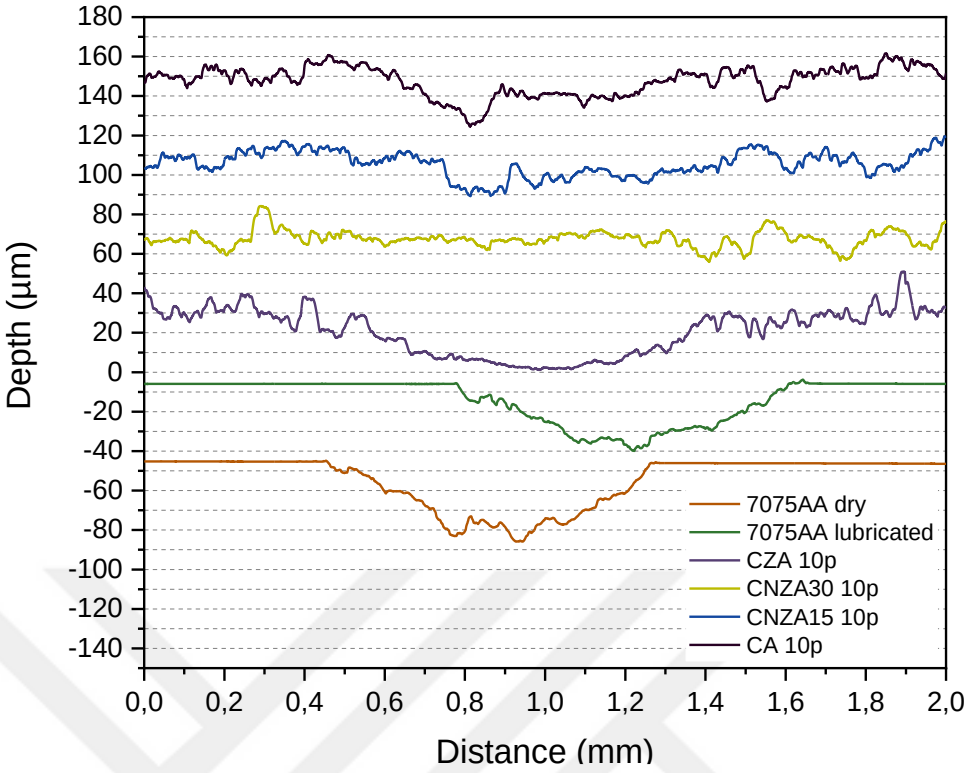
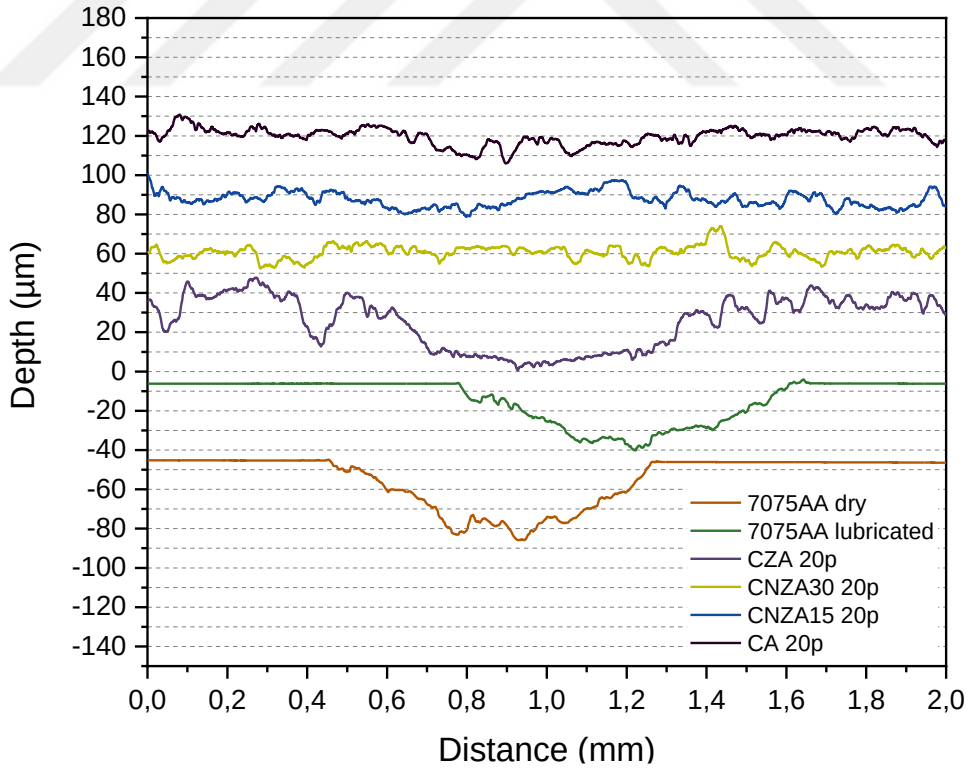


Figure 7.21 Wear rates of specimens against AISI 52100 steel ball at an applied load of 1 N



(a)



(b)

Figure 7.22 Wear profiles of specimens against AISI 52100 steel ball at an applied load of 1 N: **(a)** 10 passes and **(b)** 20 passes

Upon thorough examination of Table 7.9, Figure 7.21 and Figure 7.22, it has been determined that the volume loss and wear rate for 7075 AA are higher under both dry sliding and lubricated conditions compared to Cu-based coatings. The grease used during the tests was found to be ineffective on 7075 AA, unable to sustain the lubricating film layer on the interface. Therefore, there was only a limited improvement in both volume loss and wear rate under lubricated conditions. Additionally, it has been proven that the wear profiles obtained for 7075 AA match the ball geometry under both dry sliding and lubricated conditions, confirming that the worn material during the tests was indeed 7075 AA.

In contrast, it has been observed that the volume loss and wear rate in Cu-based coatings are lower compared to 7075 AA. Particularly, the increase in hardness values in Ni-containing coatings significantly reduces both volume loss and wear rates, with CNZA30 coatings demonstrating the most successful results among the coatings. Similarly, the worst wear performance was exhibited by CZA coatings, showing a correlation with hardness. Additionally, it has been understood that the presence of Al_2O_3 particles in the coatings contributes to enhancing wear resistance, especially in CNZA30 and other coatings. When examining the wear profiles provided in Figure 7.22, it is evident that the profile depth is lower than the coating thickness, indicating that the wear did not reach the interface. The 20 passes coatings, which are more intensively subjected to peening effects, showed a slight improvement in volume loss and wear rates compared to 10 passes coatings, accompanied by lower surface roughness.

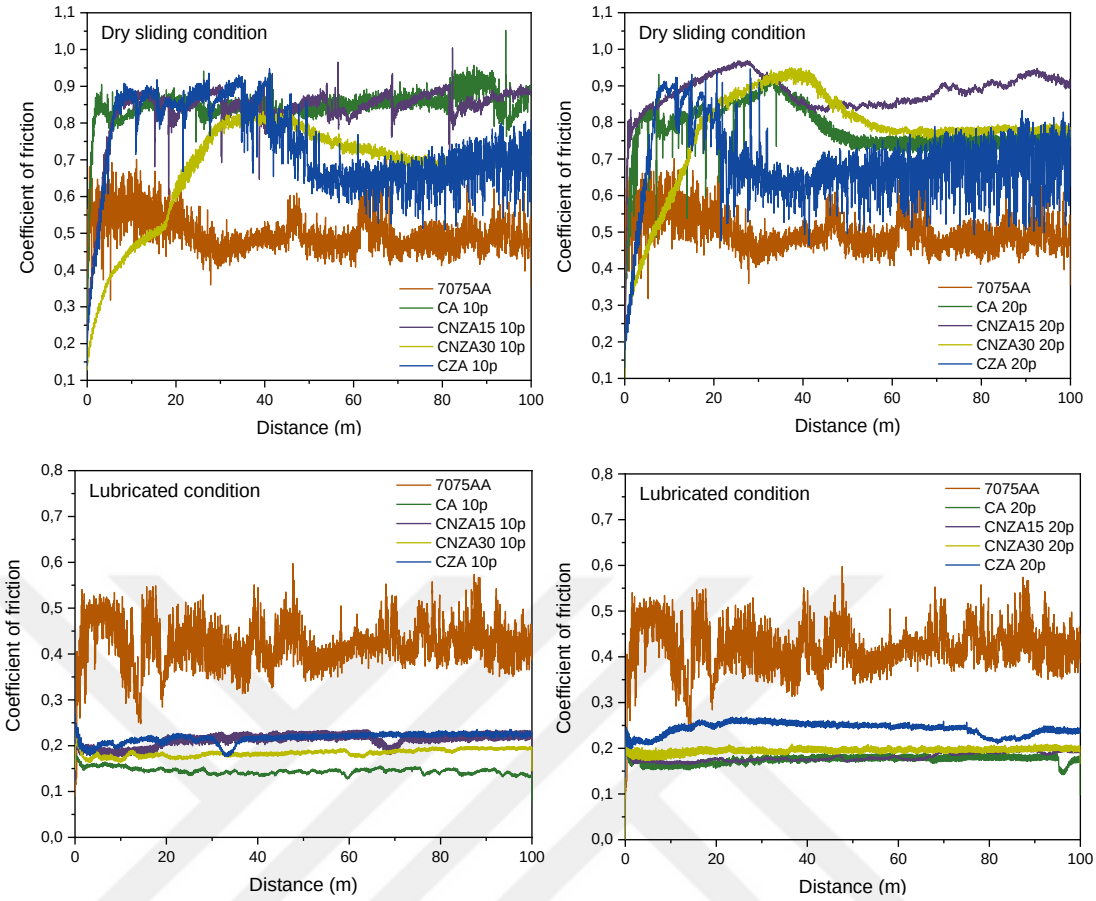


Figure 7.23 Friction coefficients of specimens with dry sliding condition and lubricated condition

When examining the friction coefficient curves provided in Figure 7.23, it is observed that under dry sliding conditions, 7075 AA exhibits a lower friction coefficient compared to Cu-based coatings. Despite the fact that the substrate material, 7075 AA, has the lowest friction coefficient, it shows the highest volume loss and wear rate. This discrepancy is attributed to the ductile nature of aluminum, establishing a metal-to-metal contact and the occurrence of cold contact bonds. Under lubricated conditions, it has been found that the applied grease has minimal effectiveness on 7075 AA, resulting in a limited decrease in the friction coefficient. Additionally, in both dry sliding and lubricated conditions, the sharp fluctuations in the curves for 7075 AA indicate an unstable variation in the friction coefficient.

In Cu-based coatings, the development curve of the friction coefficient has shown a tendency to stabilize after a slow and gradual increase under dry sliding conditions. The friction coefficient of the coatings was found to be higher compared to 7075 AA.

When evaluating the coatings among themselves, under dry sliding conditions, the lowest friction coefficient was observed in CZA coatings, consistent with the literature, indicating an improvement in antifriction performance with the addition of Zn to Cu-based coatings (L. Zhang et al., 2019). Additionally, similar to 7075 AA, sharp fluctuations were observed in the curves of CZA coatings, indicating an unstable variation in the friction coefficient. Under lubricated conditions, it was observed that the friction coefficients of Cu-based coatings exhibited a dramatic decrease and the development curves remained stable from the beginning of the measurements, indicating the significant effectiveness of the applied grease on the surface. Moreover, the minimal occurrence of wear in Cu-based coatings, leading to the inability to perform cross-sectional area measurements and measure volume losses, was corroborated by the friction coefficient curves. Finally, both under dry sliding and lubricated conditions, the number of spraying steps (10 passes or 20 passes) did not create a significant change in the friction coefficients of the coatings.

7.5.2 Optical microscopy examinations after wear tests

The wear tracks obtained from the wear tests conducted under both dry sliding and lubricated conditions were examined through OM at 50x magnification and the results are presented in Figure 7.24. The widths of the wear tracks are provided in Table 7.10. Upon inspecting the wear tracks, it was observed that scratches appeared on the surface of 7075 AA under both dry sliding and lubricated conditions, indicating the establishment of metal-metal contact. Therefore, it is understood that both abrasive and adhesive wear mechanisms operated simultaneously during the sliding wear test of 7075 AA against the steel ball. Additionally, the widest wear tracks were measured for 7075 AA, confirming through OM examinations that the lubricating grease had minimal effectiveness on 7075 AA.

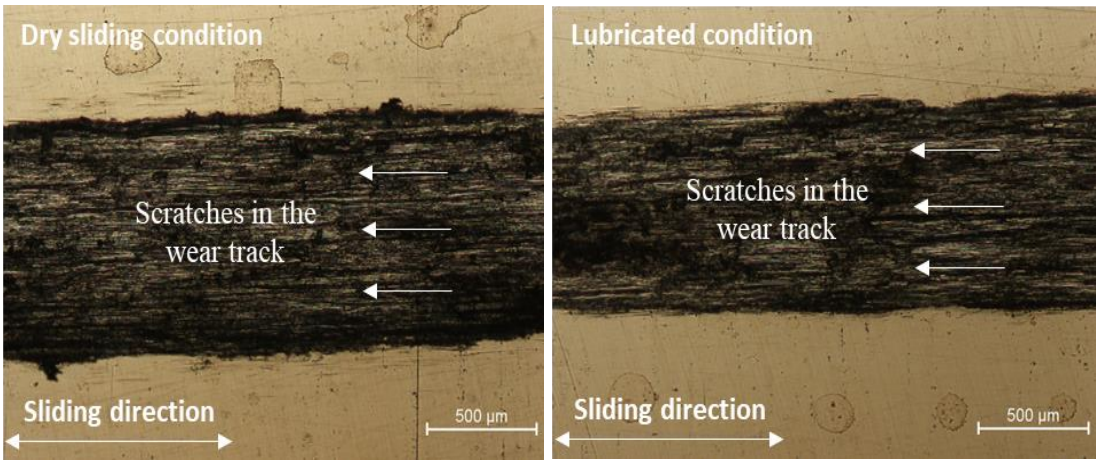
Table 7.10 Wear track width values of specimens that were obtained by OM investigation

Specimen	**Wear track width (µm)**	
	Dry	Solid Lubricant
7075 AA	963.7±7.3	868.0±6.3
CA 10p	749.8±6.5	420.2±3.8

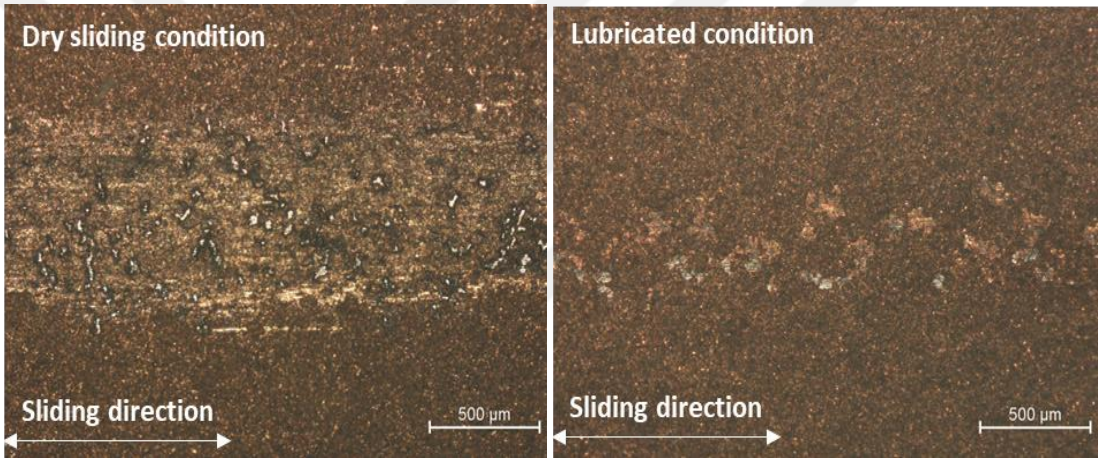
Table 7.10 continues

CA 20p	727.1±6.1	407.6±3.6
CNZA15 10p	719.6±6.1	389.8±3.3
CNZA15 20p	702.0±5.9	349.7±2.8
CNZA30 10p	551.0±4.3	319.7±2.5
CNZA30 20p	407.6±3.9	241.5±1.7
CZA 10p	898.2±6.3	674.3±4.2
CZA 20p	769.9±6.0	488.1±3.9

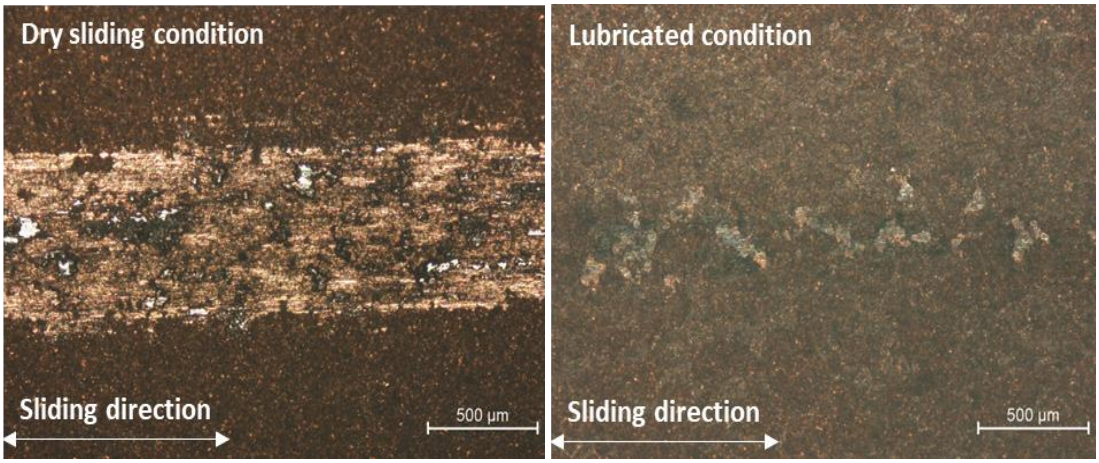
When evaluating the coatings among themselves, it was observed that both under dry sliding and lubricated conditions, the widths of the wear tracks were lower compared to 7075 AA. The number of spraying steps (10 passes or 20 passes) did not create a dramatic difference in the widths of the wear tracks and the lowest wear track widths were identified in CNZA30 coatings, while the highest widths were observed in CZA coatings. Additionally, under dry sliding conditions, scratches were observed on the CZA coating surface, indicating a more dominant abrasive wear mechanism. However, despite having a lower friction coefficient than other coatings under dry sliding conditions, CZA coatings exhibited higher volume loss, wear rate and wear track widths. This observation was attributed to the lower hardness values of CZA coatings. On the other hand, the Cu-based coating with the lowest volume loss, wear rate and wear track width was CNZA30, which proportionally contained the highest amount of Ni and had the highest hardness. Consequently, it was determined that hardness values played a prominent and determining role in the wear performance of Cu-based coatings. During the wear test, it was observed that the protrusions on the coating surface of Cu-based coatings were eliminated, resulting in a smoother surface and indicating the occurrence of abrasive wear mechanisms. Additionally, when CNZA30 coatings were rubbed against the steel ball, a significant amount of material loss occurred from the steel ball, adhering to the coating surface. Findings from the wear profile confirmed material transfer to the coating surface. Furthermore, scratches on the flattened surface of the steel ball used during the test were examined using OM. The obtained images indicated abrasive wear on the steel ball and they are presented in Figure 7.25. It was observed that initially abrasive wear occurred on the steel ball, followed by the establishment of metal-metal contact in the contact regions and leading to micro-polishing.


Dry sliding condition
Scratches in the wear track
Sliding direction
500 µm
Lubricated condition
Scratches in the wear track
Sliding direction
500 µm

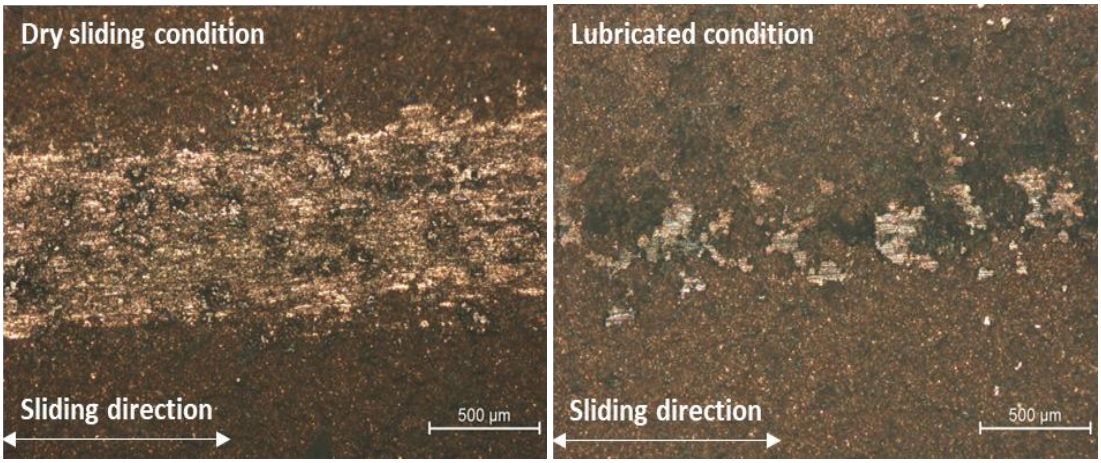
(a)


Dry sliding condition
Sliding direction
500 µm
Lubricated condition
Sliding direction
500 µm

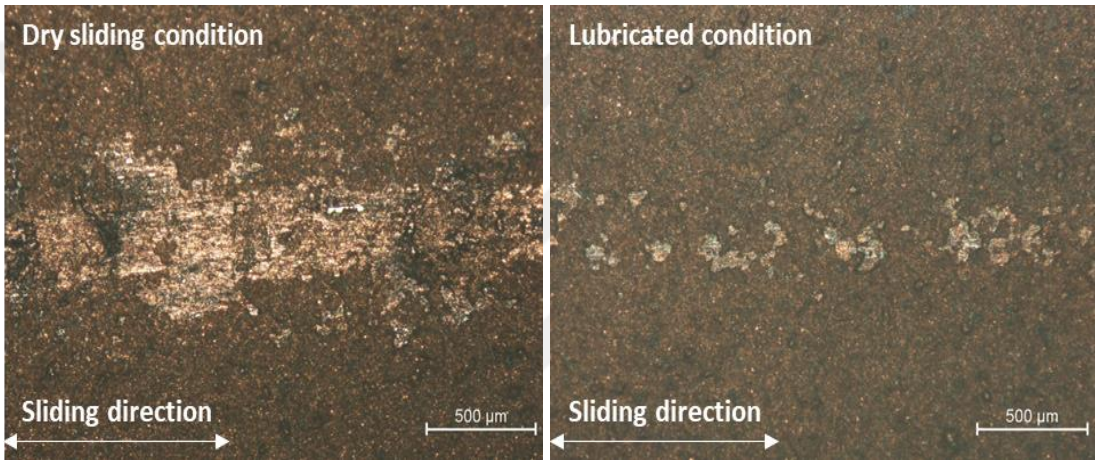
(b)


Dry sliding condition
Sliding direction
500 µm
Lubricated condition
Sliding direction
500 µm

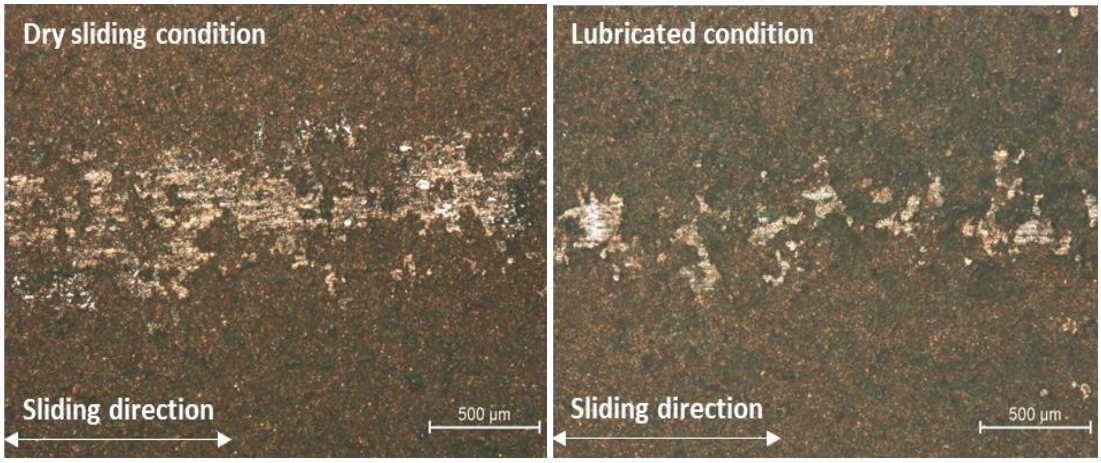
(c)


Dry sliding condition
Sliding direction
500 µm
Lubricated condition
Sliding direction
500 µm

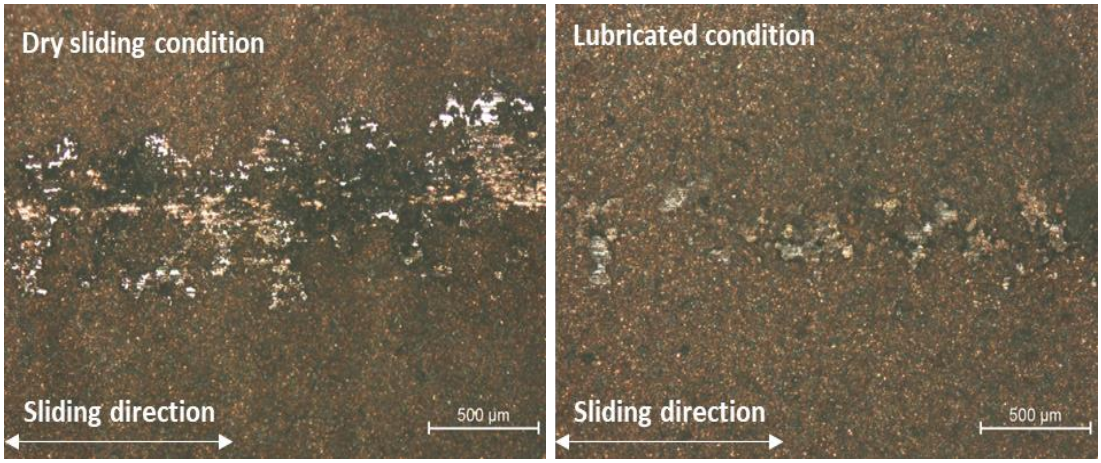
(d)


Dry sliding condition
Sliding direction
500 µm
Lubricated condition
Sliding direction
500 µm

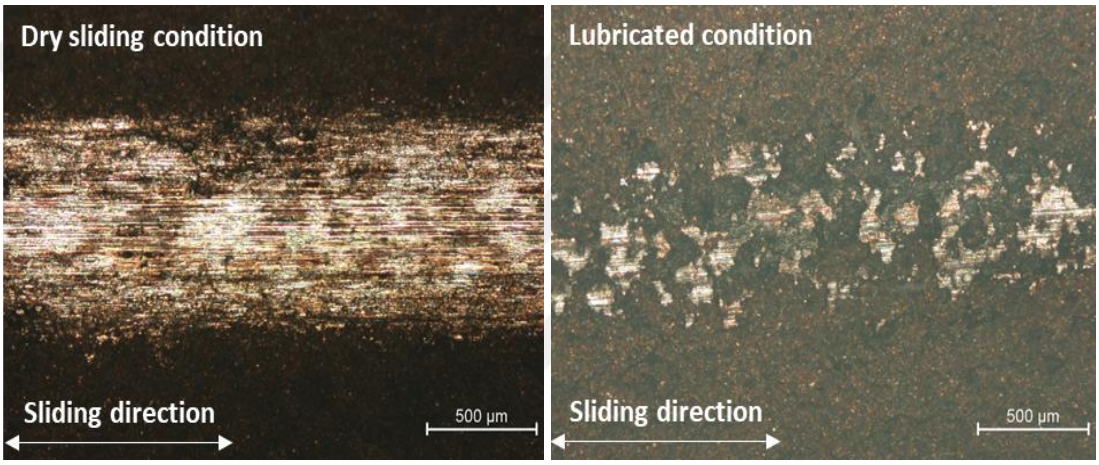
(e)


Dry sliding condition
Sliding direction
500 µm
Lubricated condition
Sliding direction
500 µm

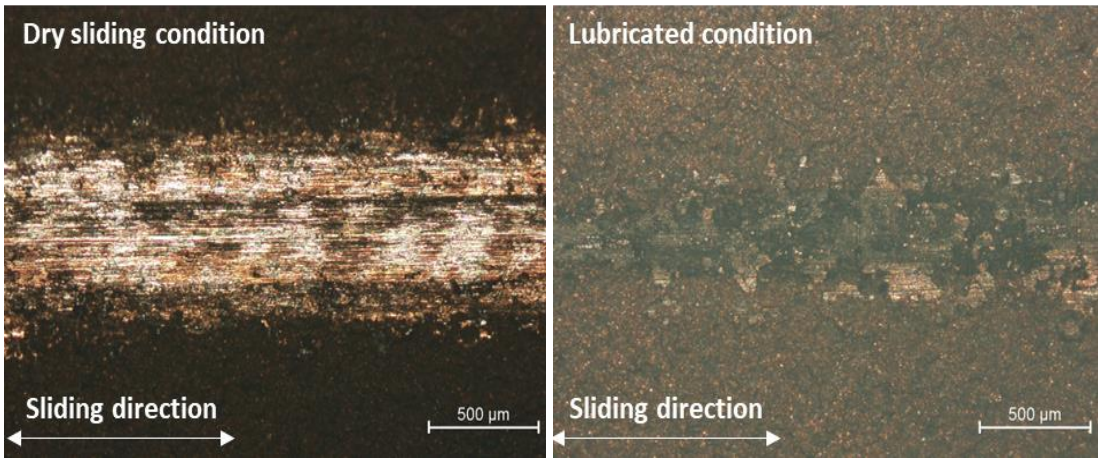
(f)



(g)



(h)



(i)

Figure 7.24 The wear traces observed on specimens: **(a)** 7075 AA, **(b)** CA 10p, **(c)** CA 20p, **(d)** CNZA15 10p, **(e)** CNZA15 20p, **(f)** CNZA30 10 p, **(g)** CNZA30 20 p, **(h)** CZA 10p and **(i)** CZA 20p

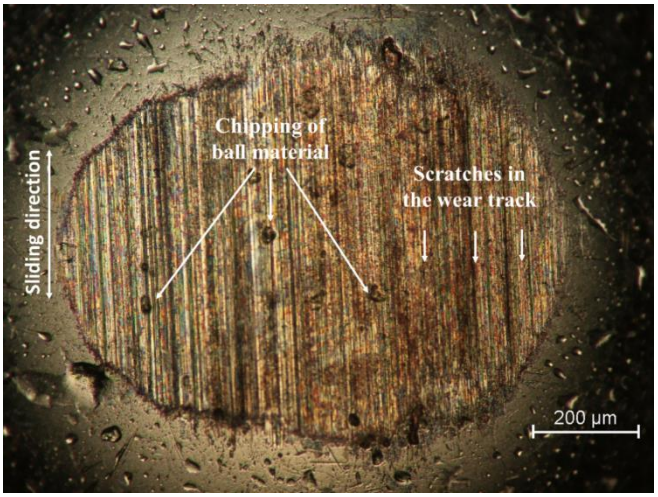


Figure 7.25 The OM image of flattened surface of steel ball rubbed against CNZA30 coating

CHAPTER EIGHT
CONCLUSIONS AND RECOMMENDATIONS

In accordance with the objectives and goals of this thesis, an investigation into state of art the technique has been conducted, a compilation of literature review has been made, experimental studies have been designed and the obtained results have been analyzed. The aim and objectives of the thesis are to enhance the service life of the 7075-T651 armor-grade aluminum alloy, which holds a significant position in defense industry applications, against the prevalent phenomena of localized corrosion, MIC and wear under operational conditions, utilizing Cu-based coatings produced through the CGDS process. Additionally, the effects of coating composition and thickness have been examined for each phenomenon individually. The generated coatings are composite coatings composed of metal and ceramic components, with the dominant metal component being Cu and the ceramic component being Al_2O_3. CA coatings include Cu and Al_2O_3 components. CZA coatings contain Cu-Zn and Al_2O_3 components, with a focus on the influence of the Zn component. CNZA coatings possess Cu-Ni-Zn and Al_2O_3 components and the effects induced by the Ni component have been evaluated. The results indicate that CA coatings exhibit successful outcomes under aggressive corrosion conditions, CZA coatings are the most effective in MIC environments and CNZA coatings perform well in applications where wear is a significant factor.

8.1 Cold Gas Dynamic Spray Process

Both domestic and imported coating powders were employed in the production of coatings and despite the utilization of various CGDS process parameters in studies conducted with domestic coating powders, a satisfactory level of DE could not be achieved. It has been determined that both powder parameters and CGDS process parameters play a crucial role in the successful deposition of coatings.

Coatings were produced by applying process parameters, including 8 bar pressure, 300 °C preheating temperature, 0.3 g/s powder feeding rate, 10 cm/s traverse speed, and 15 mm stand-off distance, using coating powders supplied by Dymet. Under these conditions, particles surpassed the critical velocity, resulting in sufficient DE during the coating production process.

The sandblasting process applied to the substrate material prior to coating production has been determined to lack crucial significance on the DE. In this study, a sandblasting process was conducted with 3.5 bar pressure and 250 μm-sized alumina particles to achieve uniform surface quality for all samples and to activate the surface before the coating process. The surface roughness of the specimens after the sandblasting process was measured as R_a: 1.90 μm and R_z: 14.4 μm.

In this study, the coating process is carried out manually using the Dymet-423 low-pressure CGDS equipment, with coating applied by hand with a spraying gun under normal conditions. Therefore, in addition to powder and process parameters, the operator's manual dexterity also affects the coating quality. As a result, variations in parameters such as stand-off distance and traverse speed occurred, leading to a lack of repeatability in the coatings. Consequently, the necessity of using semi or fully automated coating benchs in coating productions has been recognized to eliminate the operator factor.

8.2 Characterization of Coating Powders

It has been determined that the particle size distribution ranges of the coating powders are compatible with the requirements of the CGDS process. The average particle size values for CA, NZA, CNZA15, CNZA30 and CZA coating powders are determined as 25.30 μm, 27.28 μm, 25.68 μm, 26.81 μm and 22.33 μm, respectively.

It has been discerned that each component in the coating powders exhibits a distinct morphology. In this context, copper has been identified to possess a dendritic morphology, alumina exhibits an angular morphology, nickel displays a spongy morphology and zinc is determined to have a spherical morphology.

The XRD patterns of the coating powders exhibited matches consistent with the analyzed composition and no unexpected phases were detected. In all coating powders except for NZA, the dominant phases were identified as Cu and Al_2O_3. In NZA powder, the dominant phases were found to be Ni and Al_2O_3. Additionally, as expected, Ni phase was detected in CNZA15 and CNZA30 powders, while Zn phase reached significant intensity values in CZA powder.

8.3 Characterization of Cu Based Coatings

It has been determined that the dominant metal matrix in the coating microstructures is copper and the Al_2O_3 particles are uniformly distributed within the metal matrix.

The XRD patterns, microstructure analyses and EDS results have indicated that the phase contents of the powder material and the coatings produced with the same powder are similar. It has been revealed that, due to the inherent nature of the CGDS process, the powders do not undergo high temperatures during the spraying process and there is no thermal effect causing any phase transformation. Simultaneously, no diffraction peaks indicative of oxidation or chemical reaction have been detected.

The highest coating thickness (277.4 μm) and the highest hardness value (192 $HV_{0.025}$) were observed in CNZA30 20p coatings, while the lowest coating thickness (37.44 μm) and the lowest hardness value (87 $HV_{0.025}$) were detected in CZA 10p coatings. Additionally, the number of spraying steps has exerted a positive influence on coating thickness, while it did not lead to a significant change in hardness values.

As a result of the deformation of the powder materials and the deposition process involving different metal/ceramic components, it has been observed that the surface roughness values of Cu-based coatings are higher than those of sandblasted 7075 AA (Ra: 1.9 μm, Rz: 14.4 μm). When evaluating the coatings among themselves, the lowest surface roughness values were determined in the CA 20p coating (Ra: 1.99 μm, Rz: 11.51 μm), while the highest surface roughness values were found in the CZA 10p coating (Ra: 5.35 μm, Rz: 31.74 μm). Additionally, it was observed that the number of spraying steps influenced the surface roughness values and lower surface roughness values were achieved in 20 passes coatings, possibly due to the peening effect.

The scratch tests have demonstrated that the highest critical load, or in other words, the highest adhesion strength, was achieved in CNZA30 coatings. The critical load for CNZA30 coatings was determined to be 130.75 N. Considering that micro-porosity in the coating structure act as stress concentrators and initiate micro-cracks leading to coating delamination, it has been understood that CNZA coatings have the lowest micro-porosity. The low amount of micro-porosity, in conjunction with the influence

of Ni and Zn present in the coating composition, indicates that CNZA30 coatings possess a more dense and compact structure.

8.3 Electrochemical Corrosion Behavior of Cu Based Coatings

Considering the components present in the coating composition, it has been observed that the corrosion potentials undergo changes in the anodic direction due to the influence of the Al_2O_3. When comparing the coatings, except for CZA, all coatings have shifted the corrosion potential of the substrate in the cathodic direction. The highest corrosion potential was observed in CA 20p (-0.288 V), while the lowest corrosion potential was found in CZA 20p (-1.023 V) coatings, indicating that CZA coatings are more active in terms of corrosion reactions.

Under OCP conditions, it has been determined that the i_{corr} values of Cu-based coatings are significantly higher compared to 7075 AA. When comparing the coatings among themselves, the lowest i_{corr} (5.15 μA/cm^2) and CR (53.92 μm/year) were observed in CA 20p coatings, while the highest values were detected in CZA 10p coatings.

It has been determined that as the content of Ni and Zn in the coating increases, the i_{corr} and CR values exhibit a dramatic increase. This phenomenon is associated with the formation of Cu-Ni-Zn and Cu-Zn galvanic couples, specifically observed in CNZA and CZA coatings, respectively. Additionally, in 20 passes coatings displaying a more intense structural morphology along with the peening effect, lower i_{corr} and CR values were measured.

Cyclic polarization curves have demonstrated that 7075 AA rapidly activates, anodic reactions dominate, positive hysteresis occurs, pit formation initiates and passivation does not take place. However, in all Cu-based coatings, it has been determined that anodic reactions are suppressed, negative hysteresis is observed, passivation occurs and, based on the difference in ($E_{rp} – E_{corr}$) values, the coatings can be re-passivated in the order of CZA < CA < CNZA15 < CNZA30. Additionally, in accordance with the i_{corr} values determined through Tafel extrapolation, the lowest i_p

(8.71 μA) and i_f (16.79 μA) values were observed in CA 20p coating, while the highest values were detected in CZA 10p coating.

When impedance spectra were obtained at 0V (vs OCP), it was observed that bare 7075 AA has a higher resistance value compared to Cu-based coatings. However, when the EIS test was conducted at 0.1V (vs OCP) anodic potential, the resistance of 7075 AA was found to be lower. This has been associated with increased anodic currents at 0.1V, which can facilitate local corrosion and hydrogen formation. When comparing the coatings, it was observed that CA coatings have higher resistance values than CNZA and CZA coatings, indicating higher corrosion resistance. Additionally, an increase in coating thickness was observed to result in an increase in the resistance of the coatings. The lowest resistance values were obtained in CZA coatings, which have a higher CR compared to other coatings.

After corrosion tests, OM examinations were conducted to evaluate the formation and severity of corrosion in the samples. For 7075 AA, the initiation of pit formation, its spreading over a significant portion of the surface and the progression of initiated pits towards the microstructure were identified. In the CA coating, general corrosion and corrosion product formation were observed on the surface, but no evidence of pitting corrosion was found. Additionally, it was determined that there were no pits formed and the coating-substrate interface remained clean. In the case of CZA coating, white/gray corrosion products in small patches were observed on the test surface and dezincification was detected in the coating microstructure. Furthermore, dezincification areas were confirmed through point EDS and EDS mapping analyses.

8.4 MIC Behavior of Cu Based Coatings

The MIC analysis results have indicated that, compared to the *A. niger* growth medium, the specimens were more affected in the *P. aeruginosa* growth medium.

In the *P. aeruginosa* growth medium, the formation of blue-green (patina) $Cu_2CO_3(OH)_2$ (copper II carbonate hydroxide) was observed in specimens other than 7075 AA and CZA. Specifically, it was noted that the growth medium color changed from yellow to blue-green, especially where bulk Cu was present.

When evaluating the specimens in the *A. niger* growth medium, it was observed that, except for bulk Cu, all other specimens exhibited dense fungus growth in their vicinity. Additionally, in the CZA specimen, an antifungal effect and an inhibition zone were identified, with a measured zone diameter of 7 mm.

In the *P. aeruginosa* environment, MIC effects were observed in all specimens except for CZA. In this context, pits were observed on the surface of 7075 AA and oxidation of bulk Cu was identified, leading to general corrosion effects. In Cu-based coatings other than CZA, the coating-substrate interface became susceptible to corrosion along with galvanic interactions, causing a disruption in the substrate-coating integrity and resulting in delamination of the coatings. The magnitude of MIC resistance exhibited by the coatings in the *P. aeruginosa* environment was determined as CNZA30 < CNZA15 < CA < CZA, aligning with the antibacterial activity magnitude established in the literature as Ni < Cu < Zn.

In the *A. niger* environment, general corrosion effects were observed on the surfaces of 7075 AA and bulk Cu specimens. However, no signs of corrosion were detected for any of the Cu-based coatings. Among the coatings, only CZA showed no indication of MIC in both bacterial and fungus growth environments, demonstrating the best antibacterial and antifungal effects, which were associated with the significant amount of Zn present in the coating composition.

8.5 Wear Behavior of Cu Based Coatings

Wear tests were conducted under both dry sliding and lubricated conditions using PTFE-impregnated and perfluoropolyether-based high-temperature grease and wear tracks were obtained.

For 7075 AA, it has been determined that the volume loss and wear rate are higher under both dry sliding and lubricated conditions compared to Cu-based coatings. The grease used during the tests was found to be ineffective on 7075 AA and the lubricating film layer could not be sustained on the interface. However, the porous nature of the Cu-based coating surfaces enabled the grease to adhere to these pores, preserving its

presence on the surface and allowing it to be trapped in the pores, resulting in minimal wear with a low coefficient of friction.

It has been determined that the volume loss and wear rate in Cu-based coatings are lower compared to 7075 AA. Under dry sliding conditions, the volume loss was measured as 0.171 mm^3 for 7075 AA, while the CNZA30 20p coating achieved the most successful result with a volume loss of 0.021 mm^3. Particularly, an increase in hardness in Ni-containing coatings led to a significant decrease in volume loss and wear rates. Similarly, the worst wear performance was observed in CZA coatings, consistent with the relationship with hardness. Additionally, it has been understood that the presence of Al_2O_3 particles in the coatings contributes to increasing wear resistance in CNZA30 and other coatings.

When examining wear profiles in Cu-based coatings, it was observed that the profile depth is lower than the coating thicknesses and wear did not reach the interface. Coatings subjected to a more intense peening effect in the case of 20 passes exhibited a slight improvement in volume loss and wear rates compared to 10 passes coatings, along with lower surface roughness.

Under dry sliding conditions, it has been observed that 7075 AA exhibited a lower coefficient of friction compared to Cu-based coatings. Despite the substrate material 7075 AA having the lowest coefficient of friction, it displayed the highest volume loss and wear rate, which is attributed to the ductile nature of aluminum and the occurrence of cold contact bonds.

In Cu-based coatings, the development curve of the coefficient of friction showed a tendency to gradually increase before stabilizing under dry sliding conditions. When evaluating the coatings, the lowest coefficient of friction under dry sliding conditions was identified in CZA coatings, consistent with the literature and it was understood that the presence of Zn in the coating composition improved its antifriction performance.

The wear tracks obtained from wear tests conducted under both dry sliding and lubricated conditions were examined using OM. The examination of wear tracks revealed the occurrence of scratches on the surface of 7075 AA and the establishment

of metal-metal contact both under dry sliding and lubricated conditions. Therefore, it was understood that both abrasive and adhesive wear mechanisms acted together during the sliding wear test of 7075 AA. When evaluating the coatings, it was observed that the width of wear tracks was lower for Cu-based coatings compared to 7075 AA under both dry sliding and lubricated conditions. The wear performance of Cu-based coatings was determined to be primarily influenced by hardness values. During the wear test, it was observed that the protrusions on the coating surface of Cu-based coatings were eliminated, becoming smooth and indicating the presence of an abrasive wear mechanism. Additionally, when CNZA30 coatings were slid against a steel ball, a significant amount of material loss occurred from the steel ball, adhering to the coating surface. Findings suggesting material transfer to the coating surface were obtained from the wear profile.

8.6 Future Works

The CGDS process has been recognized as a promising and versatile technology for materials with temperature sensitivity. The thesis, in conjunction with Cu-based cold gas dynamic sprayed coatings, has demonstrated promising results in addressing issues related to localized corrosion, MIC and wear phenomena. It is anticipated that further improvements in results can be achieved through design studies of powder composition or the application of different post-treatment methods such as heat treatment, laser treatment, shot peening, CIP-HIP, PEO, etc.

Considering the potential of our country's aerospace and defense industry, it is believed that there is a limited level of sensitivity towards the research topic. Particularly, the reliance on imported devices, equipment and coating powders presents a barrier for researchers and users. Therefore, efforts can be directed towards the development of domestic coating powders and optimization of both powder and CGDS process parameters for their production, given the significance of the aerospace and defense industry. The establishment of domestic powder production can lead to the design of different powder compositions and their application in various fields. For instance, embargoes on the importation of carbide or boride-based coating powders

may hinder the development and production of armor featured coatings within the current circumstances.

As part of future plans for defense industry applications, research can be conducted on Cu-based coatings with electromagnetic shielding properties. Especially in the aerospace industry, where there is a rising trend in composite materials, it might be possible to develop innovative coatings that can protect composite materials from lightning or provide flame-retardant properties. Additionally, there is a rapidly increasing expectation for the application of armor-based coatings on lightweight substrate materials.

REFERENCES

Abdel-Gawad, S. A., Sadik, M. A., & Shoeib, M. A. (2019). Preparation and properties of a novel nano Ni-B-Sn by electroless deposition on 7075-T6 aluminum alloy for aerospace application. *Journal of Alloys and Compounds*, *785*, 1284–1292. https://doi.org/10.1016/J.JALLCOM.2019.01.245

Adaan-Nyiak, M. A., & Tiamiyu, A. A. (2023). Recent advances on bonding mechanism in cold spray process: A review of single-particle impact methods. *Journal of Materials Research*, *38*(1), 69–95. https://doi.org/10.1557/s43578-022-00764-2

Ajdelsztajn, L., Zúñiga, A., Jodoin, B., & Lavernia, E. J. (2006). Cold gas dynamic spraying of a high temperature Al alloy. *Surface and Coatings Technology*, *201*(6), 2109–2116. https://doi.org/10.1016/J.SURFCOAT.2005.06.001

Al-Mangour, B., Mongrain, R., Irissou, E., & Yue, S. (2013). Improving the strength and corrosion resistance of 316L stainless steel for biomedical applications using cold spray. *Surface and Coatings Technology*, *216*, 297–307. https://doi.org/10.1016/J.SURFCOAT.2012.11.061

Al-Mangour, B., Vo, P., Mongrain, R., Irissou, E., & Yue, S. (2014). Effect of heat treatment on the microstructure and mechanical properties of stainless steel 316L coatings produced by cold spray for biomedical applications. *Journal of Thermal Spray Technology*, *23*(4), 641–652. https://doi.org/10.1007/S11666-013-0053-2/FIGURES/16

AlMangour, B. (2017). Fundamentals of cold spray processing: Evolution and future perspectives. *Cold-Spray Coatings: Recent Trends and Future Perspectives*, 3–24. https://doi.org/10.1007/978-3-319-67183-3_1

Amodeo, R. J., & Ghoniem, N. M. (1990). Dislocation dynamics. I. A proposed methodology for deformation micromechanics. *Physical Review. B, Condensed Matter*, *41*(10), 6958–6967. https://doi.org/10.1103/PHYSREVB.41.6958

Archard, J. F. (1953). Contact and Rubbing of Flat Surfaces. *Journal of Applied*

Physics, *24*(8), 981–988. https://doi.org/10.1063/1.1721448

Arrabal, R., Mingo, B., Pardo, A., Mohedano, M., Matykina, E., & Rodríguez, I. (2013). Pitting corrosion of rheocast A356 aluminium alloy in 3.5 wt.% NaCl solution. *Corrosion Science*, *73*, 342–355. https://doi.org/10.1016/J.CORSCI.2013.04.023

Assadi, H., Gärtner, F., Stoltenhoff, T., & Kreye, H. (2003). Bonding mechanism in cold gas spraying. *Acta Materialia*, *51*(15), 4379–4394. https://doi.org/10.1016/S1359-6454(03)00274-X

Assadi, H., Kreye, H., Gärtner, F., & Klassen, T. (2016). Cold spraying - A materials perspective. *Acta Materialia*, *116*, 382–407. https://doi.org/10.1016/J.ACTAMAT.2016.06.034

Bae, G., Xiong, Y., Kumar, S., Kang, K., & Lee, C. (2008). General aspects of interface bonding in kinetic sprayed coatings. *Acta Materialia*, *56*(17), 4858–4868. https://doi.org/10.1016/J.ACTAMAT.2008.06.003

Bala, N., Singh, H., & Prakash, S. (2007). An Overview of Cold Spray Technique. *Materials Science Forum*, *561–565*, 2419–2422. https://doi.org/10.4028/www.scientific.net/msf.561-565.2419

Bashir, M. I., Shafiq, M., Naeem, M., Zaka-ul-Islam, M., Díaz-Guillén, J. C., Lopez-Badillo, C. M., & Zakaullah, M. (2017). Enhanced surface properties of aluminum by PVD-TiN coating combined with cathodic cage plasma nitriding. *Surface and Coatings Technology*, *327*, 59–65.

Beech, I., Bergel, A., Mollica, A., Flemming, H.-C., Scotto, V., & Sand, W. (2000). Simple methods for the investigation of the role of biofilms in corrosion. *Brite Euram Thematic Network on MIC of Industrial Materials, Task Group1, Biofilm Fundamentals, Brite Euram Thematic Network No. ERB BRRT-CT98-5084*.

Beesley, C., & Eyre, T. S. (1976). Friction and wear of aluminium alloys containing copper and zinc. *Tribology International*, *9*(2), 63–69. https://doi.org/10.1016/0301-679X(76)90047-5

Bhagat, R. B., Amateau, M. F., Papyrin, A., Conway, J. C., Stutzman, B., & Jones, B. (1997). Deposition of Nickel-Aluminum Bronze Powder by Cold Gas-Dynamic Spray Method on 2618 AI for Developing Wear Resistant Coatings. *Thermal Spray 1997: Proceedings from the United Thermal Spray Conference*, *83812*, 361–367. https://doi.org/10.31399/ASM.CP.ITSC1997P0361

Biestek, T., & Weber, J. (1976). *Electrolytic and chemical conversion coatings: a concise survey of their production, properties and testing*. Portcullis Press Limited.

Birbilis, N., & Hinton, B. (2010). Corrosion and corrosion protection of aluminium. In *Fundamentals of Aluminium Metallurgy: Production, Processing and Applications*. Woodhead Publishing Limited. https://doi.org/10.1533/9780857090256.2.574

Bock, E., & Whitley, J. (1999). *Frettıng Corrosıon In Electrıc Contacts*.

Borchers, C., Schmidt, T., Gärtner, F., & Kreye, H. (2008). High strain rate deformation microstructures of stainless steel 316L by cold spraying and explosive powder compaction. *Applied Physics A: Materials Science and Processing*, *90*(3), 517–526. https://doi.org/10.1007/S00339-007-4314-0/METRICS

Botef, I., & Villafuerte, J. (2015). Overview. *Modern Cold Spray: Materials, Process, and Applications*, 1–29. https://doi.org/10.1007/978-3-319-16772-5_1

Bray, M., Cockburn, A., & O'Neill, W. (2009). The Laser-assisted Cold Spray process and deposit characterisation. *Surface and Coatings Technology*, *203*(19), 2851–2857. https://doi.org/10.1016/J.SURFCOAT.2009.02.135

Buckley, D. H., & Johnson, R. L. (1968). The influence of crystal structure and some properties of hexagonal metals on friction and adhesion. *Wear*, *11*(6), 405–419. https://doi.org/10.1016/0043-1648(68)90550-4

Cagan, S. C., Venkatesh, B., & Buldum, B. B. (2020). Investigation of surface roughness and chip morphology of aluminum alloy in dry and minimum quantity lubrication machining. *Materials Today: Proceedings*, *27*(xxxx), 1122–1126. https://doi.org/10.1016/j.matpr.2020.01.547

Cao, G. P., & Song, R. G. (2018). Microstructure and properties of ceramic coatings prepared by micro-arc oxidation on 7075 aluminum alloy. *Materials Research Express*, *5*(2), 026407. https://doi.org/10.1088/2053-1591/AAACA7

Castaneda, H., & Benetton, X. D. (2008). SRB-biofilm influence in active corrosion sites formed at the steel-electrolyte interface when exposed to artificial seawater conditions. *Corrosion Science*, *50*(4), 1169–1183. https://doi.org/10.1016/J.CORSCI.2007.11.032

Cavaliere, P. (2017). Cold-Spray Coatings: Recent Trends and Future perspectives. *Cold-Spray Coatings: Recent Trends and Future Perspectives*, 1–570. https://doi.org/10.1007/978-3-319-67183-3/COVER

Celotto, S., Pattison, J., Ho, J. S., Johnson, A. N., & O'Neill, W. (2007). The economics of the cold spray process. *The Cold Spray Materials Deposition Process: Fundamentals and Applications*, 72–101. https://doi.org/10.1533/9781845693787.1.72

Champagne, V., & Helfritch, D. (2015). Critical Assessment 11: Structural repairs by cold spray. *Materials Science and Technology*, *31*(6), 627–634. https://doi.org/10.1179/1743284714Y.0000000723

Champagne, V., & Helfritch, D. (2016). The unique abilities of cold spray deposition. *International Materials Reviews*, *61*(7), 437–455. https://doi.org/10.1080/09506608.2016.1194948

Champagne, V. K. (2007). *The cold spray materials deposition process : fundamentals and applications*. *Woodhead Publishing. ISBN: 978-1845691813*

Champagne, V. K. (2008). The repair of magnesium rotorcraft components by cold spray. *Journal of Failure Analysis and Prevention*, *8*(2), 164–175.

https://doi.org/10.1007/S11668-008-9116-Y/METRICS

Champagne, V. K., & Barnett, B. (2012). Cold spray technology for DOD applications. *ASETS Defense*, 27–30.

Champagne, V. K., Champagne, V. K., & Widener, C. (2017). Cold spray applications. In *Cold-Spray Coatings: Recent Trends and Future perspectives*. https://doi.org/10.1007/978-3-319-67183-3_2

Champagne, V. K., & Helfritch, D. J. (2013). A demonstration of the antimicrobial effectiveness of various copper surfaces. *Journal of Biological Engineering*, *7*(1). https://doi.org/10.1186/1754-1611-7-8

Champagne, V. K., Helfritch, D. J., Trexler, M. D., & Gabriel, B. M. (2010). The effect of cold spray impact velocity on deposit hardness. *Modelling and Simulation in Materials Science and Engineering*, *18*(6), 065011. https://doi.org/10.1088/0965-0393/18/6/065011

Champagne, V. K., Helfritch, D., Leyman, P., Grendahl, S., & Klotz, B. (2005). Interface material mixing formed by the deposition of copper on aluminum by means of the cold spray process. *Journal of Thermal Spray Technology*, *14*(3), 330–334. https://doi.org/10.1361/105996305X59332/METRICS

Chavan, N. M., Kiran, B., Jyothirmayi, A., Phani, P. S., & Sundararajan, G. (2013). The corrosion behavior of cold sprayed zinc coatings on mild steel substrate. *Journal of Thermal Spray Technology*, *22*(4), 463–470. https://doi.org/10.1007/S11666-013-9893-Z/METRICS

Chen, H., Liu, C., Chu, X., Zhang, T., & Zheng, J. (2022). Corrosion Behavior and Microstructure of Cu-Based Composite Coatings Deposited by Cold Spraying. *Metals*, *12*(6). https://doi.org/10.3390/met12060955

Chen, W., Yu, Y., Ma, J., Zhu, S., Liu, W., & Yang, J. (2019). Low-Pressure Cold Spraying of Copper–Graphite Solid Lubricating Coatings on Aluminum Alloy 7075-T651. *Journal of Thermal Spray Technology*, *28*(7), 1688–1698. https://doi.org/10.1007/s11666-019-00905-w

Chen, W., Yu, Y., Tieu, A. K., Hao, J., Wang, L., Zhu, S., & Yang, J. (2020). Microstructure, mechanical properties and tribological behavior of the low-pressure cold sprayed tin bronze-alumina coating in artificial seawater. *Tribology International*, *142*(September 2019), 105992. https://doi.org/10.1016/j.triboint.2019.105992

Chen, Y., Zheng, X., Xie, Y., Ding, C., Ruan, H., & Fan, C. (2008). Anti-bacterial and cytotoxic properties of plasma sprayed silver-containing HA coatings. *Journal of Materials Science: Materials in Medicine*, *19*(12), 3603–3609. https://doi.org/10.1007/S10856-008-3529-8/METRICS

Chraska, P., Dubsky, J., Kolman, B., llavsky, J., & Forman, J. (1992). Study of phase changes in plasma sprayed deposits. *Journal of Thermal Spray Technology*, *1*(4), 301–306. https://doi.org/10.1007/BF02647157/METRICS

Conrad, H., & Rice, L. (1970). The cohesion of previously fractured Fcc metals in ultrahigh vacuum. *Metallurgical Transactions*, *1*(11), 3019–3029. https://doi.org/10.1007/BF03038415/METRICS

da Silva, F. S., Cinca, N., Dosta, S., Cano, I. G., Couto, M., Guilemany, J. M., & Benedetti, A. V. (2018). Corrosion behavior of WC-Co coatings deposited by cold gas spray onto AA 7075-T6. *Corrosion Science*, *136*, 231–243. https://doi.org/10.1016/j.corsci.2018.03.010

da Silva, F. S., Cinca, N., Dosta, S., Cano, I. G., Guilemany, J. M., & Benedetti, A. V. (2020). Effect of the Outer Layer of Al Coatings Deposited by Cold Gas Spray on the Microstructure, Mechanical Properties and Corrosion Resistance of the AA 7075-T6 Aluminum Alloy. *Journal of Thermal Spray Technology*, *29*(5), 1040–1053. https://doi.org/10.1007/s11666-020-01023-8

da Silva Savonov, G., Camarinha, M. G. G., Rocha, L. O., Barboza, M. J. R., Martins, G. V., & Reis, D. A. P. (2019). Study of the influence of the RRA thermal treatment and plasma nitriding on corrosion behavior of 7075-T6 aluminum alloy. *Surface and Coatings Technology*, *374*, 736–744.

https://doi.org/10.1016/J.SURFCOAT.2019.04.095

Davis, J. R. (1996a). ASM speciality handbook: Aluminium and aluminium alloys. *Metallic Materials*, 700. http://www.amazon.co.uk/ASM-Speciality-Handbook-Aluminium-Alloys/dp/087170496X

Davis, J. R. (1996b). ASM speciality handbook: Aluminium and aluminium alloys. *Metallic Materials*, 700. http://www.amazon.co.uk/ASM-Speciality-Handbook-Aluminium-Alloys/dp/087170496X

Davis, J. R. (2004). Handbook of Thermal Spray Technology. *Technology*. Materials Park, OH: ASM Internatiol.

Davis, J. R. (Joseph R. . (1999). *Corrosion of aluminum and aluminum alloys*. ASM Internatiol, Ohio.

Davis, J. R. (Joseph R. . (2001). *Surface engineering for corrosion and wear resistance*. ASM Internatiol,USA.

DeForce, B., Eden, T., Potter, J., Champagne, V., Leyman, P., & Helfritch, D. (2007). Application of aluminum coatings for the corrosion protection of magnesium by cold spray. *Tri-Service Corrosion Conference. Denver, USA*.

Dexter, S. C. (2003). Microbiologically Influenced Corrosion. *Corrosion: Fundamentals, Testing, and Protection*, 398–416. https://doi.org/10.31399/ASM.HB.V13A.A0003637

Dickinson, M. E., & Yamada, M. (2010). A new method for measuring shear adhesion strength of ceramic cold spray splats. *Nanoscience and Nanotechnology Letters*, *2*(4), 348–351. https://doi.org/10.1166/NNL.2010.1106

Diggle, J. W., Downie, T. C., & Goulding, C. W. (1969). Anodic oxide films on aluminum. *Chemical Reviews*, *69*(3), 365–405. https://doi.org/10.1021/CR60259A005/ASSET/CR60259A005.FP.PNG_V03

Ding, Z. (Vivian). (2019). Mechanistic study of thin film sulfuric acid anodizing rate difference between Al2024 T3 and Al6061 T6. *Surface and Coatings*

Technology, *357*, 280–288. https://doi.org/10.1016/J.SURFCOAT.2018.09.083

DOBLER, K. (2006). Reconditioning reconditioning power-generation components with thermal spray. *Welding Journal*, *85*(5), 23–25.

Dobler, K., Kreye, H., & Schwetzke, R. (2000). Oxidation of stainless steel in the high velocity oxy-fuel process. *Journal of Thermal Spray Technology*, *9*(3), 407–413. https://doi.org/10.1361/105996300770349872/METRICS

Drehmann, R., Grund, T., Lampke, T., Wielage, B., Manygoats, K., Schucknecht, T., & Rafaja, D. (2014). Interface Characterization and Bonding Mechanisms of Cold Gas-Sprayed Al Coatings on Ceramic Substrates. *Journal of Thermal Spray Technology*, *24*(1–2), 92–99. https://doi.org/10.1007/S11666-014-0189-8/METRICS

Dursun, T., & Soutis, C. (2014). Recent developments in advanced aircraft aluminium alloys. *Materials and Design*, *56*, 862–871. https://doi.org/10.1016/j.matdes.2013.12.002

Dykhuizen, R. C., Smith, M. F., Gilmore, D. L., Neiser, R. A., Jiang, X., & Sampath, S. (1999). Impact of high velocity cold spray particles. *Journal of Thermal Spray Technology*, *8*(4), 559–564. https://doi.org/10.1361/105996399770350250/METRICS

Dzhurinskiy, D., Maeva, E., Leshchinsky, E., & Maev, R. G. (2012). Corrosion protection of light alloys using low pressure cold spray. *Journal of Thermal Spray Technology*, *21*(2), 304–313. https://doi.org/10.1007/s11666-011-9729-7

Eden, T. J., Wolfe, D. E., Champagne, V., & Widener, C. (2016). Cold Spray Applications in the Defense Industry. *High Pressure Cold Spray*, 227–251. https://doi.org/10.31399/ASM.TB.HPCSPA.T54460227

Emde, K. M. E., Smith, D. W., & Facey, R. (1992). Initial investigation of microbially influenced corrosion (MIC) in a low temperature water distribution system. *Water Research*, *26*(2), 169–175. https://doi.org/10.1016/0043-

1354(92)90216-Q

Fan, Q., Fu, L., Lin, L., Lai, S., Huang, X. J., Zhang, Y., Luo, Y., Li, X., & Zhang, H. Z. (2021). Corrosion Behavior of 7075-T6 Aluminum Alloy in the Presence of Aspergillus Niger. *International Journal of Electrochemical Science*, *16*, 1–16. https://doi.org/10.20964/2021.09.24

Fauchais, P., Montavon, G., & Bertrand, G. (2010). From powders to thermally sprayed coatings. *Journal of Thermal Spray Technology*, *19*(1–2), 56–80. https://doi.org/10.1007/S11666-009-9435-X/FIGURES/21

Maria Manuel Fernandes Barbosa (2009). *Cold Spray Deposition of Titanium onto Aluminium Substrates"*. Msc.Thesis, unıversity of Porto, Portugal.

Frankel, G. S. (1998). Pitting Corrosion of Metals: A Review of the Critical Factors. *Journal of The Electrochemical Society*, *145*(6), 2186–2198. https://doi.org/10.1149/1.1838615/XML

Frankel, G. S., & McCreery, R. L. (2001). Inhibition of Al alloy corrosion by chromates. *The Electrochemical Society Interface*, *10*(4), 34.

Fukanuma, H., & Huang, R. (2009). Development of High Temperature Gas Heater in the Cold Spray Coating System. *Thermal Spray 2009: Proceedings from the International Thermal Spray Conference*, *83690*, 267–272. https://doi.org/10.31399/ASM.CP.ITSC2009P0267

Fukanuma, H., & Ohno, N. (2004). A study of adhesive strength of cold spray coatings. *Proceedings of the International Thermal Spray Conference*, 329–334. https://doi.org/10.31399/ASM.CP.ITSC2004P0329/19732/A-STUDY-OF-ADHESIVE-STRENGTH-OF-COLD-SPRAY

Gärtner, F., Stoltenhoff, T., Schmidt, T., & Kreye, H. (2006a). The cold spray process and its potential for industrial applications. *Journal of Thermal Spray Technology*, *15*(2), 223–232. https://doi.org/10.1361/105996306X108110

Gärtner, F., Stoltenhoff, T., Schmidt, T., & Kreye, H. (2006b). The cold spray process and its potential for industrial applications. *Journal of Thermal Spray Technology*, *15*(2), 223–232. https://doi.org/10.1361/105996306X108110/METRICS

Gärtner, F., Stoltenhoff, T., Voyer, J., Kreye, H., Riekehr, S., & Koçak, M. (2006). Mechanical properties of cold-sprayed and thermally sprayed copper coatings. *Surface and Coatings Technology*, *200*(24), 6770–6782. https://doi.org/10.1016/J.SURFCOAT.2005.10.007

Ghelichi, R., & Guagliano, M. (2009). Coating by the Cold Spray Process: a state of the art. *Frattura Ed Integrità Strutturale*, *3*(8), 30–44. https://doi.org/10.3221/IGF-ESIS.08.03

Ghelichi, R., MacDonald, D., Bagherifard, S., Jahed, H., Guagliano, M., & Jodoin, B. (2012). Microstructure and fatigue behavior of cold spray coated Al5052. *Acta Materialia*, *60*(19), 6555–6561. https://doi.org/10.1016/J.ACTAMAT.2012.08.020

Ghosh, M., Roy, A., Ghosh, A., Kumar, H., & Saha, G. (2020). Antibacterial and antimicrobial coatings on metal substrates by cold spray technique: Present and future perspectives. In *Green Approaches in Medicinal Chemistry for Sustainable Drug Design*. Elsevier Inc. https://doi.org/10.1016/B978-0-12-817592-7.00002-2

Gilmore, D. L., Dykhuizen, R. C., Neiser, R. A., Roemer, T. J., & Smith, M. F. (1999). Particle velocity and deposition efficiency in the cold spray process. *Journal of Thermal Spray Technology*, *8*(4), 576–582. https://doi.org/10.1361/105996399770350278/METRICS

Go, T., Sohn, Y. J., Mauer, G., Vaßen, R., & Gonzalez-Julian, J. (2019). Cold spray deposition of Cr2AlC MAX phase for coatings and bond-coat layers. *Journal of the European Ceramic Society*, *39*(4), 860–867. https://doi.org/10.1016/J.JEURCERAMSOC.2018.11.035

Goyal T, Sidhu TS, Walia RS (2010) An overview of cold spray process over

competitive technologies for electro-technical applications. In: National conference on advancements and futuristic trends in mechanical and materials engineering, pp. 364–368

Graef HW. 2003. An Analysis of Microbial Contamination in Military Aviation Fuel Systems Ohio. [PhD dissertation]. Air University

Grujicic, M., Tong, C., DeRosset, W. S., & Helfritch, D. (2003). Flow analysis and nozzle-shape optimization for the cold-gas dynamic-spray process. *Http://Dx.Doi.Org/10.1243/095440503771909980*, *217*(11), 1603–1613. https://doi.org/10.1243/095440503771909980

Grujicic, M., Zhao, C. L., DeRosset, W. S., & Helfritch, D. (2004). Adiabatic shear instability based mechanism for particles/substrate bonding in the cold-gas dynamic-spray process. *Materials & Design*, *25*(8), 681–688. https://doi.org/10.1016/J.MATDES.2004.03.008

Gudkov, S. V., Burmistrov, D. E., Smirnova, V. V., Semenova, A. A., & Lisitsyn, A. B. (2022). A Mini Review of Antibacterial Properties of Al2O3 Nanoparticles. *Nanomaterials*, *12*(15), 1–17. https://doi.org/10.3390/nano12152635

Guo, X., Zhang, G., Li, W., Gao, Y., Liao, H., & Coddet, C. (2009). Investigation of the microstructure and tribological behavior of cold-sprayed tin-bronze-based composite coatings. *Applied Surface Science*, *255*(6), 3822–3828. https://doi.org/10.1016/J.APSUSC.2008.10.041

Hagenauer, A., Hilpert, R., & Hack, T. (1994). Microbiological investigations of corrosion damages in aircraft. *Materials and Corrosion*, *45*(6), 355–360. https://doi.org/10.1002/MACO.19940450606

Hinton, B. R. W. (1991). Corrosion prevention and chromates: the end of an era? *Metal Finishing*, *89*(10), 15–20.

Huang, R., & Fukanuma, H. (2012). Study of the influence of particle velocity on adhesive strength of cold spray deposits. *Journal of Thermal Spray Technology*, *21*(3–4), 541–549. https://doi.org/10.1007/S11666-011-9707-0/METRICS

Huang, R., Ma, W., & Fukanuma, H. (2014). Development of ultra-strong adhesive strength coatings using cold spray. *Surface and Coatings Technology*, *258*, 832–

841. https://doi.org/10.1016/J.SURFCOAT.2014.07.074

Hughes, A. E., Taylor, R. J., & Hinton, B. R. W. (1997). Chromate conversion coatings on 2024 Al alloy. *Surface and Interface Analysis: An International Journal Devoted to the Development and Application of Techniques for the Analysis of Surfaces, Interfaces and Thin Films*, *25*(4), 223–234.

Hunter, M. S., Frank Jr, G. R., & Robinson, D. L. (1963). Mechanism of corrosion of 2024 alloy as revealed by electron microscopy. *Proc. 2nd Int. Cong. Metallic Corrosion (Houston, TX: NACE, 1963)*, 102.

Hussain, T. (2012). Cold Spraying of Titanium: A Review of Bonding Mechanisms, Microstructure and Properties. *Key Engineering Materials*, *533*, 53–90. https://doi.org/10.4028/www.scientific.net/kem.533.53

Hussain, T., McCartney, D. G., Shipway, P. H., & Zhang, D. (2009). Bonding mechanisms in cold spraying: The contributions of metallurgical and mechanical components. *Journal of Thermal Spray Technology*, *18*(3), 364–379. https://doi.org/10.1007/s11666-009-9298-1

Hutasoit, N., Topa, S. H., Javed, M. A., Rahman Rashid, R. A., Palombo, E., & Palanisamy, S. (2021). Antibacterial efficacy of cold-sprayed copper coatings against gram-positive staphylococcus aureus and gram-negative escherichia coli. *Materials*, *14*(22). https://doi.org/10.3390/ma14226744

Hwang, S. K., Jeong, S. H., Hwang, H. Y., Lee, O. J., & Lee, K. H. (2002). Fabrication of Highly Ordered Pore Array in Anodic Aluminum Oxide. *Korean Journal of Chemical Engineering*, *19*(3), 467–473. https://doi.org/10.1007/BF02697158/METRICS

in India, K. (2020). *Military materials - Challenges and opportunities*. *September*.

Irissou, E., Legoux, J. G., Arsenault, B., & Moreau, C. (2007). Investigation of Al-Al 2O 3 cold spray coating formation and properties. *Journal of Thermal Spray Technology*, *16*(5–6), 661–668. https://doi.org/10.1007/s11666-007-9086-8

Jeandin, M., Koivuluoto, H., & Vezzu, S. (2015). Coating properties. *Modern Cold*

Spray: Materials, Process, and Applications, 107–224. https://doi.org/10.1007/978-3-319-16772-5_4/COVER

Jin, X., Gao, L., Liu, E., Yu, F., Shu, X., & Wang, H. (2015). Microstructure, corrosion and tribological and antibacterial properties of Ti–Cu coated stainless steel. *Journal of the Mechanical Behavior of Biomedical Materials*, *50*, 23–32. https://doi.org/10.1016/J.JMBBM.2015.06.004

Jing, H., Yu, Z., & Li, L. (2008). Antibacterial properties and corrosion resistance of Cu and Ag/Cu porous materials. *Journal of Biomedical Materials Research Part A*, *87A*(1), 33–37. https://doi.org/10.1002/JBM.A.31688

Jodoin, B. (2001). Effects of Shock Waves on Impact Velocity of Cold Spray Particles. *Proceedings of the International Thermal Spray Conference*, 399–407. https://doi.org/10.31399/ASM.CP.ITSC2001P0399/19219/EFFECTS-OF-SHOCK-WAVES-ON-IMPACT-VELOCITY-OF-COLD

Jodoin, B., Ajdelsztajn, L., Sansoucy, E., Zúñiga, A., Richer, P., & Lavernia, E. J. (2006). Effect of particle size, morphology, and hardness on cold gas dynamic sprayed aluminum alloy coatings. *Surface and Coatings Technology*, *201*(6), 3422–3429. https://doi.org/10.1016/J.SURFCOAT.2006.07.232

Jones, K., & Hoeppner, D. W. (2005). Pit-to-crack transition in pre-corroded 7075-T6 aluminum alloy under cyclic loading. *Corrosion Science*, *47*(9), 2185–2198. https://doi.org/10.1016/J.CORSCI.2004.10.004

Kang, K., Yoon, S., Ji, Y., & Lee, C. (2008). Oxidation dependency of critical velocity for aluminum feedstock deposition in kinetic spraying process. *Materials Science and Engineering: A*, *486*(1–2), 300–307. https://doi.org/10.1016/J.MSEA.2007.09.010

Karthikeyan, J. (2004). Cold spray technology: International status and USA efforts. *ASBindustries Inc*, *December*, 1–14. http://www.asbindustries.com/documents/int_status_report.pdf

Karthikeyan, J. (2007). The advantages and disadvantages of the cold spray coating process. *The Cold Spray Materials Deposition Process: Fundamentals and Applications*, 62–71. https://doi.org/10.1533/9781845693787.1.62

Kaur, N., Kumar, M., Sharma, S. K., Kim, D. Y., Kumar, S., Chavan, N. M., Joshi, S. V., Singh, N., & Singh, H. (2015). Study of mechanical properties and high temperature oxidation behavior of a novel cold-spray Ni-20Cr coating on boiler steels. *Applied Surface Science*, *328*, 13–25. https://doi.org/10.1016/J.APSUSC.2014.12.033

Khan, T. I., Saha, G., & Glenesk, L. B. (2010). Nanostructured composite coatings for oil sand's applications. *Surface Engineering*, *26*(7), 540–545. https://doi.org/10.1179/174329409X439050

Kikuchi, T., Nakajima, D., Nishinaga, O., Natsui, S., & O Suzuki, R. (2015). Porous aluminum oxide formed by anodizing in various electrolyte species. *Current Nanoscience*, *11*(5), 560–571.

Kim, H. J., Lee, C. H., & Hwang, S. Y. (2005a). Fabrication of WC–Co coatings by cold spray deposition. *Surface and Coatings Technology*, *191*(2–3), 335–340. https://doi.org/10.1016/J.SURFCOAT.2004.04.058

Kim, H. J., Lee, C. H., & Hwang, S. Y. (2005b). Superhard nano WC–12%Co coating by cold spray deposition. *Materials Science and Engineering A-Structural Materials Properties Microstructure and Processing*, *391*(1–2), 243–248. https://doi.org/10.1016/J.MSEA.2004.08.082

King, P., Yandouzi, M., & Jodoin, B. (2015). The physics of cold spray. *Modern Cold Spray: Materials, Process, and Applications*, 31–72. https://doi.org/10.1007/978-3-319-16772-5_2/COVER

Klinkov, S. V., Kosarev, V. F., & Rein, M. (2005). Cold spray deposition: Significance of particle impact phenomena. *Aerospace Science and Technology*, *9*(7), 582–591. https://doi.org/10.1016/j.ast.2005.03.005

Klinkov, S. V., Kosarev, V. F., Sova, A. A., & Smurov, I. (2008). Deposition of multicomponent coatings by Cold Spray. *Surface and Coatings Technology*, *202*(24), 5858–5862. https://doi.org/10.1016/J.SURFCOAT.2008.06.171

Knight, S. P., Raman, R. K. S., Muddle, B. C., & Hinton, B. R. W. (2003). Review of heat-treatments for increasing SCC resistance of aluminium alloys. *Australasian Corrosion Association (ACA) Conference 2003: Corrosion Control and NDT Conference*, 31.

Koivuluoto, H., Coleman, A., Murray, K., Kearns, M., & Vuoristo, P. (2012). High pressure cold sprayed (HPCS) and low pressure cold sprayed (LPCS) coatings prepared from OFHC Cu feedstock: Overview from powder characteristics to coating properties. *Journal of Thermal Spray Technology*, *21*(5), 1065–1075. https://doi.org/10.1007/S11666-012-9790-X/METRICS

Koivuluoto, H., Lagerbom, J., Kylmälahti, M., & Vuoristo, P. (2008). Microstructure and mechanical properties of low-pressure cold-sprayed (LPCS) coatings. *Journal of Thermal Spray Technology*, *17*(5–6), 721–727. https://doi.org/10.1007/s11666-008-9245-6

Kosarev, V. F., Klinkov, S. V., Alkhimov, A. P., & Papyrin, A. N. (2003). On some aspects of gas dynamics of the cold spray process. *Journal of Thermal Spray Technology*, *12*(2), 265–281. https://doi.org/10.1361/10599630377034838 4/METRICS

Kumar, S., & Chavan, N. M. (2011). Cold spray coating technology: activities at ARCI. *Briefing, International Advanced Research Centre for Powder Metallurgy and New Materials (ARCI) Hyderabad*.

Kumar, S., Kumar, M., & Jindal, N. (2020). Overview of cold spray coatings applications and comparisons: a critical review. *World Journal of Engineering*, *17*(1), 27–51. https://doi.org/10.1108/WJE-01-2019-0021

Kurochkin, Y. V., Demin, Y. N., & Soldatenkov, S. I. (2002). Demonstration of the method of cold gasdynamic spraying of coatings. *Chemical and Petroleum Engineering*, *38*(3–4), 245–248.

https://doi.org/10.1023/A:1019637513791/METRICS

Lapushkina, E., & Sova, A. (2019). Effect of powder mixture composition on the deposition efficiency in cold spay: Modelling and experimental validation. *Coatings*, *9*(12). https://doi.org/10.3390/coatings9120832

Lee, H., Shin, H., & Ko, K. (2010). Effects of gas pressure of cold spray on the formation of Al-based intermetallic compound. *Journal of Thermal Spray Technology*, *19*(1–2), 102–109. https://doi.org/10.1007/S11666-009-9407-1/METRICS

Lee, H. Y., Jung, S. H., Lee, S. Y., You, Y. H., & Ko, K. H. (2005). Correlation between Al2O3 particles and interface of Al–Al2O3 coatings by cold spray. *Applied Surface Science*, *252*(5), 1891–1898. https://doi.org/10.1016/J.APSUSC.2005.03.148

Leyman, P. F., & Champagne, V. (2008). Cold spray aluminum for magnesium gearbox repair. *US Army Research Laboratory Weapons & Materials Research Directorate*.

Li, C. J., Li, W. Y., & Liao, H. (2006). Examination of the critical velocity for deposition of particles in cold spraying. *Journal of Thermal Spray Technology*, *15*(2), 212–222. https://doi.org/10.1361/105996306X108093/METRICS

Li, C. J., Wang, H. T., Zhang, Q., Yang, G. J., Li, W. Y., & Liao, H. L. (2010). Influence of spray materials and their surface oxidation on the critical velocity in cold spraying. *Journal of Thermal Spray Technology*, *19*(1–2), 95–101. https://doi.org/10.1007/S11666-009-9427-X/METRICS

Li, J. F., Agyakwa, P. A., Johnson, C. M., Zhang, D., Hussain, T., & McCartney, D. G. (2010). Characterization and solderability of cold sprayed Sn-Cu coatings on Al and Cu substrates. *Surface and Coatings Technology*, *204*(9–10), 1395–1404. https://doi.org/10.1016/j.surfcoat.2009.09.025

Li, W. Y., Li, C. J., & Liao, H. (2006). Effect of annealing treatment on the microstructure and properties of cold-sprayed Cu coating. *Journal of Thermal*

Spray Technology, *15*(2), 206–211. https://doi.org/10.1361/105996306X108066

Li, W., Yang, K., Yin, S., Yang, X., Xu, Y., & Lupoi, R. (2018). Solid-state additive manufacturing and repairing by cold spraying: A review. *Journal of Materials Science & Technology*, *34*(3), 440–457. https://doi.org/10.1016/J.JMST.2017.09.015

Li, X., Yan, J., Yu, T., & Zhang, B. (2022). Versatile nonfluorinated superhydrophobic coating with self-cleaning, anti-fouling, anti-corrosion and mechanical stability. *Colloids and Surfaces A: Physicochemical and Engineering Aspects*, *642*, 128701. https://doi.org/10.1016/J.COLSURFA.2022.128701

Li, Y. J., Luo, X. T., & Li, C. J. (2017). Dependency of deposition behavior, microstructure and properties of cold sprayed Cu on morphology and porosity of the powder. *Surface and Coatings Technology*, *328*, 304–312. https://doi.org/10.1016/j.surfcoat.2017.08.070

Li, Y. X., Zhang, P. F., Bai, P. K., Zhao, Z. Y., & Liu, B. (2018). Analysis of Geometrical Characteristics and Properties of Laser Cladding 85 wt.% Ti + 15 wt.% TiBCN Powder on 7075 Aluminum Alloy Substrate. *Materials 2018, Vol. 11, Page 1551*, *11*(9), 1551. https://doi.org/10.3390/MA11091551

Lima, R. S., Karthikeyan, J., Kay, C. M., Lindemann, J., & Berndt, C. C. (2002). Microstructural characteristics of cold-sprayed nanostructured WC–Co coatings. *Thin Solid Films*, *416*(1–2), 129–135. https://doi.org/10.1016/S0040-6090(02)00631-4

Lima, R. S., Kucuk, A., Berndt, C. C., Karthikeyan, J., Kay, C. M., & Lindemann, J. (2002). Deposition efficiency, mechanical properties and coating roughness in cold-sprayed titanium. *Journal of materials science letters, 21*, 1687–1689.

Lourenço, J. C., Faria, M. I. S. T., Robin, A., Prisco, L. P., & Puccini, M. C. (2015). Influence of process parameters on localized corrosion of AA7075 alloy during the production of aeronautic components. *Materials and Corrosion*, *66*(12), 1498–1503. https://doi.org/10.1002/MACO.201508402

Lukiyanchuk, I. V., Rudnev, V. S., Kuryavyi, V. G., Boguta, D. L., Bulanova, S. B., & Gordienko, P. S. (2004). Surface morphology, composition and thermal behavior of tungsten-containing anodic spark coatings on aluminium alloy. *Thin Solid Films*, *446*(1), 54–60. https://doi.org/10.1016/S0040-6090(03)01318-X

Lupoi, R., & O'Neill, W. (2011). Powder stream characteristics in cold spray nozzles. *Surface & Coatings Technology*, *206*(6), 1069–1076. https://doi.org/10.1016/J.SURFCOAT.2011.07.061

Lv, M., & Du, M. (2018). A review: microbiologically influenced corrosion and the effect of cathodic polarization on typical bacteria. *Reviews in Environmental Science and Biotechnology*, *17*(3), 431–446. https://doi.org/10.1007/S11157-018-9473-2/METRICS

Maev RG, Leshchynsky V (2008) Introduction to low pressure gas dynamic spray: physics & technology. Wiley-VCH, Weinheim

Mäkinen, H., Lagerbom, J., & Vuoristo, P. (2007). *Adhesion of cold sprayed coatings: effect of powder, substrate, and heat treatment* (pp. 31–36). https://researchportal.tuni.fi/en/publications/adhesion-of-cold-sprayed-coatings-effect-of-powder-substrate-and-

Marrocco, T., McCartney, D. G., Shipway, P. H., & Sturgeon, A. J. (2006). Production of titanium deposits by cold-gas dynamic spray: Numerical modeling and experimental characterization. *Journal of Thermal Spray Technology*, *15*(2), 263–272. https://doi.org/10.1361/105996306X108219/METRICS

Masuda, H., & Fukuda, K. (1995). Ordered Metal Nanohole Arrays Made by a Two-Step Replication of Honeycomb Structures of Anodic Alumina. *Science*, *268*(5216), 1466–1468. https://doi.org/10.1126/SCIENCE.268.5216.1466

Matuszak, J., Kłonica, M., & Zagórski, I. (2019). Measurements of Forces and Selected Surface Layer Properties of AW-7075 Aluminum Alloy Used in the Aviation Industry after Abrasive Machining. *Materials 2019, Vol. 12, Page 3707*, *12*(22), 3707. https://doi.org/10.3390/MA12223707

Meininger, M., Meininger, S., Groll, J., Gbureck, U., & Moseke, C. (2018). Silver and copper addition enhances the antimicrobial activity of calcium hydroxide coatings on titanium. *Journal of Materials Science: Materials in Medicine*, *29*(5), 1–9. https://doi.org/10.1007/S10856-018-6065-1/METRICS

Melendez, N. M., & McDonald, A. G. (2013). Development of WC-based metal matrix composite coatings using low-pressure cold gas dynamic spraying. *Surface and Coatings Technology*, *214*, 101–109. https://doi.org/10.1016/J.SURFCOAT.2012.11.010

Meng, X., Zhang, J., Zhao, J., Liang, Y., & Zhang, Y. (2011). Influence of Gas Temperature on Microstructure and Properties of Cold Spray 304SS Coating. *Journal of Materials Science & Technology*, *27*(9), 809–815. https://doi.org/10.1016/S1005-0302(11)60147-3

Meydanoglu, O., Jodoin, B., & Kayali, E. S. (2013). Microstructure, mechanical properties and corrosion performance of 7075 Al matrix ceramic particle reinforced composite coatings produced by the cold gas dynamic spraying process. *Surface and Coatings Technology*, *235*, 108–116. https://doi.org/10.1016/j.surfcoat.2013.07.020

Miroslaw, S., Leszek, L., Mariusz, W., & Marcin, W. (2020). Comparative Study on the Cavitation Erosion and Sliding Wear of Cold Sprayed Al/Al2O3 and Cu/Al2O3 Coatings, and Stainless Steel, Aluminum Alloy, Copper and Brass. *Metals*.

Moridi, A., Hassani-Gangaraj, S. M., Guagliano, M., & Dao, M. (2014). Cold spray coating: Review of material systems and future perspectives. *Surface Engineering*, *30*(6), 369–395. https://doi.org/10.1179/1743294414Y.0000000270

Muthukumar, N., Rajasekar, A., Ponmariappan, S., Mohanan, S., Maruthamuthu, S., Muralidharan, S., Subramanian, P., Palaniswamy, N., & Raghavan, M. (2003). Microbiologically influenced corrosion in petroleum product pipelines - A

review. *IJEB Vol.41(09) [September 2003]*. http://nopr.niscpr.res.in/handle/123456789/17162

Naimi, A., Yousfi, H., & Trari, M. (2012). Microstructure and corrosion resistance of molybdenum and aluminum coatings thermally sprayed on 7075-T6 aluminum alloy. *Protection of Metals and Physical Chemistry of Surfaces*, *48*(5), 557–562. https://doi.org/10.1134/S2070205112050061/METRICS

Nelson, V. V., Maria, O. T., Mamiè, S. V., & Maritza, P. C. (2017). Microbiologically Influenced Corrosion in Aluminium Alloys 7075 and 2024. *Aluminium Alloys - Recent Trends in Processing, Characterization, Mechanical Behavior and Applications*. https://doi.org/10.5772/intechopen.70735

Ngai, S., Ngai, T., Vogel, F., Story, W., Thompson, G. B., & Brewer, L. N. (2018). Saltwater corrosion behavior of cold sprayed AA7075 aluminum alloy coatings. *Corrosion Science*, *130*(December 2016), 231–240. https://doi.org/10.1016/j.corsci.2017.10.033

Nie, Y., Kalapos, C., Nie, X., Murphy, M., Hussein, R., & Zhang, J. (2010). Superhydrophilicity and antibacterial property of a Cu-dotted oxide coating surface. *Annals of Clinical Microbiology and Antimicrobials*, *9*(1), 25. https://doi.org/10.1186/1476-0711-9-25/FIGURES/4

Ning, X. J., Jang, J. H., & Kim, H. J. (2007). The effects of powder properties on in-flight particle velocity and deposition process during low pressure cold spray process. *Applied Surface Science*, *253*(18), 7449–7455. https://doi.org/10.1016/j.apsusc.2007.03.031

Nunthavarawong, P., Sacks, N., & Botef, I. (2016). Effect of powder feed rate on the mechanical properties of WC-5 wt%Ni coatings deposited using low pressure cold spray. *International Journal of Refractory Metals and Hard Materials*, *61*, 230–237. https://doi.org/10.1016/J.IJRMHM.2016.10.001

Ogawa, K., Ito, K., Ichimura, K., Ichikawa, Y., Ohno, S., & Onda, N. (2008). Characterization of low-pressure cold-sprayed aluminum coatings. *Journal of Thermal Spray Technology*, *17*(5–6), 728–735. https://doi.org/10.1007/S11666-

008-9254-5/METRICS

Osaki, S., Kondo, H., & Kinoshita, K. (2006). Contribution of hydrogen embrittlement to SCC process in excess Si type Al-Mg-Si alloys. *Materials Transactions*, *47*(4), 1127–1134.

Özkan, D., Özekinci, M. C., Öztürk, Z. T., & Sulukan, E. (2020). Two dimensional materials for military applications. *Defence Science Journal*, *70*(6), 672–681. https://doi.org/10.14429/DSJ.70.15879

Papyrin, A. (2001). Cold Spray Technology. *Advanced Materials & Processes*, *159*(9), 49–49. https://go.gale.com/ps/i.do?p=AONE&sw=w&issn=08827958&v=2.1&it=r&id=GALE%7CA78413443&sid=googleScholar&linkaccess=fulltext

Papyrin, A. (2007). The development of the cold spray process. *The Cold Spray Materials Deposition Process: Fundamentals and Applications*, 11–42. https://doi.org/10.1533/9781845693787.1.11

Papyrin, A., Kosarev, V., Klinkov, S., Alkimov, A., & Fomin, V. (2006). Cold Spray Technology. *Cold Spray Technology*, 1–328. https://doi.org/10.1016/B978-0-08-045155-8.X5000-5

Papyrin, A., Kosarev, V., Klinkov, S., Alkimov, A., & Fomin, V. (2007). Chapter 4 - Cold spray equipments and technologies BT - Cold Spray Technology. *Cold Spray Technology*, 179–247. http://www.sciencedirect.com/science/article/pii/B9780080451558500041

Papyrin, A. N., Klinkov, S. V., & Kosarev, V. F. (2005). Effect of the Substrate Surface Activation on the Process of Cold Spray Coating Formation. *Thermal Spray 2005: Proceedings from the International Thermal Spray Conference*, *83652*, 145–150. https://doi.org/10.31399/ASM.CP.ITSC2005P0145

Pasquet, J., Chevalier, Y., Pelletier, J., Couval, E., Bouvier, D., & Bolzinger, M. A. (2014). The contribution of zinc ions to the antimicrobial activity of zinc oxide. *Colloids and Surfaces A: Physicochemical and Engineering Aspects*, *457*(1),

263–274. https://doi.org/10.1016/j.colsurfa.2014.05.057

Pathak, S., & Saha, G. C. (2017). Development of sustainable cold spray coatings and 3D additive manufacturing components for repair/manufacturing applications: A critical review. *Coatings*, *7*(8). https://doi.org/10.3390/coatings7080122

Pathak, S., & Saha, G. C. (Eds.). (2020). *Cold Spray in the Realm of Additive Manufacturing*. https://doi.org/10.1007/978-3-030-42756-6

Pavel, C. C., & Tzimas, E. (2016). Raw materials in the European defence industry. In *European Commission Joint Research Centre*. https://doi.org/10.2790/0444

Pavel, C. C., Tzimas, E., Dias, P. A., & Blagoeva, D. T. (2020). *Raw and Processed Materials Used in the European Defence Industry BT - Advanced Materials for Defense* (R. Fangueiro & S. Rana (Eds.); pp. 1–16). Springer International Publishing.

M. Pourbaix (1966), Atlas of Electrochemical Equilibria in Aqueous Solutions, 2nd ed., National Association of Corrosion Engineers, Houston, TX, USA.

Prasad Rambabu, N. Eswara Prasad, V. V. K., & Wanhill, R. J. H. (2017). Aerospace Materials and Material Technologies, Volume 1: Aerospace Material Technologies. *Aerospace Materials and Material Technologies Volume 1: Aerospace Materials*, *1*(May), 586. https://doi.org/10.1007/978-981-10-2134-3

Rajasekar, A., & Ting, Y. P. (2010). Microbial Corrosion of Aluminum 2024 Aeronautical Alloy by Hydrocarbon Degrading Bacteria Bacillus cereus ACE4 and Serratia marcescens ACE2. *Industrial and Engineering Chemistry Research*, *49*(13), 6054–6061. https://doi.org/10.1021/IE100078U

Raletz, F., Vardelle, M., & Ezo'o, G. (2006). Critical particle velocity under cold spray conditions. *Surface and Coatings Technology*, *201*(5), 1942–1947. https://doi.org/10.1016/J.SURFCOAT.2006.04.061

Raoelison, R. N., Verdy, C., & Liao, H. (2017). Cold gas dynamic spray additive manufacturing today: Deposit possibilities, technological solutions and viable

applications. *Materials and Design*, *133*, 266–287. https://doi.org/10.1016/j.matdes.2017.07.067

Rawat, J., Khandelwal, A., Sharma, N., & Tyagi, S. (2016). Effect of Sulphate reducing bacterial-biofilm isolated from refinery cooling water system and sonication on corrosion of carbon steel. *J. Mater. Environ. Sci*, *7*(2), 596–604.

Reboul, M. C., & Baroux, B. (2011). Metallurgical aspects of corrosion resistance of aluminium alloys. *Materials and Corrosion*, *62*(3), 215–233. https://doi.org/10.1002/MACO.201005650

Rejeski, D., Zhao, F., & Huang, Y. (2018). Research needs and recommendations on environmental implications of additive manufacturing. *Additive Manufacturing*, *19*, 21–28. https://doi.org/10.1016/J.ADDMA.2017.10.019

Richer, P., Jodoin, B., Taylor, K., Sansoucy, E., Johnson, M., & Ajdelsztajn, L. (2005). Effect of Particle Geometry and Substrate Preparation in Cold Spray. *Thermal Spray 2005: Proceedings from the International Thermal Spray Conference*, *83652*, 193–198. https://doi.org/10.31399/ASM.CP.ITSC2005P0193

Rigney, D. A. (1988). Sliding wear of metals. *Annual Review of Materials Science*, *18*(1), 141–163.

Rokni, M. R., Nutt, S. R., Widener, C. A., Champagne, V. K., & Hrabe, R. H. (2017). Review of Relationship Between Particle Deformation, Coating Microstructure, and Properties in High-Pressure Cold Spray. *Journal of Thermal Spray Technology 2017 26:6*, *26*(6), 1308–1355. https://doi.org/10.1007/S11666-017-0575-0

Rooy, E. L. (1990). Introduction to Aluminum and Aluminum Alloys. *Properties and Selection: Nonferrous Alloys and Special-Purpose Materials*, 3–14. https://doi.org/10.31399/ASM.HB.V02.A0001057

Runge, J. M. (2018). A Brief History of Aluminum and Its Alloys. In *The Metallurgy of Anodizing Aluminum*. https://doi.org/10.1007/978-3-319-72177-4_1

Sakaki, K., Tajima, T., Li, H., Shinkai, S., & Shimizu, Y. (2004). Influence of substrate conditions and traverse speed on cold sprayed coatings. *Proceedings of the International Thermal Spray Conference*, 358–362. https://doi.org/10.31399/ASM.CP.ITSC2004P0358/19737/INFLUENCE-OF-SUBSTRATE-CONDITIONS-AND-TRAVERSE

Sander, W., & Meissner, K. L. (1926). Der Einfluß der Verbindung MgZn2 auf die Vergütbarkeit von Aluminiumlegierungen. *Zeitschrift Für Anorganische Und Allgemeine Chemie*, *154*(1), 144–151. https://doi.org/10.1002/ZAAC.19261540111

Sanpo, N., Ang, S. M., Cheang, P., & Khor, K. A. (2009). Antibacterial property of cold sprayed chitosan-cu/al coating. *Journal of Thermal Spray Technology*, *18*(4), 600–608. https://doi.org/10.1007/S11666-009-9391-5/METRICS

Sanpo, N., Hailan, C., Loke, K., Keng, K. P., Cheang, P., Berndt, C. C., & Khor, K. A. (2011). *Biocompatibility and Antibacterial property of Cold Sprayed ZnO /Titanium Composite Coating* . 140–144. https://doi.org/10.1142/9789814354868_0027

Sanpo, N., Saraswati, Lu, T. M., & Cheang, P. (2008). Anti-bacterial property of cold sprayed ZnO-Al coating. *BioMedical Engineering and Informatics: New Development and the Future - Proceedings of the 1st International Conference on BioMedical Engineering and Informatics, BMEI 2008*, *1*, 488–491. https://doi.org/10.1109/BMEI.2008.291

Sanpo, N., & Tharajak, J. (2017). Antimicrobial Property of Cold-Sprayed Transition Metals-Substituted Hydroxyapatite/PEEK Coating. *Applied Mechanics and Materials*, *866*, 77–80. https://doi.org/10.4028/WWW.SCIENTIFIC.NET/AMM.866.77

Scamans, G. M., & Holroyd, N. J. H. (1986). Stress-corrosion of aluminium aerospace alloys. *Journal of the Electrochemical Society*, *133*(8), C308–C308.

Scamans, G. M., Holroyd, N. J. H., & Tuck, C. D. S. (1987). The role of magnesium segregation in the intergranular stress corrosion cracking of aluminium alloys. *Corrosion Science*, *27*(4), 329–347. https://doi.org/10.1016/0010-938X(87)90076-X

Schmidt, T., Assadi, H., Gärtner, F., Richter, H., Stoltenhoff, T., Kreye, H., & Klassen, T. (2009). From particle acceleration to impact and bonding in cold spraying. *Journal of Thermal Spray Technology*, *18*(5–6), 794–808. https://doi.org/10.1007/S11666-009-9357-7/FIGURES/22

Schmidt, T., Gaertner, F., & Kreye, H. (2006). New developments in cold spray based on higher gas and particle temperatures. *Proceedings of the International Thermal Spray Conference*, *15*(4), 488–494. https://doi.org/10.1361/105996306X147144/METRICS

Schmidt, T., Gärtner, F., Assadi, H., & Kreye, H. (2006). Development of a generalized parameter window for cold spray deposition. *Acta Materialia*, *54*(3), 729–742. https://doi.org/10.1016/J.ACTAMAT.2005.10.005

Seo, D., Sayar, M., & Ogawa, K. (2012). SiO2 and MoSi2 formation on Inconel 625 surface via SiC coating deposited by cold spray. *Surface and Coatings Technology*, *206*(11–12), 2851–2858. https://doi.org/10.1016/J.SURFCOAT.2011.12.010

Shi, T., Liang, J., Li, X., Zhang, C., & Yang, H. (2022). Improving the Corrosion Resistance of Aluminum Alloy by Creating a Superhydrophobic Surface Structure through a Two-Step Process of Etching Followed by Polymer Modification. *Polymers*, *14*(21). https://doi.org/10.3390/polym14214509

Shi, X., Xie, N., & Gong, J. (n.d.). *Recent Progress in the Research on Microbially Influenced Corrosion: A Bird's Eye View through the Engineering Lens*.

Shkodkin, A., Kashirin, A., Klyuev, O., & Buzdygar, T. (2006). Metal particle deposition stimulation by surface abrasive treatment in gas dynamic spraying. *Journal of Thermal Spray Technology*, *15*(3), 382–386. https://doi.org/10.1361/105996306X124383/METRICS

Shockley, J. M., Descartes, S., Vo, P., Irissou, E., & Chromik, R. R. (2015). The influence of Al2O3 particle morphology on the coating formation and dry sliding wear behavior of cold sprayed Al–Al2O3 composites. *Surface and Coatings Technology*, *270*, 324–333. https://doi.org/10.1016/J.SURFCOAT.2015.01.057

Singh, H., Sidhu, T. S., Kalsi, S. B. S., & Karthikeyan, J. (2013). Development of cold spray from innovation to emerging future coating technology. *Journal of the Brazilian Society of Mechanical Sciences and Engineering*, *35*(3), 231–245. https://doi.org/10.1007/s40430-013-0030-1

Singh, S., Raman, R. K. S., Berndt, C. C., & Singh, H. (2021). Influence of cold spray parameters on bonding mechanisms: A review. *Metals*, *11*(12). https://doi.org/10.3390/met11122016

Smith, M. F. (2007). Comparing cold spray with thermal spray coating technologies. *The Cold Spray Materials Deposition Process: Fundamentals and Applications*, *1911*, 43–61. https://doi.org/10.1533/9781845693787.1.43

Smith, R. N. (1991). Developments in fuel microbiology. *Biodeterioration and Biodegradation*, *8*, 112–124.

Staley, J. T. (2017). Corrosion of aluminum aerospace alloys. *Materials Science Forum*, *877*, 485–491. https://doi.org/10.4028/www.scientific.net/MSF.877.485

Starke, E. A., & Staley, J. T. (2010). Application of modern aluminium alloys to aircraft. *Fundamentals of Aluminium Metallurgy: Production, Processing and Applications*, *32*(95), 747–783. https://doi.org/10.1533/9780857090256.3.747

Steenkiste, T. H. V., Smith, J. R., & Teets, R. E. (2002). Aluminum coatings via kinetic spray with relatively large powder particles. *Surface and Coatings Technology*, *154*(2–3), 237–252. https://doi.org/10.1016/S0257-8972(02)00018-X

Stoltenhoff, T., Borchers, C., Gärtner, F., & Kreye, H. (2006). Microstructures and key properties of cold-sprayed and thermally sprayed copper coatings. *Surface*

and Coatings Technology, *200*(16–17), 4947–4960. https://doi.org/10.1016/j.surfcoat.2005.05.011

Stoltenhoff, T., Kreye, H., & Richter, H. J. (2002). An analysis of the cold spray process and its coatings. *Journal of Thermal Spray Technology*, *11*(4), 542–550. https://doi.org/10.1361/105996302770348682/METRICS

T. Stoltenhoff, F. Zimmermann, (2012). LOXPlate® coatings for aluminum aerospace components exposed to high dynamic stresses, Praxair Surface Technologies GmbH, Ratingen, Germany.

Subramanian, C. (1992). Some considerations towards the design of a wear resistant aluminium alloy. *Wear*, *155*(1), 193–205. https://doi.org/10.1016/0043-1648(92)90118-R

Subramanian, C. (2010). Wear properties of aluminium-based alloys. *Surface Engineering of Light Alloys: Aluminium, Magnesium and Titanium Alloys*, 40–57. https://doi.org/10.1533/9781845699451.1.40

Subramanian, C., Asaithambi, P., & Kishore. (1986). Friction and Wear of Epoxy Resin Containing Graphite. *Http://Dx.Doi.Org/10.1177/073168448600500304*, *5*(3), 200–208. https://doi.org/10.1177/073168448600500304

Sudharshan Phani, P., Srinivasa Rao, D., Joshi, S. V., & Sundararajan, G. (2007). Effect of process parameters and heat treatments on properties of cold sprayed copper coatings. *Journal of Thermal Spray Technology*, *16*(3), 425–434. https://doi.org/10.1007/s11666-007-9048-1

Sun, C., Hui, R., Qu, W., Yick, S., Sun, C., & Qian, W. (2010). Effects of processing parameters on microstructures of TiO2 coatings formed on titanium by plasma electrolytic oxidation. *Journal of Materials Science*, *45*(22), 6235–6241. https://doi.org/10.1007/S10853-010-4718-7/METRICS

Sundberg, K., Wang, Y., Mishra, B., Carl, A., Grimm, R., Te, A., Lozeau, L., Sisson, R., & Cote, D. (2019). The Effect of Corrosion on Conventional and Nanomaterial Copper Cold Spray Surfaces for Antimicrobial Applications.

Biomedical Journal of Scientific & Technical Research, *22*(3), 16753–16763. https://doi.org/10.26717/BJSTR.2019.22.003768

Suo, X. K., Guo, X. P., Li, W. Y., Planche, M. P., & Liao, H. L. (2012). Investigation of deposition behavior of cold-sprayed magnesium coating. *Journal of Thermal Spray Technology*, *21*(5), 831–837. https://doi.org/10.1007/S11666-012-9777-7/METRICS

Tait, W. S. (1994). *An introduction to electrochemical corrosion testing for practicing engineers and scientists*. PairODocs Publications.

Taylor, K., Jodoin, B., & Karov, J. (2006). Particle loading effect in cold spray. *Journal of Thermal Spray Technology*, *15*(2), 273–279. https://doi.org/10.1361/105996306X108237/METRICS

Tekin, K. C. (2016). Electrochemical Mechanical and Tribological Properties of Plasma Electrolytic Oxide Coatings on Titanium Alloys [Unpublished doctoral dissertation]. Dokuz Eylül University.

Thakur, A., Raman, R., & Malhotra, S. N. (2007). Hydrogen embrittlement studies of aged and retrogressed-reaged Al–Zn–Mg alloys. *Materials Chemistry and Physics*, *101*(2–3), 441–447. https://doi.org/10.1016/J.MATCHEMPHYS.2006.08.004

Tiamiyu, A. A., & Schuh, C. A. (2020). Particle flattening during cold spray: Mechanistic regimes revealed by single particle impact tests. *Surface and Coatings Technology*, *403*, 126386. https://doi.org/10.1016/J.SURFCOAT.2020.126386

Tiamiyu, A. A., Sun, Y., Nelson, K. A., & Schuh, C. A. (2021). Site-specific study of jetting, bonding, and local deformation during high-velocity metallic microparticle impact. *Acta Materialia*, *202*, 159–169. https://doi.org/10.1016/J.ACTAMAT.2020.10.057

Tinashe, S. E. (2010). *Conceptual Design of a Low Pressure Cold Gas Dynamic Spray (LPCGDS) System*.

Tokarev, A. O. (1996). Structure of aluminum powder coatings prepared by cold gasdynamic spraying. *Metal Science and Heat Treatment*, *38*(3), 136–139. https://doi.org/10.1007/BF01401446/METRICS

Triantou, K. I., Pantelis, D. I., Guipont, V., & Jeandin, M. (2015). Microstructure and tribological behavior of copper and composite copper+alumina cold sprayed coatings for various alumina contents. *Wear*, *336–337*, 96–107. https://doi.org/10.1016/j.wear.2015.05.003

US5302414A - Gas-dynamic spraying method for applying a coating - Google Patents. (n.d.). Retrieved December 14, 2023, from https://patents.google.com/patent/US5302414A/en?oq=P.+Alkhimov%2C+A.+N.+Papyrin%2C+V.+P.+Dosarev%2C+N.+J.+Nesterovich%2C+M.+M.+Shuspanov%2C+US+Patent+5%2C302%2C414+-+April+12%2C+1994.

Van Der Walde, K., Brockenbrough, J. R., Craig, B. A., & Hillberry, B. M. (2005). Multiple fatigue crack growth in pre-corroded 2024-T3 aluminum. *International Journal of Fatigue*, *27*(10–12), 1509–1518. https://doi.org/10.1016/J.IJFATIGUE.2005.06.026

Vandelli, G. (1968). The Resıstance To Dry Slıdıng Wear Of Some Cast Heat-Resıstant Alumınum Alloys. *Alluminio*, *37*(3), 121–129.

Vaughn-Thomas, D. M. (n.d.). *Microbial Influenced Corrosion: Role of Bacterial Attachment and Biofilm*.

Villafuerte, J. (2010). Current and future applications of cold spray technology. *Metal Finishing*, *108*(1), 37–39. https://doi.org/10.1016/S0026-0576(10)80005-4

Villafuerte, J., & Zheng, W. (n.d.). *Corrosion Protection of Magnesium by Cold Spray Corrosion Protection of Magnesium Alloys by Cold Spray*. https://doi.org/10.5772/13985

Vucko, M. J., King, P. C., Poole, A. J., Carl, C., Jahedi, M. Z., & de Nys, R. (2012). Cold spray metal embedment: an innovative antifouling technology. *Biofouling*,

28(3), 239–248. https://doi.org/10.1080/08927014.2012.670849

Wang, J., & Villafuerte, J. (2009). Low pressure cold spraying of tungsten carbide composite coatings. *Advanced Materials & Processes*, *167*(2), S8–S8. https://go.gale.com/ps/i.do?p=AONE&sw=w&issn=08827958&v=2.1&it=r&id=GALE%7CA198941421&sid=googleScholar&linkaccess=fulltext

Wang, Q., Birbilis, N., & Zhang, M. X. (2012). On the formation of a diffusion bond from cold-spray coatings. *Metallurgical and Materials Transactions A: Physical Metallurgy and Materials Science*, *43*(5), 1395–1399. https://doi.org/10.1007/S11661-012-1098-4/METRICS

Wang, X., Feng, F., Klecka, M. A., Mordasky, M. D., Garofano, J. K., El-Wardany, T., Nardi, A., & Champagne, V. K. (2015). Characterization and modeling of the bonding process in cold spray additive manufacturing. *Additive Manufacturing*, *8*, 149–162. https://doi.org/10.1016/J.ADDMA.2015.03.006

Widener, C. A., Carter, M. J., Hrabe, R. H., Hoiland, B., Stamey, T. E., Champagne, V. K., & Eden, T. J. (2015). Navy valve actuator repair using cold spray. *International Thermal Spray Conference and Exposition, ITSC 2015*, 1092–1097.

Widener, C., Hrabe, R., James, B., & Champagne, V. (2013). B1 Bomber-FEB panel repair by cold spray. *Cold Spray Action Team (CSAT) Meeting*.

Winnicki, M., Małachowska, A., Baszczuk, A., Rutkowska-Gorczyca, M., Kukla, D., Lachowicz, M., & Ambroziak, A. (2017). Corrosion protection and electrical conductivity of copper coatings deposited by low-pressure cold spraying. *Surface and Coatings Technology*, *318*, 90–98. https://doi.org/10.1016/j.surfcoat.2016.12.101

Wino, W., Gathut, Y. ;, Gunadi, I., & Kasim, ; (2022). Metal as a Ballistic-Resistant Lightweight Protective Material in the Military Field. *International Journal of Social Science Research and Review*, *5*(12), 287–297. http://dx.doi.org/10.47814/ijssrr.v5i12.808

Wrona, A., Bilewska, K., Lis, M., Kamińska, M., Olszewski, T., Pajzderski, P., Więcław, G., Jaśkiewicz, M., & Kamysz, W. (2017). Antimicrobial properties of protective coatings produced by plasma spraying technique. *Surface and Coatings Technology*, *318*, 332–340. https://doi.org/10.1016/J.SURFCOAT.2017.01.101

Wu, J., Fang, H., Yoon, S., Kim, H., & Lee, C. (2006). The rebound phenomenon in kinetic spraying deposition. *Scripta Materialia*, *54*(4), 665–669. https://doi.org/10.1016/J.SCRIPTAMAT.2005.10.028

Wu, J., Yang, J., Fang, H., Yoon, S., & Lee, C. (2006). The bond strength of Al–Si coating on mild steel by kinetic spraying deposition. *Applied Surface Science*, *252*(22), 7809–7814. https://doi.org/10.1016/J.APSUSC.2005.09.015

Wu, L. K., Liu, L., Li, J., Hu, J. M., Zhang, J. Q., & Cao, C. N. (2010). Electrodeposition of cerium (III)-modified bis-[triethoxysilypropyl]tetra-sulphide films on AA2024-T3 (aluminum alloy) for corrosion protection. *Surface and Coatings Technology*, *204*(23), 3920–3926. https://doi.org/10.1016/J.SURFCOAT.2010.05.027

Xiong, Y., Zhuang, W., & Zhang, M. (2015). Effect of the thickness of cold sprayed aluminium alloy coating on the adhesive bond strength with an aluminium alloy substrate. *Surface and Coatings Technology*, *270*, 259–265. https://doi.org/10.1016/j.surfcoat.2015.02.048

Xu, L., Wang, R., Gen, M., Lu, L., & Han, G. (2019). Preparation and Properties of Graphene/Nickel Composite Coating Based on Textured Surface of Aluminum Alloy. *Materials 2019, Vol. 12, Page 3240*, *12*(19), 3240. https://doi.org/10.3390/MA12193240

Xuewu, L., Hongxing, W., Tian, S., Chuanwei, Z., Xiaona, J., Xuegang, Z., & Chen, L. (2022). Efficient preparation and anticorrosion mechanism of superhydrophobic 7075 aviation aluminum alloy. *Rare Metal Materials and Engineering*, *51*(1), 6–10.

Yandouzi, M., Richer, P., & Jodoin, B. (2009). SiC particulate reinforced Al–12Si

alloy composite coatings produced by the pulsed gas dynamic spray process: Microstructure and properties. *Surface and Coatings Technology*, *203*(20–21), 3260–3270. https://doi.org/10.1016/J.SURFCOAT.2009.04.001

Yang, B., Shan, H., Liang, Y., Ma, Y., Niu, S., Zhu, X., & Li, Y. (2022). Effect of adhesive application on friction self-piercing riveting (F-SPR) process of AA7075-T6 aluminum alloy. *Journal of Materials Processing Technology*, *299*, 117336. https://doi.org/10.1016/J.JMATPROTEC.2021.117336

Yin, S., Aldwell, B., & Lupoi, R. (2017). Cold spray additive manufacture and component restoration. *Cold-Spray Coatings: Recent Trends and Future Perspectives*, 195–224. https://doi.org/10.1007/978-3-319-67183-3_6/COVER

Yin, S., Cavaliere, P., Aldwell, B., Jenkins, R., Liao, H., Li, W., & Lupoi, R. (2018). Cold spray additive manufacturing and repair: Fundamentals and applications. *Additive Manufacturing*, *21*(April), 628–650. https://doi.org/10.1016/j.addma.2018.04.017

Zhang, L., Yang, S., Lv, X., & Jie, X. (2019). Wear and Corrosion Resistance of Cold-Sprayed Cu-Based Composite Coatings on Magnesium Substrate. *Journal of Thermal Spray Technology*, *28*(6), 1212–1224. https://doi.org/10.1007/s11666-019-00887-9

Zhang, Z., Liu, F., Han, E. H., & Xu, L. (2020). Mechanical and corrosion properties in 3.5% NaCl solution of cold sprayed Al-based coatings. *Surface and Coatings Technology*, *385*(August 2019), 125372. https://doi.org/10.1016/j.surfcoat.2020.125372

Zhao, X., & Frankel, G. S. (2007). Quantitative study of exfoliation corrosion: Exfoliation of slices in humidity technique. *Corrosion Science*, *49*(2), 920–938. https://doi.org/10.1016/J.CORSCI.2006.05.037

Zhou, B., Liu, B., & Zhang, S. (2021). The advancement of 7xxx series aluminum alloys for aircraft structures: A review. *Metals*, *11*(5). https://doi.org/10.3390/met11050718

Zhu, L., Xu, B., Zhou, M., Hu, S., & Zhang, G. (2020). Fabrication and characterization of Al–Zn–Cu composite coatings with different Cu contents by cold spraying. *Surface Engineering*, *36*(10), 1090–1096. https://doi.org/10.1080/02670844.2020.1748339

Ziemian, C. W., Wright, W. J., & Cipoletti, D. E. (2018). Influence of Impact Conditions on Feedstock Deposition Behavior of Cold-Sprayed Fe-Based Metallic Glass. *Journal of Thermal Spray Technology*, *27*(5), 843–856. https://doi.org/10.1007/S11666-018-0720-4/FIGURES/18